Indirect methods of obtaining activity and mobility of structure-borne sound sources

Thesis submitted in accordance with the requirements of the University of Liverpool for the degree of Doctor in Philosophy

by

Christoph Höller

November 2013

Indirect methods of obtaining activity and mobility of structure-borne sound sources

by
Christoph Höller

The work reported in this thesis focuses on the development of indirect methods for the experimental determination of important source parameters for structure-borne sound source characterization. In the first part of the thesis, matrix inversion methods for the determination of blocked forces are investigated. A simplified measurement procedure is proposed which offers a solution to the two major challenges to these methods, namely the acquisition of the FRF matrix and the problems associated with matrix inversion. The proposed procedure involves a free, low-mobility receiver plate which is modelled numerically. Calculated FRFs are used together with measured velocity responses to inversely determine the blocked forces. It is found that while the method has great potential in principle, in practice the accurate modelling of the receiver plate is of critical importance. In the second part of the thesis, three formulations are considered for the indirect determination of source mobility. Instead of performing measurements on the source in the free state, the source mobility is obtained from measurements made *in-situ*. This approach is beneficial if the source is difficult to suspend, or if it contains non-linear structural elements. The three formulations are validated numerically and experimentally. It is found that the methods can quantify source mobilities of single-contact and multi-contact sources from *in-situ* measurements. However, typical measurement errors, such as background noise or inaccuracies in sensor positioning, can significantly reduce the accuracy and reliability of the methods. In the final part of the thesis, the reception plate method for the determination of the power injected by a high-mobility source into a low-mobility receiver is reviewed, and a source substitution method proposed as a development. The substitution method circumvents problems that may arise when the reception plate method is applied to coupled walls and floors. A special focus of investigation is on the calibration of the receiver structure. It is found that the calibration can be performed with shaker or hammer, and that an average calibration factor may be used. The source substitution method thus offers a potential alternative to the reception plate method, for application with coupled plates.

Acknowledgements

The work presented in this thesis has been carried out at the Acoustics Research Unit at the University of Liverpool. The financial support by the Engineering and Physical Sciences Research Council of the UK under grant EP/H040293/1 is gratefully acknowledged.

I would like to express my sincere gratitude to Prof. Barry Gibbs. He has made these last three years an enjoyable and valuable experience, and without his guidance and support this thesis would not have been possible. His incessant encouragement and permanent availability are qualities that are not to be taken for granted in a supervisor. On a more personal note, I would like to thank him for many good conversations, particularly on music and concert hall acoustics. Barry, it was a pleasure.

Dr. Gary Seiffert deserves my thanks for his tireless assistance regarding all things practical, and for imparting his wisdom concerning a plethora of issues, from the perfect cup of tea to the subtleties of British humour. The ARU would be different without him.

I would also like to thank the other members of the Acoustics Research Unit. In particular, I am grateful to Dr. Carl Hopkins, Dr. Matthew Robinson, David Wilson, and Nuno Ferreira, for help with measurements and for valuable discussions on signal processing, structural acoustics, and SEA.

Last but not least, I would like to thank my family for their unfailing support and encouragement. I would also like to thank the staff and members of Christ Church Liverpool, for friendship and fellowship that are rare to find, and for encouraging me to seek the glory of God in all I do.

Soli Deo Gloria.

Contents

List of Figures

List of Tables

List of Symbols

Abbreviations

BK	Brüel & Kjær
BS	British Standard
CEN	European Committee for Standardization
CHP	Combined heating and power unit
DOF	Degree of freedom
EDC	Energy decay curve
EN	European Norm
FEA	Finite element analysis
FFFF	Rectangular plate with free boundary conditions
FFT	Fast Fourier Transform
FRF	Frequency response function
ISO	International Standards Organization
LDS	Ling Dynamic Systems
MDOF	Multiple degrees of freedom
SDOF	Single degree of freedom
SEA	Statistical Energy Analysis
SNR	Signal-to-noise ratio
SVR	Singular value rejection
TC	Technical Committee
TPA	Transfer Path Analysis
WG	Working Group

Lower case letters

Symbol	**Unit**	**Description**
c_B	m/s	Bending wavespeed

c_L	m/s	Quasi-longitudinal wavespeed
f	Hz	Frequency
f_0	Hz	Resonance frequency
f_s	Hz	Sampling frequency
h	m	Plate thickness
j	–	Imaginary unit $\sqrt{-1}$
k	N/m	Spring stiffness
k_B	1/m	Bending wavenumber
l_x, l_y, l_z	m	Geometrical dimension
m	kg	Mass
m'	kg/m	Mass per unit length
m''	kg/m^2	Mass per unit area
n, n_∞	1/Hz	(Asymptotic) modal density
v_x, v_y, v_z	m/s	Velocity in x, y, z direction
v_f	m/s	Free velocity
$\langle v^2 \rangle$	m/s	Mean square velocity

Upper case letters

Symbol	**Unit**	**Description**
A	m^2	Area
B	Nm^2	Bending stiffness
C_f	–	Coupling function
E	N/m^2	Young's modulus of elasticity
E_i	J	Energy of subsystem i
F_x, F_y, F_z	N	Force in x, y, z direction
F_b	N	Blocked force
M_x, M_y, M_z	Nm	Moment in x, y, z direction
M	–	Modal overlap factor
N	–	Mode count
P	W	Real part of source power
Q	W	Complex source power
R	W	Imaginary part of source power
S_c	W	Source descriptor
S_{FF}	N^2	Force auto-spectrum
S_{vv}	(m/s)^2	Velocity auto-spectrum

S_{Fv}	Nm/s	Cross-spectrum between force and velocity
T_s	s	Structural reverberation time
Y	$\mathrm{ms}^{-1}/\mathrm{N}$	Mechanical mobility
Y_∞	$\mathrm{ms}^{-1}/\mathrm{N}$	Infinite plate/beam mobility
Z	$\mathrm{N/ms}^{-1}$	Mechanical impedance

Bold symbols

Symbol	**Unit**	**Description**
$\mathbf{F_b}$	N	Generalized blocked force vector
$\mathbf{F_r}$	N	Receiver force vector
$\mathbf{v_f}$	m/s	Generalized free velocity vector
$\mathbf{v_r}$	m/s	Receiver velocity vector
$\mathbf{Y_S}$	$\mathrm{ms}^{-1}/\mathrm{N}$	Source mobility matrix
$\mathbf{Y_R}$	$\mathrm{ms}^{-1}/\mathrm{N}$	Receiver mobility matrix
$\mathbf{Y_C}$	$\mathrm{ms}^{-1}/\mathrm{N}$	Coupled mobility matrix

Greek symbols

Symbol	**Unit**	**Description**
γ^2	–	Coherence
η	–	Loss factor
η_{ii}	–	Internal loss factor
η_{ij}	–	Coupling loss factor
$\theta_x, \theta_y, \theta_z$	rad/s	Angular velocity in x, y, z direction
κ	–	Condition number
λ	–	Regularization parameter
λ_B	m	Bending wavelength
ν	–	Poisson's ratio
ρ	$\mathrm{kg/m}^3$	Density
σ	–	Singular value
ϕ	rad	Phase
ϕ_n	–	Beam mode shape
ψ_{mn}	–	Plate mode shape
ω	1/s	Angular frequency
ω_{mn}	1/s	Eigenfrequency

1 Introduction

1.1 Background and motivation

Noise in buildings is often the result of the transmission of structure-borne sound. *Structure-borne sound* [38] is defined as vibrational energy, propagating in the form of elastic waves through a solid medium. It is generated by sources such as engines, industrial machinery, or household appliances, and is subsequently transmitted via structure-borne paths to living spaces within buildings, or to passenger compartments in vehicles, trains, or ships.

Compared with airborne sound, structure-borne sound travels faster and further. For example, a spinning washing machine in the basement of a dwelling emits both airborne sound and vibrational energy. While the airborne component is usually contained within the source room, provided the doors are closed, the structure-borne component may propagate throughout the building structure, and be radiated in other parts of the house, remote from the source. Thus, structure-borne paths play a crucial role in sound transmission, and structure-borne sound sources are among the most important contributors to noise in many situations.

For effective noise control, low-noise design of machinery, prediction of sound pressure levels in buildings or vehicles not yet constructed, and troubleshooting in buildings or vehicles already constructed, a thorough understanding of the structural-acoustic process between a structure-borne sound source and a target sound pressure is required, see Figure 1.1.

There are four stages. In the first stage, *generation*, vibration is generated within a structure-borne sound source. The internal mechanisms can be manifold, for example friction, rotation, pressure variations, impacts, or a combination of these. In the second stage, *transmission*, the vibration is transmitted,

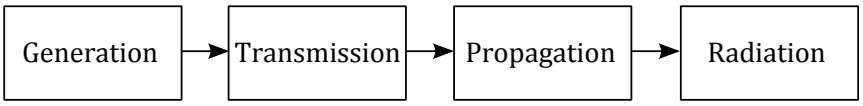

Figure 1.1: Structural-acoustic process, after [38].

first within the source itself, and then to a passive receiver structure, for example a wall or floor in a building. The vibrational energy is then distributed throughout the building structure in the third stage, *propagation*. In the fourth stage, *radiation*, a proportion of the vibrational energy is radiated as audible sound.

The focus of this thesis lies within the second stage of the model in Figure 1.1, specifically on the transmission between source and receiver. Information about both source and receiver is required for an adequate description of the transmission. While a linear passive receiver structure can be characterized by one quantity, namely its structural mobility, a proper source characterization generally requires at least two quantities: information about the source activity, describing the type and strength of the vibration generated, and information about the structural mobility, indicating how the source behaves when coupled to a receiver structure.

According to [99], the characterization of structure-borne sound sources has the following objectives:

- Comparison of sources;
- Definition of limits of emission;
- Prediction of sound pressure levels when installed;
- Quantification of the improvement of new low-noise design.

Several approaches to characterize structure-borne sound sources and describe the transmission of vibrational energy have been developed; the most important are discussed in Chapter 2. A limitation to many methods is often the experimental determination of required parameters, such as source activity and mobility. One reason for this is that a large amount of data needs to be collected for a complete description of the transmission process. While some parameters are relatively easy to obtain (e. g. free velocities), others are more difficult to determine (e. g. structural mobilities involving rotational motion). Experimen-

tal errors can become significant, and can introduce uncertainties regarding the reliability of the source characterization. In conjunction with economic considerations (speed and cost of measurements etc.), this raises the question of how much information is required for an adequate source description.

Two approaches are distinguished. In high-technology sectors, such as the automotive or aerospace industries, engineers often employ refined methods to obtain full sets of data. The expertise required for a successful implementation of these methods is usually available. Measurement methods in these sectors are characterized by their deterministic nature, by the use of narrowband data, and by thorough theoretical foundations. Procedures are sometimes tailor-made to individual problems and troubleshooting.

In industrial sectors such as building engineering, reduced sets of data are required [58]. Engineers in these industries often have to deal with a wide range of sources and receivers, and time and money to perform measurements are limited. Expertise and resources required to successfully implement refined methods are often lacking. Therefore, simple and robust measurement procedures are used, sometimes standardized for a range of sources. Measurement methods are characterized by their statistical nature, by the use of third-octave band levels, and by an emphasis on practicality and applicability.

The two domains outlined above overlap in many ways. One aspect that both have in common is, that often the only option to determine certain source parameters lies in applying indirect methods. For example, the direct measurement of forces exerted by a source on a receiver structure is difficult, as it requires the insertion of transducers into the transmission path. Therefore, indirect methods are required to obtain the forces. A method is termed "indirect," if the required quantity is obtained from a set of other, directly measured quantities. In the case of forces, these could be velocities and mobilities, as described in Chapter 3.

1.2 Thesis objectives

The aim of this thesis is to develop practical measurement methods for quantities required in the description of the transmission of vibrational energy from sources to receivers. In particular, indirect methods for the acquisition of source

parameters are investigated. The thesis examines methods that require a high degree of engineering expertise (e. g. Chapters 5, 6, and 7), and methods that are aimed at application in building engineering (e. g. Chapters 8 and 9). Another focus of the thesis is on simplifying methods that are already used in high-technology industries, such as the automotive industry, to make them available for applications in the building industry (e. g. Chapters 3 and 4).

1.3 Thesis outline

The thesis is divided into three parts, each dealing with one of the following source properties: blocked force, source mobility, and source power. Each part contains a literature review, focusing on the relevant theory and previous research on the topic.

Chapter 2 provides a general introduction to the field of structure-borne sound source characterization and the transmission of vibrational energy between sources and receivers. The basic concepts are explained and the two defining source parameters introduced: source activity and mobility. Common measurement procedures are described, and challenges in obtaining these quantities highlighted. Also provided is an introduction to inverse problems, with a review of the mathematical background of inverse methods.

Chapter 3 and Chapter 4 form the first part of the core of the thesis, focussing on obtaining blocked forces indirectly. In Chapter 3, the matrix inversion method for the indirect determination of operational forces is reviewed, and the inverse problem discussed. A simplified measurement procedure, using a fully-defined receiver structure, is proposed for the determination of approximate blocked forces and moments, for applications in building acoustics. A numerical model for the calculation of point and transfer mobilities of free plates is key to the proposed method, and is described and evaluated.

In Chapter 4, the procedure proposed in Chapter 3 is investigated experimentally. The operational forces of a representative source on a free plate are obtained indirectly, using the proposed method. Calculated transfer mobilities are used, to minimize the required measurement effort. Results using measured transfer mobilities serve as a reference.

The second part of this work (Chapters 5, 6, and 7) examines indirect methods to determine source mobilities. In Chapter 5, structural dynamic relationships of coupled structures are reviewed. Three methods are proposed to indirectly determine the mobility of a structure-borne sound source, from measurements made on a receiver structure, and on the coupled source-receiver structure.

In Chapter 6, the three methods described in Chapter 5 are investigated numerically. Analytical models of coupled rods are employed to prove the validity of the theoretical derivations. Numerical simulations of coupled beams are used to study the effect of common experimental errors on the indirectly determined mobilities. The causes of error studied include random noise, and systematic errors due to positioning uncertainties or due to neglecting rotational degrees of freedom.

The methods from Chapter 5 are investigated experimentally in Chapter 7. Free aluminium plates are used as receivers. A variety of source structures are examined, ranging from single contact mass-spring systems, to beams connected at multiple positions, and to representative multi-contact sources.

The third part of the thesis (Chapters 8 and 9) focuses on measurement of source power. Chapter 8 presents a review of the reception plate method, an established method to indirectly determine the power injected by a structure-borne sound source into a heavyweight building element. The assumptions and limitations of the reception plate method are highlighted, and an alternative substitution method is proposed, for use with real walls and floors connected to other building elements.

In Chapter 9, the substitution method described in Chapter 8 is examined experimentally. In two case studies, the structure-borne power from a test source into a free plate and into a connected plate is indirectly determined, and compared with reference values. In a third study, an example of a typical practical implementation of the substitution method is provided.

Chapter 10 concludes the thesis, summarizing the findings and offering suggestions for future work. An extensive list of references and several appendices are provided at the end of the thesis.

1.4 Main contributions

The main contributions of this thesis study are:

- Based on the established matrix inversion method for the inverse determination of operational forces, a simplified measurement procedure for the determination of blocked forces is proposed and investigated (Chapter 3). The potential of using a numerical model of the receiver structure to determine FRFs is highlighted, and two numerical models of a free plate are implemented and discussed (Chapter 3). The method is then evaluated experimentally, and it is found that the accuracy of the numerical models is of critical importance (Chapter 4). As a compromise, a hybrid approach is proposed which employs calculated and measured FRFs of the receiver structure (Chapter 4).
- Methods are proposed and investigated for the determination of source mobility from *in-situ* measurements. Three formulations for the calculation of source mobilities from coupled and uncoupled receiver mobilities are derived theoretically and discussed (Chapter 5). They are then investigated numerically and experimentally (Chapters 6 and 7). It is found that the methods can successfully quantify source mobilities of single-contact and multi-contact sources from *in-situ* measurements. However, typical measurement errors, such as background noise or inaccuracies in sensor positioning, can significantly reduce the accuracy and reliability of the methods.
- A source substitution method for the determination of injected structure-borne sound power is proposed and investigated, as a development of the reception plate method (Chapter 8). A special focus of investigation is on the calibration of the receiver structure. It is found that the calibration can be performed with shaker or hammer, and that an average calibration factor may be used (Chapter 9).

2 Introduction to Structure-Borne Sound Source Characterization

2.1 Introduction

This chapter serves as introduction to the field of structure-borne sound source characterization and the associated fields of structure-borne sound power and inverse methods.

The basic concepts of structure-borne sound source characterization are explained and the two defining source parameters introduced: source activity and mobility. Definitions are given for free velocity, blocked force, and source

mobility. Common measurement procedures are described, and challenges in obtaining these quantities highlighted.

The concept of structure-borne sound power is explained and the advantages in characterizing a source in terms of its power emission are emphasized. Analogies to airborne sound sources are drawn, and similarities and differences discussed. The most common methods of obtaining the structure-borne source power are described, providing the foundation for later chapters.

An introduction into the inverse problem is given. The inverse problem is reviewed on a mathematical basis, introducing the notions of matrix condition and singular value decomposition, and describing regularization methods.

2.2 Source parameters

Structure-borne sound sources are classically characterized in terms of source activity and structural dynamic properties. Figure 2.1 illustrates the model. A black-box approach is employed: internal source mechanisms induce some form of excitation, which is transmitted via a passive linear structure to the source interface [119]. Sources are therefore described in terms of observations at their output terminals only, while the internal workings of the source are generally not considered and are assumed to be inaccessible. The active properties of the source (i. e. internal excitation) are expressed by either the blocked force F_b or the free velocity v_f at the terminals. The passive components of the source are expressed by the mechanical impedance Z_s or the mechanical mobility Y_s.

2.2.1 Source activity

The source activity (or source strength) depends on the type and level of internal excitation. A variety of internal excitation mechanisms are known, such as friction, rotation, pressure variations, or impacts. Sources are often activated by a combination of these mechanisms. Direct measurement of the internal mechanisms is difficult and often impossible. Therefore, the source activity is described in terms of observations at the source terminals.

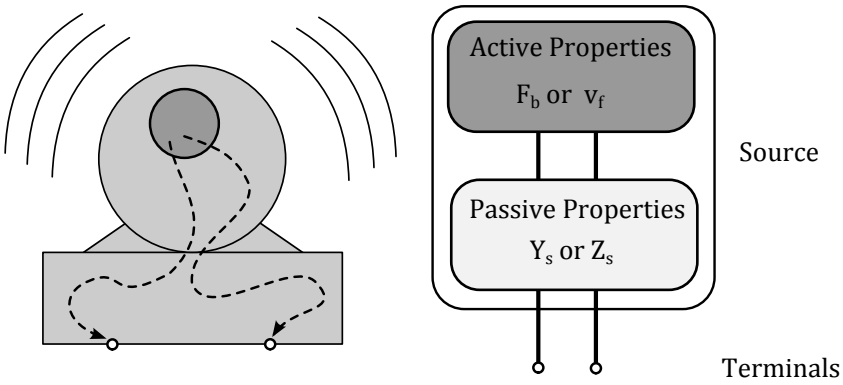

Figure 2.1: Schematic of structure-borne sound source.

Free Velocity

The *free velocity* v_f is defined as the generalized velocity,[1] measured at the terminals of the source in the *free state*. The *free state* is that state in which the generalized forces at the terminals are zero. This means that no other structure is limiting the movement of the source in any way. For small sources, this can be approximated by elastically suspending the source with springs, i. e. having no connection at the coupling points. For larger sources, resilient layers on a stiff foundation can be used to approximate the free state. The stiffness of the springs or the resilient layers must be so low as to not influence the measurement in the frequency range of interest. The measurement of free velocity has been standardized in ISO 9611:1996 [10] and is generally considered one of the easier measurements in structure-borne source characterization.

Blocked Force

The *blocked force* F_b is defined as the generalized force,[2] measured at the terminals of the source in the *blocked state*. The *blocked state* is that state in which the generalized velocity at the terminals is zero. This means that the movement of the source is completely restricted. In practice, this situation can be approximated by placing the source on an inert receiver structure such

[1] The term *generalized velocity* is used to describe both linear and angular velocities.
[2] The term *generalized forces* is used to describe both forces and moments.

as a massive floor. Force transducers need to be inserted between source and receiver to measure the force. For many sources this modifies the mounting situation, yielding blocked force data that is not representative. The measurement of blocked force is generally considered one of the more difficult measurements in structure-borne source characterization. An indirect method to obtain approximate blocked forces is the topic of Chapter 3.

Source activity for multiple terminals

Free velocity and blocked force are both complex functions of frequency, and are linked by the mobility Y_s or impedance Z_s of the source:

$$\mathbf{v_f}(\omega) = \mathbf{Y_s}(\omega)\mathbf{F_b}(\omega) \tag{2.1}$$

$$\mathbf{F_b}(\omega) = \mathbf{Z_s}(\omega)\mathbf{v_f}(\omega) \tag{2.2}$$

For conciseness the frequency dependence is omitted in the following. Equations (2.1) and (2.2) use vectors and matrices to indicate multiple terminals and multiple degrees of freedom at each terminal. An overview of the matrix notation used in this thesis is provided in Appendix A. For a source with $n = N$ terminals and $m = M$ degrees of freedom at each terminal, the free velocity and the blocked force terms expand to vectors with size $(NM) \times 1$:

$$\mathbf{v_f} = \begin{pmatrix} v_{f_{n=1,m=1}} \\ v_{f_{n=1,m=2}} \\ \vdots \\ v_{f_{n=N,m=M}} \end{pmatrix} \qquad \mathbf{F_b} = \begin{pmatrix} F_{b_{n=1,m=1}} \\ F_{b_{n=1,m=2}} \\ \vdots \\ F_{b_{n=N,m=M}} \end{pmatrix}$$

Each of the vector entries in $\mathbf{v_f}$ describes linear or angular velocities at one of the source terminals. Each of the vector entries in $\mathbf{F_b}$ describes forces or moments at one of the source terminals.

Source invariance

When using free velocity or blocked force to characterize the source strength, it is assumed that the activity is invariant of the constraints exerted on the source by any receiver structure, i. e. the internal source mechanisms are assumed to

act identically in the free state and in the blocked state, and in every intermediate state. It has been recognized that this assumption may have limits for some categories of structure-borne sound sources [42, 71]. For example, an electrical motor will experience some form of feedback if it is heavily constrained, due to changes in the electromagnetic field. This feedback will have an effect on the source activity. With this in mind, measurements *in-situ*, i. e. mounted in a way that resembles the installation condition, seem better suited for a representative source characterization.

2.2.2 Source mobility

The dynamic characteristics of structure-borne sound sources are expressed using the concepts of mobility and impedance. A comprehensive overview on the history and origins of these are provided in [56]. Impedance is the reciprocal of mobility, and can readily be derived from it. However, mobility offers some advantages in terms of measurement. While the measurement of mobility requires the source terminals to be free, the measurement of impedance requires the source terminals to be blocked in all degrees of freedom [105]. The latter is much harder to achieve in practice. Therefore, only the concept of mobility is now described in detail.

Basic definition

The mobility Y of a structure is defined as the complex ratio of the (generalized) velocity response of that structure to a (generalized) force input:

$$Y(\omega) = \frac{v(\omega)}{F(\omega)} \tag{2.3}$$

Again, the frequency dependence is omitted in the following for conciseness. It is assumed that this ratio is invariant of level, spectral shape or time characteristics of the input force. This assumption is in line with the black-box approach described in Section 2.2.1. The source structure is presumed to be a linear and time-invariant system.

Types of mobility

The most commonly used mobility is the *driving point mobility*. It usually refers to the ratio of translational velocity to a force in the same direction, at the point of excitation. However, the location and direction of excitation and response may differ.

Transfer mobility is the ratio between response velocity and applied force in the same direction, but where the position of the response is different to that of the force. *Cross mobility* is the ratio between response velocity and applied force in different directions, at the point of excitation. *Cross-transfer mobility* is the ratio between response velocity and applied force in different directions, at different positions. Table 2.1 provides a summary.

Name	**Excitation and Response**		**Example**
	Location	Direction	
Point mobility	$=$	$=$	$Y_{ii}^{v_z F_z} = \frac{v_{z,i}}{F_{z,i}}$
Transfer mobility	$\neq$	$=$	$Y_{ij}^{v_z F_z} = \frac{v_{z,i}}{F_{z,j}}$
Cross mobility	$=$	$\neq$	$Y_{ii}^{\theta_x F_z} = \frac{\theta_{x,i}}{F_{z,i}}$
Cross-transfer mobility	$\neq$	$\neq$	$Y_{ij}^{\theta_x F_z} = \frac{\theta_{x,i}}{F_{z,j}}$

Table 2.1: Terminology of mobility.

Source mobility for multiple terminals

For sources with N terminals and M degrees of freedom at each terminal, the mobility term expands to a square matrix of size $(NM) \times (NM)$. Figure 2.2 shows the general case for a single point excitation ($N = 1$). Six degrees of freedom are involved in the excitation of the receiver structure: the forces F_x, F_y, and F_z, and the moments M_x, M_y, and M_z. With the corresponding response quantities v_x, v_y, v_z, θ_x, θ_y, and θ_z, the mobility matrix of size 6×6

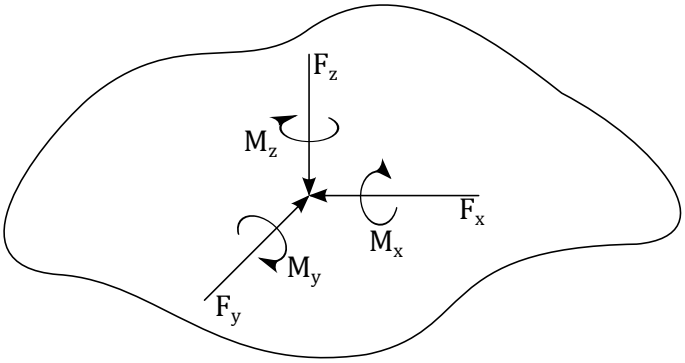

Figure 2.2: Point excitation, general case (after [109]). Six degrees of freedom are involved: three translational and three rotational components.

has the following form:

$$\mathbf{Y} = \begin{pmatrix} Y_{v_x F_x} & Y_{v_x F_y} & Y_{v_x F_z} & Y_{v_x M_x} & Y_{v_x M_y} & Y_{v_x M_z} \\ Y_{v_y F_x} & Y_{v_y F_y} & Y_{v_y F_z} & Y_{v_y M_x} & Y_{v_y M_y} & Y_{v_y M_z} \\ Y_{v_z F_x} & Y_{v_z F_y} & Y_{v_z F_z} & Y_{v_z M_x} & Y_{v_z M_y} & Y_{v_z M_z} \\ Y_{\theta_x F_x} & Y_{\theta_x F_y} & Y_{\theta_x F_z} & Y_{\theta_x M_x} & Y_{\theta_x M_y} & Y_{\theta_x M_z} \\ Y_{\theta_y F_x} & Y_{\theta_y F_y} & Y_{\theta_y F_z} & Y_{\theta_y M_x} & Y_{\theta_y M_y} & Y_{\theta_y M_z} \\ Y_{\theta_z F_x} & Y_{\theta_z F_y} & Y_{\theta_z F_z} & Y_{\theta_z M_x} & Y_{\theta_z M_y} & Y_{\theta_z M_z} \end{pmatrix} \tag{2.4}$$

In the most general case of N source terminals, the interaction between the terminals must also be included. The source mobility matrix in this case has size $6N \times 6N$. The experimental determination of all matrix elements is extremely time-consuming, especially if one considers the difficulties in obtaining mobilities containing rotational degrees of freedom. Petersson and Gibbs [109] point out that three quarters of the mobility matrix involve rotations or moments, while only one quarter consists purely of translational motion.

In a practical situation, often only three degrees of freedom are considered: the force/velocity normal to the surface (F_z), and the two moments/angular velocities about the in-plane axes (M_x and M_y). These three components are deemed most important for the excitation of out-of-plane bending waves, which in turn are most important for the radiation of audible sound.

Reciprocity

The theorem of reciprocity [150, 135, 137] relates the transfer function between positions 1 and 2 to the transfer function between positions 2 and 1. For "stable, finite, lumped, passive, linear dynamical systems which only contain reversible (bilateral) elements" [137], the transfer functions are equal. Cremer points out that the prerequisite of the theorem of reciprocity is that "the product of the variables to be interchanged yields the power or energy" [38, p. 18].

For a point mobility matrix as in Equation (2.4), reciprocity plays an important role. The mobility matrix is symmetric, and the off-diagonal elements are related as follows:

$$\frac{v_i}{F_j} = \frac{v_j}{F_i}, \tag{2.5}$$

where v and F are the generalized velocity and force. For example, the matrix elements $Y_{\theta_x F_z}$ and $Y_{v_z M_x}$ are equal. Instead of determining 36 separate matrix elements, it is therefore in principle only necessary to determine 21 elements: the six elements on the main diagonal (point mobilities), and half of the remaining 30 elements (cross-mobilities). For the general case of an $(NM) \times (NM)$ matrix, application of the reciprocity theorem reduces the number of elements to be determined from $(NM)^2$ to $((NM)^2 + NM)/2$.

If all matrix elements are determined individually, the reciprocity property of the point mobility matrix offers a way to verify measurement data. A simple comparison between off-diagonal matrix elements can reveal problems with the measured data and give an indication of the quality of the calculated mobilities. If the off-diagonal elements are of high quality, it is likely that the point mobilities on the diagonal are also of good quality.

Mobilities of real sources

Mobilities of structure-borne sound sources are a function of structural geometries, boundary conditions, material properties, and damping. Fulford and Gibbs [52] state that many sources show a typical behaviour: In the low frequency region, they are dominated by the mass of the source; then follows an anti-resonance and a stiffness-controlled region, before the mobility moves into a resonance-controlled region. At high frequencies, infinite or semi-infinite

behaviour is observed. Studies of source mobilities indicate that most sources can be characterized as one of four types: compact, plate-based, flange-based, or frames [52, 62]. While there have been efforts to predict mobilities of real sources from parameters such as structural geometries and boundary conditions [112, 111, 60], source mobilities generally need to be measured. The experimental determination of mobility is the topic of Chapter 5.

2.3 Structure-borne sound power

When a vibrating source is connected to a receiver structure, as in Figure 2.3, vibrational energy is transmitted from source to receiver. Once in the receiver structure, the energy can propagate to other connected elements, and lead to unwanted noise.

There is increased consensus that structure-borne sound sources should be characterized in terms of the power they inject into receiver structures [109]. The use of power instead of velocity or force has several advantages:

- Structure-borne source power is a single (frequency-dependent) quantity, regardless of the number of connection points between source and receiver, and regardless of the degrees of freedom involved. The source power calculation effectively summarizes and simplifies the complicated transmission process. The result corresponds to the need of manufacturers for a *single number quantity*.
- Dimensional incompatibilities between force and moment transmission are eliminated. While it is impossible to gauge the effectiveness of vibration transmission between source and receiver by comparing forces and moments alone, their contributions can be compared on a power basis.
- Calculation models such as EN 12354-5:2009 [16] and Statistical Energy Analysis [89, 36] are used by industry, for legislation, and in research and development. They allow the prediction of propagation of (structure-borne or airborne) sound in buildings and other structures. The sound pressure levels in different rooms can thus be calculated, without physically installing the source in the building. A basic requirement is the availability of source data in the form of injected power into the building structure.

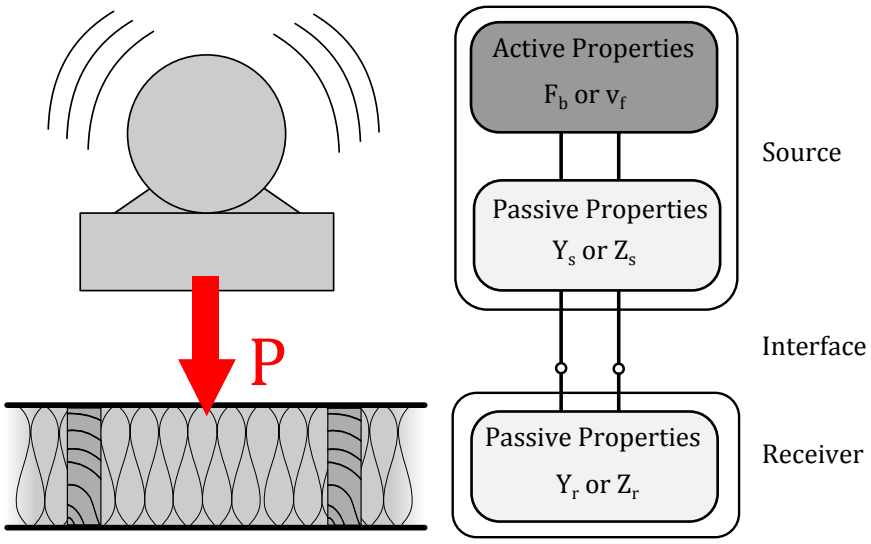

Figure 2.3: Schematic of source-receiver coupling.

- Sources can be compared on a power basis, as is done for airborne sound sources. The equivalence to the airborne case is an advantage, as airborne sound power is a well-known and well-studied parameter.

While the analogy with airborne source power is helpful for the understanding and acceptance of structure-borne source power, there is an important difference between the two. An airborne source emits the same energy in almost every environment (exceptions include very small rooms). The power emitted by a vibration source, on the other hand, generally is a function of both source and receiver characteristics. The reason for this is found in the change in receiver impedance. For most environments, the receiver impedance for airborne sound is the characteristic impedance of air ($Z = \rho_0 c \approx 415\,\mathrm{Ns/m^3}$ at room temperature). The receiver impedance (or mobility) of structural receivers, on the other hand, tends to vary considerably. This results in large variations in the transmitted source power. The dependency of the transmitted power on source and receiver quantities is explored in detail in Section 2.3.2.

The vibrational power Q, which the source injects into the receiver structure, is a complex quantity, consisting of a real part P and an imaginary part R:

$$Q = P + jR \tag{2.6}$$

The real part P describes the *active power*, which is transmitted to the receiver structure. This is the power that is of importance for the far-field, and for sound propagation to other building elements. The imaginary part R describes the *reactive power* that fluctuates between the source and the receiver near-field, without effectively being transmitted to the receiver. Therefore, in source characterization the active power P is most important.

There are several methods of determining the injected structure-borne source power. Overviews of available methods are given in [138, 107, 125]. Some of the most important methods are discussed in the following sections.

2.3.1 Direct measurement

Direct measurement of structure-borne power transmission is the most straightforward approach. It has recently been standardized in ISO 18312-1:2012 [19]. By measuring the forces and velocities at the coupling interface between source and receiver, the direct calculation of the injected power is possible. The complex power Q is defined as the sum of the products of force and velocity at the contact points[3]:

$$Q = \mathbf{v_r^T}\ \mathbf{F_r^*} = \sum_i v_{r_i} F_{r_i}^* \tag{2.7}$$

$$P = \mathrm{Re}\{Q\} = \mathrm{Re}\left\{\mathbf{v_r^T F_r^*}\right\}. \tag{2.8}$$

While the direct measurement seems straightforward, there are practical disadvantages. First, no prediction of the injected source power is possible for the unassembled source-receiver combination. Secondly, moments may be important in the transmission process, but there is currently no sensor or method available to directly measure moments. Thirdly, the method requires the direct measurement of forces between source and receiver. This is only possible by inserting force transducers into the transmission path. These can significantly change the behaviour of the coupled system, making the measured values meaningless for the desired installation without force transducers. Therefore, the direct measurement method is usually only used in a research environment, as a benchmark method to compare with other methods.

[3] In this thesis, the Fourier spectra of field quantities such as $\mathbf{v}$ and $\mathbf{F}$ are normalized by a factor of $1/\sqrt{2}$, so that their modulus corresponds to the root-mean-square value [115].

2.3.2 Mobility method

In the mobility method, the injected source power is calculated from independent source and receiver data. The receiver can be fully characterized by its mobility, and the source can be fully characterized by its activity and mobility, see Figure 2.3. The interaction between source and receiver is expressed in terms of source and receiver mobilities. The great advantage of this method is that these quantities can be measured independently of each other, without assembling source and receiver. It is thus possible to predict the installed situation, and to virtually place various sources on various receivers.

The injected power is calculated using either free velocity or blocked force[4]:

$$Q = \mathbf{v_f^T}\,(\mathbf{Y_s} + \mathbf{Y_r})^{-\mathbf{1T}}\,\mathbf{Y_r^T}\,(\mathbf{Y_s} + \mathbf{Y_r})^{-\mathbf{1}*}\,\mathbf{v_f^*} \tag{2.9}$$

$$Q = \mathbf{F_b^T}\,\mathbf{Y_s^T}\,(\mathbf{Y_s} + \mathbf{Y_r})^{-\mathbf{1T}}\,\mathbf{Y_r^T}\,(\mathbf{Y_s} + \mathbf{Y_r})^{-\mathbf{1}*}\,\mathbf{Y_s^*}\,\mathbf{F_b^*} \tag{2.10}$$

Simplifications are possible if a strong mismatch exists between source and receiver mobility[5].

If the receiver mobility is much higher than the source mobility ($|Y_r| \gg |Y_s|$, LMS = low-mobility source), the source acts as a *constant velocity source*, and $\mathbf{Y_s}$ in the reciprocal term can be neglected. Equations (2.9) and (2.10) reduce to

$$Q_{\mathrm{LMS}} \approx \mathbf{v_f^T}\,\mathbf{Y_r^{-1}}^{*}\,\mathbf{v_f^*} \tag{2.11}$$

and

$$Q_{\mathrm{LMS}} \approx \mathbf{F_b^T}\,\mathbf{Y_s^T}\,\mathbf{Y_r^{-1}}^{*}\,\mathbf{Y_s^*}\,\mathbf{F_b^*}. \tag{2.12}$$

In practice this situation is not very common, since the receiver structure usually has to statically support the source. It can sometimes be encountered when a heavy machine is placed on a lightweight wooden floor.

[4] Equation (2.9) is sometimes incorrect in the literature. The often-quoted formulation in [99, Equation (7)] looks slightly different, but is in fact equal to Equation (2.9) if the correct definition of the Hermitian transpose is used: $()^{\mathbf{H}} = ()^{\mathbf{T}*}$. The equations in [109, Equation (11)] and [38], on the other hand, are incorrect. Equation (6) in [63] gives the correct real part, but the wrong sign of the imaginary part.

[5] The limit for a strong mobility mismatch is not clearly defined. Source-receiver mobility ratios between 3 [23] and 10 [158] have been used in the literature. In the author's experience, a ratio of 10 as lower limit for a strong mobility mismatch is most appropriate.

If the receiver mobility is much lower than the source mobility ($|Y_r| \ll |Y_s|$, HMS = high-mobility source), the source acts as a *constant force source*, and $\mathbf{Y_r}$ in the reciprocal term can be neglected. Equations (2.9) and (2.10) reduce to

$$Q_{\mathrm{HMS}} \approx \mathbf{v_f^T}\ \mathbf{Y_s^{-1T}}\ \mathbf{Y_r^T}\ \mathbf{Y_s^{-1*}}\ \mathbf{v_f^*} \tag{2.13}$$

and

$$Q_{\mathrm{HMS}} \approx \mathbf{F_b^T}\ \mathbf{Y_r^T}\ \mathbf{F_b^*}. \tag{2.14}$$

This situation is quite common in building acoustics. For heavyweight construction (concrete or masonry structures), the mobility of most sources is usually much higher than the receiver mobility, in the frequency range of interest.

While the mobility method is beneficial in terms of understanding the source-receiver interaction, and provides a convenient way to characterize a multitude of sources in theory, there are challenges to its applicability.

First, the measurement of all involved parameters can be a very time-consuming task. This is especially true if more than one degree of freedom is included. The measurement of source mobilities alone can be quite challenging in this case. If only one degree of freedom (usually the normal force component) is taken into account at each of the N source terminals, the mobility matrices have size $N \times N$. Even utilizing reciprocity, $(N^2 + N)/2$ mobility terms need to be measured. If more than one degree of freedom is taken into account, this number grows dramatically, as was seen in Section 2.2.2. With regards to the measurement of the source activity, the measurement of free velocities is usually relatively straightforward, while the measurement of blocked forces is difficult (see Section 2.2.1).

Once all necessary data has been acquired, Equation (2.9) and Equation (2.10) pose the next challenge. Both require the inverse term $(\mathbf{Y_s} + \mathbf{Y_r})^{-1}$. For $N > 1$ or $M > 1$, this involves a matrix inversion, which can lead to the obtained source power estimate being subject to amplified random errors. Section 2.4 provides an introduction to the inverse problem and an explanation of the difficulties involved. The matrix inversion in Equation (2.9) and Equation (2.10) means, that the mobility method should only be used with caution. It can give the right answers, if all the necessary quantities have been correctly determined and the problem is well-conditioned, but it may also lead to large errors if either of these is not the case.

Finally, the mobility method in particular makes use of the *black-box* approach explained in Section 2.2.1. The source activity (free velocity, blocked force) is assumed to be invariant with regards to the mounting situation. As explained in Section 2.2.1, this assumption may not always hold. As the mobility method uses free velocity or blocked force to predict the injected power in the installed condition, any variance of the source activity will necessarily lead to systematic errors in the prediction. Furthermore, the description of the source-receiver coupling by source and receiver mobilities may introduce additional errors, if source or receiver structures contain non-linear structural elements or local flexibility. In this case, it can be useful to determine the mobilities *in-situ*, meaning in the coupled state. The indirect determination of source mobilities from *in-situ* measurements is the topic of Chapters 5, 6, and 7.

The mobility method has many advantages, in particular when it comes to understanding the interaction between source and receiver. However, due to the problems described, it should be used with caution.

2.3.3 Source descriptor and coupling function

For a better understanding of the transmission process, the injected power can be expressed as a function of a source descriptor and a coupling function [96]. For the case of only one contact point ($N = 1$) and one degree-of-freedom ($M = 1$), Equation (2.9) is written in scalar form:

$$Q = |v_f|^2 \frac{Y_r}{|Y_s + Y_r|^2}. \tag{2.15}$$

This can be re-formulated as

$$Q = \frac{|v_f|^2}{Y_s^*} \frac{Y_s^* Y_r}{|Y_s + Y_r|^2} = S_c C_f. \tag{2.16}$$

Here, S_c is termed the *source descriptor*:

$$S_c = |v_f|^2 \frac{1}{Y_s^*} = |F_b|^2 Y_s = v_f F_b^*. \tag{2.17}$$

It is a measure of the source's ability to deliver power, and only depends on source characteristics. Since it has the dimension of power, the source descriptor

can be used to compare the source strength of different sources, without knowledge of the installed condition, allowing rank-ordering of different sources.

C_f is termed the *coupling function*:

$$C_f = \frac{Y_s^* Y_r}{|Y_s + Y_r|^2}. \tag{2.18}$$

It describes the dynamic interaction between source and receiver structures, and determines how much of the source descriptor power is transmitted to the receiver structure.

Whilst the source descriptor allows the comparison of different sources, the coupling function provides insight into the transmission process in the installed situation. Figure 2.4 shows the magnitude of the ratio $|Q| \,/\, |S_c|$ for the case of a single contact, single degree-of-freedom source, as a function of source-receiver mobility ratio and phase difference between source and receiver mobility. Three regions can be distinguished:

1. When the source mobility is significantly lower than the receiver mobility ($|Y_s| < 0.1\,|Y_r|$), the (LMS) source behaves as a constant velocity source, and Equations (2.11) and (2.12) may be used to estimate the injected power. The phase difference between source and receiver mobility does not come into play.

2. When the source mobility is significantly higher than the receiver mobility ($|Y_s| > 10\,|Y_r|$), the (HMS) source behaves as a constant force source, and Equations (2.13) and (2.14) may be used to estimate the injected power. The phase difference between source and receiver mobility does not come into play.

3. When source and receiver mobility are in the same order of magnitude ($0.1\,|Y_r| < |Y_s| < 10\,|Y_r|$), one speaks of a *matched condition*. Simplifications are not possible, and Equations (2.9) and (2.10) must be used to estimate the injected power. The phase relationship between source and receiver mobility assumes importance, and strongly affects the amount of transmitted power.

The plot of the coupling function in Figure 2.4 highlights the fact that the maximum power transmission occurs for a source-receiver mobility ratio of

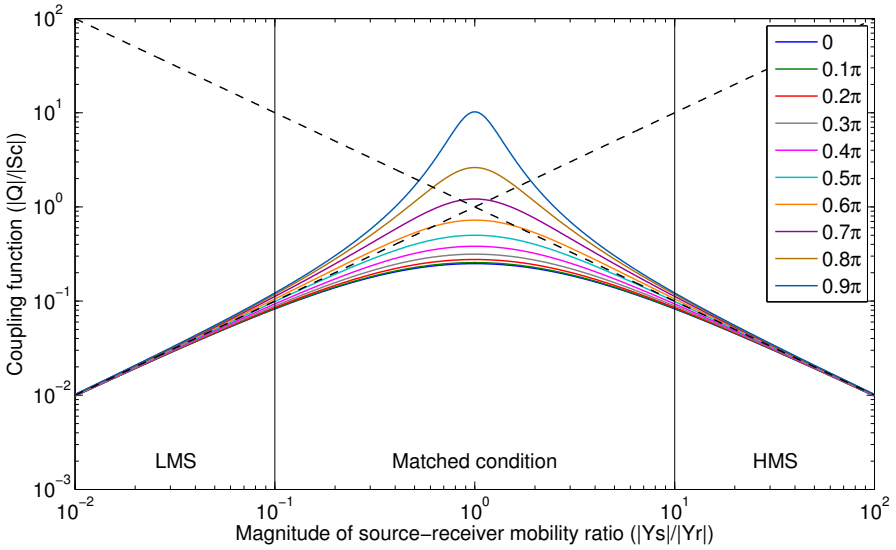

Figure 2.4: The coupling function $|Q| \,/\, |S_c|$ for the SDOF case.

unity. For strong mobility mismatches ($|Y_s| < 0.1\,|Y_r|$ or $|Y_s| > 10\,|Y_r|$), the transmission decreases considerably. The matched condition is by far the most difficult to deal with, as simplifications are generally not possible, and the phase relationship between source and receiver assumes importance.

The concept of source descriptor and coupling function was developed for the (scalar) case of a single contact, single degree of freedom system. For sources with multiple contacts or degrees of freedom, separating the matrix formulation for Q (Equation (2.9)) as in Equation (2.16) is not immediately possible. However, the concept of characteristic power may be used as an extension of the source descriptor, and the concept of effective mobilities may be used to calculate the coupling function for the multi-point and multi-component case.

Characteristic power

The concept of *characteristic power* [99] extends the concept of the source descriptor to the multi-point and multi-component case. The characteristic power is defined as the product of complex conjugate blocked force and free velocity:

$$S_c = \mathbf{v_f^H Y_s^{-H} v_f} = \mathbf{F_b^H v_f} \tag{2.19}$$

For the single-point and single-component case, S_c collapses to the definition in Equation (2.17). It is thus a generalization of the source descriptor to multi-point and multi-component cases. However, no such generalization exists for the coupling function within the framework of characteristic power.

Effective mobilities and interface mobilities

The concept of effective mobilities offers a different approach of utilizing the source descriptor and coupling function for multi-point and multi-component cases. It was introduced by Petersson and Plunt [110, 111] in order to reduce a multi-point and multi-component case to equivalent single-point and single-component cases. An equivalent, "effective" mobility is calculated for each component of excitation at each contact point, accounting for the contributions from all other terminals and degrees of freedom:

$$Y_{ii}^{nn\sum} = Y_{ii}^{nn} + \sum_{\substack{k=1 \\ k\neq n}}^{6} Y_{ii}^{nk} \frac{F_i^k}{F_i^n} + \sum_{\substack{j=1 \\ j\neq i}}^{N} Y_{ij}^{nn} \frac{F_j^n}{F_i^n} + \sum_{\substack{k=1 \\ k\neq n}}^{6} \sum_{\substack{j=1 \\ j\neq i}}^{N} Y_{ij}^{nk} \frac{F_j^k}{F_i^n} \tag{2.20}$$

The first term is the driving point mobility at the contact. The second term describes the coupling between the six degrees of freedom at the contact. The third term accounts for coupling between each of the six degrees of freedom at different contacts. The fourth term represents the remaining mobility terms, describing coupling between different degrees of freedom at different contact points. The ratios F/F_i^n between the generalized forces at different contact points are required for an accurate determination of the effective mobility.

In case only the force normal to the surface is considered, Equation (2.20) reduces to

$$Y_{ii}^{\sum} = Y_{ii} + \sum_{\substack{j=1 \\ j\neq i}}^{N} Y_{ij} \frac{F_j}{F_i}. \tag{2.21}$$

With effective mobilities, the source descriptor concept can be used for multi-point and multi-component sources [108]. The total injected structure-borne source power is calculated by summing the injected powers at each contact

point:

$$Q = \sum_{i=1}^{N} |v_{f,i}|^2 \frac{Y_{r,ii}^{\sum}}{\left|Y_{s,ii}^{\sum} + Y_{r,ii}^{\sum}\right|^2}. \tag{2.22}$$

Equation (2.22) is an exact reformulation of Equation (2.9), without the need for a matrix inversion. However, because of the required force and moment ratios in Equation (2.20), the effective mobilities are no longer an independent property of the source. One way of circumventing this problem is by assuming or predicting force and moment ratios [51, 53, 90, 91]. Common assumptions are ratios of unity, with either zero-phase or random-phase distribution.

A similar approach to the effective mobility approach treats the series of contact points between source and receiver as a single continuous interface. The *interface mobilities* [31] are calculated using a spatial Fourier decomposition:

$$Y_{pq} = \frac{1}{C^2} \int_0^C \int_0^C Y(s|s_0) e^{-jk_p s} e^{-jk_q s_0} \, \mathrm{d}s \mathrm{d}s_0 \tag{2.23}$$

As for effective mobilities, a matrix inversion is avoided using interface mobilities. Furthermore, line or area contacts can be treated, but post-processing is more involved than for the regular matrix formulation.

2.3.4 Reception plate method

Some methods for structure-borne sound source characterization emphasize practicability and usability, sometimes at the expense of accuracy and generality. The reception plate method [17] is a prime example of such an approach. The source of interest is operated on a reception plate that is representative of the installed condition, and the spatially-averaged response of the plate is measured. Using simple relationships between the velocity on the plate and its kinetic energy, the injected source power is obtained. For meaningful results, it is important that the mobility ratio between source and reception plate resembles the source-receiver mobility ratio in the installed condition. This is an inherent limit of the method. Nevertheless, for some common situations, such as light sources in heavyweight buildings, the reception plate method yields representative source data with engineering accuracy, with comparably little measurement effort. The method is discussed in detail in Chapter 8.

2.3.5 Summary and Discussion

Various methods exist to determine the structure-borne power injected by a vibration source into a receiver structure. Some of the most important, in particular with regards to the work reported in this thesis, were discussed in the previous sections. Included here is a brief summary and discussion.

The direct measurement of force and velocity at the source-receiver interface is the most straightforward approach. Unfortunately, due to the necessity of inserting a force transducer in the transmission path, it is impractical and prone to errors due to the changing of the transmission path. Furthermore, it does not allow the prediction of power flow in the installed condition.

The mobility method uses independent source and receiver data to predict the injected power from any source into any receiver. Simplifications are possible if a strong mobility mismatch exists between source and receiver. The main disadvantage of the method lies in the amount of data required for the calculation of the source power. Besides the source activity data (in the form of free velocity or blocked force), the mobility matrices of source and receiver need to be determined. Depending on the number of source terminals and on the number of relevant components of excitation at each terminal, this may result in a significant measurement effort. Even if all data can be obtained experimentally, the involved matrix inversion means that the mobility method should be used with caution.

The concept of source descriptor and coupling function is a useful reformulation of the mobility method. It provides insight into the physical transmission process between source and receiver. Exact results are obtained, provided all necessary data can be acquired (by measurement or otherwise). As for the mobility method, the main difficulty lies in the experimental determination of source and receiver mobility data. The concepts of effective mobilities or interface mobilities extend the source descriptor approach to the multi-point and multi-component case. Additional information is needed for a successful implementation of these methods, for example force ratios.

The reception plate method yields the injected structure-borne source power into a representative receiver structure. The details of the transmission process are neglected, and only the effect of the source in the receiver far field are

considered. The method emphasizes practicability, and is only valid for source-receiver mobility ratios that resemble the installation condition.

Depending on the situation and the requirements, one or the other of these methods may be appropriate. For the building industry, it is important to provide practicable measurement methods that yield single-equivalent values. The reception plate method is a good approach for sources in heavyweight construction. In the automotive or aerospace industry, a wide variety of receiver structures can be found. Also, measurements with higher complexity are possible in these industries. It is therefore better to obtain independent source and receiver data, for example using the mobility method, to be able to virtually place one source on different receivers.

2.4 The inverse problem

The *inverse problem* is an extensively researched topic in linear algebra, which can be encountered in many engineering applications. In this section, an introduction to the inverse problem is provided. The fundamentals and terminology of matrix inversion are described, and the most common approaches to mitigate inverse problems are presented: over-determination, singular value rejection, and regularization methods. The relevant literature with regards to the inverse problem in vibro-acoustics is reviewed in Chapter 3.

2.4.1 Fundamentals of matrix inversion

A system of n linear equations can be written in matrix form [153, 65, 39]:

$$\mathbf{b} = \mathbf{A}\mathbf{x}. \tag{2.24}$$

Here, $\mathbf{b}$ and $\mathbf{x}$ are $n \times 1$ column vectors, and $\mathbf{A}$ is an $n \times n$ square matrix. For an overview of matrix notations and definitions, see Appendix A. Solving Equation (2.24) for $\mathbf{x}$ requires an inversion of the matrix $\mathbf{A}$:

$$\mathbf{x} = \mathbf{A}^{-1}\mathbf{b}. \tag{2.25}$$

The inverse $\mathbf{A^{-1}}$ of an $n \times n$ matrix $\mathbf{A}$ is defined such that

$$\mathbf{A^{-1}A} = \mathbf{AA^{-1}} = \mathbf{I}, \tag{2.26}$$

where $\mathbf{I}$ is the $n \times n$ identity matrix. If $\mathbf{A^{-1}}$ exists, $\mathbf{A}$ is said to be *non-singular*. Otherwise, $\mathbf{A}$ is said to be *singular*. If $\mathbf{A}$ is singular, Equation (2.25) has no solution or infinitely many solutions.

For a non-singular matrix $\mathbf{A}$, a perturbation in $\mathbf{x}$ leads to a perturbation in $\mathbf{b}$:

$$\mathbf{b} + \Delta\mathbf{b} = \mathbf{A}(\mathbf{x} + \Delta\mathbf{x}) \tag{2.27}$$

Similarly, a perturbation in $\mathbf{b}$ will lead to a perturbation in $\mathbf{x}$:

$$\mathbf{x} + \Delta\mathbf{x} = \mathbf{A^{-1}}(\mathbf{b} + \Delta\mathbf{b}) \tag{2.28}$$

Eliminating $\mathbf{x}$ on both sides of Equation (2.28) yields

$$\Delta\mathbf{x} = \mathbf{A^{-1}}\Delta\mathbf{b}. \tag{2.29}$$

Equations (2.28) and (2.29) present one of the central problems of matrix inversion: the propagation and in some cases amplification of input errors to the output. The stability of $\mathbf{x}$ with regards to errors in $\mathbf{b}$ depends on the condition of $\mathbf{A}$. If small changes in $\Delta\mathbf{b}$ result in small changes in $\Delta\mathbf{x}$, the matrix $\mathbf{A}$ is said to be *well-conditioned*. If small changes in $\Delta\mathbf{b}$ result in large changes in $\Delta\mathbf{x}$, the matrix $\mathbf{A}$ is said to be *ill-conditioned*. The matrix condition therefore describes the sensitivity of the output $\mathbf{x}$ to changes in the input $\mathbf{b}$. A measure for the stability of the solution is the condition number of $\mathbf{A}$.

Matrix condition

For a perturbation in $\mathbf{b}$, an upper bound of the relative error in $\mathbf{x}$ is given [39]:

$$\frac{\|\mathbf{\Delta x}\|}{\|\mathbf{x}\|} \leq \|\mathbf{A}\| \left\|\mathbf{A^{-1}}\right\| \frac{\|\mathbf{\Delta b}\|}{\|\mathbf{b}\|} \tag{2.30}$$

Here, $\|\cdot\|$ indicates a matrix norm, see Appendix A. The term

$$\kappa(\mathbf{A}) = \|\mathbf{A}\| \left\|\mathbf{A^{-1}}\right\| \tag{2.31}$$

is called the *condition number* of the matrix $\mathbf{A}$ [39]. From Equation (2.30):

- For small κ, the error $\|\boldsymbol{\Delta}\mathbf{x}\| / \|\mathbf{x}\|$ will be small when $\|\boldsymbol{\Delta}\mathbf{b}\| / \|\mathbf{b}\|$ is small.
- For large κ, the error $\|\boldsymbol{\Delta}\mathbf{x}\| / \|\mathbf{x}\|$ can be large, even when $\|\boldsymbol{\Delta}\mathbf{b}\| / \|\mathbf{b}\|$ is small.

Values for the condition number lie between 1 and infinity: $1 \leq \kappa < \infty$. A high condition number ($\kappa \gg 1$) indicates an ill-conditioned matrix. The condition of a matrix is an intrinsic property of the matrix, and independent of the algorithm used for inversion.

When using the 2-norm in Equation (2.31), the condition number can be expressed as the ratio of the smallest and the largest singular value of $\mathbf{A}$:

$$\kappa(\mathbf{A}) = \|\mathbf{A}\|_2 \left\|\mathbf{A}^{-\mathbf{1}}\right\|_2 = \frac{\sigma_{max}(\mathbf{A})}{\sigma_{min}(\mathbf{A})}. \tag{2.32}$$

Singular value decomposition

To obtain the singular values of a matrix, a *singular value decomposition* (SVD) is required. The SVD factorizes an $m \times n$ matrix $\mathbf{A}$ into the three matrices $\mathbf{U}$, $\mathbf{S}$, and $\mathbf{V}$ [65]:

$$\mathbf{A} = \mathbf{U}\mathbf{S}\mathbf{V}^{\mathbf{H}}. \tag{2.33}$$

$\mathbf{U}$ is an $m \times m$ real or complex unitary matrix; $\mathbf{S}$ is an $m \times n$ rectangular diagonal matrix with non-negative real elements; $\mathbf{V}^{\mathbf{H}}$ is an $n \times n$ real or complex unitary matrix.

The diagonal entries of $\mathbf{S}$ are the singular values σ_i of $\mathbf{A}$:

$$\mathbf{S} = \mathrm{diag}(\sigma_1, \ldots, \sigma_p), \quad p = \min\{m, n\}. \tag{2.34}$$

The m columns of $\mathbf{U}$ and the n columns of $\mathbf{V}$ are called the left-singular vectors and right-singular vectors of $\mathbf{A}$, respectively [65].

The generalized inverse

For a rectangular matrix $\mathbf{A}$ of size $m \times n$, where $m \neq n$, the inverse is not defined. Instead, a *generalized inverse* or *pseudo-inverse* can be calculated[6]:

$$\mathbf{A^{-1}} = (\mathbf{A^H A})^{-1}\mathbf{A^H} \tag{2.35}$$

The inverse matrix $\mathbf{A^{-1}}$ has size $n \times m$. The generalized inverse was first proposed by Moore [97], and later by Penrose [106]. For this reason it is often called the *Moore-Penrose pseudo-inverse*.

The generalized inverse uses a least square solution to solve Equation (2.25). The SVD is employed for the calculation of $\mathbf{A^{-1}}$. From Equation (2.33), the inverse of $\mathbf{A}$ is readily available:

$$\mathbf{A^{-1}} = \mathbf{V S^{-1} U^H}. \tag{2.36}$$

Equation (2.36) still requires the inversion of $\mathbf{S}$. However, $\mathbf{S}$ is a diagonal matrix which can be easily inverted by replacing the singular values on the diagonal by their reciprocal values: $\mathbf{S^{-1}} = \mathrm{diag}(1/\sigma_1, \ldots, 1/\sigma_p)$. The SVD therefore is a convenient tool to calculate the generalized inverse.

2.4.2 Methods to mitigate matrix inversion problems

A variety of methods exist to improve the matrix inversion process, and mitigate problems associated with ill-conditioned matrices and the subsequent amplification of errors in the input data as described in Section 2.4.1. The three most common methods are considered in this thesis and are described here.

Over-determination

Over-determination is the technique of providing more input data to a problem than is actually necessary to solve it. For example, for a system as in Equation (2.25) with n unknown variables ($\mathbf{x}$ has size $n \times 1$) , m known variables ($\mathbf{b}$

[6] In this thesis, the notation $()^{-1}$ is used for inverse and generalized inverse.

has size $m \times 1$) are supplied to solve the problem, where $m > n$. The matrix $\mathbf{A}$ therefore has size $m \times n$, and Equation (2.25) has the following form:

$$\mathbf{x_{n\times 1}} = (\mathbf{A_{m\times n}})^{-1}\mathbf{b_{m\times 1}}. \tag{2.37}$$

As noted above, the matrix $(\mathbf{A_{m\times n}})^{-1}$ has size $n\times m$. The use of the generalized inverse to obtain $\mathbf{A^{-1}}$ leads to a best-fit approximation for the solution.

Singular value rejection

In Equation (2.36) the generalized inverse is calculated by taking the reciprocal of the singular values along the main diagonal of $\mathbf{S}$. For small singular values ($\sigma \ll 1$), which can be influenced significantly by measurement noise, the reciprocal $1/\sigma$ is large and has a large effect on the inverse. It can therefore be beneficial to eliminate or reject small singular values by replacing them with 0. The matrix $\mathbf{S^{-1}}$ then becomes $\mathbf{S^{-1}} = \mathrm{diag}(1/\sigma_1, \ldots, 1/\sigma_{p-r}, 0, \ldots, 0)$, where r indicates the number of rejected singular values.

The difficulty of this method lies in finding an appropriate threshold for the rejection of singular values. If too few singular values are rejected, the solution will remain unstable. If too many singular values are rejected, the solution of the inverse calculation will under-estimate the true value. Strategies for the choice of an appropriate threshold include:

1. Rejection based on an absolute threshold. This technique requires *a priori* knowledge of the problem to set a suitable threshold. The set threshold is invariant of the initial matrix condition, and singular value rejection may lead to improvement or degradation of the results. This method should therefore be avoided.

2. Rejection based on a relative threshold. In this approach, the largest singular value is taken as reference, and all singular values below a certain percentage of it are rejected. This introduces an upper limit for the condition number, since $\kappa = \sigma_{max}/\sigma_{min}$. For example, a relative threshold of 2% of the largest singular value will prevent the condition number from exceeding a value of 50 (since $\sigma_{max}/(0.02\sigma_{max}) = 50$). This method is easy to implement and does not require much information about the

system. However, it is also quite coarse, and an appropriate relative threshold (in percent) must be chosen manually.

3. Rejection based on errors in $\mathbf{A}$ or $\mathbf{b}$. Provided some information is available on the reliability of $\mathbf{A}$ and/or $\mathbf{b}$, for example in the form of coherence values [26], a threshold for the rejection of singular values can be calculated as a function of the estimated errors in $\mathbf{A}$ and/or $\mathbf{b}$. The reader is referred to [140] for a general explanation of this method and an application to a vibro-acoustic problem.

Tikhonov regularization

More advanced methods such as Tikhonov regularization make use of a regularization parameter to modify singular values instead of completely discarding them. *Tikhonov regularization* is named after A. N. Tikhonov [144], who introduced the parameter λ into the SVD equation:

$$\mathbf{A^{-1}} = \mathbf{V}(\mathbf{S^T S} + \mathbf{I}\lambda)^{-1}\mathbf{S^T U^H} \tag{2.38}$$

The parameter λ modifies the reciprocal singular values in the inverse. The diagonal matrix $\mathbf{S^{-1}}$ is replaced by the diagonal matrix $(\mathbf{S^T S} + \mathbf{I}\lambda)^{-1}\mathbf{S^T}$, in which the elements take on the form $\sigma_i/(\sigma_i^2 + \lambda)$ instead of $1/\sigma_i$. This introduces a bias error into the solution, and the choice of λ assumes importance. For matrices with high condition numbers, regularization restricts the effect of small singular values. In this case the small bias error is a negligible side-effect compared with the reduction in condition number. For matrices with low condition numbers, the bias error will be non-negligible and should be avoided.

While Tikhonov regularization can improve the matrix inversion, the main problem of singular value rejection methods remains. The problem of selecting an appropriate threshold parameter is replaced with that of finding an appropriate regularization parameter. A variety of methods exist for determining a suitable regularization parameter [33], the most important of which are: ordinary cross-validation [22], generalized cross-validation [64], and the L-curve method [67, 68].

2.5 Summary

In this chapter, an introduction was given to the field of structure-borne sound source characterization and the associated fields of structure-borne sound power and inverse methods.

The two basic source parameters (source activity and mobility) were described, and common measurement procedures explained. Free velocity and blocked force may be used as measures of source activity, though both parameters assume the source to be invariant of constraints placed on it by the receiver. Different types of mobilities were introduced, and it was shown that the experimental determination of full mobility matrices can require significant measurement effort, depending on the number of terminals and components of excitation at each terminal.

The importance of structure-borne sound power was explained, and reasons were given why a source characterization should be based on the power emitted by the source. Some of the most important methods for the determination of source power were described: direct measurement, mobility method, source descriptor and coupling function, and the reception plate method. Advantages and disadvantages of each method were highlighted, and it was concluded that depending on the requirements, one or the other of these methods may be appropriate.

The inverse problem was reviewed on a purely mathematical basis, introducing the concepts of matrix condition, singular value decomposition, and generalized matrix inverse. The problem of ill-conditioned matrices amplifying random measurement noise was illustrated, and common methods to mitigate these problems described: over-determination, singular value rejection, and Tikhonov regularization.

The following chapters will further expand on the theory and application of structure-borne sound source characterization and inverse methods, and will review more literature where necessary. The basic concepts described in this chapter form the basis for everything that follows.

3 Indirect Methods to Obtain Blocked Forces

3.1 Introduction

The determination of forces and moments plays an important role in many applications in noise control engineering. For instance, operational forces and moments are required as input data for Transfer Path Analysis (TPA) methods in the automotive and aerospace industries [5, 113, 130], for vibro-acoustic finite element software [3], and for the calculation of injected power into a

receiver structure (cf. Section 2.3). Furthermore, blocked forces may be used as descriptor of the activity of structure-borne sound sources, for an independent source characterization (cf. Section 2.2.1).

Direct measurement of forces and moments poses greater challenges than measurement of linear or angular accelerations. Transducers must be inserted between source and receiver, inevitably altering the transmission paths and the transmitted structure-borne power. With regards to moments, there is currently not a method or transducer to measure moments directly, and it is not obvious how such a transducer could work. The direct measurement of operational moments therefore is assumed not possible at present.

To circumvent these problems, indirect methods of obtaining operational forces and moments have been developed, for example the mount stiffness method [145], transmissibility methods [55], and the matrix inversion method. The last was used in this study, and is outlined in Section 3.2.1.

Operational contact forces are specific to the particular source-receiver combination under test. For the automotive and aerospace industries, this usually is not an important limitation, as engineers often deal with specific source-receiver combinations, for example one particular engine in one particular car. In building acoustics, however, greater flexibility is required. Structure-borne sound sources in buildings can be attached to a variety of building structures, from heavyweight concrete floors to lightweight timber-frame walls. Therefore, an independent description of source strength is required, irrespective of receiver mobility, for example in the form of free velocity or blocked force.

In this chapter, the matrix inversion method for the indirect determination of operational forces is reviewed, together with a modified approach which yields the blocked forces. The inverse problem associated with these methods is discussed. A simplified measurement procedure, using a fully-defined receiver structure, is proposed for the determination of approximate blocked forces and moments. A resiliently supported free plate is used as receiver structure, as most receiver structures in buildings are plate-like. A numerical model for the calculation of point and transfer mobilities of free plates is reviewed, and results are compared with measurements and finite element models. An experimental investigation follows in Chapter 4.

3.2 Review of inverse force determination

Methods for the indirect quantification of operational forces have received much attention, in particular in the automotive industry, and a substantial body of literature exists. Early work on the indirect identification of structural loads was published during the 1980s [24, 114, 70, 145], and since then a steady stream of publications has followed, e. g. [41, 118, 69, 86, 146, 30]. In this section, the main developments and findings are reviewed, under four sections: inverse force determination, associated errors, over-determination and regularization methods, and optimization of response measurement locations.

3.2.1 Inverse force determination

A vibrating source, connected to a receiver structure, exerts a varying force at the interface, which in turn excites the receiver. The contact force F_r and the contact velocity v_r are linked by the receiver point mobility Y_r: $v_r = Y_r F_r$. If there is more than one contact or component of motion, F_r and v_r are vectors, and Y_r is a matrix, see Sections 2.2.1 and 2.2.2:

$$\mathbf{v_r} = \mathbf{Y_r F_r} \tag{3.1}$$

As in Chapter 2, the frequency-dependence of the three quantities in Equation (3.1) is omitted for conciseness. For velocities $\mathbf{v_r}$ on the receiver structure remote from the contacts, $\mathbf{Y_r}$ is a transfer mobility matrix, see Figure 3.1. The (transfer) mobility matrix is also termed the FRF matrix in the following discussion. To obtain the operational forces at the source-receiver interface, Equation (3.1) can be solved for $\mathbf{F_r}$:

$$\mathbf{F_r} = \mathbf{Y_r^{-1} v_r} \tag{3.2}$$

Equation (3.2) yields a three-step procedure for indirectly obtaining the contact forces between source and receiver:

1. The FRF matrix $\mathbf{Y_r}$ of the uncoupled receiver structure is measured, by applying forces at each of the contact positions one at a time, and recording the responses at all response positions.

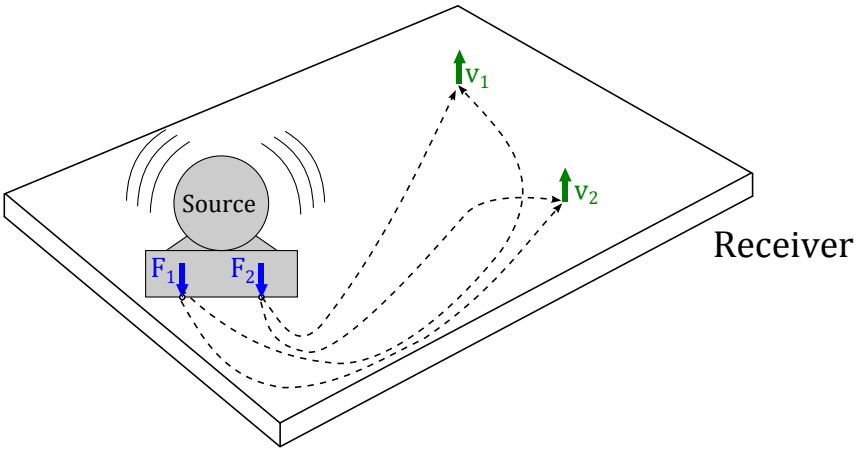

Figure 3.1: Structure-borne sound source connected to a receiver structure, resulting in vibration responses at the source-receiver interface and at remote positions on the receiver structure.

2. The source is connected to the structure, and the velocities $\mathbf{v_r}$ at the same response positions are recorded during operation of the source.

3. The operational contact forces are calculated from Equation (3.2). The FRF matrix is inverted frequency by frequency, and multiplied with the velocity response vector.

This approach is commonly termed the *matrix inversion method*, and is used for example in classical Transfer Path Analysis, where the contributions of each source of excitation and along each transmission path are analysed individually and rank-ordered [5, 54].

There are two principal challenges to matrix inversion methods. The first concerns the determination of the FRF matrix $\mathbf{Y_r}$. FRF matrices increase considerably in size when the number of contact points and/or components of excitation increases, cf. Section 2.2.2. No significant forces or transmission paths may be omitted, meaning all relevant FRFs have to be determined, usually by measurement. This can result in a significant measurement effort, which limits the applicability of this approach, in particular in building acoustics.

The second challenge stems from the necessary inversion of the FRF matrix. The general inverse problem was described in Section 2.4. A detailed review with a focus on structural load identification is provided in Section 3.2.2.

Modified method to determine blocked forces

Again, the operational forces obtained using Equation (3.2) are specific to the source-receiver combination under consideration. If the receiver structure is modified or the source is moved, a new calculation of the operational forces is required, which entails a new set of measurements of the altered FRF matrix.

To overcome this limitation, Moorhouse et al. [100] suggested a modification to Equation (3.2). Instead of inverting the FRF matrix of the uncoupled receiver mobilities, $\mathbf{Y_r}$, they proposed to invert the FRF matrix of the coupled mobilities, $\mathbf{Y_c}$:

$$\mathbf{F_b} = \mathbf{Y_c^{-1}} \mathbf{v_r}. \tag{3.3}$$

Equation (3.3) yields the blocked forces, which are independent of the receiver structure. Similar approaches have also been suggested by other authors [49, 50, 80]. The attractiveness of Equation (3.3) is that it yields blocked forces of the source when coupled to a receiver structure. As highlighted in Section 2.2, the direct measurement of blocked forces poses practical challenges. Furthermore, *in-situ* determination of blocked forces circumvents the problem of source invariance (cf. Section 2.2.1). Since the source activity is obtained in a representative mounting condition, results can be assumed to be similar to those in other similar mounting conditions.

Equation (3.3) requires the determination of the coupled (transfer) mobility matrix. Provided there is access to the source-receiver interface to attach accelerometers, this is similar to the determination of the uncoupled mobility matrix. Equation (3.3) was successfully used in several studies [43, 79, 81], but it does not solve problems associated with matrix inversion, or the challenge of obtaining all necessary mobility terms.

3.2.2 Errors associated with inverse force determination

Generally, two types of errors can be distinguished: statistical or random errors, and deterministic or systematic errors. Both play a role in inverse force determination.

Statistical errors

Statistical errors in inverse force determination include [54]:

- random noise in the FRF estimates;
- random noise in the operational response signals.

The general introduction to the inverse problem in Section 2.4 addressed the problem of random errors. Small errors in vector $\mathbf{b}$ can result in large errors in vector $\mathbf{x}$, depending on the condition of the matrix $\mathbf{A}$ that is inverted, cf. Equation (2.29). In inverse force determination, random errors in the response vector are almost inevitable, due to background noise and resonant behaviour of the receiver structure. Therefore, the condition of the FRF matrix $\mathbf{Y}$ assumes importance. Noisy measurement data in combination with an ill-conditioned FRF matrix can give rise to extremely large errors in the force estimates. If the errors in the response velocity vector are large, but the condition numbers of the FRF matrix are small, the errors in the measured velocities are simply propagated to the force estimates without much amplification.

Blau [29] investigated the influence of errors in typical FFT-based measurements of FRF and response spectra on inversely determined excitation forces. He developed an error model that allows the estimation of statistical errors in individual force estimates, based on statistical errors in the FRFs and responses. Some of the main results of Blau's investigations are summarized in [28]. For example, it was shown that random errors due to matrix inversion tend to be evenly distributed over all force spectra, with the result that relative errors will be larger for weak forces.

Deterministic errors

Deterministic errors in inverse force determination include [54]:

- non-linear behaviour of the receiver structure;
- neglected degrees of freedom in the FRF matrix, e. g. rotational motion;
- excitation misalignment during FRF measurements;
- sensor mass loading;
- inconsistencies between elements of the FRF matrix, due to changing conditions during multi-run measurements.

Deterministic errors are more difficult to address than random errors. Most previous research has focused on the latter, and only few publications exist on the effect of deterministic errors.

Fabunmi [48] argued that for inverse force determination to yield reliable results, the number of structural modes contributing to the response at a certain frequency must be at least equal to the number of unknown forces. Over-determination of the system (see Section 3.2.3), i. e. using more response signals than forces to be determined, does not improve the reliability of the force estimates if this is not the case. Although Fabunmi based his conclusions on work with beams only, his recommendations apply to a range of structures.

Gajdatsy [54] used a simplified FE model of an aeroplane to estimate errors in the determined forces due to inconsistent FRFs. He concluded that some methods are more robust than others, and that even small systematic errors may result in significant errors in the estimated forces. However, it is difficult to quantify these errors in advance.

3.2.3 Over-determination and regularization methods

Mathematical methods exist to mitigate problems associated with random errors in matrix inversion, see Section 2.4. The most important are over-determination, singular value rejection, and regularization techniques. All of these have been studied in detail, with a focus on inverse force determination.

Thite and Thompson [139, 140, 141] systematically investigated the use of inverse methods for the quantification of structure-borne transmission paths. Several virtual forces of varying magnitude were applied to a numerical model of a rectangular plate. Results were validated experimentally, using a freely suspended plate excited by several shakers. The findings of these studies are directly applicable to the experimental studies described in Chapter 4. Some of the most important conclusions from [139, 140, 141] include:

- Over-determination reduced condition numbers and hence improved force estimates considerably at high frequencies, where the modal overlap was large. At low frequencies, over-determination was not effective. Increased over-determination did not reduce the minimum condition numbers significantly, although it reduced the occurrence of high condition numbers.

- Singular value rejection proved to be a powerful tool for reducing error amplification. Threshold criteria based on error estimates in FRFs or operational responses were explored, but neither is universally applicable. The selection of a suitable threshold for SVR remains a challenge.
- Tikhonov regularization was investigated using ordinary cross-validation to select the regularization parameter. Also investigated was an alternative method, referred to as iterative inversion. Both methods produced better results than over-determination or singular value rejection. However, they also required more attention to detail, and were computationally more intensive. Following these findings, Choi et al. studied the Tikhonov regularization parameter in detail in [32, 33].
- Condition numbers were found to depend on the noise level in the FRFs. Greater noise generally reduced the condition numbers at low frequencies, where the modal density was very small, whereas it increased the condition numbers at high frequencies. The worst performance was found when the noise levels in the FRFs were small (high condition numbers) and the noise level in the responses was large.

Gajdatsy [54] investigated inverse force determination in the context of the automotive industries. He states that in the automotive industry, singular value rejection is generally applied with a relative threshold of 1% of the largest singular value, based on experience. Furthermore, he states that generally an over-determination factor of 2 is recommended.

3.2.4 Optimization of response measurement locations

Errors associated with matrix inversion can be reduced by careful selection of response measurement positions. The placement of accelerometers affects two important parameters, namely, the measurement noise in the response signals, and the condition number of the FRF matrix [27]. Placing sensors on or near a nodal line should be avoided, because it causes the output signal to drop at the resonance frequencies resulting in a low SNR [54]. When two indicator points are located too close to each other with respect to the bending wavelength of the structure, their respective FRFs are nearly identical. Using these FRFs in the inversion process creates two linearly dependent rows in the FRF matrix, which in turn yields a high condition number [54]. Optimizing the location of

the response sensors is therefore potentially one of the most effective methods to overcome the inverse problem. However, finding the optimal combination of response positions is not straightforward.

Thite and Thompson [139, 143] reviewed several methods of optimizing response measurement locations, including: the Guyan reduction approach, methods of maximum/average modal kinetic energy or average driving point residue, the effective independence method, and Gram-Schmidt orthogonalization. Also considered was a sensor placement criterion specifically for inverse force determination, proposed by Blau. Thite and Thompson suggest a procedure based on a "composite condition number" to find the best combination of response positions. This procedure is examined in Section 4.3.3.

Zheng et al. [159] proposed a similar method, based on a coherence factor of the transfer function matrix. The method requires the determination of a large number of FRFs, from which the best possible combinations are calculated. This technique will also be examined in Section 4.3.3.

3.3 Inverse determination of blocked forces in the context of building acoustics

3.3.1 Review of inverse force determination in building acoustics

Matrix inversion methods are commonly used in the automotive and aerospace industries, in particular in the framework of TPA [5, 113, 130]. However, despite the strong research record and many publications on the topic, inverse force determination remains a topic for experts. Obtaining the FRF matrices requires technical expertise in the measurement of mobilities, and handling the subsequent data processing requires judgement on how to set parameters for over-determination and regularization.

For these and other reasons, such methods have not been applied to building acoustics, where the requirement is that measurements are not complicated and can be performed without in-depth knowledge of the subject. Engineers deal with a wide range of measurements and sources, and procedures must therefore be robust.

In the author's opinion, many of the existing procedures for structure-borne sound are too complicated for the building industry, although they may be well-suited for "high-engineering" industries. The objective therefore is to simplify the procedures developed for the latter, to make them available to the former. These simplifications will in many cases result in loss of accuracy and detail, but such a trade-off is worthy of investigation. There have been a limited number of studies of inverse methods in building acoustics, reported in the literature.

Yap and Gibbs [156, 157] published on the indirect measurement of contact forces in the field of building acoustics. In [156], they introduced an indirect method to measure contact forces and moments, and used it to determine the contact forces between an industrial fan unit with four contact points and a supporting concrete floor. Also measured was the contact force for attachment of only one of the four contact points. The fan was connected to the floor through thin driving rods and a force transducer, and was placed in an acoustic enclosure to suppress secondary airborne transmission paths. For the single-contact case, the force could be determined within $\pm 3\,\mathrm{dB}$. For the multiple-contact case, the indirectly determined forces were positively biased by approximately $3\,\mathrm{dB}$, compared with the directly measured forces; also, the largest deviations were found for frequencies where the difference between the four contact forces was large. The deviations in force estimates often exceeded $10\,\mathrm{dB}$. They were attributed to practical difficulties of applying pure forces, and to secondary transmission paths. At the time, the significance of the involved matrix inversion for the multiple-contact case was not recognized. In [157], the indirect method was employed for a single-contact built-up machine base, to investigate the role of moments in the transmission of structure-borne sound power to masonry structures, and the influence of source location. The determined forces and moments were not seen as independent source quantities, but were only used for laboratory case studies.

Scheck [120, 122] used a similar method to determine relevant components of excitation of a lightweight stair connected to a heavyweight wall through one contact. The normal force component and the two moments perpendicular to the wall surface were considered, and three response positions were used, rendering a 3×3 FRF matrix. The three components of excitation were compared on a power basis, by multiplying the force/moments with the corresponding linear/angular velocities. It was found that for the lightweight stair system under

test, the normal force component was most important. Scheck investigated the reciprocal measurement of (cross-)transfer mobilities, and found that for the source under test, moment induced powers were significantly over-estimated as a result of small experimental errors in the reciprocal measurement. The question of the FRF matrix condition was not addressed, however.

Schevenels [125, 126] examined structural-acoustical methods together with reciprocity measurements to determine the contact forces and transmitted power between a tonal, low-frequency vibrating platform and a heavyweight floor. He employed structural-acoustical transfer paths, instead of purely structural paths. In the first measurement stage, a low-frequency volume velocity source, in a receiver room below the source room, provided the excitation, and the velocity responses at the source contacts were recorded. In the second stage, the source was operated on the floor, and the pressure responses in the receiver room recorded. From the structural-acoustical FRF matrix and the pressure response vector, the contact forces were determined. It was highlighted that for inverse force determination to yield accurate results, all important transmission paths need to be represented in the inverted matrix. Paths not included will result in "pseudo-forces", which over-estimate the actual forces. In this case, the vibrating platform excited the floor acoustically, adding a path to the purely structural paths. Furthermore, if the measured responses are contaminated by noise, this will also result in an over-estimate of the forces. Schevenels also employed over-determination and singular value rejection.

Lievens [87, 88] used structural-acoustical inverse relationships to investigate the importance of the degrees of freedom for the characterization of structure-borne sound sources. He proposed a method in which the sound pressure level in a receiver room is predicted from inversely determined blocked forces and directly measured coupled FRFs, and is compared with the directly measured sound pressure level in the room. From the difference between predicted and measured sound pressure levels, the relative importance of rotational and in-plane degrees of freedom may be assessed. The method is based on the assumption that the required FRFs can be determined exactly, and that the errors due to matrix inversion are negligible. The case study was a washing machine, connected at three points to a wooden joist floor. It was concluded that neglecting five of the six degrees of freedom resulted in only limited loss of accuracy.

All of the studies reviewed in this section relied on the measurement of FRFs,

and were designed for use by well-informed technical personnel in the laboratory. In the next section, a simplified procedure for the inverse determination of blocked forces with a broader range of applicability is proposed.

3.3.2 Simplified inverse method for blocked forces

The objective is to develop a measurement procedure for the inverse determination of blocked forces, suitable for applications in building acoustics. The requirements for the method are:

1. The involved measurement effort should be minimal.
2. The measurement setup should be simple. If a special rig is required, it should be easy to construct, assemble and disassemble. It should be robust enough to be placed in a workshop rather than in a laboratory.
3. Mobility measurements should be avoided if possible.
4. The method should yield independent source data.
5. Data is required as third-octave band values.
6. The method should avoid advanced simulation techniques such as FEA, and should not require intensive signal processing.
7. The procedure should be robust against measurement errors.

With these requirements in mind, a method based on Equation (3.2) is proposed. A free (FFFF) plate is chosen as receiver structure, because most receiver elements in building acoustics are plate-like, and because free boundary conditions are easiest to achieve in terms of construction and assembly.

A fully-defined receiver plate opens up possibilities of reducing the measurement effort and opportunities to deal efficiently with the inverse problem. If the receiver structure can be described analytically or numerically, the FRF matrix required in Equation (3.2) can be calculated. The only measurements then required are the velocity responses at remote positions. Furthermore, the condition of the FRF matrix to be inverted depends strongly on the location of excitation and response positions, cf. Section 3.2.4. A numerical model of the receiver structure allows the determination of a favourable combination of response positions, and therefore a reduction of the errors associated with the matrix inversion.

From Equation (3.2), the operational contact forces $\mathbf{F_r}$ between a source and a receiver structure can be determined from receiver mobilities and response velocities. For a proper source characterization, the blocked forces $\mathbf{F_b}$ are more appropriate than the operational forces. The contact forces $\mathbf{F_r}$ can be expressed as a function of blocked forces $\mathbf{F_b}$ and source and receiver mobilities, $\mathbf{Y_s}$ and $\mathbf{Y_r}$ respectively:

$$\mathbf{F_r} = (\mathbf{Y_s} + \mathbf{Y_r})^{-1}\mathbf{Y_s}\mathbf{F_b} \tag{3.4}$$

If the source point mobility is significantly higher than the receiver point mobility ($\mathbf{Y_s} \gg \mathbf{Y_r}$), the contact forces approximate the blocked forces:

$$\mathbf{F_r} \approx \mathbf{F_b} \qquad \text{for} \qquad \mathbf{Y_s} \gg \mathbf{Y_r} \tag{3.5}$$

Substituting Equation (3.5) into Equation (3.2) yields

$$\mathbf{F_b} \approx \mathbf{Y_r^{-1}}\mathbf{v_r} \qquad \text{for} \qquad \mathbf{Y_s} \gg \mathbf{Y_r}. \tag{3.6}$$

The blocked forces can be approximated from receiver mobilities and operational response velocities, provided the source mobility is significantly higher than the receiver mobility. This can be ensured by careful selection of the plate parameters (material, dimensions, thickness).

The proposed measurement procedure for the simplified inverse determination of approximate blocked forces is as follows:

1. The geometrical distance between source contacts is measured, and the source placed on the plate at a position that ensures that for the lowest eigenfrequencies of the plate, the source contacts are not at nodal lines.
2. Based on the numerical model of the plate, suitable response positions are determined automatically. Various procedures can be used for the determination of favourable response positions, see Section 3.2.4.
3. The FRF matrix is calculated, using a numerical model of the receiver.
4. Velocity spectra are measured at the response positions during operation of the source. This is the only required measurement.
5. From the calculated FRF matrix and the measured velocity responses, the contact forces are determined using Equation (3.2). For a high-mobility source, these approximate the blocked forces, cf. Equation (3.6).

The requirements for a simple measurement method, listed above, are addressed by the proposed procedure as follows:

1. *The involved measurement effort should be minimal.*
   ⇒ Only one measurement is required, namely recording the velocity responses on the plate during operation of the source.
2. *The measurement setup should be simple.*
   ⇒ Free plates are easy to construct, compared with other possible receiver structures or different boundary conditions.
3. *Mobility measurements should be avoided if possible.*
   ⇒ No mobility measurements are required, the FRF matrix is calculated.
4. *The method should yield independent source data.*
   ⇒ Provided appropriate plate parameters are chosen, the plate mobility will be significantly lower than most source mobilities, yielding approximate blocked forces.
5. *Data is required as third-octave band values.*
   ⇒ Though the calculation in Equation (3.2) is performed using narrowband data, the results can easily be converted to third-octave band values.
6. *The method should avoid advanced simulation techniques such as FEA.*
   ⇒ A numerical model based on beam functions is used to describe the free plate and calculate the FRF matrix, see Section 3.4.
7. *The procedure should be robust against measurement errors.*
   ⇒ The robustness of the method is investigated in Chapter 4.

In building acoustics, the reception plate method, as described in EN 15657-1:2009 [17], offers a convenient way to determine the injected source power if the source mobility is much higher than the plate mobility. The method requires a 100 mm thick concrete plate with free boundary conditions as receiver structure. It therefore fulfils the requirements for the proposed simplified method to obtain the approximate blocked forces. The proposed method would be an ideal complement to the reception plate method, if more information than the injected source power is required about the source under test. The blocked forces allow a quantification and qualification of the most important source terminals.

The key to the proposed measurement procedure is the analytical or numerical description of the receiver plate. This is discussed in the next section.

3.4 Numerical model of a FFFF plate

The analytical and numerical description of plates has been studied in detail for many years. One of the standard texts on this topic was written by Leissa [84], who compiled a compendium of formulations for plates with different boundary conditions. The problem of plates with free edges in particular has received much attention. A comprehensive overview on plate vibrations is beyond the scope of this thesis. Instead, reference is made to the literature (e. g. [84, 85, 129]), and one well-established model is implemented with a focus on application.

3.4.1 Modal summation and beam function model

The following calculation of point and transfer mobilities of thin rectangular plates is based on the description in [57, Section 9.8.4], which in turn is based on [151] and [129]. An overview is given in this section, and detailed information on the calculation of mobilities of rods, beams and plates using modal summation is provided in Appendix B.

The point and transfer mobilities for out-of-plane vibration of thin, finite plates can be expressed in terms of a modal summation. A rectangular plate is considered. The plate is excited by a force or moment at position (x_1, y_1), and the linear or angular response velocity determined at position (x_2, y_2). The point and transfer mobilities for force excitation are given as

$$Y_{v_z F_z}(\omega) = j\omega \sum_{m=1}^{\infty} \sum_{n=1}^{\infty} \frac{\psi_{mn}(x_2, y_2)\psi_{mn}(x_1, y_1)}{\rho h l_x l_y \left[\omega_{mn}^2(1 + j\eta) - \omega^2\right]}. \tag{3.7}$$

Here, ψ_{mn} is the (m, n)th bending mode shape, ω_{mn} is the associated eigenfrequency, h, l_x and l_y are the geometric dimensions of the plate, ρ is the material density, and η is the total loss factor.

The eigenfrequencies of rectangular plates are given as [151]

$$\omega_{mn} = \sqrt{\frac{Eh^2}{12\rho(1-\nu^2)}} \left(\frac{\pi}{l_x}\right)^2 q_{mn}. \tag{3.8}$$

E is Young's modulus, ν is Poisson's ratio, and q is described in Appendix B.

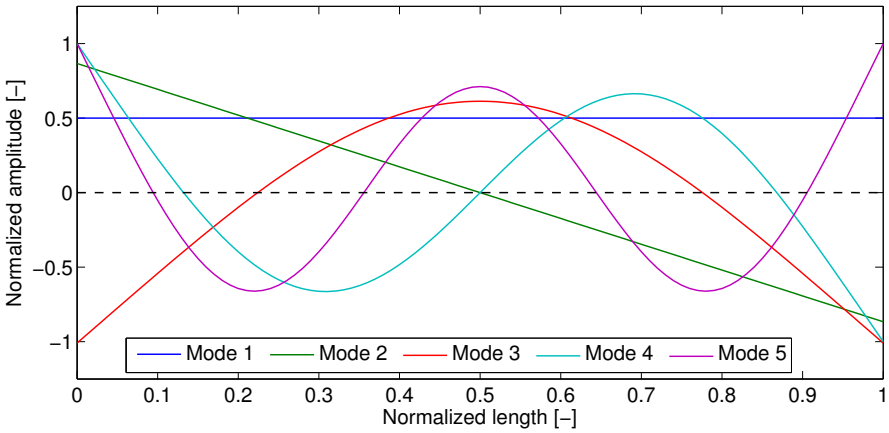

Figure 3.2: First five eigenmode shapes of a free beam.

The plate mobility is calculated by summing the contributions of each combination of mode shapes. In practice, the upper limit of the sum must be adjusted according to the frequency range of interest. Mode shapes with eigenfrequencies above the highest frequency of interest also have an influence on the mobilities, in particular at high frequencies. The more mode shapes are included in the modal summation, the more accurate the result will be.

The plate mode shapes may be calculated approximately as products of the beam mode shapes ϕ_m and ϕ_n:

$$\psi_{mn}(x, y) = \phi_m(x)\phi_n(y). \tag{3.9}$$

Equations for the eigenfrequencies and beam mode shapes for the most common boundary conditions are provided in [57], and are reproduced in Appendix B for free boundary conditions. The first five eigenmode shapes of a free beam are shown in Figure 3.2. The first two modes represent whole-body movement (even and rocking mode), while higher modes represent bending motion.

In a similar fashion to Equation (3.7), the (cross-)point and (cross-)transfer mobilities involving the two out-of-plane moments M_x and M_y can be calculated (see Appendix B), as well as in-plane mobilities (see [57, Section 9.8.5]). However, the focus is on out-of-plane force excitation in the following.

3.4.2 Comparison with measured mobilities

The numerical model described in Section 3.4.1 was implemented in MATLAB and was validated by comparing measured mobilities on a free aluminium plate with calculated mobilities from Equation (3.7). The plate, also used in Chapter 4, has size 2.12 m × 1.50 m × 20 mm. It was supported at the corners and edges by visco-elastic patches (Getzner SyloDamp HD30). This configuration attempts to simulate free boundary conditions, and additionally provides damping. The following material parameters for aluminium were used: Young's modulus $E = 70\,\text{GPa}$, density $\rho = 2700\,\text{kg/m}^3$, Poisson's ratio $\nu = 0.33$. The loss factor of the plate was measured in third-octave bands, using the method described in Appendix D, and was interpolated for the calculation of narrowband mobilities. It is shown in Figure 3.3. The measurement of FRFs on the plate is described in Section 4.2.1.

Figure 3.4 shows the measured and calculated point mobility of the plate at position (0.325 m, 0.380 m), measured from the origin in one of the corners of the plate. A reduced frequency range is displayed for ease of comparison. The calculated eigenfrequencies of the plate are indicated at the top of the plot. Below 100 Hz, there are large differences between calculated and measured mobilities. The resonance frequencies are shifted, and the damping of the measured mobilities is higher than that of the calculated mobilities. Above 100 Hz, there is good agreement between calculated and measured mobilities in terms of "signature". However, there is a shift in the resonance frequencies, resulting in large differences in magnitude and phase. For example, at 172 Hz, measured and calculated mobilities are equal in magnitude, but almost opposite in phase. At 178 Hz, they are almost equal in phase, but differ in magnitude by a factor of 10.

For the accurate prediction of forces using Equation (3.6), a high degree of agreement is required between measured and calculated mobilities. Therefore, the effects of adjusting relevant quantities used in the calculation (density, Young's modulus, Poisson's ratio, and loss factor) were investigated, in order to fit the calculated mobilities to the measured values. Figure 3.5 shows the effects when changing one of the involved plate parameters at a time. Changing the plate dimensions was not investigated, as these parameters can be determined with high accuracy. Changing the density value shifts resonance

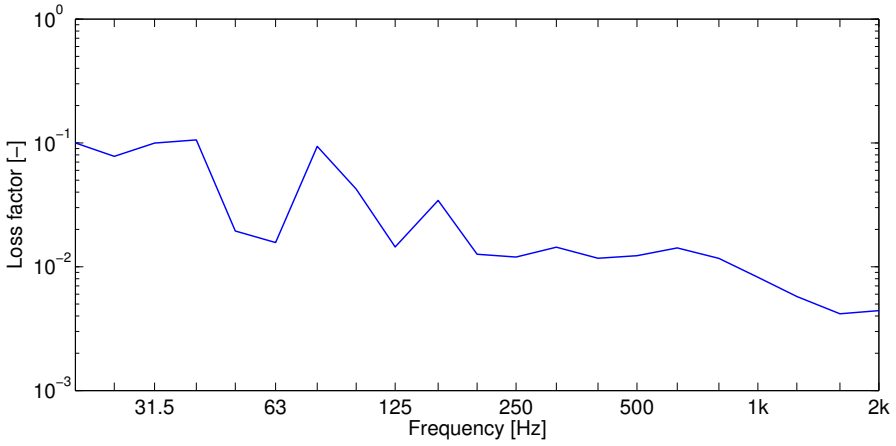

Figure 3.3: Loss factor of free aluminium receiver plate.

frequencies by a factor of $\sqrt{\rho/(\rho + \Delta\rho)}$, but does not affect amplitudes significantly. Changing Young's modulus shifts the resonance frequencies by a factor of $\sqrt{(E + \Delta E)/E}$. Changing Poisson's ratio has more complicated effects on the calculated resonance frequencies, but the effects are relatively small. The loss factor only changes the quality of peaks and troughs, but not the resonance frequencies.

Closer inspection of Figure 3.4 reveals that it is impossible to exactly match the calculated mobilities to the measured mobilities by simply adjusting the calculation parameters (density, Young's modulus, Poisson's ratio, and loss factor). The calculated resonance frequencies do not deviate by a constant shift, but are compressed and expanded compared with the measured values.

Two possible reasons for the deviations between measured and calculated mobilities are identified:

- The resiliently supported plate may not behave like a true free plate. The beam functions used to calculate the mode shapes describe a beam with perfectly free boundary conditions. In practice, the boundary conditions of the plate will approximate a free state, but the supporting patches may introduce some restriction on the plate movement. A better approximation of the free condition could be achieved by resiliently suspending the plate at the nodal lines of the lowest eigenfrequencies [46]. However, for a plate of this size and mass this poses practical difficulties. Furthermore,

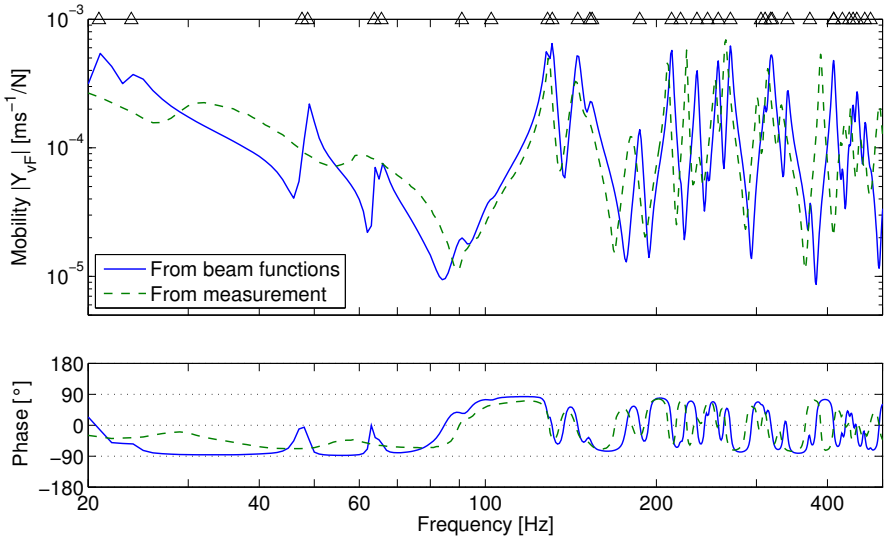

Figure 3.4: Point mobility of aluminium plate at position (0.325 m, 0.380 m), measured and calculated according to Equation (3.7).

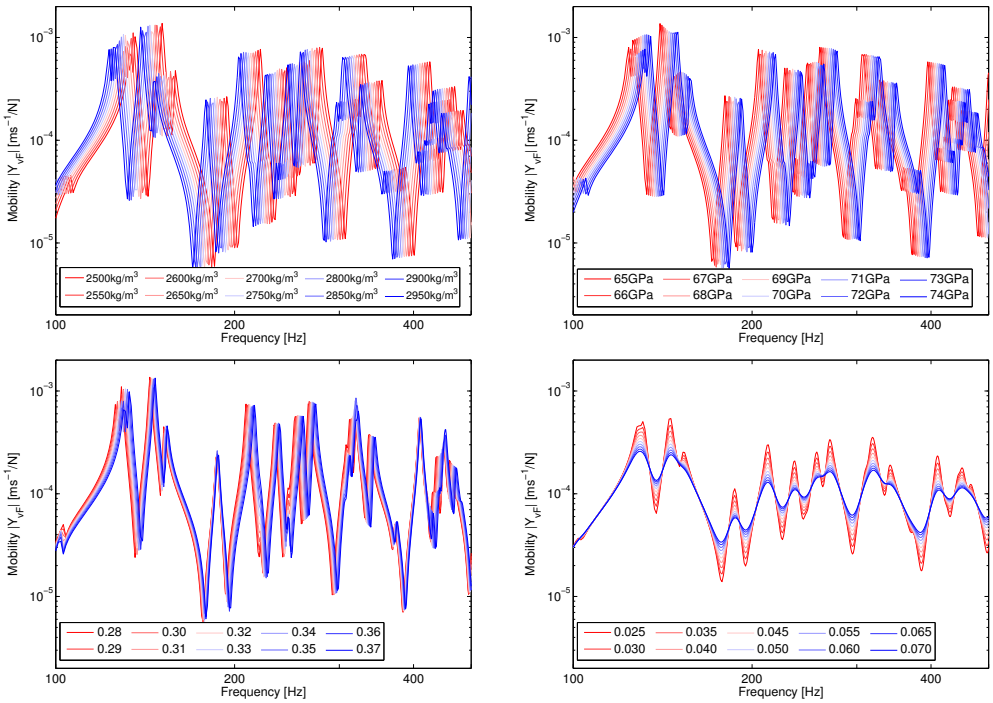

Figure 3.5: Effects of changing plate parameters on the calculated plate point mobility: density (top left), Young's modulus (top right), Poisson's ratio (bottom left), and loss factor (bottom right).

a suspension at the nodal lines would limit the usability of the plate, as structure-borne sound sources need to be operated on it.

- The mode shapes calculated from beam functions are not exact for plates with free edges [151, 25]. For plates with at least two opposite sides simply-supported, the product of beam functions yields exact mode shapes. For other boundary conditions, however, the mode shapes calculated from beam functions only approximate the real mode shapes.

3.4.3 Comparison with finite element model

To further investigate the deviations between measured and calculated mobilities, a free plate was modelled, using the finite element software package ABAQUS [3]. The plate was meshed using S4R shell elements, with one node every 2.5 cm, resulting in 86×61 nodes. Assuming a minimum of six elements per wavelength [72], the upper limit of the usable frequency range lies at around 8.4 kHz, much higher than the upper limit of 2 kHz used in the measurements. The calculations were performed with the same parameters as in the beam function model: E = 70 GPa, $\rho = 2700\,\mathrm{kg/m^3}$, $\nu = 0.33$.

The mode shapes and eigenfrequencies of the free plate were evaluated in ABAQUS and exported to MATLAB for further processing and plotting. The point mobility at position (0.325 m, 0.380 m) was calculated from Equation (3.7), using the mode shapes and eigenfrequencies from ABAQUS, and is shown in Figure 3.6. Below 100 Hz, the deviations between measured and calculated mobilities are considerable. The resonance frequencies are shifted, and the damping of the measured mobilities is significantly higher than that of the calculated mobilities. Above 100 Hz, the agreement between calculation and measurement is better than in Figure 3.4. Occasional frequency shifts still occur, but generally the eigenfrequencies calculated by FEA approximate the measured values with better accuracy than the eigenfrequencies calculated using Equation (3.8).

The beam function model and the FE model were further investigated by considering the mode shapes and the eigenfrequencies directly. Figures 3.7 and 3.8 show the first ten mode shapes calculated by each method, together with the associated eigenfrequencies. Visual inspection reveals the main difference between the two models: The beam function model calculates the plate mode

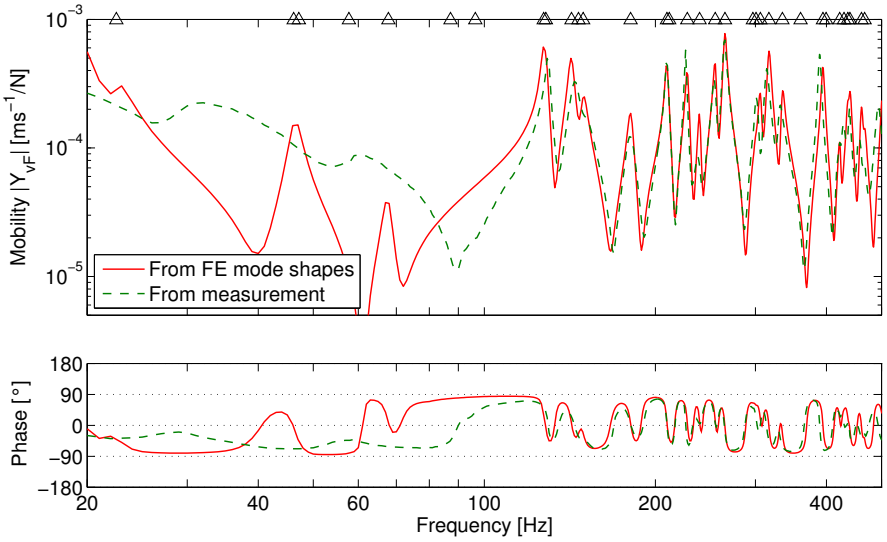

Figure 3.6: Point mobility of aluminium plate at position (0.325 m, 0.380 m), measured and calculated using FE mode shapes.

shapes as a superposition of two beams in x and y direction, with no cross-coupling. In practice, and in the FE model, movement in one direction has an effect on the other direction, due to Poisson contraction. This influence is most important at free edges or free corners of the plate.

To verify this, the mode shapes were calculated in ABAQUS, with Poisson's ratio ν set to 0. Figure 3.9 shows one mode shape for the three different calculations: from beam functions, from FE model with $\nu = 0$, and from FE model with $\nu = 0.33$. The effect of Poisson's ratio is clearly seen.

In addition to the differences in mode shapes, the eigenfrequencies calculated from FEA and from Equation (3.8) deviate from each other. Generally the values from Equation (3.8) are higher than those from FEA. Also, occasionally the order of the modes is changed, when sorted by the eigenfrequency. For example, while mode $(0, 2)$ has a higher eigenfrequency than mode $(2, 1)$ in the left column of Figure 3.7 (rows 3 and 4, respectively), it is the opposite in the right column.

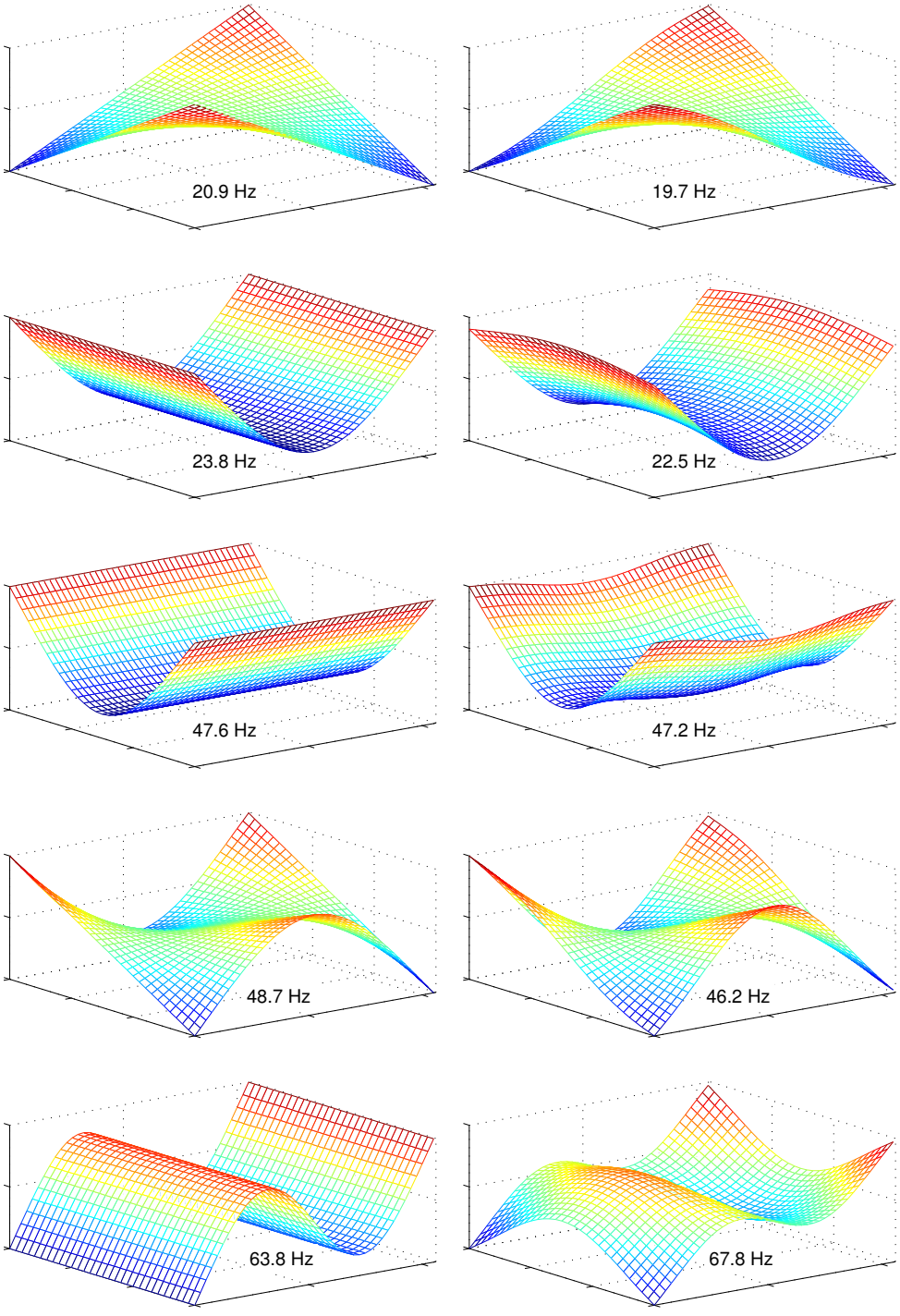

Figure 3.7: Plate mode shapes calculated from beam functions (left) and from FE model (right).

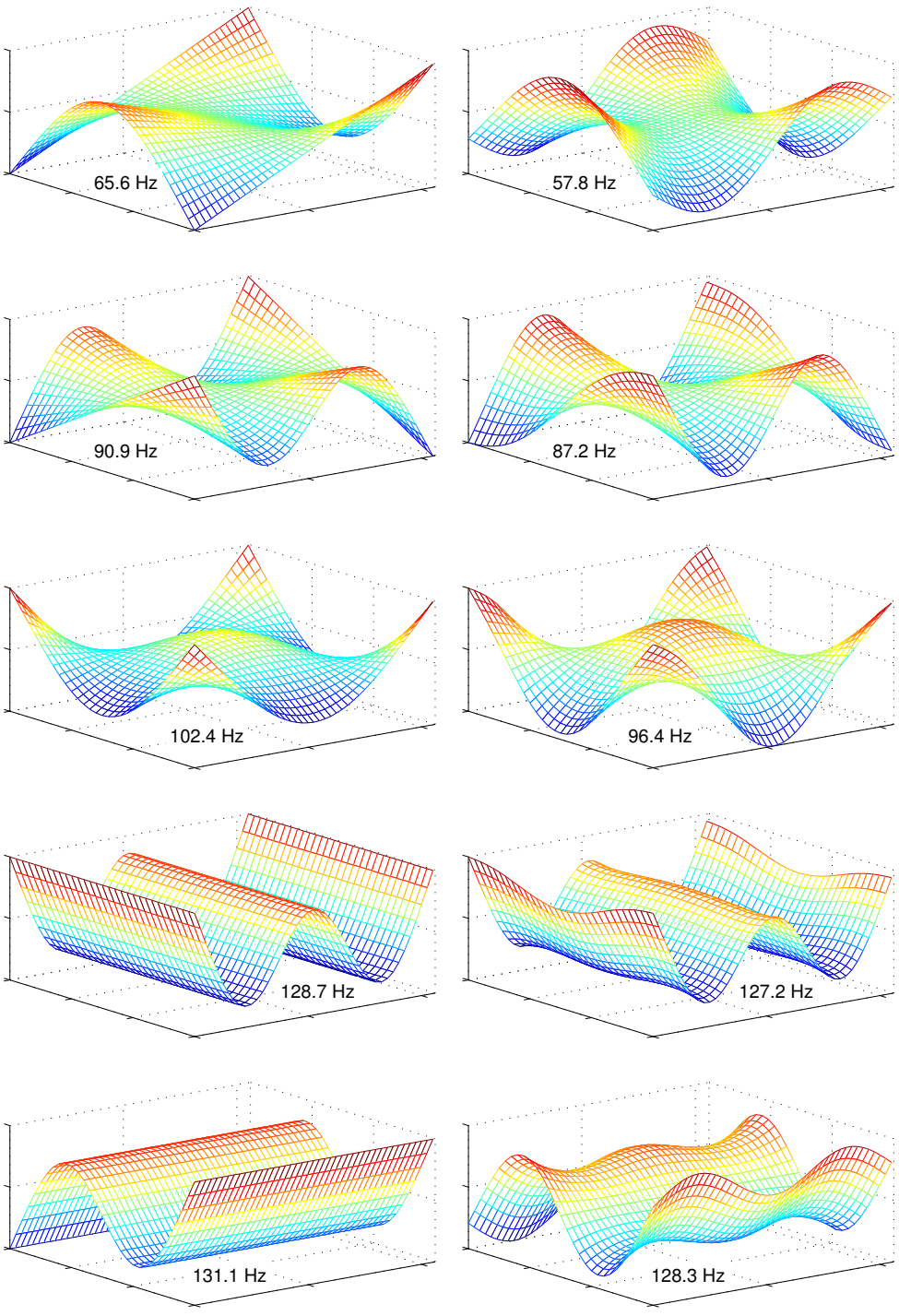

Figure 3.8: Plate mode shapes calculated from beam functions (left) and from FE model (right).

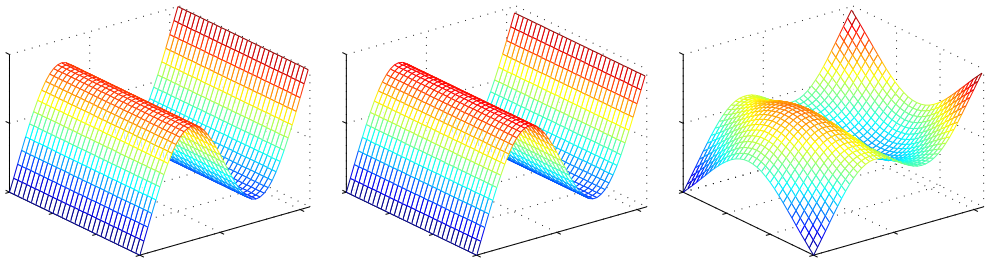

Figure 3.9: Plate mode shape $(0, 3)$, calculated from beam functions (left), from FE model with $\nu = 0$ (centre), and with $\nu = 0.33$ (right).

3.4.4 Discussion

The difficulties in modelling a free plate numerically have consequences for the implementation of the practical method described in Section 3.3.2. The effect on the inversely determined forces, when using calculated instead of measured mobilities, is investigated in Chapter 4. While the use of a beam function model limits the accuracy of the proposed procedure, an FE model may offer an alternative. Although the simplicity of the beam function model is lost, the advantage of a significantly reduced measurement effort can be retained. In addition, the use of FE mode shapes allows the usage of a variety of structures as receivers. Once the mode shapes have been acquired, the procedure described in Section 3.3.2 can be used to obtain blocked forces.

3.5 Summary

Matrix inversion methods for the indirect determination of operational and blocked forces have been described. Two major challenges for these methods were identified: The experimental acquisition of the complete (transfer) mobility matrices is time-consuming and prone to experimental errors. The necessary matrix inversion poses problems if the mobility matrix is ill-conditioned, prompting the use of methods to mitigate the inverse problem. Both the mobility measurements and the subsequent data processing require insight into the physical and theoretical problem that is usually not evident in building acoustics. Therefore, a way is sought to simplify the approach to make it usable for applications in building acoustics.

The use of a standardized receiver structure has the potential to greatly reduce the required measurement effort. If a fully-defined receiver structure is used, mobilities can be calculated from numerical or analytical solutions. Furthermore, if the receiver structure is chosen to be of significantly lower mobility than typical sources, the acquired forces approximate the blocked forces, yielding one part of a receiver-invariant source characterization. Importantly, the use of a fully-defined receiver structure allows the determination of favourable response positions without the need to perform measurements. This can have a significant influence on the condition of the (transfer) mobility matrix.

The numerical approach that has been described to calculate point and transfer mobilities of plates uses modal summation and mode shapes calculated from beam functions. On comparing calculated and measured mobilities, there is agreement in the trends, but difference in detail, resulting in large errors at individual frequencies. The deviations were further investigated using a finite element model of a free plate. The results from this model highlighted the effect of neglecting Poisson contraction in the beam function model, where the plate eigenfrequencies are generally under-estimated. The calculated mobilities from the finite element model agreed better with the measured results. The effect of the use of inaccurate calculated mobilities on the determined forces is investigated in Chapter 4.

4 Experimental Validation of Indirect Methods to Obtain Blocked Forces

4.1 Introduction

The experimental investigation of the use of a free receiver plate for the inverse determination of (blocked) forces of structure-borne sound sources is described. The chapter is divided into two sections. In Section 4.2, the operational forces exerted by typical sources on a free receiver plate are inversely calculated using measured FRFs and operational velocity responses. The accuracy of the force estimates is investigated, and the effectiveness of over-determination and singular value rejection is studied. Furthermore, the importance of velocity response positions is examined.

In Section 4.3, the use of calculated FRFs for the inverse determination of contact forces is described. The same data sets as in Section 4.2 are used. FRFs are calculated from either beam function mode shapes or FE mode shapes, using the procedures described in Chapter 3. The force level differences are evaluated and compared to the benchmark results from Section 4.2, to verify whether the use of calculated FRFs offers a viable alternative to measured FRFs. Furthermore, calculated FRFs are used to determine favourable combinations of response positions.

4.2 Inverse force determination using measured FRFs

An industrial fan unit and a modified shaker source were attached to a free aluminium receiver plate. The velocity responses at remote positions were recorded during operation of the sources, and the FRFs between source contacts and velocity response positions were measured. The operational contact forces were inversely determined using the procedure described in Section 3.2.1, and were also measured directly for comparison.

4.2.1 Measurement setup

An aluminium plate of size 2.12 m × 1.50 m × 20 mm was used as receiver structure (Figure 4.1). The plate was supported at the corners and edges by visco-elastic patches (Getzner SyloDamp HD30). This configuration creates free boundary conditions for the plate, and additionally provides damping, mainly at low frequencies. The loss factor of the plate is shown in Figure 3.3. The critical frequency of the plate was calculated from the plate and material properties [72]:

$$f_c = \frac{c_0^2\sqrt{3}}{\pi h c_L} \tag{4.1}$$

Here, $c_0 = 343\,\mathrm{m/s}$ is the speed of sound in air at room temperature, $h = 20\,\mathrm{mm}$ is the plate thickness, and $c_L = 5100\,\mathrm{m/s}$ [72] is the quasi-longitudinal wavespeed on the aluminium plate. With these parameters, the critical frequency of the plate was calculated at approximately 635 Hz.

An industrial fan unit on four feet was considered as source (Figure 4.2). The fan unit was mounted on the receiver plate via four force transducers (BK 8200)

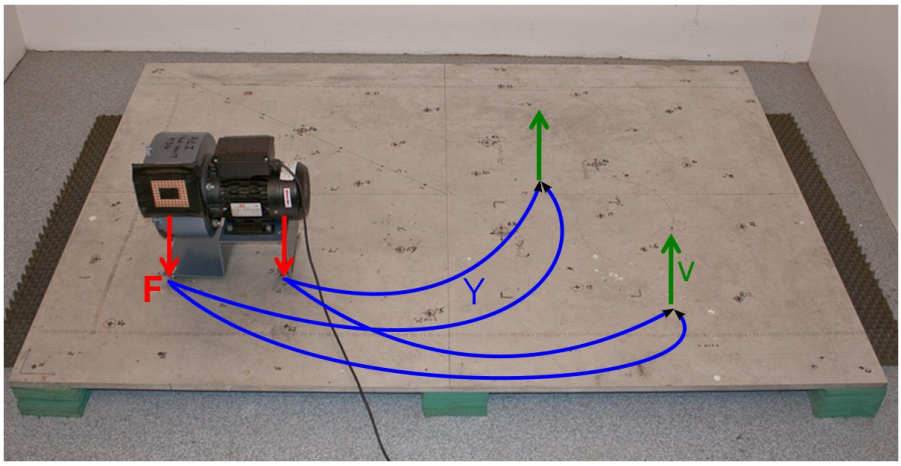

Figure 4.1: Aluminium reception plate. Forces **F** at the source-receiver interface result in velocities **v** on the plate. **F** and **v** are linked by the transfer mobility matrix **Y**.

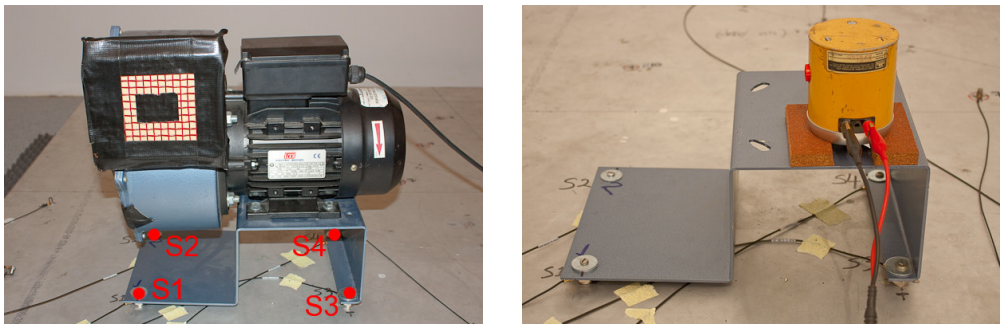

Figure 4.2: Industrial fan unit (left) and modified shaker source (right).

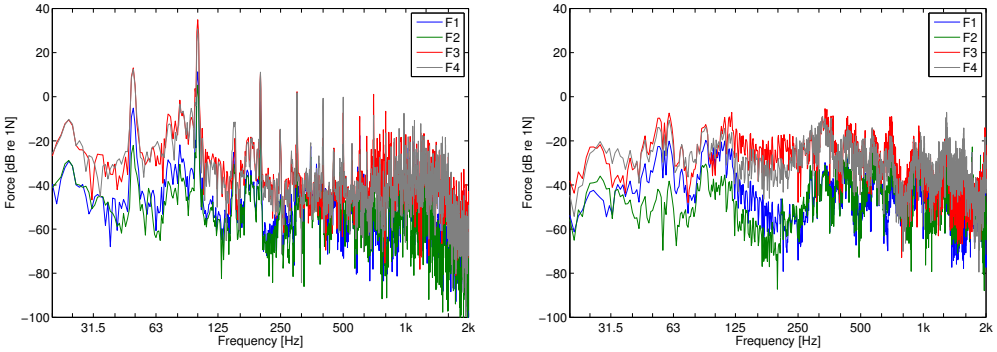

Figure 4.3: Excitation spectra of fan unit (left) and shaker source (right).

which were screwed into the source and plate. The transducers were considered to be part of the source, and were used to record the contact forces directly for comparison. Measured forces at the stiff end of the fan base (F3 and F4) were generally much higher than the forces at the resilient end (F1 and F2). The fan unit generated a tonal excitation spectrum, with frequency components at 50 Hz, 100 Hz, 200 Hz, and 300 Hz dominating, see Figure 4.3.

As an alternative source, the fan motor was replaced by a small electrodynamic shaker (LDS V201), resulting in a source with similar mechanical mobility, but with variable and controllable excitation (Figure 4.2). Broadband noise was used as excitation signal, see Figure 4.3.

The distances between the source mounting points were 0.17 m (between F1 and F2 and between F3 and F4), 0.31 m (between F1 and F3 and between F2 and F4), and 0.35 m (between F1 and F4 and between F2 and F3). Figure 4.4 shows the ratio of these distances and the bending wavelength on the plate. The bending wavelength λ_B is calculated as

$$\lambda_B = \frac{2\pi}{k_B}, \tag{4.2}$$

where k_B is the bending wavenumber:

$$k_B = \sqrt[4]{\frac{\omega^2 m''}{B}} \tag{4.3}$$

m'' is the mass per unit area and B is the bending stiffness:

$$B = \frac{Eh^3}{12(1-\nu^2)} \tag{4.4}$$

$E = 70\,\text{GPa}$ is Young's modulus, $\rho = 2700\,\text{kg/m}^3$ is the material density, and $\nu = 0.33$ is Poisson's ratio. For accurate force estimates, the mounting points should ideally be more than half a wavelength apart. This ensures a good separation of the contact forces in the inverse calculation. If the mounting points are too close together with respect to the bending wavelength, differences among the FRFs between the different mounting points and remote response positions will be small. As a consequence, condition numbers of the FRF matrix will be high, and the force estimates will be prone to errors. For the source-receiver combination under consideration, the distances between the mounting

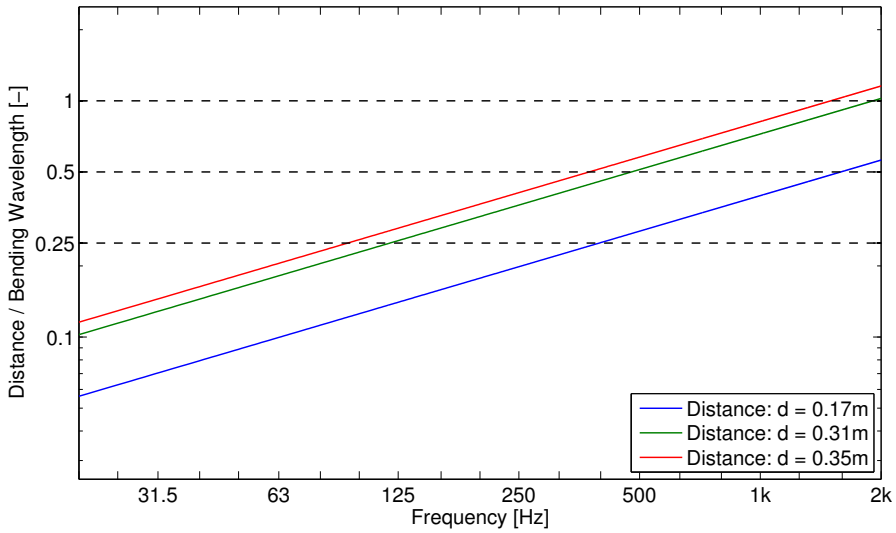

Figure 4.4: Ratio of the distance between the source mounting points and the bending wavelength on the plate.

points are relatively small with respect to the bending wavelength. Only above 95 Hz are some of the mounting points separated by at least a quarter of a wavelength. Only above 375 Hz are some of the mounting points separated by at least half a wavelength. The proximity of the source contacts to each other provides a challenging case study.

The response velocities, during operation of the sources, were recorded at 32 positions evenly distributed over the plate (Figure 4.5), using eight accelerometers at a time (BK 4393V). The contact forces were measured simultaneously by the force transducers. The measurement time was 5 s, the frequency resolution $\Delta f = 1$ Hz, the sampling rate $f_s = 16384$ Hz. Eight measurements were performed for each source, with the accelerometers at different positions. Table 4.1 specifies the combinations of accelerometer locations.

Point mobilities at the four source contacts (F1, F2, F3, F4) and transfer mobilities from the source contacts to all 32 velocity response positions (= 128 FRFs) were measured as narrowband spectra with an impulse hammer (BK 8202). Five averages per FRF were performed. The frequency resolution of measurements was 1 Hz, the sampling rate $f_s = 16384$ Hz. A plastic hammer tip was used, ensuring a sufficient excitation force up to 2 kHz. Results above

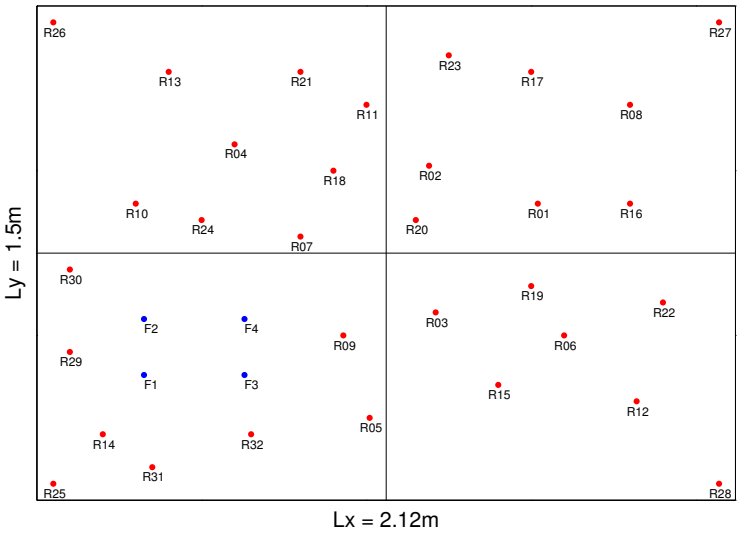

Figure 4.5: Source and response positions on the receiver plate.

Measurement	Acc1	Acc2	Acc3	Acc4	Acc5	Acc6	Acc7	Acc8
M01	R08	R16	R17	R25	R27	R28	R30	R31
M02	R05	R07	R09	R14	R21	R23	R24	R30
M03	R01	R08	R12	R15	R17	R26	R27	R28
M04	R01	R02	R03	R04	R05	R06	R07	R31
M05	R07	R08	R09	R10	R11	R12	R13	R31
M06	R13	R14	R15	R16	R17	R18	R19	R31
M07	R19	R20	R21	R22	R23	R24	R25	R31
M08	R25	R26	R27	R28	R29	R30	R32	R31

Table 4.1: Overview of combinations of response positions.

2 kHz were not evaluated in this study. A review of the practicalities of FRF measurement is provided in Section 5.2.

Figure 4.6 shows representative point mobilities of plate and fan unit, as narrowband and third-octave band spectra. In third-octave bands, the source mobility exceeds the receiver mobility by a factor of 10 above 50 Hz, indicating that the high-mobility source assumption ($|Y_s| \gg |Y_r|$) is fulfilled. However, the narrowband mobility spectra reveal that there are frequency regions where this is not the case (for example around 400 Hz, 500 Hz, 1250 Hz). This means that the contact forces do not approximate the blocked forces at these frequencies.

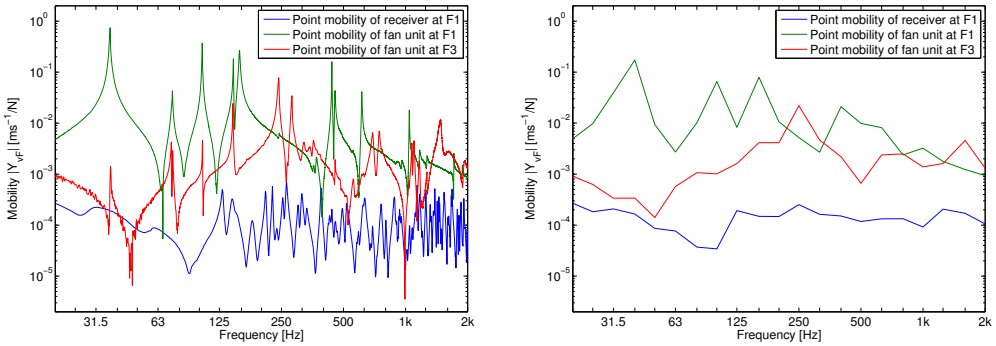

Figure 4.6: Source and receiver mobility in narrowband and 1/3-octave bands.

4.2.2 Inverse force determination

The forces exerted on the receiver plate by the fan unit and the modified shaker source were calculated from measured operational velocities and measured transfer mobilities according to Equation (3.2). The calculations were performed frequency by frequency, using narrowband FFT spectra. Figure 4.7 shows measured and calculated third-octave band force levels for the shaker source for one measurement (M01). All eight responses were taken into account, but neither singular value rejection nor regularization was applied. The conversion of narrowband force spectra to third-octave band levels was performed for reasons of presentation and comparison, and for the quantification of deviations between measured and calculated values.

Several observations can be made from Figure 4.7. First, as pointed out before, the measured forces at the stiff end of the source (F3 and F4) exceed the measured forces at the resilient end (F1 and F2) by more than 10 dB ($20 \log |F_3|/|F_1|$) for most of the frequency range of interest, sometimes significantly more. Only above 1 kHz are all forces in the same order of magnitude. Secondly, while the estimated forces F3 and F4 generally agree well with the measured forces, the estimated forces F1 and F2 are generally over-predicted.

Extending the evaluation to all eight measurements, see Table 4.1, confirms these findings. Figure 4.8 shows the force level differences ($20 \log |F_{calc}|/|F_{meas}|$) between measured and calculated forces for the fan unit. Figure 4.9 shows the same for the modified shaker source. Also indicated are the median values of all eight cases. The median value is used because it attaches less importance

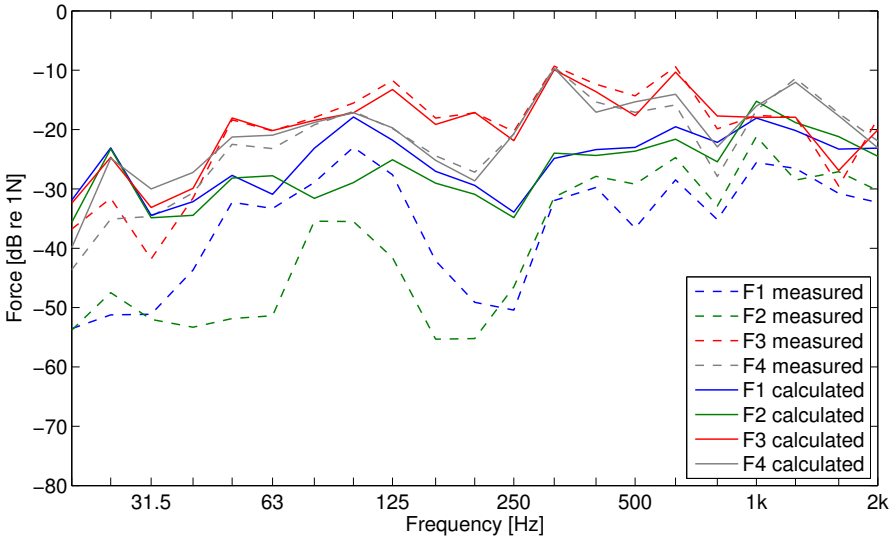

Figure 4.7: Measured and calculated forces for measurement M01 of the modified shaker source.

to outliers than the mean value. Outliers such as at 160 Hz in Figure 4.9 are likely the result of measurement errors. Positive values in Figures 4.8 and 4.9 indicate over-estimated forces.

Above 50 Hz, the estimated forces F3 and F4 (high forces) are mostly within ±5 dB of the directly measured values. Below 50 Hz, the deviations are larger, with median errors of up to 10 dB. One reason for the worse performance at low frequencies may be the lack of contributing eigenmodes. A recommendation based on [48] is, that the number of structural modes contributing to the response at a certain frequency should be at least equal to the number of unknown forces, see Section 3.2.2. The lowest calculated eigenfrequencies of the free receiver plate lie at 19.7 Hz, 22.5 Hz, 46.2 Hz, 47.2 Hz, 57.8 Hz, and 67.8 Hz, cf. Figure 3.7. Below 46 Hz, only two eigenmodes contribute to the velocity responses, besides whole-body movement. Estimating four contact forces at these frequencies therefore results in errors.

Compared with the forces F3 and F4, the estimated forces F1 and F2 (lower forces) perform significantly worse. They show systematic over-estimates of about 10 dB, with some frequency bands showing deviations up to 30 dB and more. This observation is in line with findings in the literature, that low forces in the presence of high forces are generally over-predicted [28, 140].

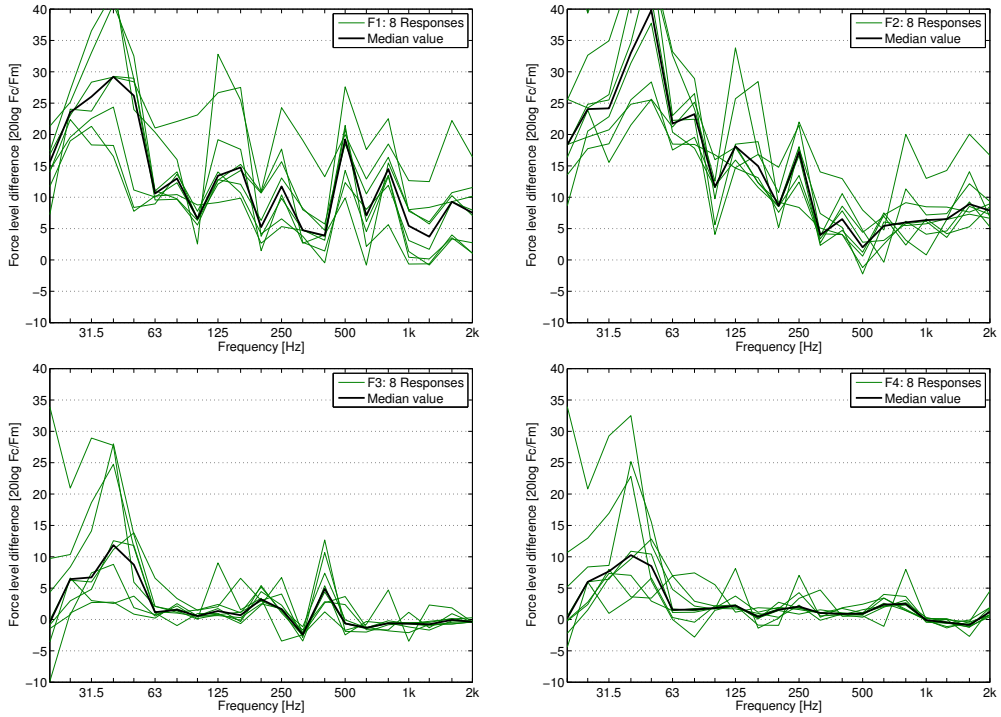

Figure 4.8: Force level differences for fan unit.

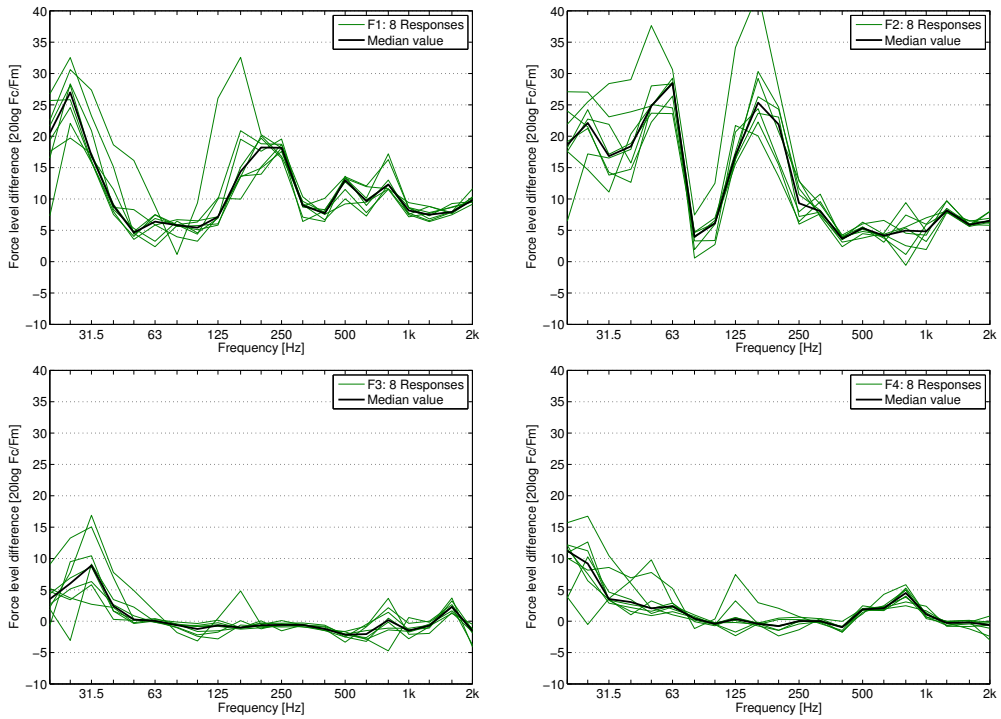

Figure 4.9: Force level differences for modified shaker source.

Both high and low forces are generally over-predicted in Figures 4.8 and 4.9, rather than under-predicted. One reason for this is, that direct and indirect forces are compared on a third-octave band level basis. If a single FFT line in the inversely determined narrowband force contains strong amplification due to matrix ill-conditioning, the entire frequency band is over-estimated, because the FFT lines are added in each band to obtain third-octave band values. Furthermore, the reference value for the level differences in Figures 4.8 and 4.9 is the directly measured force. While the force transducers only register translational motion, there may also be a rotational excitation component, which contributes to the response velocities. An inverse calculation of excitation forces from these response velocities yields a pseudo-force representing both translational and rotational excitation components. For these reasons, it is far more likely to over-estimate the contact forces than to under-estimate them.

4.2.3 Effects of over-determination

The matrix inversion involved in Equation (3.2) potentially amplifies random errors in the measured velocity responses, resulting in large errors in the force estimates. Several mitigating techniques are available, as explained in Section 3.2.3. In this section and the next, the effects of over-determination and singular value rejection were investigated.

The minimum number of responses is given by the number of forces acting on the receiver [48]. Since both sources under test have four contacts, at least four responses must be used. In each of the eight measurements in Table 4.1, eight responses were recorded simultaneously. For each measurement, there are $\binom{8}{4} = 70$ combinations to select four responses from eight. Hence, there are $8 \times 7 = 560$ possible combinations. Combining velocity responses from different measurements increases the number of possible combinations dramatically, to $\binom{32}{4} = 35960$. In the following data evaluation, only response velocities from the same measurement were combined. For the 560 possible combinations, the contact forces were inversely determined, converted to third-octave bands, and compared with the directly measured forces of the same measurement. The same calculations were performed using five (448 combinations), six (224 combinations), and seven (64 combinations) responses.

Figure 4.10 shows the results for the modified shaker source, as the broadband

excitation spectrum allows evaluation in all frequency bands. The force level differences for F1 and F3 are shown, as representatives of low and high forces, respectively. To account for the large amount of data, results are presented as box plots, with the following parameters:

- On each box, the central red line indicates the *median* value.
- The upper and lower edges of the box represent the 25th and 75th percentiles, meaning that 25% (75%) of the population lie below the value indicated by the lower (upper) box edge. These values are also termed the *lower quartile* Q_1 and *upper quartile* Q_3. The *interquartile range* is defined as the distance between upper and lower quartile, and gives an indication of the statistical dispersion: $\mathrm{IQR} = Q_3 - Q_1$.
- The whiskers extend to the most extreme data points not considered outliers. The limits of the whiskers are calculated as $Q_1 - 1.5(Q_3 - Q_1)$ and $Q_3 + 1.5(Q_3 - Q_1)$.
- All other data points are considered outliers, and are plotted as dots.

Increasing the number of responses generally reduces the median force level differences, and also reduces the spread between different combinations. This can be observed for both low (F1) and high (F3) forces. For F1, the median force level difference decreases from values up to 26 dB (above 50 Hz) to values below 20 dB, when increasing the number of responses from 4 to 7. The interquartile range reduces from 20 dB to 8 dB and less in the frequency range of interest. For F3, the median force level difference decreases from values of up to 9 dB (above 50 Hz) to values within ±2 dB. The interquartile range reduces from 8 dB to 4 dB and less above 50 Hz.

On examining the lower left plots in Figure 4.10 (F1 for 6 or 7 responses), in the 125 Hz and 160 Hz bands, a group of results deviates considerably from the rest. In this group, no response position is considered in the bottom left corner of the receiver plate (see Figure 4.5). This highlights the importance of the selection of suitable response locations, which is further investigated in Section 4.2.5. Over-determination is not able to compensate for the selection of an unfavourable combination of response positions.

Figure 4.11 shows the median values of the force level differences for four, five, six, seven, and eight responses. Over-determination generally improves the results. However, the effects of over-determination are most significant

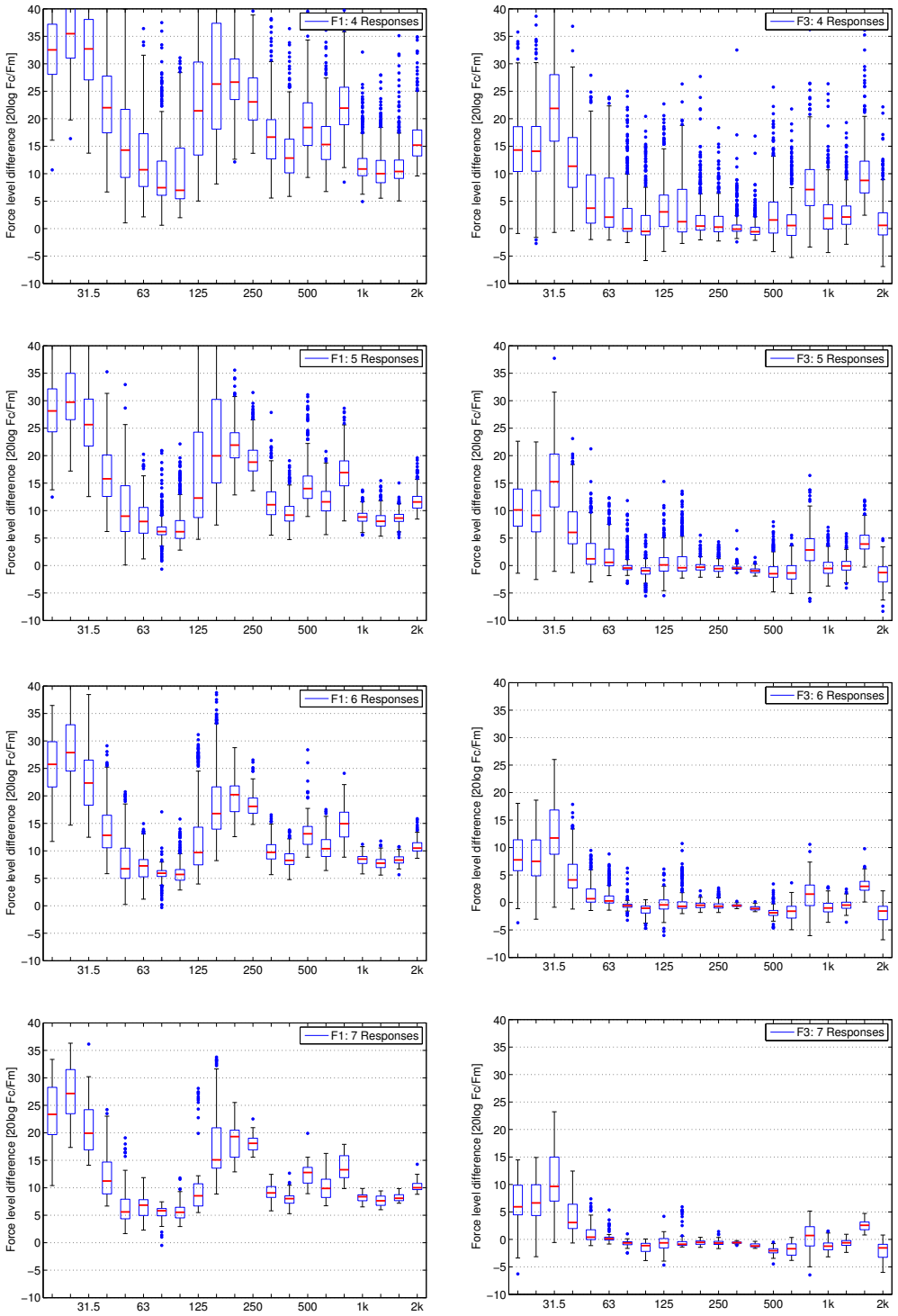

Figure 4.10: Force level differences at F1 and F3 for modified shaker source, for different numbers of response positions.

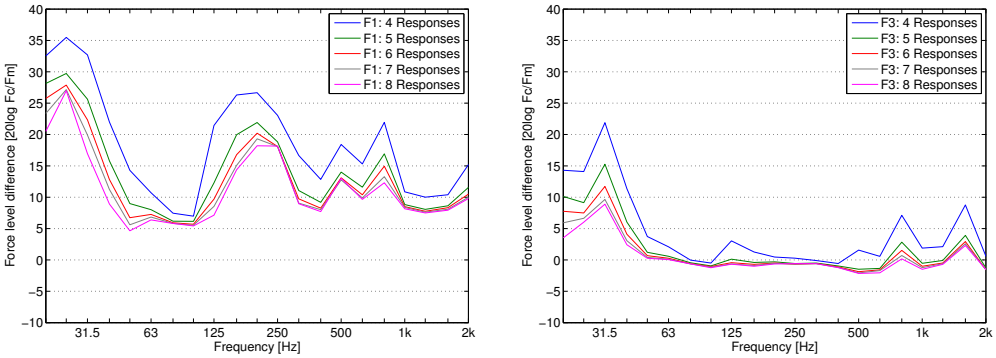

Figure 4.11: Force level differences for modified shaker source.

for the first additional response (five responses), and become less important for additional responses. This behaviour can be described to follow a "law of diminishing return."

4.2.4 Effects of singular value rejection

Singular value rejection (SVR) is another method to mitigate problems associated with matrix inversion. The difficulty of SVR lies in finding an appropriate rejection threshold. If too few singular values are rejected, the solution remains unstable. If too many singular values are rejected, the solution under-estimates the true value. Four SVR thresholds were considered in this study:

- Rejection of the smallest singular value;
- Rejection of singular values smaller than 1% of the highest SV;
- Rejection of singular values smaller than 2% of the highest SV;
- Rejection of singular values smaller than 10% of the highest SV.

In each of these cases, four responses were used. Singular value rejection may also be combined with over-determination. Though the results are likely to be better than for "pure" singular value rejection, the individual effects of the two methods can no longer be distinguished in this case. For this reason, singular value rejection without over-determination was considered in this study.

Figure 4.12 shows the force level differences at F1 and F3 for the modified shaker source, for the four cases mentioned above. Compared with the results without SVR in Figure 4.10 (top row), the greatest improvements are achieved

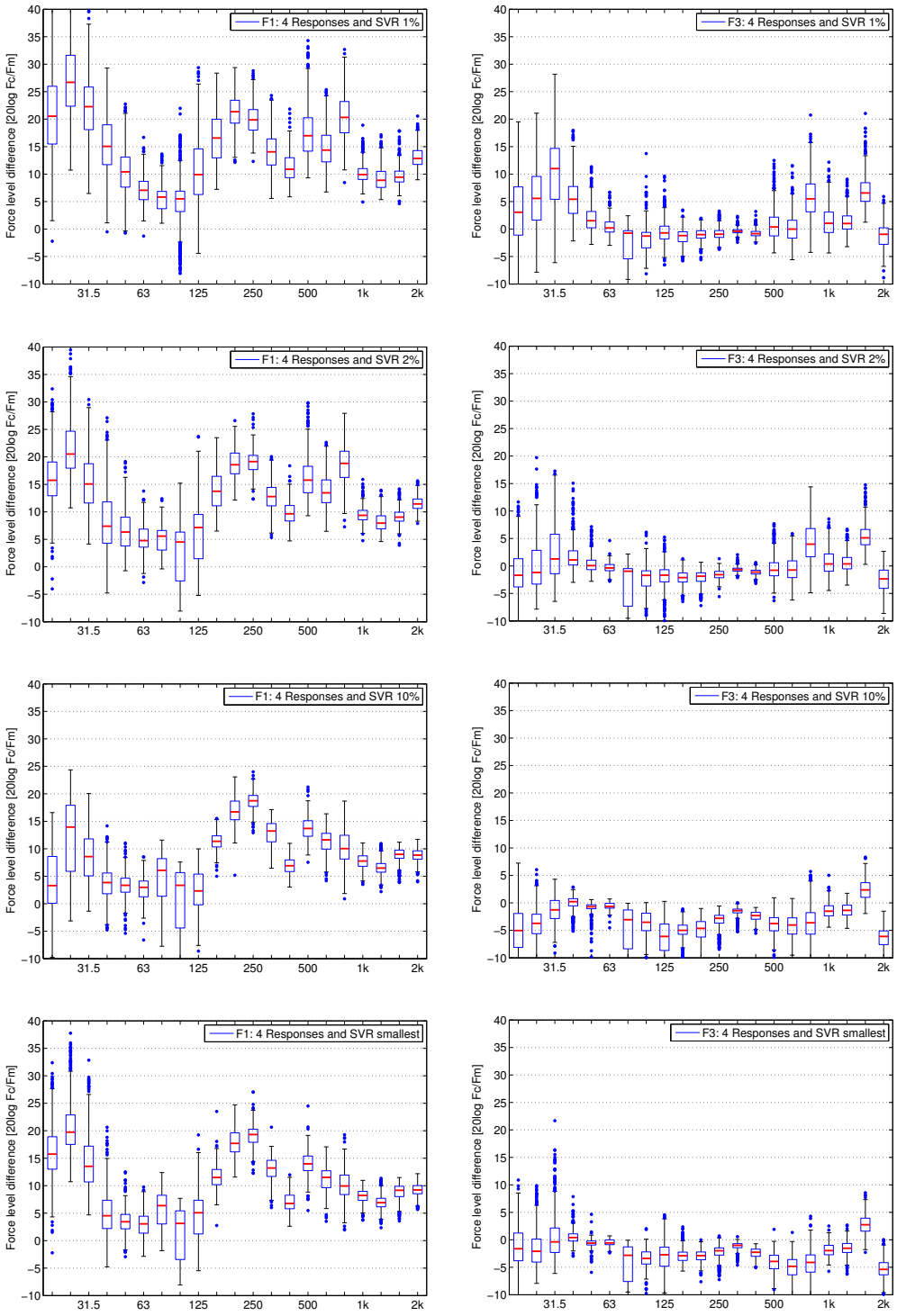

Figure 4.12: Force level differences at F1 and F3 for modified shaker source, using different thresholds for singular value rejection.

in the low-frequency region, below 100 Hz. For F1, the peak in the force level differences at 25 Hz reduces from 35 dB in Figure 4.10 to 26 dB, 21 dB, and 14 dB, for SVR 1%, SVR 2%, and SVR 10%, respectively. For F3, the peak in the force level differences at 31.5 Hz decreases from 22 dB to 11 dB, 2 dB, and -2 dB, for SVR 1%, SVR 2%, and SVR 10%, respectively. In the low-frequency range, the improvement due to SVR is significantly greater than the improvement obtained by over-determination. However, for a threshold of 10%, forces are under-predicted by up to 5 dB.

Between 50 Hz and 500 Hz, the high force (F3) in Figure 4.10 agrees within 4 dB with the measured value. If SVR is applied, the predicted forces are systematically under-estimated, by up to 1 dB for SVR 1%, 2 dB for SVR 2%, and 6 dB for SVR 10%. Regularizing can therefore have a detrimental effect, depending on the threshold used. For F1, changing the SVR threshold from 1% to 2% and 10% improves the force estimates by about 3 dB on average. Under-prediction is not encountered here, the forces are still strongly over-predicted (by up to 20 dB).

In the frequency range above 500 Hz, the improvements due to SVR are generally less than in the other frequency ranges. For F1, a gradual improvement from up to 20 dB in Figure 4.10 to about 10 dB for SVR 10% can be observed. For F3, the force level differences reduces from up to 9 dB in Figure 4.10 to about 5 dB for SVR 2%. For SVR 10%, F3 is under-predicted by about 4 dB.

The results from Figure 4.12 highlight the potential of singular value rejection to improve force estimates, in particular at low frequencies, where over-determination only has a limited effect for the cases considered. On the other hand, the results from Figure 4.12 also highlight the challenges associated with the choice of an appropriate threshold. If the threshold is too high, as for example for SVR 10%, the forces are under-estimated. Without detailed knowledge of the system under test and without constant monitoring of the results, it may be difficult to choose an appropriate threshold.

4.2.5 Effects of velocity response positions

The choice of velocity response positions influences the matrix inversion, see Section 3.2.4. Whether a combination of positions is favourable or not can be determined by reference to the condition number of the corresponding FRF

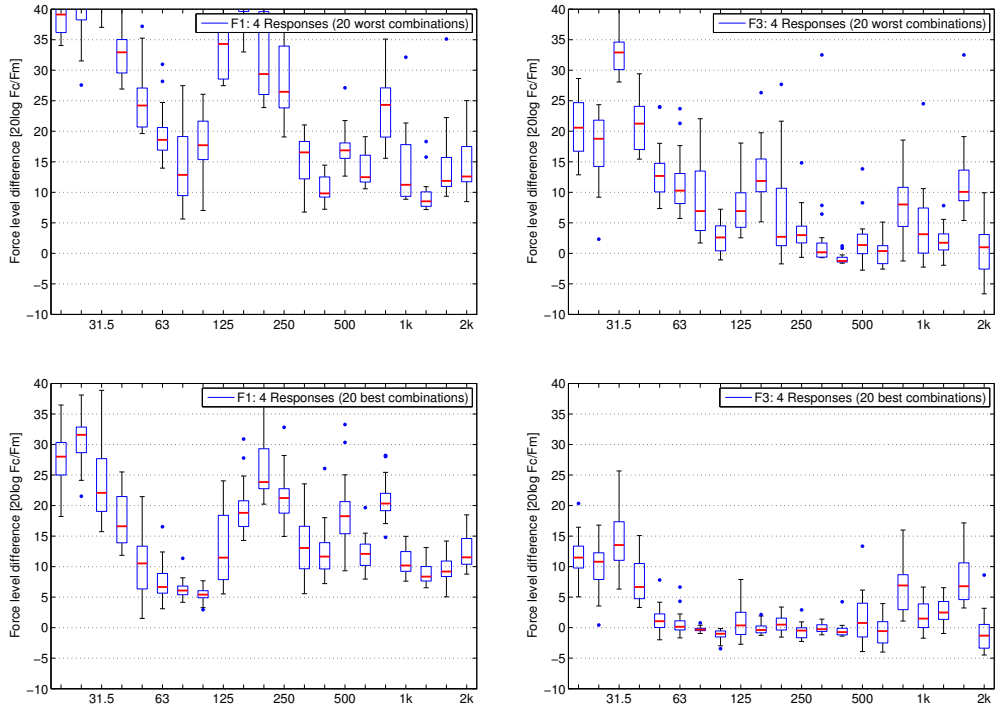

Figure 4.13: Force level differences for modified shaker source: 20 combinations using four responses with the highest and lowest average condition numbers.

matrix. High condition numbers indicate ill-conditioned matrices, which may lead to large errors in the force estimates.

Condition numbers were calculated for the 560 combinations described in Section 4.2.3. The condition numbers were then averaged over the frequency range of interest (20 Hz – 2 kHz), to obtain a single number quantity for comparison. Whilst this can hide large discrepancies at certain frequencies, the data reduction provides an early indicator of favourable and unfavourable combinations. Inverse force determination was performed for the 20 combinations with the lowest average condition number, and for the 20 combinations with the highest average condition number. The force level differences for F1 and F3 are shown in Figure 4.13. In Figure 4.14 are shown the corresponding condition numbers over frequency.

The improvement in force estimates between bad combinations and good combinations is noticeable for both low (F1) and high (F3) forces. The frequency range between 100 Hz and 400 Hz is most affected. The median force level dif-

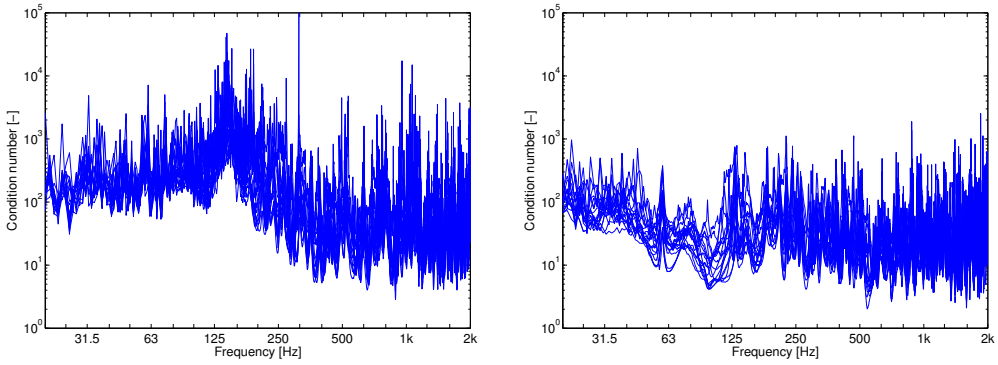

Figure 4.14: Condition numbers for 20 combinations using four responses with the highest (left) and lowest (right) average condition numbers.

ferences decrease from values between 10 dB and 45 dB to values between 5 dB and 24 dB for F1, and from values between −1 dB and 12 dB to values within ±0.5 dB for F3. The condition numbers in Figure 4.14 show a significant drop in this frequency range. Below 100 Hz, the improvement in the force estimates is also significant. An average improvement of about 12 dB is obtained in this frequency range, for both F1 and F3. Above 400 Hz, the median values of the force level differences are approximately the same. Only small improvements up to 3 dB are observed. This is partly due to the average condition numbers being dominated by the frequency region between 100 Hz and 400 Hz, cf. Figure 4.14. The condition numbers of the 40 cases considered are similar above 400 Hz.

The significant improvement between the left and right plots in Figure 4.13 suggests that optimization of response locations should be a primary objective for accurate force estimates. Other methods such as over-determination and regularization may be applied, but the selection of a favourable combination of response positions should be the first step. A bad combination of response positions cannot fully be compensated for by over-determination. This is illustrated in Figure 4.15. Force level differences are shown for the 20 best and worst combinations, for four and six responses. In particular at low frequencies, it is better to use only four responses and a good combination than six responses and a bad combination.

In this study, the number of possible combinations was limited to combinations using responses from the same measurement, cf. Section 4.2.3 and Table 4.1. In the general case, the number of possible combinations is virtually unlim-

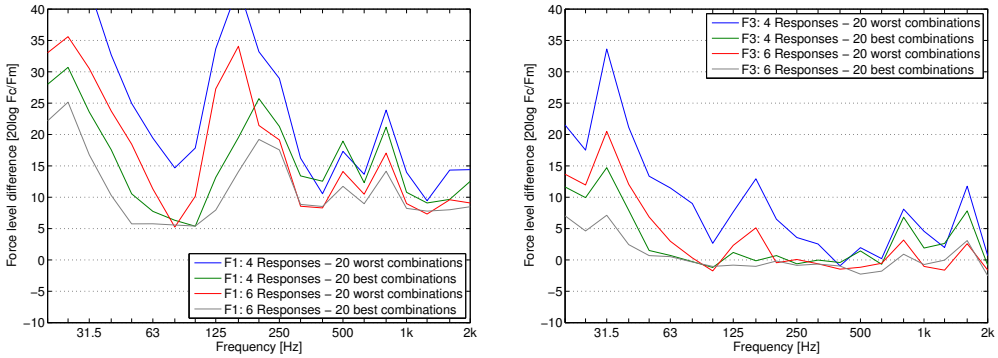

Figure 4.15: Average deviations in force estimates for shaker source, for various configurations.

ited, and the selection of a favourable combination therefore poses a challenge. For example, for the receiver plate depicted in Figure 4.5, there are already $\binom{32}{4} = 35960$ combinations to select four responses out of 32, but many more response positions are possible. Comparing the condition numbers of all these combinations requires a significant measurement and computational effort.

The use of a numerical model of the receiver plate has the potential to simplify the selection process considerably. The required FRFs can simply be calculated, and no measurements are necessary to determine a favourable combination of response positions. Methods to reduce the computational effort are examined in Section 4.3.3.

4.3 Inverse force determination using calculated FRFs

In this study, the forces exerted on the receiver plate by the sources described in Section 4.2.1 were determined inversely using calculated FRF matrices. Transfer mobilities were calculated using the beam function model described in Section 3.4.1, and the finite element model described in Section 3.4.3. As was seen in Section 3.4, the agreement between measured and calculated mobilities is not perfect, due to inaccurate modelling of free edges and corners, and due to experimental inaccuracies. One objective of this investigation is to quantify the error introduced by deviations between measured and calculated transfer mobilities. A second objective concerns the selection of beneficial combinations of response locations.

4.3.1 Calculation of FRF matrices

Transfer mobilities between the four source contacts and the 32 response locations (Figure 4.5) were calculated using the beam function model described in Section 3.4.1. The following parameters were used in the model: Young's modulus $E = 70\,\text{GPa}$, density $\rho = 2700\,\text{kg/m}^3$, Poisson's ratio $\nu = 0.33$. The loss factor of the plate was measured in third-octave bands, using the method described in Appendix D, and was interpolated to be used in the calculation of the narrowband mobilities. Transfer mobilities between the four source contacts and the 32 response locations were also calculated using plate mode shapes and eigenfrequencies exported from ABAQUS. The mode shapes were calculated using the same plate parameters as in the beam function model, and were then used in a modal summation routine in MATLAB. The same loss factor as for the beam function model was used. Mode shapes with eigenfrequencies up to 4 kHz were considered in the modal summation.

4.3.2 Inverse force determination

The forces exerted by the fan unit and the modified shaker source were calculated from measured operational velocities and calculated transfer mobilities according to Equation (3.2). The same evaluation as in Section 4.2.2 was performed. For conciseness, only a selection of the results is presented. Figures 4.16 and 4.17 show results using FRFs calculated from beam function mode shapes and calculated from FE mode shapes, respectively. Four cases are presented: using four responses, using seven responses, using SVR with a relative threshold of 1%, and using SVR with a relative threshold of 2%.

When using the minimum number of responses and FRFs calculated from beam function mode shapes (Figure 4.16 top row), the errors in the force estimates significantly exceed the errors that were found when using measured FRFs (Figure 4.10 top row). For the low force (F1), the median errors of the 560 evaluated cases range between 19 dB and 48 dB, compared to a range between 6 dB and 35 dB in Figure 4.10. When using FRFs calculated from FE mode shapes, the median errors range between 16 dB and 43 dB. The spread of the force level differences is slightly larger when using calculated FRFs (from beam functions or FE mode shapes) compared with measured FRFs. For the high force (F3), the median errors in Figure 4.16 and Figure 4.17 are lower than

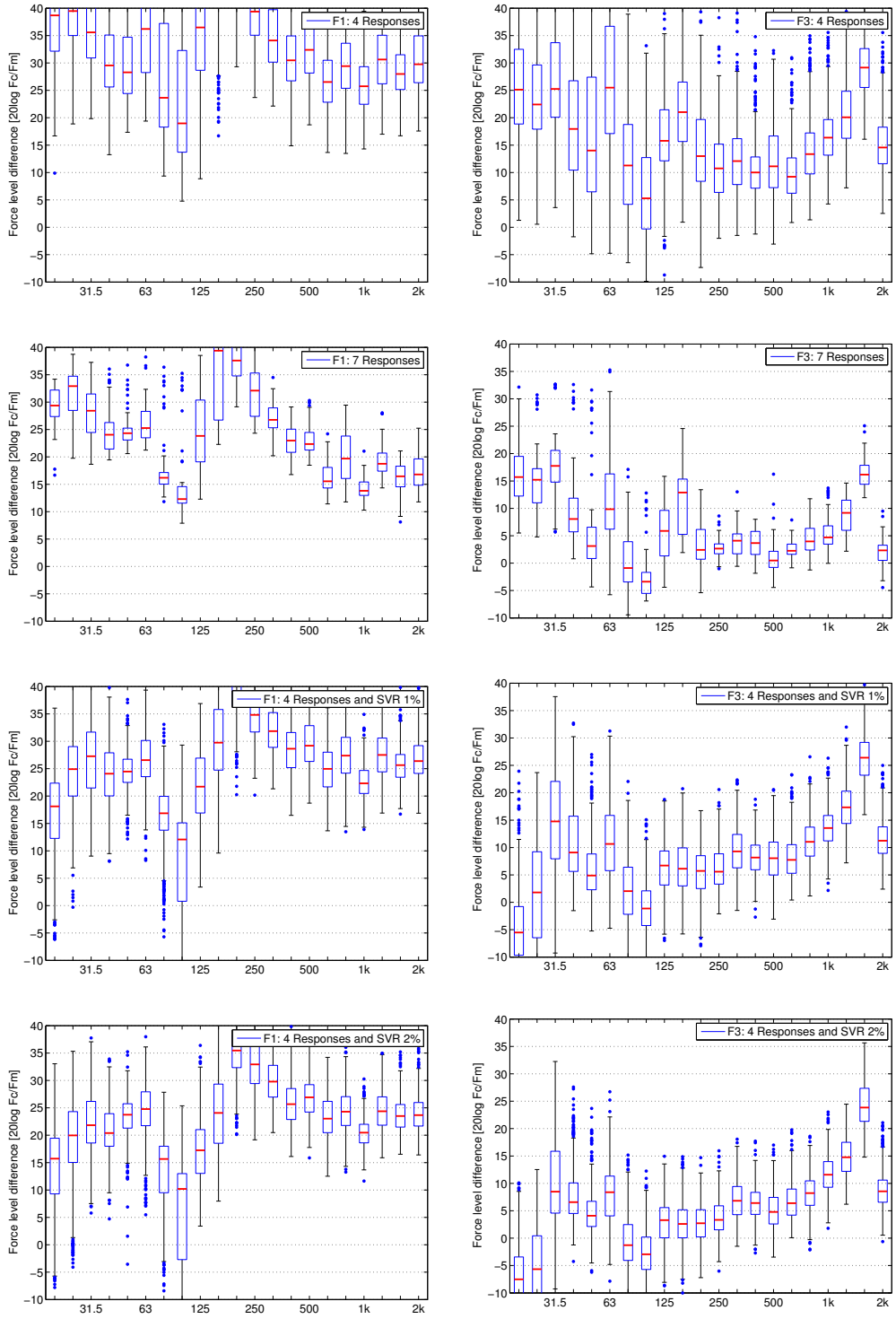

Figure 4.16: Force level differences at F1 and F3 for modified shaker source, using calculated FRFs from beam function mode shapes.

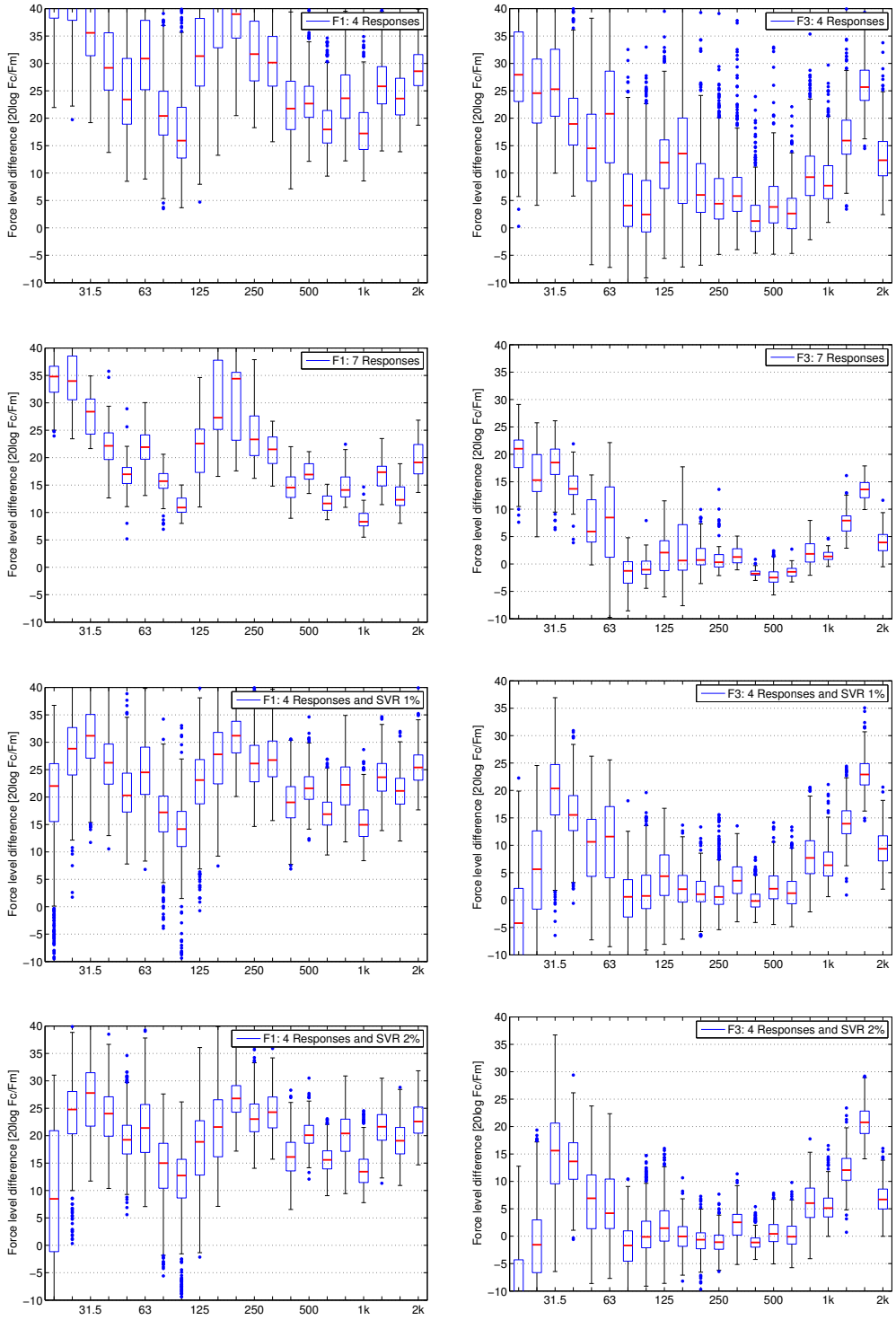

Figure 4.17: Force level differences at F1 and F3 for modified shaker source, using calculated FRFs from FE mode shapes.

for the low force, but are significantly larger than in Figure 4.10. The median errors range between 5 dB and 29 dB when using beam function mode shapes, with most bands showing deviations between 10 dB and 20 dB. The median errors range between 1 dB and 28 dB when using FE mode shapes, with most bands above 50 Hz showing deviations between 0 dB and 15 dB. These results may be compared to Figure 4.10 (top row), where median errors between 0 dB and 3 dB were obtained for most frequency bands above 50 Hz. In addition to this degradation in median errors, the spread of results increases when using calculated FRFs.

The second row in Figures 4.16 and 4.17 shows force level differences when using over-determination with seven instead of four responses. As in Figure 4.10, significant reductions in the spread of results are observed. The median force level differences lie between 12 dB and 40 dB (F1 using beam function mode shapes), −3 dB and 18 dB (F3 using beam function mode shapes), 8 dB and 35 dB (F1 using FE mode shapes), and −2 dB and 21 dB (F3 using FE mode shapes). Between 80 Hz and 1 kHz, the agreement for F3 when using FE mode shapes is within ±2 dB, with all quartiles except one within ±5 dB. Though these values are not as good as the corresponding values in Figure 4.10 (all median values and quartiles within ±2 dB between 50 Hz and 1 kHz), they are in a range that would be deemed acceptable for most situations in building acoustics. Below 80 Hz and above 1 kHz, on the other hand, the median force level differences exhibit values up to 21 dB. This would not be deemed acceptable.

Applying singular value rejection to matrices comprised of calculated FRFs proves to have a similar effect as in Figure 4.12. The force level differences below 100 Hz are generally lower than without SVR, both for the high and the low force. However, a systematic under-estimation is observed in the 20 Hz band. Between 100 Hz and 630 Hz, the force estimates are improved as well. Above 630 Hz, singular value rejection again has only limited effect for the case considered. The spread of results decreases across the frequency range of interest. Comparing the two lower rows of Figures 4.16 and 4.17 once again highlights the better performance of the FRFs from FE mode shapes compared with the FRFs from beam function mode shapes.

In Figures 4.18 and 4.20, the effect of the velocity response positions is considered. The 20 combinations with the lowest and the highest average condition

numbers are used to inversely calculate the operational forces. Figures 4.19 and 4.21 show the corresponding condition numbers.

Three frequency regions are distinguished. Below 100 Hz, the median force level differences in Figure 4.18 are significantly reduced by changing the response positions, from values between 38 dB and 55 dB to values between 17 dB and 38 dB for F1, and from values between 28 dB and 43 dB to values between 5 dB and 23 dB for F3. The spread of results remains constant for F3, but decreases for F1. In Figure 4.20, the situation is similar. The median force level differences reduce from values between 21 dB and 58 dB to values between 19 dB and 40 dB for F1, and from values between 5 dB and 38 dB to values between 0 dB and 21 dB for F3. The spread of results decreases for both forces. The condition numbers in this frequency region reduce from up to 100000 in Figure 4.19 and 10000 in Figure 4.21 to about 1000 in both cases. These values are significantly higher than the corresponding values in Figure 4.14. A certain extent of noise can have beneficial effects on the condition of the FRF matrices, as discussed in [142].

Between 100 Hz and 630 Hz, the median force level differences in Figure 4.18 reduce from values between 26 dB and 53 dB to values between 14 dB and 43 dB for F1, and from values between 9 dB and 29 dB to values between −2 dB and 16 dB for F3. In Figure 4.20, the force level differences reduce from values between 16 dB and 53 dB to values between 16 dB and 38 dB for F1, and from values between −1 dB and 22 dB to values between 0 dB and 9 dB, with most frequency bands in this range between 0 dB and 5 dB. This last result again approximates values that would be deemed acceptable, though the results in Figure 4.14 are even better (all medians within ±1 dB, all quartiles except one within ±2.5 dB).

Above 630 Hz, changing from combinations with a high average condition number to combinations with low average condition numbers has only limited effect on the accuracy of the force estimates. This corresponds to the observations in Section 4.2.5, and is partly due to the fact that the average condition number over the frequency range of interest (20 Hz – 2 kHz) is dominated by the lower frequency regions. If the sorting criterion was the average condition number in the high frequency region (800 Hz – 2 kHz), the deviations between “good” and “bad” combinations would be more obvious.

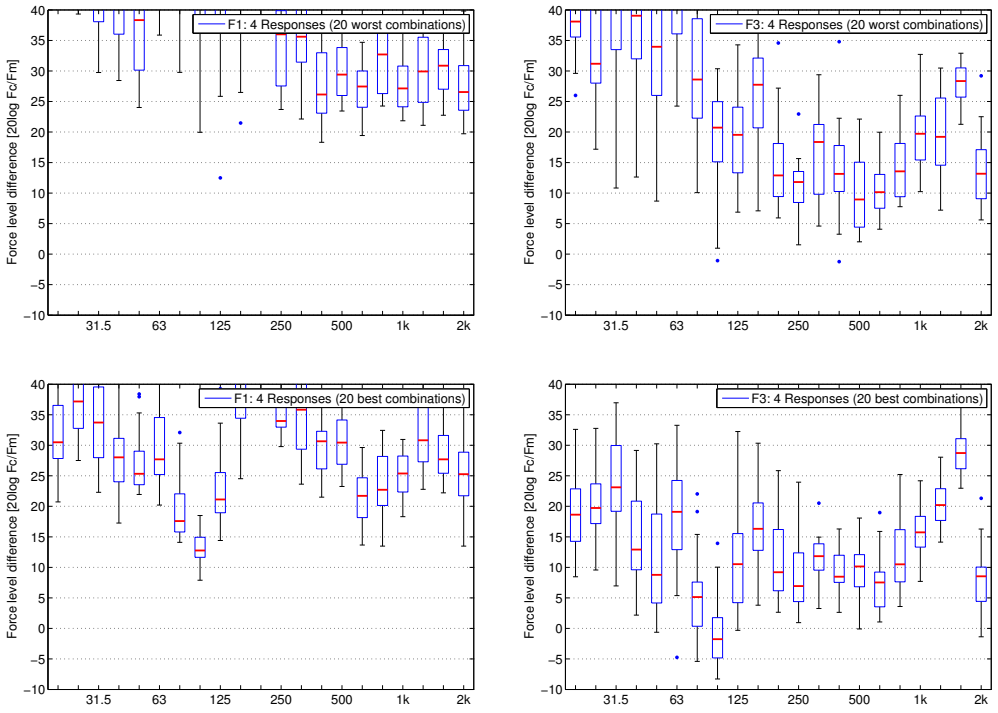

Figure 4.18: Force level differences for modified shaker source: 20 combinations using four responses with the highest and lowest average condition numbers. Using FRFs calculated from beam function mode shapes.

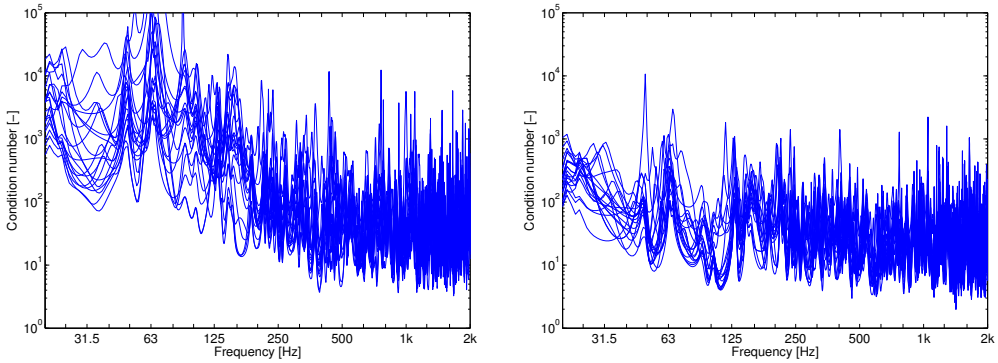

Figure 4.19: Condition numbers for 20 combinations using four responses with the highest (left) and lowest (right) average condition numbers. Using FRFs calculated from beam function mode shapes.

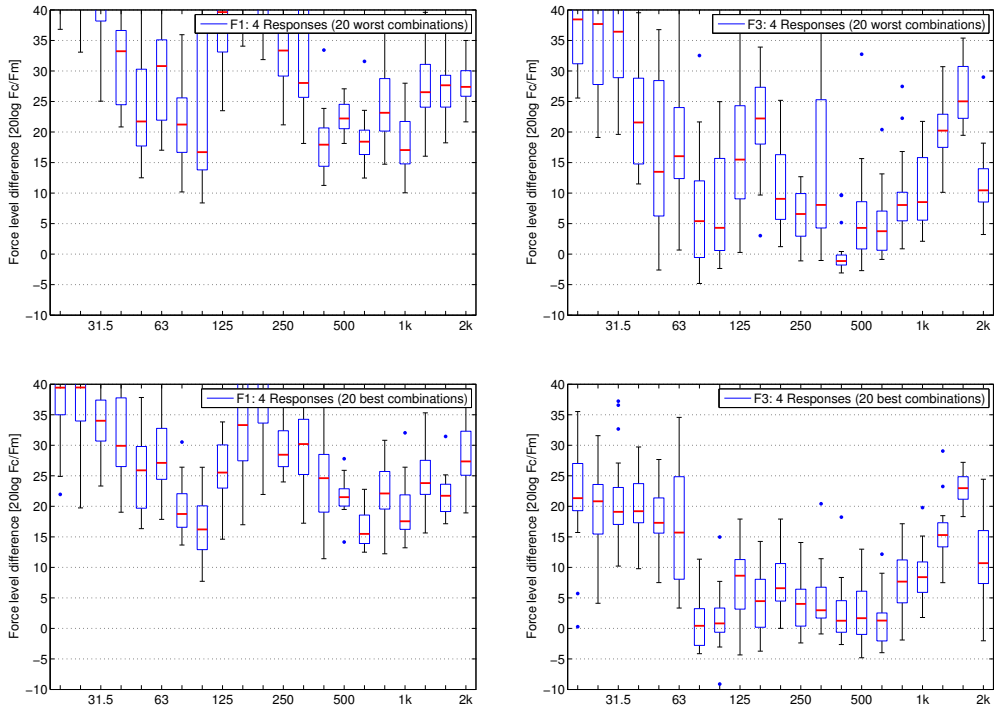

Figure 4.20: Force level differences for modified shaker source: 20 combinations using four responses with the highest and lowest average condition numbers. Using FRFs calculated from FE mode shapes.

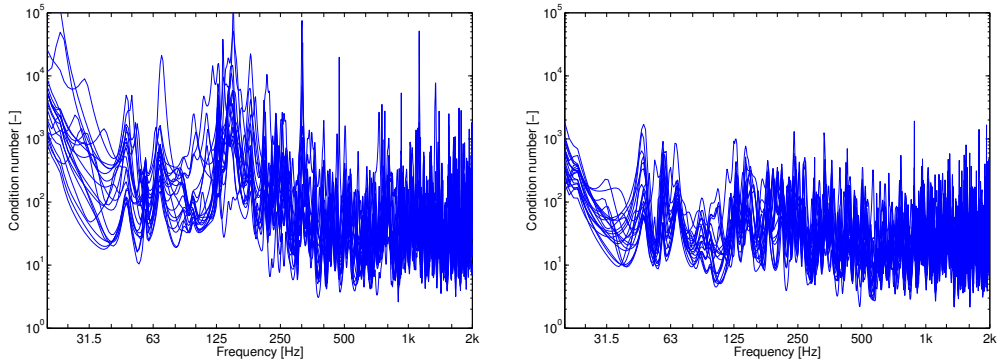

Figure 4.21: Condition numbers for 20 combinations using four responses with the highest (left) and lowest (right) average condition numbers. Using FRFs calculated from FE mode shapes.

Summarizing, the use of calculated instead of measured FRFs can lead to considerable errors in the force estimates. Forces obtained using calculated FRFs from beam function mode shapes in particular exhibited large deviations, up to 40 dB and more. FRFs calculated from FE mode shapes yielded better results. This corresponds to the better agreement of the latter with measured FRFs, as described in Section 3.4.3. The best results with calculated FRFs were achieved in the mid-frequency range (100 Hz – 630 Hz), when employing over-determination (seven responses instead of four). When using calculated FRFs, over-determination does not entail a significant increase in measurement effort; only some additional velocity responses must be recorded. Therefore, over-determination should always be used in this case.

4.3.3 Optimization of response measurement locations

The velocity response measurement locations have a significant effect on the accuracy of the force estimates, as discussed in Section 3.2.4 and seen in Section 4.2.5. Determining a set of favourable response positions therefore is of primary importance. The suitability of a particular combination of response positions can be assessed by the condition number of the corresponding FRF matrix. However, in order to select a favourable combination of response positions from a large pool of possible positions, the FRFs between the source contacts and all possible positions must be known. Using calculated FRFs provides a solution to this challenge. Furthermore, the number of possible combinations increases significantly if the pool of possible positions grows. The comparison of all combinations then becomes computationally costly and time-consuming. In this section, procedures are investigated to optimize response measurement locations, and to reduce the computational effort. Both measured and calculated FRFs are used in the analysis, in order to verify whether favourable combinations of response positions can be obtained using calculated FRFs.

Methods to obtain favourable combinations of response positions

Three approaches were considered. The most straightforward approach calculates the average condition number for each possible combination across the frequency range of interest. This method was used in Sections 4.2.2 and 4.3.2,

to generate the results displayed in Figures 4.13, 4.18 and 4.20. The FRF matrices for all possible combinations were assembled and the narrowband condition number calculated. The condition numbers were then averaged across the frequency range of interest, to obtain a single number quantity for comparison and sorting. Whilst this can hide large discrepancies at certain frequencies, the data reduction provides an indicator of favourable and unfavourable combinations. Figures 4.13, 4.18 and 4.20 demonstrate the effectiveness of this approach. However, for a more detailed analysis, it would be necessary to consider different frequency ranges.

The second approach was proposed by Thite and Thompson [143], and is based on a *composite condition number*. The procedure involves the following steps:

1. The average condition number over the frequency range of interest is calculated for pairs of response positions.
2. The composite condition number for each combination is calculated by averaging the contribution of each pair in this combination.
3. A low composite condition number indicates a good combination.

The third approach was proposed by Zheng et al. [159]. It uses a *composite coherence factor*, and involves the following steps:

1. The frequency-dependent coherence between $\mathbf{h_1}$ and $\mathbf{h_2}$ is calculated for pairs of response positions. $\mathbf{h_1}$ and $\mathbf{h_2}$ are row vectors in the FRF matrix, containing transfer functions from one response to all forces. The coherence indicates the level of dependence of the two sets of transfer functions.[1]
2. The coherence matrix is assembled from the calculated coherence values.
3. The frequency-dependent coherence factor is obtained by assembling submatrices of the coherence matrix and calculating the norm of these.
4. The coherence factor is averaged across the frequency range of interest, to give the composite coherence factor. This operation is not described in [159], but is necessary to obtain a single number quantity for comparison.
5. A low composite coherence factor indicates a good combination.

The three quantities of interest (average condition number, composite condition number, composite coherence factor) were calculated for all 560 combinations

[1] It should be noted that the coherence defined in this way is not the same as the coherence typically used for the assessment of measured FRFs (e. g. [26]).

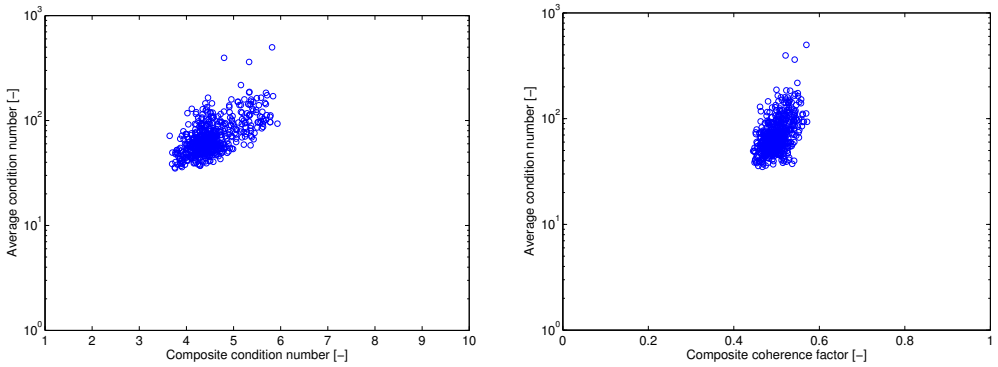

Figure 4.22: Average condition number as a function of composite condition number (left) and composite coherence factor (right).

to select 4 responses out of 32 possible, with the restrictions imposed by the measured combinations (see Table 4.1). FRFs calculated from FE mode shapes were used. Figure 4.22 shows the average condition number as function of composite condition number and of composite coherence factor. Whilst low composite condition numbers and low composite coherence factors almost always correlate with a low average condition number, higher values for composite condition number or composite coherence factor may correspond to low or high average condition numbers. Therefore, both algorithms return reliable results for good combinations, but not necessarily for bad combinations.

Hybrid approach of using calculated and measured FRFs

In Section 4.3.2 it was shown that using calculated instead of measured FRFs can lead to considerable errors in the force estimates. Nevertheless, calculated transfer mobilities may still be useful to determine favourable combinations of response positions. Once a favourable combination of response positions has been found (using calculated FRFs), the corresponding FRFs can be obtained experimentally. This procedure reduces the measurement effort needed to determine a good set of response positions, while at the same time retaining the accuracy of ordinary inverse force determination.

Combinations of response positions with the 20 lowest and highest average condition numbers across the frequency range of interest were identified using FRFs calculated from FE mode shapes. The contact forces were then inversely

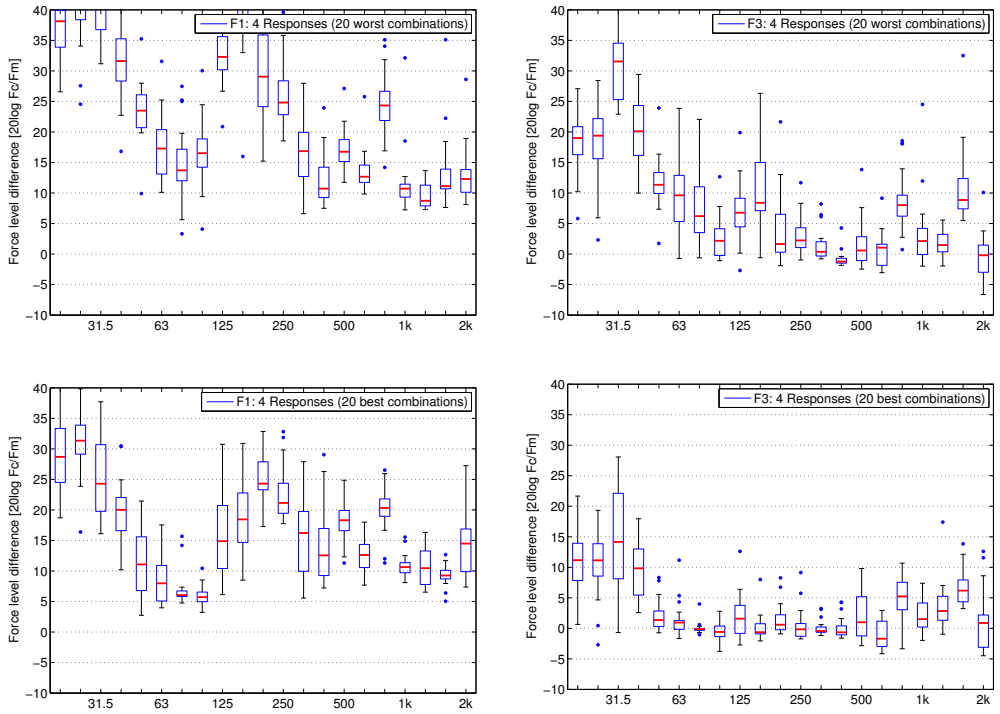

Figure 4.23: Force level differences for modified shaker source: 20 combinations using four responses with the highest and lowest average condition numbers, using FRFs calculated from FE mode shapes. Inverse force determination was then performed with measured FRFs.

determined using measured FRFs, and compared with the directly measured values. Figure 4.23 shows the force level differences, for the 20 best and the 20 worst combinations.

Even though the calculated FRFs used to determine good and bad combinations of response positions deviate from the measured FRFs used to inversely determine the forces, the improvements between the top row of Figure 4.23 and the bottom row are significant. For the low force (F1), the median force level difference decreases by more than 10 dB below 250 Hz. For higher frequencies, the median values are approximately the same, but the statistical spread reduces when using combinations with a low average condition number. The improvement for the high force (F3) lies between 5 dB and 20 dB below 250 Hz, and around 2 dB above 250 Hz. The median force level differences for F3 using good combinations are all within ±1.5 dB between 50 Hz and 630 Hz, between 10 dB and 15 dB below 50 Hz, and between 0 dB and 6 dB above 630 Hz. This

accuracy would be considered acceptable in many situations. The combination of calculated and measured FRFs therefore offers a convenient alternative to increase the accuracy of the force estimates by optimizing response positions, without the need of a greatly increased measurement effort.

4.4 Summary

In this chapter, inverse force determination was investigated experimentally using typical sources encountered in building acoustics. The forces exerted by an industrial fan unit and a modified shaker source onto a free aluminium receiver plate were examined.

In the first stage, measured FRFs were used, together with measured operational velocities, to indirectly determine the contact forces between source and plate. It was found that low forces in the presence of high forces tend to be over-estimated. Methods to improve the inverse force determination were examined. The greatest improvement in the force estimates was obtained when one response location was added to the minimum number. Singular value rejection proved to be useful, too, in particular at low frequencies. However, the choice of an appropriate threshold is critical, as too high a value can yield under-estimates. For a simple measurement method, over-determination offers the best strategy for the problem considered. It is easy to apply, does not require monitoring of thresholds etc., and results are not degraded because of a loss of information. On the other hand, its effects are limited at low frequencies where few modes contribute.

The choice of appropriate response locations was found to be of importance. Over-determination and singular value rejection methods are not capable of compensating for the choice of a bad combination of response positions. Optimizing and selecting favourable response positions should therefore be of primary importance in the pursuit of accurate force estimates.

In the second part of this chapter, FRFs calculated from beam function mode shapes or FE mode shapes were used together with measured operational velocities to determine the contact forces between source and plate. The accuracy of the force estimates decreased considerably, due to imperfect agreement of measured and calculated FRFs. FRFs calculated from FE mode shapes yielded

better results than FRFs calculated from beam function mode shapes. However, the errors in both cases were probably too large for the methods to be considered viable alternatives.

Although errors in the force estimates can be considerable when using calculated instead of measured FRFs, it was found that the optimization of response positions may still be performed with calculated FRFs. Using response positions determined from calculated FRFs, inverse force determination was performed with measured FRFs, and the results were within ± 1.5 dB between 50 Hz and 630 Hz. With this approach, the measurement effort can be reduced, while the accuracy of ordinary inverse force determination can be retained.

5 Indirect Methods to Obtain Source Mobilities

5.1 Introduction

For a full characterization of structure-borne sound sources, both source activity and source mobility must be known, cf. Chapter 2. In Chapters 3 and 4, methods were examined to indirectly obtain the source activity in the form of blocked forces. In Chapters 5, 6, and 7, methods to indirectly obtain the source mobility are investigated.

Structural properties of vibration sources in the form of mobilities are a quantity often required, for example for low-noise design, FE simulations, (experimental) modal analysis, and noise control. Though there exist methods to estimate source mobilities from geometric parameters [59, 60], usually both source activity and source mobility have to be determined experimentally. The measurement of source mobility is generally performed by freely suspending the source and exciting it at each contact point, with each relevant component of excitation. Careful decisions are required regarding a range of measurement parameters, and direct measurement of moment mobility is problematical. Furthermore, problems can arise if the source contains non-linear elements such as springs or isolators. In this case it is important that the source mobility be measured with boundary conditions resembling the installed condition.

This chapter presents methods to indirectly determine the mobility of a source structure, without the need to suspend and excite it directly. Instead, the source mobility is derived from measurements made on a receiver structure. The advantages are that the source mobility can be determined *in-situ*, with the same or similar boundary conditions as in the installed condition.

The chapter begins with a review of direct measurement methods to obtain source mobility (Section 5.2), with a focus on practicalities and measurement techniques. Section 5.3 follows with a review of the theory of coupled mobilities, presenting formulations for the calculation of coupled point and transfer mobilities from uncoupled source and receiver mobilities. Section 5.4 contains the core novel contribution of this chapter, namely three methods to indirectly obtain the source mobility, from coupled and uncoupled receiver mobilities. Three formulations are derived and compared with each other on a theoretical basis. In Chapters 6 and 7, these three methods are examined numerically and experimentally.

5.2 Review of direct measurement of mobility

The objective of this section is to give an overview of the required measurement and signal processing steps for the direct determination of structural mobility. Much of the current and the following chapters relies on the successful and accurate measurement of mobilities.

Measurement of (source or receiver) mobility is a task very familiar to engineers working in the field of structural acoustics. Comprehensive overviews of measurement techniques are available in the literature [46, 92]. ISO 7626-1:1986 [7], ISO 7626-2:1990 [8], and ISO 7626-5:1994 [9] give guidelines on how to obtain structural mobilities using steady-state or transient excitation. Since these measurement methods are well-known, only a brief overview will be provided here.

As explained in Section 2.2.2, the mobility $\mathbf{Y}$ of a structure describes the effect of an applied (generalized) force vector $\mathbf{F}$ on the (generalized) response velocity vector $\mathbf{v}$:

$$\mathbf{v}(\omega) = \mathbf{Y}(\omega)\mathbf{F}(\omega). \tag{5.1}$$

To measure the mobility of a structure-borne sound source, without influence of any connected structure, the source must be freely suspended, for example using bungees with a low stiffness. For very large machinery, such as generators or power transformers, freely suspending them can be a challenge. In this case, resilient supports, as recommended in ISO 9611:1996 [10], may be an alternative. However, excitation and measurement at the contact then may be problematical.

Once the source has been brought into the free state, the mobility measurement can be performed. O'Hara [105] describes the necessary steps to determine each element Y_{ij} of the mobility matrix $\mathbf{Y}$:

1. The forces F_i are applied sequentially to each source terminal.
2. The structure is allowed to respond freely.
3. The individual matrix element is the complex ratio of the velocity response to the single exciting force: $Y_{ij} = \frac{v_i}{F_j}$, with $F_k = 0, k \neq j$.

By applying the excitation force to one terminal at a time and measuring the response, the mobility matrix can be determined element by element, or column by column, if all responses are recorded at the same time.

In practice, care is required regarding the measurement setup:

- Which source of excitation is most appropriate? An electrodynamic shaker provides steady-state excitation signals, and allows control over type and length of the excitation. The attachment to the structure can

become a critical issue, and generally thin, flexible rods called stingers should be used. Compared to a shaker, an impulse hammer offers less control, but is easier to use.

- Which accelerometers should be used, and where and how should they be attached to the structure? Larger accelerometers generally offer higher sensitivity, but may mass-load the structure. Also, access can be an issue. Regarding the attachment of accelerometers, ISO 5348:1999 [6] offers guidelines on appropriate methods.
- Which excitation signal should be used? For an impulse hammer, the control of the excitation is limited to an appropriate choice of hammer mass and tip. For a shaker, the signal is controllable (random, swept-sine, sine), along with the level and length.
- How many averages are required for a good estimate? The coherence should be monitored to ensure good quality data. Which window type and length should be used for force and velocity signals? For transient excitation, force windows and exponential windows can be used [66]. For steady-state excitation, a variety of window types is available, though usually Hanning windows are used.

The choice of appropriate measurement parameters requires good understanding and experience on the part of the operator. Different measurement parameters may result in different mobility estimates. When a hammer is used, experience is required by the hammer operator to perform repeatable hits.

In 1981, Ewins and Griffin [47] conducted a survey to assess the state-of-the-art in mobility measurement techniques. They observed a "considerable degree of inconsistency" in the results. Although more than 30 years have passed, mobility measurements of the same structure can still yield significant deviations, depending on the operator skill and the chosen measurement parameters. Therefore, mobility measurements should be checked for reasonableness and consistency. Several simple checks are available:

- For point mobilities, the phase data should always be between $-90°$and $+90°$. In other words, the real part must be positive. Transfer mobilities can have a positive or negative real part.
- The symmetric property of point mobility matrices (see Section 2.2.2) can be taken advantage of to verify transfer mobilities. Off-diagonal entries should be equal due to reciprocity: $Y_{ij} = Y_{ji}$.

- The eigenvalues of the real part of any point mobility matrix should be positive [103]. Negative eigenvalues indicate measurement errors in some of the matrix entries. Since this property holds for any point mobility matrix, "measurement errors in an n×n mobility matrix may be located by calculating the eigenvalues of all 2×2 sub-matrices formed by each pair of points" [103].

The basic steps of mobility measurement have been outlined, and potential pitfalls highlighted. With regards to non-linear structural elements such as springs and dampers, an *in-situ* measurement procedure might provide better estimates than a measurement in the free state.

5.3 Review of coupled mobilities

Before the focus is directed to the indirect determination of source mobilities in Section 5.4, a more general review of the indirect determination of coupled mobilities is presented. In this section, equations are derived for the calculation of coupled mobilities from source and receiver mobilities. Both point and transfer mobilities at arbitrary positions on the coupled structure can be determined from independent source and receiver data.

In the following, receiver structure and source structure are termed structures R and S, respectively. Figure 5.1 shows a schematic of the two structures, and indicates the location and direction of the acting forces and velocities at the interfaces a, b, and c. The two structures are connected at interface c.

All formulations are given in vector/matrix notation (cf. Appendix A), and hold both for the SDOF and the multi-point, MDOF case. Mobilities are indicated by matrices $\mathbf{Y}$, forces and velocities by vectors $\mathbf{F}$ and $\mathbf{v}$. Forces and velocities have two subscripts, the first one indicating the structure the force or velocity is applied to, and the second indicating the interface. Here is a short description of the acting forces and velocities **in the coupled state**:

- $\mathbf{F_{R,a}}$ is the force at remote points a on the receiver structure;
- $\mathbf{F_{R,c}}$ is the force at contact points c on the receiver structure;
- $\mathbf{F_{S,c}}$ is the force at contact points c on the source structure;
- $\mathbf{F_{S,b}}$ is the force at remote points b on the source structure;
- $\mathbf{v_{R,a}}$ is the velocity at remote points a on the receiver structure;

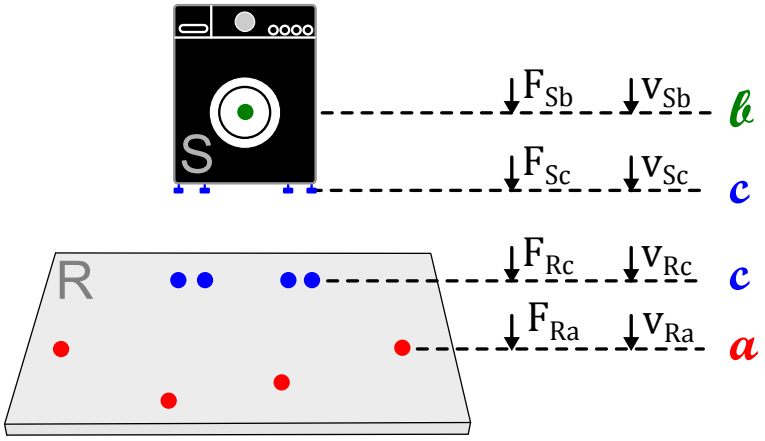

Figure 5.1: Diagram of receiver structure R and source structure S, coupled at c, showing the forces and velocities acting at interfaces a, b, and c.

- $\mathbf{v_{R,c}}$ is the velocity at contact points c on the receiver structure;
- $\mathbf{v_{S,c}}$ is the velocity at contact points c on the source structure;
- $\mathbf{v_{S,b}}$ is the velocity at remote points b on the source structure.

The notation for mobilities follows a slightly different pattern, as mobilities are needed both in the coupled state and in the uncoupled state. All mobilities are denoted as $\mathbf{Y_{X,yz}}$, where a force is acting at z on structure X (with $X \in \{R, S, C\}$), which results in a velocity at y. The subscripts indicate the following: R is the receiver structure; S is the source structure; C is the coupled structure. a indicates one or more remote points on the receiver structure, where the structure can be excited; b indicates a remote interface on the source; c indicates the contacts between source and receiver. Some examples:

- $\mathbf{Y_{R,cc}}$ is the receiver mobility at the contacts c in the uncoupled state;
- $\mathbf{Y_{R,ca}}$ is the transfer mobility on the uncoupled structure, with excitation at remote points a and response at the contacts c;
- $\mathbf{Y_{S,cc}}$ is the source mobility at the contacts c in the uncoupled state;
- $\mathbf{Y_{C,ca}}$ is the transfer mobility on the coupled structure, with excitation at remote points a and response at the contacts c;
- $\mathbf{Y_{C,cc}}$ is the point mobility of the coupled structure at the contacts c;
- $\mathbf{Y_{C,aa}}$ is the point mobility of the coupled structure at remote points a on the receiver structure.

In the next sections, formulations are presented for the calculation of point and transfer mobilities on the coupled structure from independent source and receiver mobility data. Four cases are considered:

- The coupled point mobility at contact position c: $\mathbf{Y_{C,cc}}$.
- The coupled point mobility at remote position a: $\mathbf{Y_{C,aa}}$.
- The coupled transfer mobility between remote position a and contact position c, and vice versa: $\mathbf{Y_{C,ca}}$ and $\mathbf{Y_{C,ac}}$.
- The coupled transfer mobility between two remote positions a and d: $\mathbf{Y_{C,da}}$ and $\mathbf{Y_{C,ad}}$.

5.3.1 Coupled point mobility at contact position

The coupled point mobility at the contacts can be calculated simply by adding the source and receiver impedances. The alternative formulations are derived using the matrix identities in Appendix A, in particular Equation (A.8):

$$\mathbf{Y_{C,cc}} = (\mathbf{Y_{R,cc}^{-1}} + \mathbf{Y_{S,cc}^{-1}})^{-1} \tag{5.2}$$

$$= \mathbf{Y_{R,cc}}(\mathbf{Y_{R,cc}} + \mathbf{Y_{S,cc}})^{-1}\mathbf{Y_{S,cc}} \tag{5.3}$$

$$= \mathbf{Y_{S,cc}}(\mathbf{Y_{R,cc}} + \mathbf{Y_{S,cc}})^{-1}\mathbf{Y_{R,cc}} \tag{5.4}$$

Alternatively, Moorhouse [101, Equation (11)] gives a formulation for the coupled point mobility, determined from measurements on the coupled structure only:

$$\mathbf{Y_{C,cc}} = \mathbf{Y_{C,cb}}\mathbf{Y_{C,ab}^{-1}}\mathbf{Y_{C,ca}^{T}}. \tag{5.5}$$

Combining Equations (32) and (33) from [101] gives yet another formulation for the coupled point mobility:

$$\mathbf{Y_{C,cc}} = \mathbf{Y_{R,cc}}\mathbf{Y_{R,ca}^{-T}}\mathbf{Y_{C,ca}^{T}}. \tag{5.6}$$

5.3.2 Coupled point mobility at remote position

Evans [45, Equation (5.22)] derives a formulation for the calculation of coupled point mobilities at remote positions, from source and receiver mobilities. For better understanding, this derivation is reproduced here.

Structures R and S, as depicted in Figure 5.1, are coupled together. The relationships between forces $\mathbf{f}$ and velocities $\mathbf{v}$ for each individual structure can be formulated in the partitioned matrix form:

$$\begin{bmatrix} \mathbf{v}_{\mathbf{R},\mathbf{a}} \\ \mathbf{v}_{\mathbf{R},\mathbf{c}} \end{bmatrix} = \begin{bmatrix} \mathbf{Y}_{\mathbf{R},\mathbf{aa}} & \mathbf{Y}_{\mathbf{R},\mathbf{ac}} \\ \mathbf{Y}_{\mathbf{R},\mathbf{ca}} & \mathbf{Y}_{\mathbf{R},\mathbf{cc}} \end{bmatrix} \begin{bmatrix} \mathbf{F}_{\mathbf{R},\mathbf{a}} \\ \mathbf{F}_{\mathbf{R},\mathbf{c}} \end{bmatrix} \tag{5.7}$$

$$\begin{bmatrix} \mathbf{v}_{\mathbf{S},\mathbf{c}} \\ \mathbf{v}_{\mathbf{S},\mathbf{b}} \end{bmatrix} = \begin{bmatrix} \mathbf{Y}_{\mathbf{S},\mathbf{cc}} & \mathbf{Y}_{\mathbf{S},\mathbf{cb}} \\ \mathbf{Y}_{\mathbf{S},\mathbf{bc}} & \mathbf{Y}_{\mathbf{S},\mathbf{bb}} \end{bmatrix} \begin{bmatrix} \mathbf{F}_{\mathbf{S},\mathbf{c}} \\ \mathbf{F}_{\mathbf{S},\mathbf{b}} \end{bmatrix} \tag{5.8}$$

Structures R and S are connected at the interface c such that the *continuity of motion* and the *equilibrium of forces* are fulfilled:

$$\mathbf{v}_{\mathbf{R},\mathbf{c}} = \mathbf{v}_{\mathbf{S},\mathbf{c}} \tag{5.9}$$

$$\mathbf{F}_{\mathbf{R},\mathbf{c}} = -\mathbf{F}_{\mathbf{S},\mathbf{c}}. \tag{5.10}$$

To obtain the mobility $\mathbf{Y}_{\mathbf{C},\mathbf{aa}}$ of the coupled structure at remote positions a, force $\mathbf{F}_{\mathbf{R},\mathbf{a}}$ and velocity $\mathbf{v}_{\mathbf{R},\mathbf{a}}$ are required. From Equations (5.7) and (5.8):

$$\mathbf{v}_{\mathbf{R},\mathbf{c}} = \mathbf{Y}_{\mathbf{R},\mathbf{ca}}\mathbf{F}_{\mathbf{R},\mathbf{a}} + \mathbf{Y}_{\mathbf{R},\mathbf{cc}}\mathbf{F}_{\mathbf{R},\mathbf{c}} \tag{5.11}$$

$$\mathbf{v}_{\mathbf{S},\mathbf{c}} = \mathbf{Y}_{\mathbf{S},\mathbf{cc}}\mathbf{F}_{\mathbf{S},\mathbf{c}} + \mathbf{Y}_{\mathbf{S},\mathbf{cb}}\mathbf{F}_{\mathbf{S},\mathbf{b}}. \tag{5.12}$$

With Equation (5.9), this can be rearranged:

$$\mathbf{Y}_{\mathbf{R},\mathbf{ca}}\mathbf{F}_{\mathbf{R},\mathbf{a}} + \mathbf{Y}_{\mathbf{R},\mathbf{cc}}\mathbf{F}_{\mathbf{R},\mathbf{c}} = \mathbf{Y}_{\mathbf{S},\mathbf{cc}}\mathbf{F}_{\mathbf{S},\mathbf{c}} + \mathbf{Y}_{\mathbf{S},\mathbf{cb}}\mathbf{F}_{\mathbf{S},\mathbf{b}}. \tag{5.13}$$

For the determination of the mobility of the coupled structure at position a, all external forces except $\mathbf{F}_{\mathbf{R},\mathbf{a}}$ must be zero, hence $\mathbf{F}_{\mathbf{S},\mathbf{b}} = \mathbf{0}$. Where structure S is a source, $\mathbf{F}_{\mathbf{S},\mathbf{b}}$ represents the internal excitation forces. For the measurement of mobility, the source has to be switched off, so that again $\mathbf{F}_{\mathbf{S},\mathbf{b}} = \mathbf{0}$:

$$\mathbf{Y}_{\mathbf{R},\mathbf{ca}}\mathbf{F}_{\mathbf{R},\mathbf{a}} + \mathbf{Y}_{\mathbf{R},\mathbf{cc}}\mathbf{F}_{\mathbf{R},\mathbf{c}} = \mathbf{Y}_{\mathbf{S},\mathbf{cc}}\mathbf{F}_{\mathbf{S},\mathbf{c}}. \tag{5.14}$$

Substituting $\mathbf{F}_{\mathbf{S},\mathbf{c}}$ by $-\mathbf{F}_{\mathbf{R},\mathbf{c}}$, using Equation (5.10), yields

$$\mathbf{Y}_{\mathbf{R},\mathbf{ca}}\mathbf{F}_{\mathbf{R},\mathbf{a}} + \mathbf{Y}_{\mathbf{R},\mathbf{cc}}\mathbf{F}_{\mathbf{R},\mathbf{c}} = -\mathbf{Y}_{\mathbf{S},\mathbf{cc}}\mathbf{F}_{\mathbf{R},\mathbf{c}}. \tag{5.15}$$

Rearranging for $\mathbf{F_{R,c}}$ yields

$$\mathbf{F_{R,c}} = -(\mathbf{Y_{R,cc}} + \mathbf{Y_{S,cc}})^{-1}\mathbf{Y_{R,ca}}\mathbf{F_{R,a}}. \tag{5.16}$$

From Equation (5.7):

$$\mathbf{v_{R,a}} = \mathbf{Y_{R,aa}}\mathbf{F_{R,a}} + \mathbf{Y_{R,ac}}\mathbf{F_{R,c}}. \tag{5.17}$$

Substituting $\mathbf{F_{R,c}}$ from Equation (5.16) yields

$$\mathbf{v_{R,a}} = \mathbf{Y_{R,aa}}\mathbf{F_{R,a}} - \mathbf{Y_{R,ac}}(\mathbf{Y_{R,cc}} + \mathbf{Y_{S,cc}})^{-1}\mathbf{Y_{R,ca}}\mathbf{F_{R,a}}. \tag{5.18}$$

Finally, applying one force F_{R,a_j} at a time ($F_{R,a_k} = 0, k \neq j$), the elements of the coupled mobility matrix $\mathbf{Y_{C,aa}}$ are determined:

$$\mathbf{Y_{C,aa}} = \mathbf{Y_{R,aa}} - \mathbf{Y_{R,ca}^{T}}(\mathbf{Y_{R,cc}} + \mathbf{Y_{S,cc}})^{-1}\mathbf{Y_{R,ca}}. \tag{5.19}$$

With this equation, any point mobility at remote position a on the coupled structure can be calculated from independent source and receiver data. Required are the uncoupled source and receiver point mobilities at the contacts, the uncoupled receiver point mobility at remote position a, and the uncoupled receiver transfer mobilities between contact points c and remote points a.

5.3.3 Coupled transfer mobility between remote position and contact position (and vice versa)

With only small modifications, the coupled transfer mobility between a remote point on the receiver structure and the contact point between source and receiver can be derived. The derivation follows the same steps as in Section 5.3.2. From Equation (5.7):

$$\mathbf{v_{R,c}} = \mathbf{Y_{R,ca}}\mathbf{F_{R,a}} + \mathbf{Y_{R,cc}}\mathbf{F_{R,c}}. \tag{5.20}$$

Substituting $\mathbf{F_{R,c}}$ from Equation (5.16) yields

$$\mathbf{v_{R,c}} = \mathbf{Y_{R,ca}}\mathbf{F_{R,a}} - \mathbf{Y_{R,cc}}(\mathbf{Y_{R,cc}} + \mathbf{Y_{S,cc}})^{-1}\mathbf{Y_{R,ca}}\mathbf{F_{R,a}}. \tag{5.21}$$

Solving for $\mathbf{Y_{C,ca}}$ yields a formulation for the coupled transfer mobility:

$$\mathbf{Y_{C,ca}} = \mathbf{Y_{R,ca}} - \mathbf{Y_{R,cc}}(\mathbf{Y_{R,cc}} + \mathbf{Y_{S,cc}})^{-1}\mathbf{Y_{R,ca}}. \tag{5.22}$$

With this equation, any transfer mobility between the contact points and remote points a on the coupled structure can be calculated from independent source and receiver data. Required are the uncoupled source and receiver point mobilities at the contacts, and the uncoupled receiver transfer mobilities between contact points and remote points.

5.3.4 Coupled transfer mobility between two sets of remote positions

Coupled transfer mobilities can also be calculated between two sets of remote positions on the receiver structure. For this, Figure 5.1 has to be modified to include another set of force and velocity positions on the receiver structure, see Figure 5.2.

The derivation is similar to that in Section 5.3.2.

$$\begin{bmatrix} \mathbf{v_{R,a}} \\ \mathbf{v_{R,d}} \\ \mathbf{v_{R,c}} \end{bmatrix} = \begin{bmatrix} \mathbf{Y_{R,aa}} & \mathbf{Y_{R,ad}} & \mathbf{Y_{R,ac}} \\ \mathbf{Y_{R,da}} & \mathbf{Y_{R,dd}} & \mathbf{Y_{R,dc}} \\ \mathbf{Y_{R,ca}} & \mathbf{Y_{R,cd}} & \mathbf{Y_{R,cc}} \end{bmatrix} \begin{bmatrix} \mathbf{F_{R,a}} \\ \mathbf{F_{R,d}} \\ \mathbf{F_{R,c}} \end{bmatrix} \tag{5.23}$$

$$\begin{bmatrix} \mathbf{v_{S,c}} \\ \mathbf{v_{S,b}} \end{bmatrix} = \begin{bmatrix} \mathbf{Y_{S,cc}} & \mathbf{Y_{S,cb}} \\ \mathbf{Y_{S,bc}} & \mathbf{Y_{S,bb}} \end{bmatrix} \begin{bmatrix} \mathbf{F_{S,c}} \\ \mathbf{F_{S,b}} \end{bmatrix} \tag{5.24}$$

To obtain the coupled transfer mobility $\mathbf{Y_{C,da}}$, force $\mathbf{F_{R,a}}$ and velocity $\mathbf{v_{R,d}}$ are required. From Equation (5.23) and Equation (5.24):

$$\mathbf{v_{R,c}} = \mathbf{Y_{R,ca}}\mathbf{F_{R,a}} + \mathbf{Y_{R,cd}}\mathbf{F_{R,d}} + \mathbf{Y_{R,cc}}\mathbf{F_{R,c}} \tag{5.25}$$

$$\mathbf{v_{S,c}} = \mathbf{Y_{S,cc}}\mathbf{F_{S,c}} + \mathbf{Y_{S,cb}}\mathbf{F_{S,b}}. \tag{5.26}$$

With Equations (5.9) and (5.10), and $\mathbf{F_{R,d}} = \mathbf{0}$ and $\mathbf{F_{S,b}} = \mathbf{0}$, this is solved for $\mathbf{F_{R,c}}$:

$$\mathbf{F_{R,c}} = -(\mathbf{Y_{R,cc}} + \mathbf{Y_{S,cc}})^{-1}\mathbf{Y_{R,ca}}\mathbf{F_{R,a}}. \tag{5.27}$$

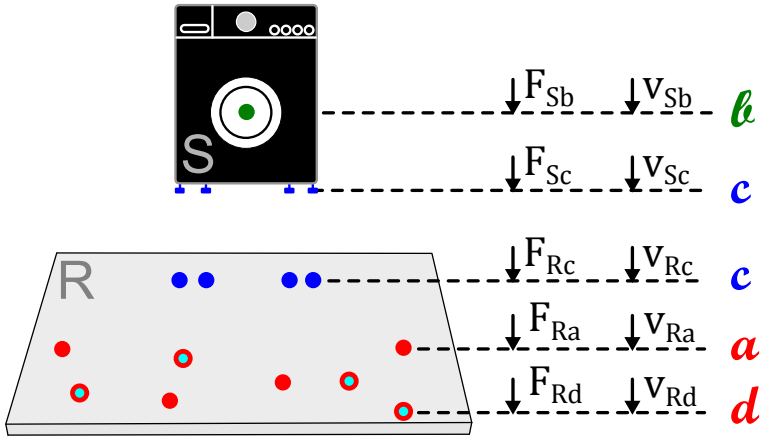

Figure 5.2: Diagram of receiver structure R and source structure S showing the forces and velocities acting at the interfaces, including the additional interface d on the receiver structure.

From Equation (5.23):

$$\mathbf{v_{R,d}} = \mathbf{Y_{R,da}F_{R,a}} + \mathbf{Y_{R,dd}F_{R,d}} + \mathbf{Y_{R,dc}F_{R,c}}. \tag{5.28}$$

Substituting $\mathbf{F_{R,c}}$ from Equation (5.27), and setting $\mathbf{F_{R,d}} = \mathbf{0}$ yields

$$\mathbf{v_{R,d}} = \mathbf{Y_{R,da}F_{R,a}} - \mathbf{Y_{R,dc}}(\mathbf{Y_{R,cc}} + \mathbf{Y_{S,cc}})^{-1}\mathbf{Y_{R,ca}F_{R,a}}. \tag{5.29}$$

Finally, solving for $\mathbf{Y_{C,da}}$ yields a formulation for the coupled transfer mobility between remote points on the receiver structure:

$$\mathbf{Y_{C,da}} = \mathbf{Y_{R,da}} - \mathbf{Y_{R,dc}}(\mathbf{Y_{R,cc}} + \mathbf{Y_{S,cc}})^{-1}\mathbf{Y_{R,ca}}. \tag{5.30}$$

With this equation, any transfer mobility between two sets of remote points a and d on the coupled structure can be calculated from independent source and receiver data. Required are the uncoupled source and receiver point mobilities at the contacts and the uncoupled receiver transfer mobilities between contact points c, remote points a, and remote points d.

5.4 Indirect determination of source mobility

In this section, formulations for the indirect determination of source mobilities are presented. The mobilities are not measured directly, instead they are calculated from the dynamic loading effect the source has on the receiver structure. The procedure is as follows:

1. Measure receiver structure without source (*receiver mobility*);
2. Measure receiver structure with source attached (*coupled mobility*);
3. Determine *source mobility* from difference between receiver mobility and coupled mobility.

5.4.1 Method 1

This derivation [98] is based on Equations (8) and (11) from [101]:

$$\mathbf{Y_{R,cc}} = \mathbf{Y_{C,cb}} \mathbf{Y_{C,ab}^{-1}} \mathbf{Y_{R,ca}^{T}} \tag{5.31}$$

$$\mathbf{Y_{C,cc}} = \mathbf{Y_{C,cb}} \mathbf{Y_{C,ab}^{-1}} \mathbf{Y_{C,ca}^{T}}. \tag{5.32}$$

The inverses of these matrices read

$$\mathbf{Y_{R,cc}^{-1}} = \mathbf{Y_{R,ca}^{-T}} \mathbf{Y_{C,ab}} \mathbf{Y_{C,cb}^{-1}} \tag{5.33}$$

$$\mathbf{Y_{C,cc}^{-1}} = \mathbf{Y_{C,ca}^{-T}} \mathbf{Y_{C,ab}} \mathbf{Y_{C,cb}^{-1}}. \tag{5.34}$$

Also known is the relationship between source point mobility, receiver point mobility, and coupled point mobility (see Equation (5.2)), which can be solved for $\mathbf{Y_{S,cc}}$:

$$\mathbf{Y_{S,cc}^{-1}} = \mathbf{Y_{C,cc}^{-1}} - \mathbf{Y_{R,cc}^{-1}}. \tag{5.35}$$

Substituting $\mathbf{Y_{R,cc}^{-1}}$ and $\mathbf{Y_{C,cc}^{-1}}$ from Equations (5.33) and (5.34) yields

$$\mathbf{Y_{S,cc}^{-1}} = \mathbf{Y_{C,ca}^{-T}} \mathbf{Y_{C,ab}} \mathbf{Y_{C,cb}^{-1}} - \mathbf{Y_{R,ca}^{-T}} \mathbf{Y_{C,ab}} \mathbf{Y_{C,cb}^{-1}} \tag{5.36}$$

$$= (\mathbf{Y_{C,ca}^{-T}} - \mathbf{Y_{R,ca}^{-T}}) \mathbf{Y_{C,ab}} \mathbf{Y_{C,cb}^{-1}} \tag{5.37}$$

$$= (\mathbf{Y_{C,ca}^{-T}} - \mathbf{Y_{R,ca}^{-T}}) \mathbf{T}. \tag{5.38}$$

The term $\mathbf{Y_{C,ab}Y_{C,cb}^{-1}} = \mathbf{T}$ behind the brackets is the generalized transmissibility matrix, as described in [116]. It can be obtained from operational measurements, if all responses at a and c can be measured while the source is operating (which means forces at b). The number and location of the forces must not change, as the transmissibility matrix is only valid for a specific set of excitation positions. Alternatively, the transfer mobility matrices may be used. This approach is pursued here.

Inverting Equation (5.37) yields

$$\mathbf{Y_{S,cc}} = \mathbf{Y_{C,cb}Y_{C,ab}^{-1}}(\mathbf{Y_{C,ca}^{-T}} - \mathbf{Y_{R,ca}^{-T}})^{-1}. \tag{5.39}$$

With Equation (A.8), the term in brackets can be rewritten to give

$$\mathbf{Y_{S,cc}} = \mathbf{Y_{C,cb}Y_{C,ab}^{-1}Y_{R,ca}^{T}}(\mathbf{Y_{R,ca}^{T}} - \mathbf{Y_{C,ca}^{T}})^{-1}\mathbf{Y_{C,ca}^{T}}. \tag{5.40}$$

The term before the brackets is the point mobility of the receiver structure at the contacts, as defined in Equation (5.31). Substituting it yields a formulation for the determination of the source mobility from receiver and coupled mobilities only:

$$\mathbf{Y_{S,cc}} = \mathbf{Y_{R,cc}}(\mathbf{Y_{R,ca}^{T}} - \mathbf{Y_{C,ca}^{T}})^{-1}\mathbf{Y_{C,ca}^{T}}. \tag{5.41}$$

With this approach, any source point mobility can be calculated from receiver and coupled mobilities. Required are the uncoupled receiver point mobility at the contacts, the uncoupled receiver transfer mobilities between contact points c and remote points a, and the transfer mobilities between a and c in the coupled state.

5.4.2 Method 2

A second set of formulations for the indirect determination of source mobility is found by solving the equations from Section 5.3 for the source mobility $\mathbf{Y_{S,cc}}$.

Equation (5.19) can be solved for $\mathbf{Y_{S,cc}}$ to give

$$\mathbf{Y_{S,cc}} = \mathbf{Y_{R,ca}}(\mathbf{Y_{R,aa}} - \mathbf{Y_{C,aa}})^{-1}\mathbf{Y_{R,ca}^{T}} - \mathbf{Y_{R,cc}}. \tag{5.42}$$

This formulation does not require force sensors or accelerometers at the contacts in the coupled state. In the coupled state, only point mobilities at remote positions a on the receiver structure need to be measured.

Correspondingly, Equations (5.22) and (5.30) can be solved for $\mathbf{Y_{S,cc}}$ to give

$$\mathbf{Y_{S,cc}} = \mathbf{Y_{R,ca}}(\mathbf{Y_{R,ca}} - \mathbf{Y_{C,ca}})^{-1}\mathbf{Y_{R,cc}} - \mathbf{Y_{R,cc}} \tag{5.43}$$

and

$$\mathbf{Y_{S,cc}} = \mathbf{Y_{R,ca}}(\mathbf{Y_{R,da}} - \mathbf{Y_{C,da}})^{-1}\mathbf{Y_{R,dc}} - \mathbf{Y_{R,cc}}. \tag{5.44}$$

These two last formulations require the measurement of more quantities than Equation (5.42), without additional benefit. Therefore, they will not be investigated further in this thesis.

5.4.3 Method 3

An alternative formulation for the indirect determination of source mobility is derived, using the concept of *reactive forces*. Consider the receiver structure R **in the uncoupled state**. If excited at interface a, the response of the uncoupled receiver structure at d is:

$$\mathbf{v_{R,d,uncoupled}} = \mathbf{Y_{R,da}}\mathbf{F_{R,a}}. \tag{5.45}$$

Now, the structure is again excited at a, but this time the source structure S is attached at interface c. The excitation at a results in a reactive force at c, and the velocity at d can now be expressed as a superposition of two terms: The first one describing the initial velocity "as if the source wasn't attached", the second describing the reduction of velocity due to the reactive force at c:

$$\mathbf{v_{R,d,coupled}} = \mathbf{v_{R,d,uncoupled}} - \mathbf{Y_{C,dc}}\mathbf{F_{R,c}}. \tag{5.46}$$

The reactive force $\mathbf{F_{R,c}}$ at the contact can be expressed by the source mobility $\mathbf{Y_{S,cc}}$, and the initial, uncoupled velocity at c:

$$\mathbf{F_{R,c}} = \mathbf{Y_{S,cc}^{-1}}\mathbf{v_{R,c,uncoupled}}. \tag{5.47}$$

Substituting $\mathbf{v_{R,d,uncoupled}}$ from Equation (5.45), and $\mathbf{F_{R,c}}$ from Equation (5.47) into Equation (5.46) yields

$$\mathbf{v_{R,d,coupled}} = \mathbf{Y_{R,da}F_{R,a}} - \mathbf{Y_{R,dc}Y_{S,cc}^{-1}v_{R,c,uncoupled}}. \tag{5.48}$$

With $\mathbf{v_{R,c,uncoupled}} = \mathbf{Y_{R,ca}F_{R,a}}$, this is

$$\mathbf{v_{R,d,coupled}} = \mathbf{Y_{R,da}F_{R,a}} - \mathbf{Y_{R,dc}Y_{S,cc}^{-1}Y_{R,ca}F_{R,a}}. \tag{5.49}$$

Rearranging for $\mathbf{Y_{C,da}}$ yields

$$\mathbf{Y_{C,da}} = \mathbf{Y_{R,da}} - \mathbf{Y_{C,dc}Y_{S,cc}^{-1}Y_{R,ca}}. \tag{5.50}$$

This can be solved for $\mathbf{Y_{S,cc}}$:

$$\mathbf{Y_{S,cc}} = \mathbf{Y_{R,ca}}(\mathbf{Y_{R,da}} - \mathbf{Y_{C,da}})^{-1}\mathbf{Y_{C,dc}} \tag{5.51}$$

$$= \mathbf{Y_{R,ca}}(\mathbf{Y_{R,da}} - \mathbf{Y_{C,da}})^{-1}\mathbf{Y_{C,cd}^{T}}. \tag{5.52}$$

With this approach, any source point mobility can be calculated from receiver and coupled mobilities. Required are the uncoupled receiver transfer mobilities between positions a, c, and d, and the coupled transfer mobilities between positions a, c, and d.

5.4.4 Summary and discussion

Three formulations for the indirect determination of source mobility from receiver and coupled mobilities were considered:

Method 1: $$\mathbf{Y_{S,cc}} = \mathbf{Y_{R,cc}}(\mathbf{Y_{R,ca}^{T}} - \mathbf{Y_{C,ca}^{T}})^{-1}\mathbf{Y_{C,ca}^{T}} \tag{5.53}$$

Method 2: $$\mathbf{Y_{S,cc}} = \mathbf{Y_{R,ca}}(\mathbf{Y_{R,aa}} - \mathbf{Y_{C,aa}})^{-1}\mathbf{Y_{R,ca}^{T}} - \mathbf{Y_{R,cc}} \tag{5.54}$$

Method 3: $$\mathbf{Y_{S,cc}} = \mathbf{Y_{R,ca}}(\mathbf{Y_{R,da}} - \mathbf{Y_{C,da}})^{-1}\mathbf{Y_{C,cd}^{T}} \tag{5.55}$$

Each of the three methods requires the determination of multiple mobility terms, in the coupled and in the uncoupled state. For none of the methods is

excitation at the contact points necessary. This is of significant practical benefit, and distinguishes the methods from the "sum-of-impedance" formulation in Equation (5.2). Furthermore, Method 2 does not require measurement of responses at the contact points in the coupled state. However, it requires measurement of one more mobility term than Method 1. Also, while for Method 1 the accelerometers can remain attached at the contact points (provided the source can be removed with the accelerometers in place), they have to be moved between positions a and c for Method 2.

As one important factor in the calculation of the source mobility is the difference between coupled and uncoupled state (term in brackets), clean measurement data and a sufficient difference in mobilities is of importance. The difference in mobility will most likely be smaller at remote positions, compared with at the contacts. Therefore, results are expected to be more accurate for Method 1 than for Method 2, since the former uses the contact velocities. Furthermore, it is expected that all three methods will perform best if source and receiver point mobilities are in the same order of magnitude. In this case, the attached source should have significant influence on the velocity at the contacts. For a high-mobility source ($|Y_s| \gg |Y_r|$), the difference between coupled and uncoupled mobilities will be small, and the accuracy of the methods is expected to degrade as a consequence.

Method 3 appears to be a hybrid of Method 1 and Method 2. It uses the mobility differences at remote positions on the receiver structure, as in Equation (5.54), but retains the same structure as Equation (5.53). Four mobility terms are required, compared with three terms for Method 1, and four terms for Method 2. Compared to Method 2, the advantage of not having to measure at the contact positions in the coupled state is lost, because the coupled term $\mathbf{Y}^{\mathbf{T}}_{\mathbf{C,cd}}$ is required. At the same time, the mobility difference at remote points will most likely give larger errors than at the contacts, thus decreasing the accuracy of the method, compared with Method 1.

From a practical perspective, it appears advisable to use Method 1 if the contact points in the coupled state are accessible, to allow the attachment of accelerometers. If this is not the case, Method 2 provides a convenient alternative, though the involved measurement effort is greater. Method 3 does not promise any advantage over the other two methods, but is investigated for completeness.

5.5 Summary

The determination of structural (source and receiver) mobilities is an important task in structure-borne sound source characterization. Direct mobility measurement methods are well-established, though they pose challenges and pitfalls not immediately obvious to non-experts. For sources with non-linear elements, mobility measurements in the free state may yield incorrect results. Therefore, indirect methods to obtain the source mobility *in-situ* were investigated. In conjunction with indirectly determined blocked forces [100], a full *in-situ* source characterization appears possible.

Three methods were presented for the indirect determination of source mobility. Each requires measurement or calculation of several mobility terms. All formulations were given using matrix notation, and are valid for both the SDOF case and for sources with multiple terminals and/or multiple components of excitation. The advantages and disadvantages of each method were discussed.

In Chapter 6, the three methods are investigated numerically, using analytical and numerical simulations of rods and beams. In Chapter 7, the three methods are investigated experimentally.

6 Numerical Validation of Indirect Methods to Obtain Source Mobilities

6.1 Introduction

To test the validity of the methods to indirectly determine source mobilities, presented in Chapter 5 (Equations (5.53), (5.54), and (5.55)), analytical and numerical studies were conducted. The objective of this chapter is to compare the three methods, and to investigate their limits and sensitivity to experimental errors such as noise, positioning uncertainties, or due to neglect of DOFs. Numerical simulations offer a controlled environment, essential for systematic investigations into errors. A free rod is treated analytically, representing the scalar cases of the three formulations. A free beam serves as example for a MDOF system, and is treated numerically.

6.2 Analytical model of coupled free rods

A free source rod S was virtually connected end-to-end with a free receiver rod R, yielding the coupled free rod C, see Figure 6.1.

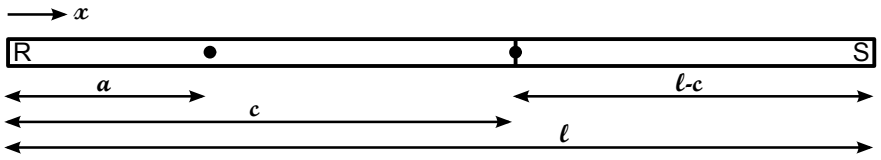

Figure 6.1: Free rods R and S, connected end-to-end at position c.

The analytical solutions for mobilities of a free rod are [101]

$$Y_{x_2x_1}(\omega) = \frac{v_{x_2}(\omega)}{F_{x_1}(\omega)} = \begin{cases} -\dfrac{j}{\rho A c_L}\dfrac{\cos kx_2 \cos k(l-x_1)}{\sin kl} & x_2 \leq x_1 \\ -\dfrac{j}{\rho A c_L}\dfrac{\cos k(l-x_2) \cos kx_1}{\sin kl} & x_2 \geq x_1 \end{cases}, \tag{6.1}$$

where ρ is the material density, A is the cross-sectional area, c_L is the longitudinal wavespeed, and l is the length of the rod. j is the imaginary unit, and k is the wavenumber. The longitudinal wavespeed c_L of a rod is given by $c_L = \sqrt{E/\rho}$, where E is Young's modulus. The rod wavenumber is calculated as $k = \omega/c_L$. The rod is excited at position x_1 by a force F, which results in a velocity response v at position x_2.

The mobilities required for Equations (5.53), (5.54), and (5.55) can be calculated by inserting the appropriate values for x_1, x_2, and l into Equation (6.1):

$$Y_{R,cc} = -\frac{j}{\rho A c_L}\frac{\cos kc}{\sin kc}$$

$$Y_{R,ca} = -\frac{j}{\rho A c_L}\frac{\cos ka}{\sin kc} \qquad Y_{C,ca} = -\frac{j}{\rho A c_L}\frac{\cos k(l-c)\cos ka}{\sin kl}$$

$$Y_{R,aa} = -\frac{j}{\rho A c_L}\frac{\cos ka \cos k(c-a)}{\sin kc} \qquad Y_{C,aa} = -\frac{j}{\rho A c_L}\frac{\cos ka \cos k(l-a)}{\sin kl}$$

$$Y_{R,da} = -\frac{j}{\rho A c_L}\frac{\cos kd \cos k(c-a)}{\sin kc} \qquad Y_{C,da} = -\frac{j}{\rho A c_L}\frac{\cos kd \cos k(l-a)}{\sin kl}$$

$$Y_{C,dc} = -\frac{j}{\rho A c_L}\frac{\cos kd \cos k(l-c)}{\sin kl}$$

The mobility of the source rod is also calculated directly:

$$Y_{S,cc} = -\frac{j}{\rho A c_L} \frac{\cos k(l-c)}{\sin k(l-c)} \tag{6.2}$$

Now, by substituting $Y_{R,cc}$, $Y_{R,ca}$, and $Y_{C,ca}$ into Equation (5.53), $Y_{R,cc}$, $Y_{R,ca}$, $Y_{R,aa}$, and $Y_{C,aa}$ into Equation (5.54), and $Y_{R,ca}$, $Y_{R,da}$, $Y_{C,da}$, and $Y_{C,dc}$ into Equation (5.55), the source rod mobility $Y_{S,cc}$ is calculated indirectly.

For Method 1, the substitution yields

$$\begin{aligned} Y_{S,cc} &= -\frac{j}{\rho A c_L} \frac{\cos kc}{\sin kc} \left[\frac{\cos ka}{\sin kc} - \frac{\cos k(l-c) \cos ka}{\sin kl} \right]^{-1} \frac{\cos k(l-c) \cos ka}{\sin kl} \\ &= -\frac{j}{\rho A c_L} \frac{\cos k(l-c) \cos kc}{\sin kl - \cos k(l-c) \sin kc}. \end{aligned} \tag{6.3}$$

For Method 2, the substitution yields

$$\begin{aligned} Y_{S,cc} = &-\frac{j}{\rho A c_L} \\ &\left(\frac{\cos ka}{\sin kc} \left[\frac{\cos ka \cos k(c-a)}{\sin kc} - \frac{\cos k(l-a) \cos ka}{\sin kl} \right]^{-1} \frac{\cos ka}{\sin kc} - \frac{\cos kc}{\sin kc} \right) \\ = &-\frac{j}{\rho A c_L} \\ &\frac{\cos ka \sin kl - \cos k(c-a) \sin kl \cos kc + \cos k(l-a) \sin kc \cos kc}{\cos k(c-a) \sin kl \sin kc - \cos k(l-a) \sin^2 kc}. \end{aligned} \tag{6.4}$$

For Method 3, the substitution yields

$$\begin{aligned} Y_{S,cc} = &-\frac{j}{\rho A c_L} \\ &\left(\frac{\cos ka}{\sin kc} \left[\frac{\cos kd \cos k(c-a)}{\sin kc} - \frac{\cos kd \cos k(l-a)}{\sin kl} \right]^{-1} \frac{\cos kd \cos k(l-c)}{\sin kl} \right) \\ = &-\frac{j}{\rho A c_L} \frac{\cos ka \cos k(l-c)}{\cos k(c-a) \sin kl - \cos k(l-a) \sin kc}. \end{aligned} \tag{6.5}$$

Equations (6.3), (6.4), and (6.5) can be shown to be equivalent and to equal the directly calculated result in Equation (6.2). The proofs are somewhat lengthy, and are presented in Appendix C.

For this case of only one degree of freedom, Equations (5.53), (5.54), and (5.55) take on scalar form, and the results are exact. In the next section, the validity of these formulations for the matrix case is investigated.

6.3 Numerical model of coupled free beams

For the validation of Equations (5.53), (5.54) and (5.55) for the matrix case, a free source beam S was virtually connected end-to-end with a free receiver beam R, yielding the coupled free beam C. Figure 6.2 illustrates the setup.

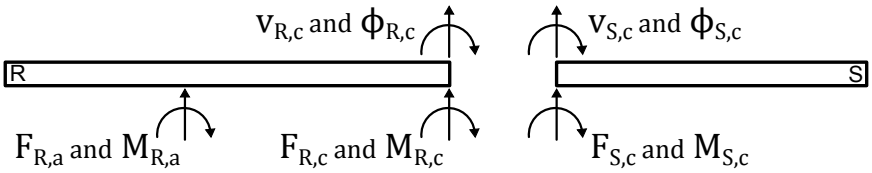

Figure 6.2: Free beams R and S, connected end-to-end at position c.

Analytical solutions for (cross-)point and (cross-)transfer mobilities of free beams are given in Appendix B. They were implemented in MATLAB for the following investigations. Circular aluminium beams with radius $r = 10\,\text{mm}$ and frequency-independent loss factor $\eta = 0.02$[1] were used in the simulations. Beam R has a length of 2 m, beam S has a length of 1.4 m, and beam C has a length of 3.4 m. The locations of a, c, and d are given in Table 6.1.

The point mobilities of source and receiver beam at the interface c are shown in Figure 6.3. The receiver beam has resonances at 22 Hz, 62 Hz, 122 Hz, 202 Hz, 302 Hz, 422 Hz, 562 Hz, 722 Hz, and 902 Hz. The source beam has resonances at 46 Hz, 128 Hz, 250 Hz, 413 Hz, 618 Hz, and 863 Hz. At most of the receiver beam resonances, the receiver mobility is significantly higher than the source mobility. At most of the source beam resonances, the source mobility is significantly higher than the receiver mobility. The third receiver beam resonance and the second source beam resonance coincide approximately, as do the third receiver beam anti-resonance and the second source beam anti-resonance.

[1] The measured internal loss factor of aluminium is $\eta \leq 0.001$ [72]. The higher value of $\eta = 0.02$ was used for clarity of presentation. Using a loss factor of $\eta = 0.001$ in the simulations yields essentially the same results, though error magnitudes tend to be larger.

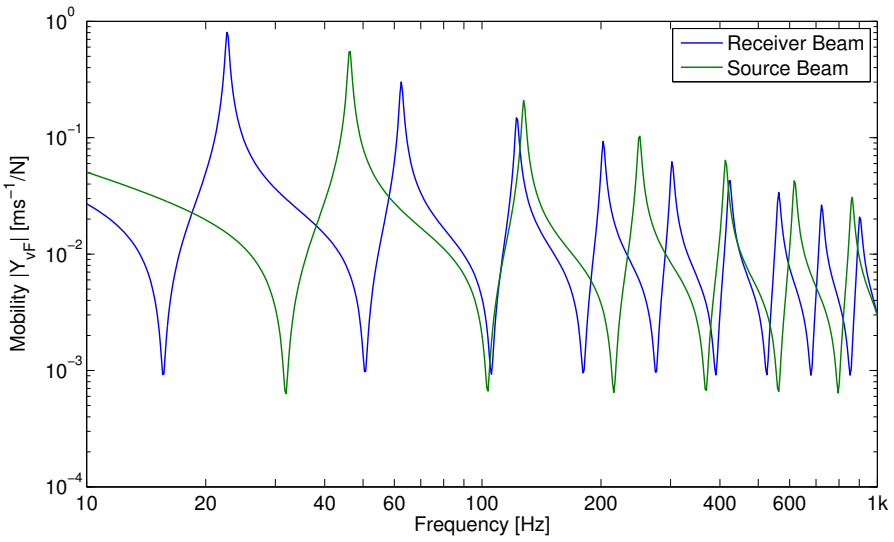

Figure 6.3: Point mobility of receiver beam and source beam at c.

Translational and rotational movement must be considered for an adequate description of the out-of-plane motion of beams. The generalized point mobility matrix for one point therefore has size 2×2. For the case of one contact point c and one response point a, Equation (5.53) has the form

$$\begin{pmatrix} \frac{v_{S,c}}{F_{S,c}} & \frac{v_{S,c}}{M_{S,c}} \\ \frac{\theta_{S,c}}{F_{S,c}} & \frac{\theta_{S,c}}{M_{S,c}} \end{pmatrix} =$$
$$\begin{pmatrix} \frac{v_{R,c}}{F_{R,c}} & \frac{v_{R,c}}{M_{R,c}} \\ \frac{\theta_{R,c}}{F_{R,c}} & \frac{\theta_{R,c}}{M_{R,c}} \end{pmatrix} \left[\begin{pmatrix} \frac{v_{R,c}}{F_{R,a}} & \frac{v_{R,c}}{M_{R,a}} \\ \frac{\theta_{R,c}}{F_{R,a}} & \frac{\theta_{R,c}}{M_{R,a}} \end{pmatrix}^T - \begin{pmatrix} \frac{v_{C,c}}{F_{C,a}} & \frac{v_{C,c}}{M_{C,a}} \\ \frac{\theta_{C,c}}{F_{C,a}} & \frac{\theta_{C,c}}{M_{C,a}} \end{pmatrix}^T \right]^{-1} \begin{pmatrix} \frac{v_{C,c}}{F_{C,a}} & \frac{v_{C,c}}{M_{C,a}} \\ \frac{\theta_{C,c}}{F_{C,a}} & \frac{\theta_{C,c}}{M_{C,a}} \end{pmatrix}^T ,$$

where v and θ are translational and rotational velocities, respectively, and F and M are forces and moments, respectively. Using this equation and the corresponding version of Equation (5.54) and Equation (5.55), the source beam mobility matrix was determined numerically. The first matrix element of $\mathbf{Y_{S,cc}}$ (v/F) is shown in Figure 6.4. There is no discernible difference between direct and indirect calculations for all three methods, except for some numerical instabilities at high frequencies. These are due to computational round-off errors in MATLAB's internal `svd` command. The agreement in Figure 6.4 confirms the validity of Equations (5.53), (5.54) and (5.55) for the matrix case.

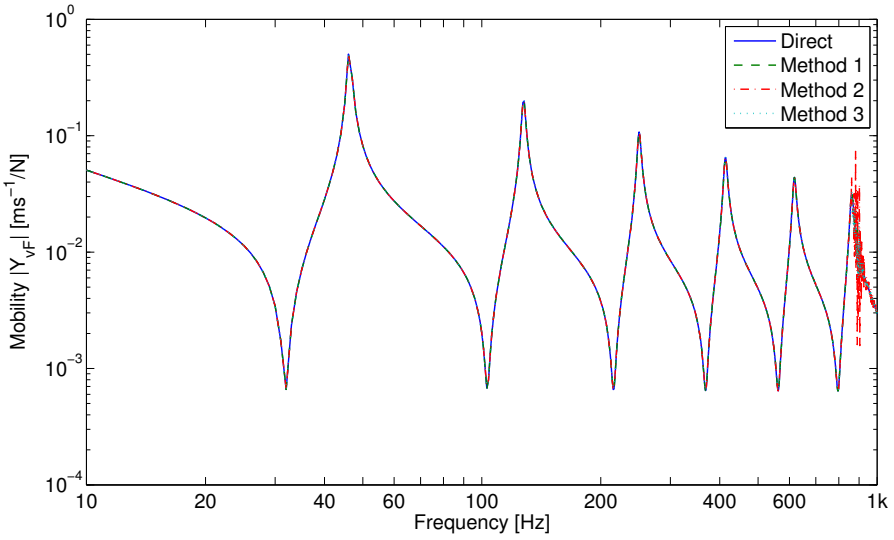

Figure 6.4: Mobility of source beam, using translational and rotational DOFs at one response position, without noise or other errors.

In the following sections, the robustness of the three methods with regard to typical measurement errors is examined. The following causes of error are investigated: neglect of DOFs, random measurement noise, changes in resonances/anti-resonances due to positioning uncertainties, frequency resolution, and phase differences between accelerometers.

6.3.1 Effect of neglecting DOFs

When dealing with coupled structures, often only translational degrees of freedom (v/F) are considered, because they are assumed more important than rotational degrees of freedom, and because they are easier to measure. However, it has been shown by Elliott [44] that this simplification may lead to large errors. If only translational mobilities are considered for one contact point and one response point, Equations (5.53), (5.54), and (5.55) reduce to the scalar case. For example, Equation (5.53) becomes

$$\frac{v_{S,c}}{F_{S,c}} = \frac{v_{R,c}}{F_{R,c}} \left[\frac{v_{R,c}}{F_{R,a}} - \frac{v_{C,c}}{F_{C,a}} \right]^{-1} \frac{v_{C,c}}{F_{C,a}}.$$

Figure 6.5 shows the consequences of this simplification for the indirectly determined source beam mobility. The calculations for all three formulations fail over the entire frequency range.

The consequences of neglecting rotational degrees of freedom can be compensated by considering more translational mobilities than would usually be necessary. A single point characterized in terms of translation and rotation may alternatively be considered as two points in translation. Using for example two remote response positions a_1 and a_2, Equation (5.53) has the form:

$$\frac{v_{S,c}}{F_{S,c}} = \frac{v_{R,c}}{F_{R,c}} \left[\begin{pmatrix} \frac{v_{R,c}}{F_{R,a1}} & \frac{v_{R,c}}{F_{R,a2}} \end{pmatrix}^T - \begin{pmatrix} \frac{v_{C,c}}{F_{C,a1}} & \frac{v_{C,c}}{F_{C,a2}} \end{pmatrix}^T \right]^{-1} \begin{pmatrix} \frac{v_{C,c}}{F_{C,a1}} & \frac{v_{C,c}}{F_{C,a2}} \end{pmatrix}^T .$$

This version of Equation (5.53) consists entirely of translational mobilities. The term in brackets is no longer a square matrix, and the inversion is performed using a least-square solution (see Section 2.4.1).

Figure 6.6 shows the result of the calculation. The indirectly determined source mobilities for Methods 2 and 3 agree once again with the direct calculation. However, the result for Method 1 does not converge towards the true solution, even when more response positions are considered. The reason for this becomes apparent when considering the matrix to be inverted in Equation (5.53). For one contact position c, two or more response positions a_n, two or more response positions d_m, and translational force mobilities only, it has size $n \times 1$ and rank 1. The inverted matrices in Equations (5.54) and (5.55), on the other hand, have size $n \times n$ and $n \times m$, and rank n and $\min(n, m)$, respectively. It is concluded that the rank of the matrix to be inverted must at least equal the number of relevant DOFs at the interface. If this requirement is fulfilled, it is possible to compensate for missing rotational DOFs by additional translational DOFs.

If Equation (5.53) is adjusted to have rank 2, Method 1 also yields the correct result. This can be achieved by adding a "virtual" contact position. In measurement, often two matched accelerometers are placed either side of one contact, to measure translational and rotational motion [44]. Instead of calculating a linear velocity (by averaging the two accelerometer signals) and a rotational velocity (by calculating the difference), two linear velocities can be considered. For the coupled beam system, an additional contact position is considered in the calculation. For contact positions c_1 and c_2, and response

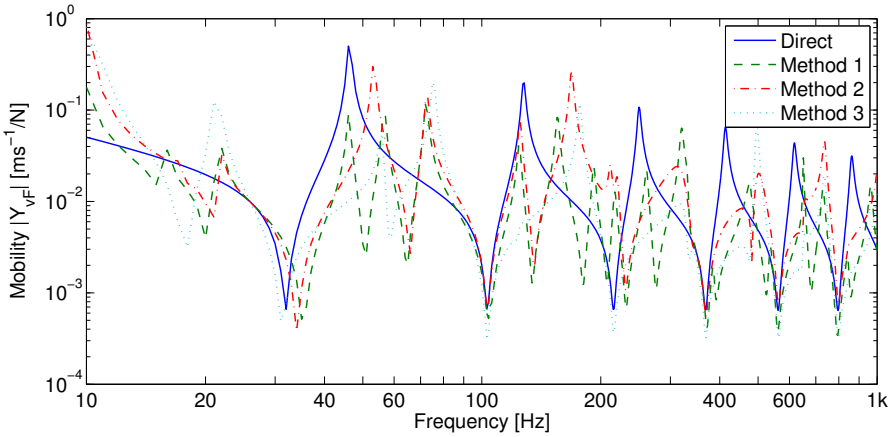

Figure 6.5: Using only translational DOFs at 1 response position.

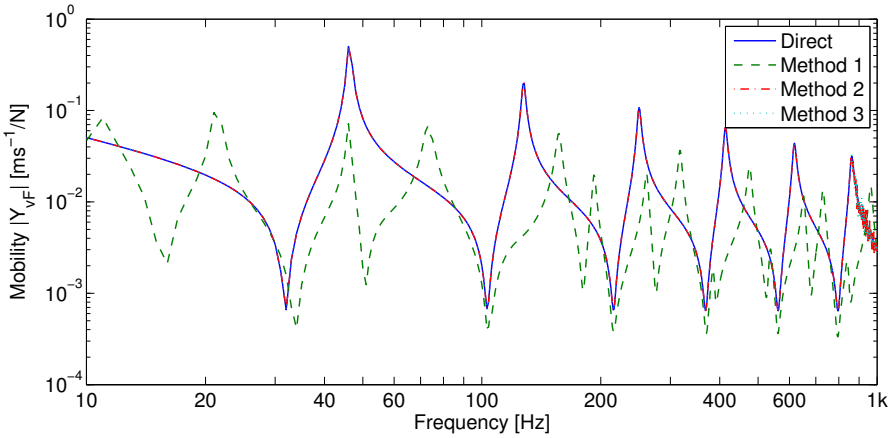

Figure 6.6: Using only translational DOFs at 2 response positions.

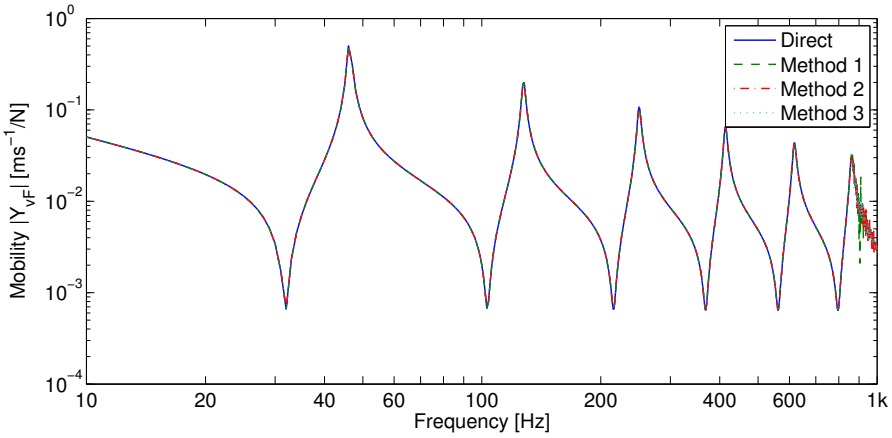

Figure 6.7: Using translational DOFs at 2 response and 2 contact positions.

positions a_1 and a_2, Equation (5.53) has the following form:

$$\begin{pmatrix} \frac{v_{S,c1}}{F_{S,c1}} & \frac{v_{S,c1}}{F_{S,c2}} \\ \frac{v_{S,c2}}{F_{S,c1}} & \frac{v_{S,c2}}{F_{S,c2}} \end{pmatrix} = \begin{pmatrix} \frac{v_{R,c1}}{F_{R,c1}} & \frac{v_{R,c1}}{F_{R,c2}} \\ \frac{v_{R,c2}}{F_{R,c1}} & \frac{v_{R,c2}}{F_{R,c2}} \end{pmatrix} \left[\begin{pmatrix} \frac{v_{R,c1}}{F_{R,a1}} & \frac{v_{R,c1}}{F_{R,a2}} \\ \frac{v_{R,c2}}{F_{R,a1}} & \frac{v_{R,c2}}{F_{R,a2}} \end{pmatrix}^T - \begin{pmatrix} \frac{v_{C,c1}}{F_{C,a1}} & \frac{v_{C,c1}}{F_{C,a2}} \\ \frac{v_{C,c2}}{F_{C,a1}} & \frac{v_{C,c2}}{F_{C,a2}} \end{pmatrix}^T \right]^{-1} \begin{pmatrix} \frac{v_{C,c1}}{F_{C,a1}} & \frac{v_{C,c1}}{F_{C,a2}} \\ \frac{v_{C,c2}}{F_{C,a1}} & \frac{v_{C,c2}}{F_{C,a2}} \end{pmatrix}^T .$$

Figure 6.7 shows the result of the calculation. The source mobility can once again be determined correctly with all three methods, using translational DOFs only. This is of significant practical advantage, since mobilities involving rotational motion are not required. Table 6.1 gives an overview of all simulations performed in this section, and specifies the locations of contact and response positions.

F/M	**Contacts c**	**Responses a**	**Responses d**	**M1**	**M2**	**M3**
F & M	$c = 2.0\,\mathrm{m}$	$a = 1.80\,\mathrm{m}$	$d = 0.80\,\mathrm{m}$	✓	✓	✓
F only	$c = 2.0\,\mathrm{m}$	$a = 1.80\,\mathrm{m}$	$d = 0.80\,\mathrm{m}$	–	–	–
F only	$c = 2.0\,\mathrm{m}$	$a_1 = 0.05\,\mathrm{m}$ $a_2 = 1.80\,\mathrm{m}$	$d_1 = 0.45\,\mathrm{m}$ $d_2 = 0.80\,\mathrm{m}$	–	✓	✓
F only	$c_1 = 1.99\,\mathrm{m}$ $c_2 = 2.00\,\mathrm{m}$	$a_1 = 0.05\,\mathrm{m}$ $a_2 = 1.80\,\mathrm{m}$	$d_1 = 0.45\,\mathrm{m}$ $d_2 = 0.80\,\mathrm{m}$	✓	✓	✓

Table 6.1: Overview of simulations investigating the effect of neglecting DOFs.

6.3.2 Effect of uncertainties in measurement position

In measurement, the location of excitation and response positions may not be exactly reproducible. Small changes in the positioning of accelerometers or force transducers may occur. For a beam, this results in a shift in the anti-resonances of the mobilities. The location of the resonances is not affected. The consequences of these shifts depend on damping, frequency, and on the degree of positioning uncertainty.

A Monte-Carlo simulation was performed with the coupled beam model, to investigate the influence of positioning uncertainties on the determined source

beam mobility. It was assumed that accelerometers are not moved once they are attached to the structure. Hence, the positioning error is constant for each mobility during one set of measurements. The excitation position, on the other hand, is altered for each mobility measurement. Therefore, the positioning error of the force location is different for each mobility.

The uncertainty in force and velocity positions was implemented as a normal distribution, with zero mean and a standard deviation of 1 mm. The number of simulations was $n = 100$. Results for all three methods are shown in Figure 6.8. The following discussion is based on qualitative observations made by visual inspection, rather than on error values in dB. This is because it is not immediately obvious how errors in the coupled beam model could be used to predict errors in a measurement involving different source and receiver structures. However, the general trends in the simulations give an indication of the robustness of the three methods.

Although measurement with a positioning accuracy of 1 mm would be considered good, the effects of positioning uncertainties in Figure 6.8 are dramatic. All three methods show significant deviations from the exact solution, in particular at higher frequencies. The largest deviations at low frequencies occur at 22 Hz and 62 Hz, coinciding with the receiver beam's first two eigenfrequencies. Method 1 copes best with uncertainties in force and response positioning, while Method 3 displays extremely large errors at high frequencies. It is interesting to note that for Method 1 and Method 2, the anti-resonances of the source beam mobility are less affected than the resonances.

6.3.3 Effect of phase errors

While it is possible to perfectly determine magnitude and phase of mobility data in simulations, uncertainties in accelerometer responses cannot always be excluded in experiment. State-of-the-art accelerometers have a phase response accuracy of 1° or better (cf. for example [1]). To investigate the effect of phase errors, the phase of the exact beam mobilities was modified before the indirect calculation of the source mobilities. A random phase difference (normally distributed with zero mean and standard deviation of 1°) was added to the existing phase data. The magnitudes were not altered. As in Section 6.3.2, the number of simulations was $n = 100$.

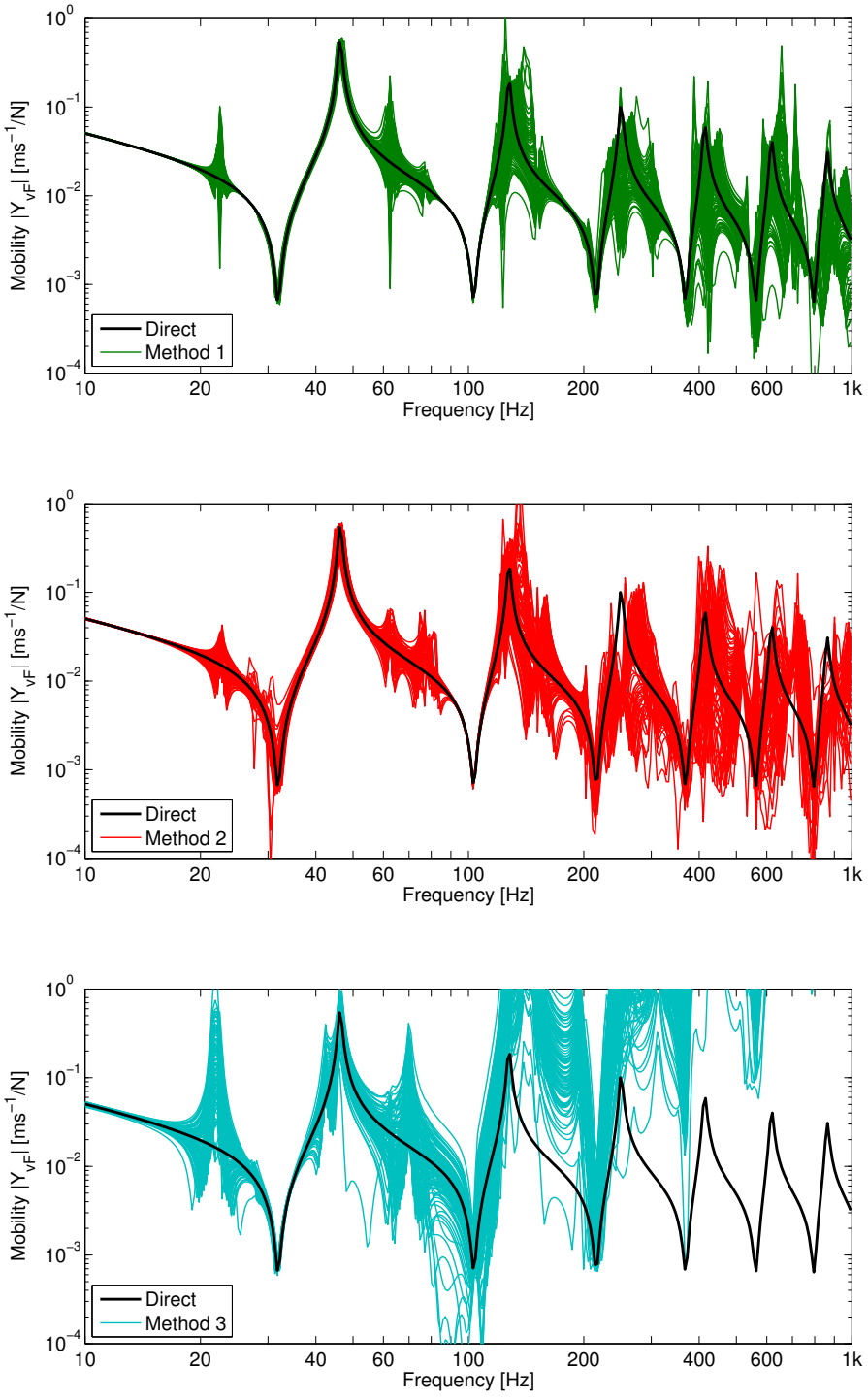

Figure 6.8: Effects of sensor positioning uncertainties.

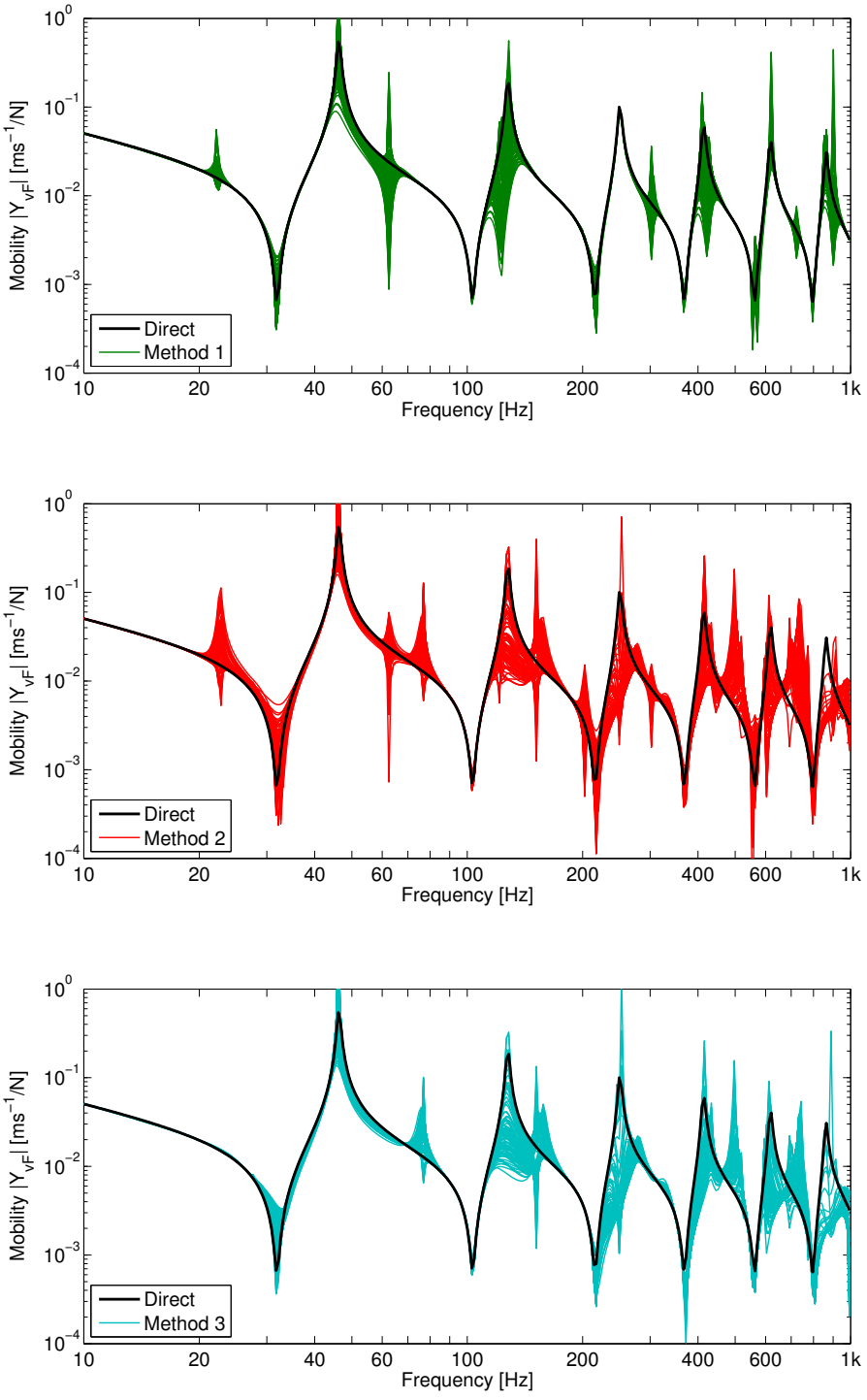

Figure 6.9: Effects of phase shifts in individual mobilities.

Figure 6.9 shows that all three methods are affected, but generally the trend of the direct calculation is traced. Once again the largest deviations are observed at the resonance frequencies of the receiver beam. Figure 6.9 highlights the importance of accurate phase data in measured mobilities. Moderate errors may be expected in the indirectly determined mobilities, in particular around the resonance frequencies of the receiver structure. However, compared to the errors encountered in Section 6.3.2, phase errors are less important.

6.3.4 Effect of frequency resolution

Most building acoustics measurements and calculations use frequency-band averages instead of narrowband spectra. For example, the reception plate method, discussed in Chapter 8, requires the measurement of mobilities in third-octave bands. Some building acoustics analyzers give both magnitude and phase data in frequency bands, and it is possible to calculate average magnitude and phase from narrowband spectra. However, the appropriateness of frequency-averaged phase in particular depends strongly on the structure under test, mainly on how slowly the phase changes with frequency, and if positive and negative values occur within the same frequency band.

To investigate whether Equations (5.53), (5.54) and (5.55) can be used in frequency bands, the calculated narrowband mobilities were converted to third-octave bands. The indirect calculation of source mobility was then performed in third-octave bands. The results in Figure 6.10 confirm that complex narrowband data (including accurate phase data) is required for all three methods. Only after the narrowband calculations have been performed may the results be converted to frequency band values.

A similar question concerns the importance of the frequency resolution of the narrowband mobilities. Does changing the frequency resolution, for example from 1 Hz to 2 Hz, improve or worsen the results? For inverse force determination, Gajdatsy [54] suggests that decreasing the resolution can have a positive effect on the accuracy of the estimated forces, provided that all essential structural information is contained in the FRFs. For the indirect source mobility determination, the same may be true. For simulations, however, decreasing the frequency resolution does not have a measurable effect, as long as all essential structural information is represented in the FRFs.

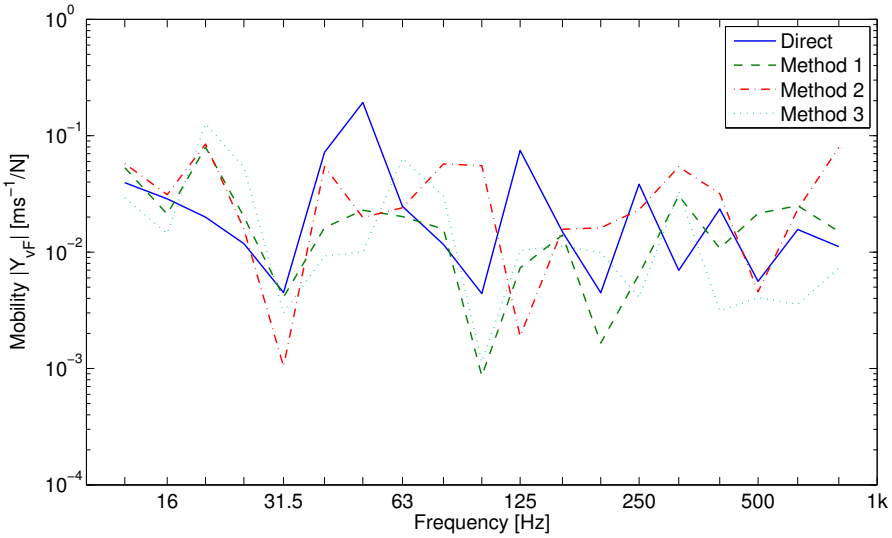

Figure 6.10: Effects of using frequency-averaged mobility data.

6.3.5 Effect of measurement noise

In experimental work, measurement noise often influences the quality of the acquired data. To investigate the effect of random noise on the indirect determination of mobility, the beam simulations were artificially contaminated.

A noise model [139], illustrated in Figure 6.11, was used to simulate measurement noise in the FRFs. The following procedure was used to estimate the corrupted FRFs:

1. The exact FRFs were calculated using the analytical solutions given in Appendix B. A unit force input was assumed, and an exact velocity response obtained.

2. A Gaussian distribution was used to generate random measurement noise:

$$N_0(\omega) = N_{nd} e^{j2\pi N_{ud}} \tag{6.6}$$

Here, N_{nd} is a normally distributed random value with zero mean and a standard deviation of unity. N_{ud} is a uniformly distributed random value between 0 and 1. The random measurement noise for the velocity signals

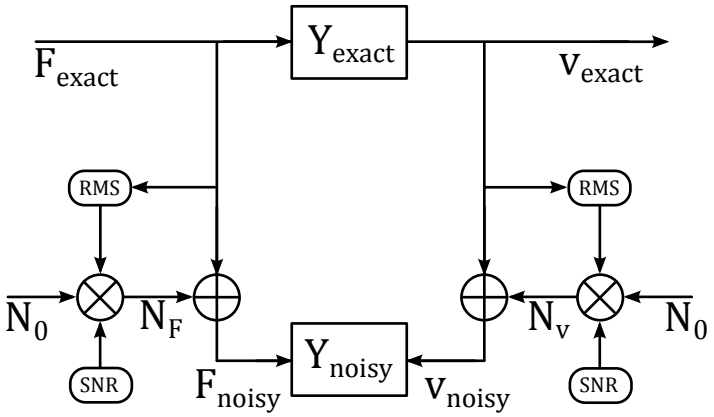

Figure 6.11: Model used for the simulation of noise in the mobility estimates.

was multiplied by a factor of $1/\omega$, to account for the conversion from acceleration to velocity.

3. The average values of the exact signals (unit force F or velocity response v) were calculated. Then the average values of the noise signals ($N_{0,F}$ or $N_{0,v}$) were calculated. From these values, the noise level was adjusted to meet a predefined signal-to-noise ratio (SNR in dB, see Table 6.2):

$$N_F(\omega) = N_{0,F}(\omega)\frac{F_{\text{av}}}{N_{\text{av}}10^{\text{SNR}/20}}$$
$$N_v(\omega) = N_{0,v}(\omega)\frac{v_{\text{av}}}{N_{\text{av}}10^{\text{SNR}/20}}$$

The level-adjusted noise signals were then added to the exact unit force signal and the exact velocity responses.

4. The cross-spectrum S_{Fv} between force and velocity and the force power spectrum S_{FF} [26] were calculated according to

$$S_{Fv}(\omega) = \frac{1}{n_{av}}\sum_{k=1}^{n_{av}} F_k^*(\omega)v_k(\omega), \tag{6.7}$$

$$S_{FF}(\omega) = \frac{1}{n_{av}}\sum_{k=1}^{n_{av}} F_k^*(\omega)F_k(\omega). \tag{6.8}$$

The number of averages used in the simulations was $n_{av} = 100$.

5. Finally, the contaminated FRFs were obtained using the H_1 estimator:

$$Y(\omega) = \frac{S_{Fv}(\omega)}{S_{FF}(\omega)}. \tag{6.9}$$

The coherence γ^2 indicates the degree of dependence between force input and velocity response. It is calculated as

$$\gamma^2(\omega) = \frac{|S_{Fv}(\omega)|^2}{S_{FF}(\omega)S_{vv}(\omega)}. \tag{6.10}$$

The coherence has values between 0 and 1. The greater the influence of noise, the lower the coherence. The coherence may be used to calculate the frequency-dependent SNR [104]:

$$\mathrm{SNR}(\omega) = \frac{\gamma^2(\omega)}{1-\gamma^2(\omega)} \tag{6.11}$$

To decide on suitable signal-to-noise-ratios, the following considerations were made. First, the measurement noise in the force signals was assumed negligible. The measurement noise from accelerometers is generally more influential, due to modal behaviour of the receiver structure. Secondly, as can be seen from Figure 6.4, the infinite beam mobility (v/F) decreases with $\sqrt{\omega}$. Measurement noise in the velocity signals decreases with ω. Therefore, the SNR will be smaller for low frequencies. For plates, the situation is similar. While the infinite plate mobility is frequency-invariant, the measurement noise decreases with frequency. Therefore, SNR will mainly be an issue at low frequencies.

Three combinations of force and velocity noise levels were considered, summarized in Table 6.2. Figure 6.12 shows the velocity noise levels and a typical beam response to a unit force input. The decrease of the background noise level with frequency is clearly visible.

Figure 6.13 shows an example of an exact and a corrupted FRF, for the case of low and moderate SNR. Figure 6.14 and Figure 6.15 show the corresponding coherence and SNR, respectively. From Figure 6.13, the differences between the two FRFs are almost undetectable, both in magnitude and phase. Examination of the coherence reveals the influence of noise at the anti-resonances. The resonances are less affected. Both the coherence and the SNR improve with

Name	SNR Force	SNR Velocity
Low SNR	80 dB	20 dB
Moderate SNR	80 dB	40 dB
High SNR	80 dB	60 dB

Table 6.2: Predefined noise levels used in the simulations.

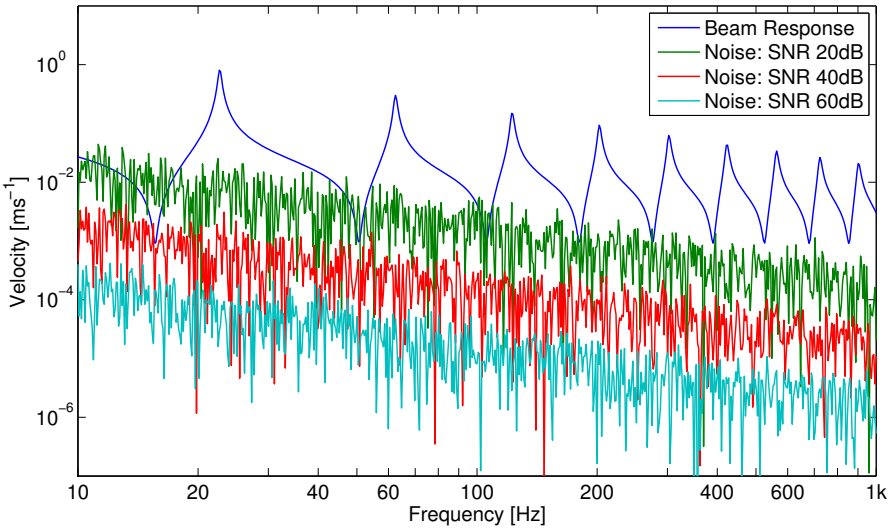

Figure 6.12: Typical beam velocity response to a unit force input, together with background noise set to levels as in Table 6.2.

frequency. Again, random noise is expected to cause errors mainly at low frequencies.

Figures 6.16, 6.17, and 6.18 show results of the simulations, with the noise levels set as in Table 6.2. Method 1 yields good agreement for the highest SNR (Figure 6.16 top). For a moderate SNR (Figure 6.16 centre), deviations occur mainly at the source beam resonances, and at 22 Hz and 62 Hz, the receiver beam resonances. For a low SNR (Figure 6.16 bottom), Method 1 still traces the general trend of the source beam mobility, though with larger random errors. The anti-resonances of the source beam mobility are least affected by random noise. There are two explanations for this. Firstly, the anti-resonance frequencies of the source beam mobility are those frequencies where the difference between source and receiver mobility is large, cf. Figure 6.3. Therefore,

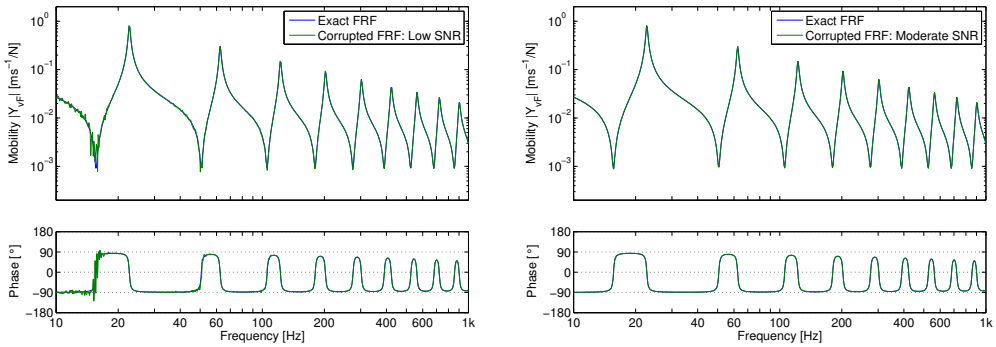

Figure 6.13: Example of exact and corrupted FRF (low and moderate SNR).

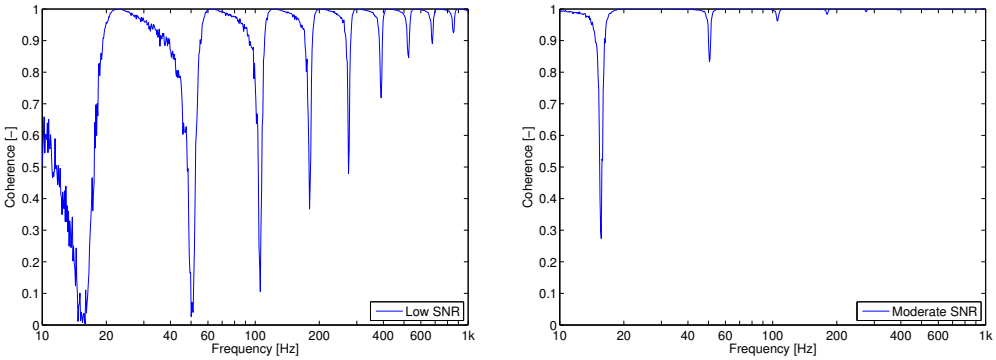

Figure 6.14: Coherence of corrupted FRFs displayed in Figure 6.13.

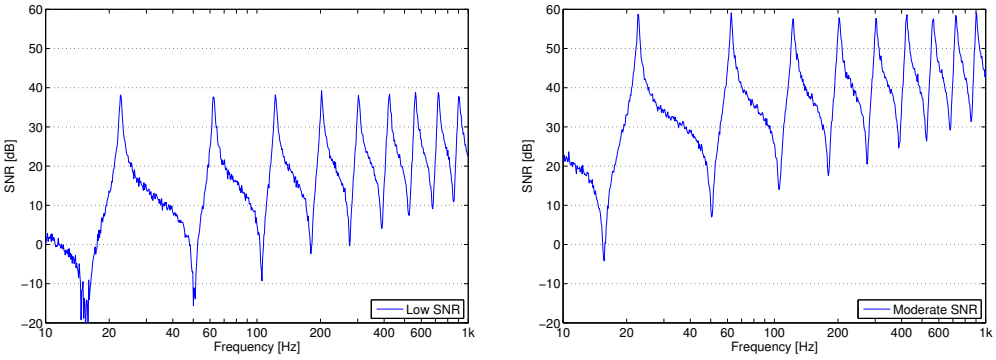

Figure 6.15: Signal-to-noise-ratio of corrupted FRFs displayed in Figure 6.13.

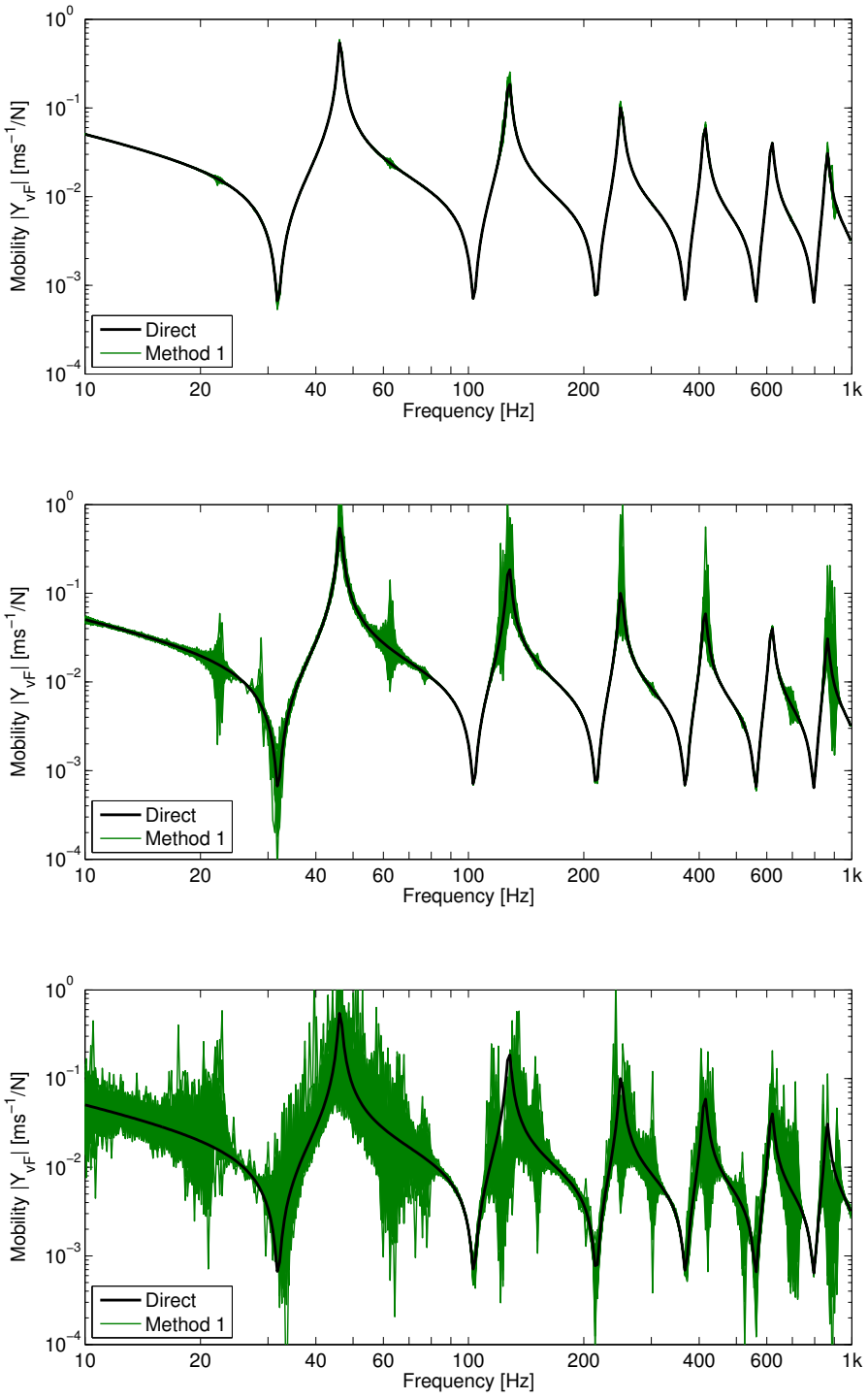

Figure 6.16: Simulations with random noise, showing the results of Method 1. Top: High SNR. Middle: Moderate SNR. Bottom: Low SNR.

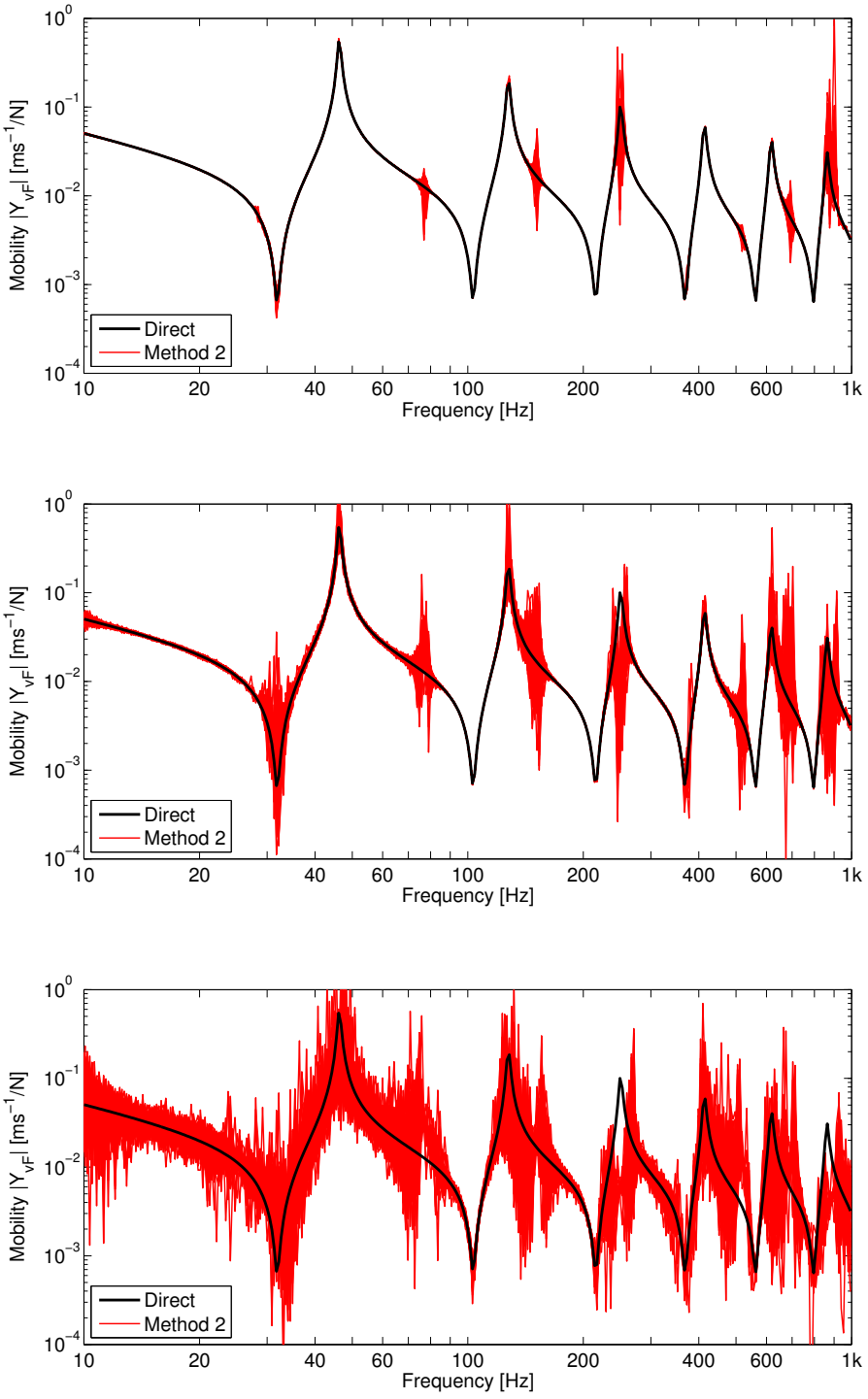

Figure 6.17: Simulations with random noise, showing the results of Method 2. Top: High SNR. Middle: Moderate SNR. Bottom: Low SNR.

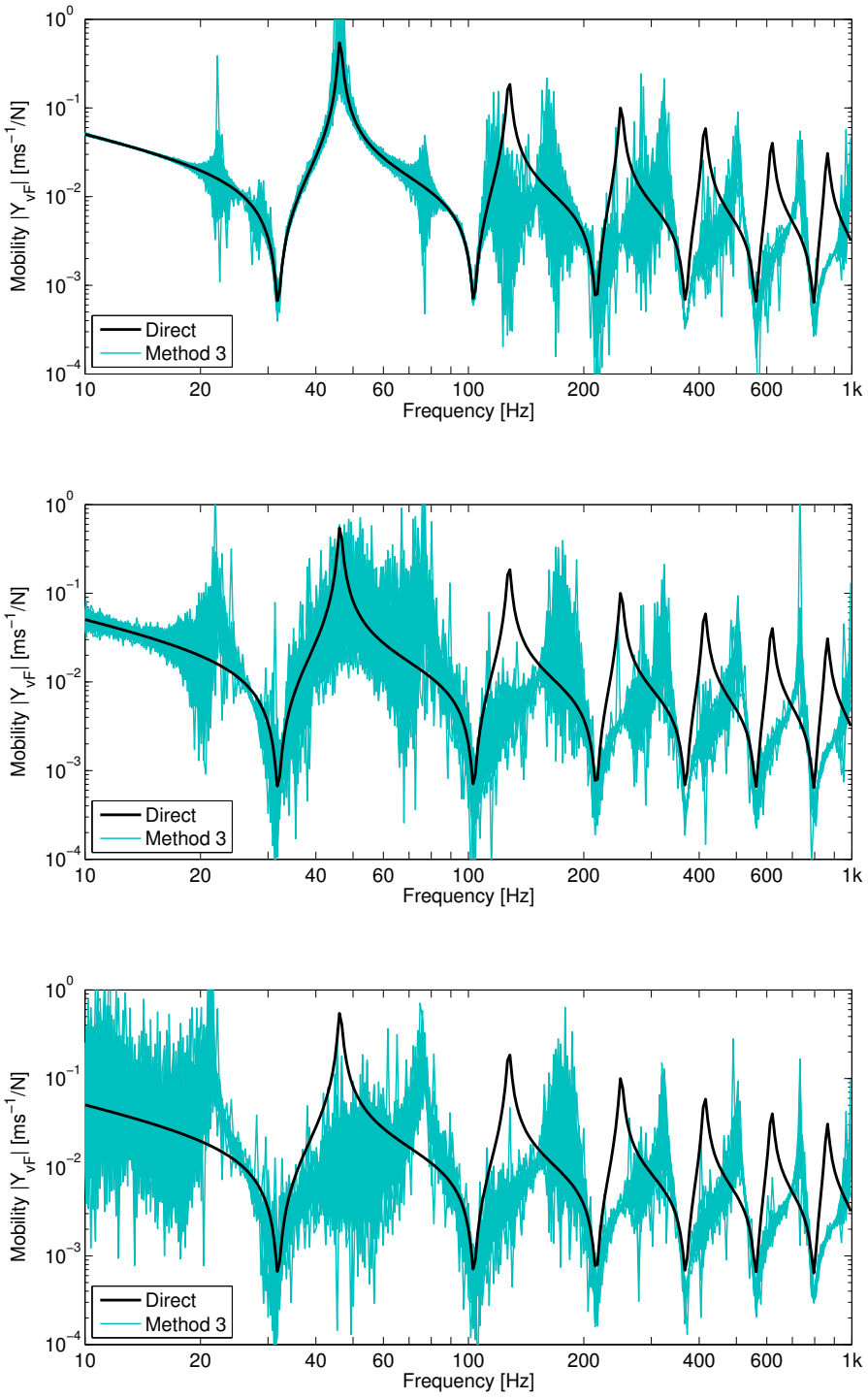

Figure 6.18: Simulations with random noise, showing the results of Method 3. Top: High SNR. Middle: Moderate SNR. Bottom: Low SNR.

the difference between coupled and uncoupled receiver beam mobilities is large at these frequencies, and the inversion of the difference term in Equation (5.53) produces reliable results. Secondly, random noise most severely affects the anti-resonances of the simulated mobilities of coupled and uncoupled receiver, while the resonances of these mobilities are not affected. Through the inversion operation, anti-resonances become resonances, and vice versa. Therefore, the resonances of the indirectly determined source mobilities are most affected by random noise in the input data.

The results for Method 2 are similar to but not as good as those of Method 1. For a high SNR (Figure 6.17 top), some deviations occur at 76 Hz, 150 Hz, and 250 Hz. For a moderate SNR (Figure 6.17 centre), these deviations increase, and additional errors at the first source beam anti-resonance and at higher frequencies are visible. For a low SNR (Figure 6.17 bottom), results are worse than for Method 1, though the general trend of the source beam mobility is still traced. The third source beam resonance at 250 Hz is no longer identified reliably.

Method 3 performs considerably worse in the presence of random noise than Methods 1 and 2. Even for the highest SNR (Figure 6.18 top), the method fails above the second anti-resonance frequency at 100 Hz. Below 100 Hz, some deviations occur at 22 Hz and 76 Hz. For moderate and low SNR, errors at low frequencies increase, but the (non-)agreement at higher frequencies remains constant.

The results from Figures 6.16, 6.17, and 6.18 highlight the sensitivity of the three methods to random measurement noise in the mobility data. Method 3 in particular is highly sensitive to even small errors caused by noise. Methods 1 and 2 are more robust. Errors may be expected for moderate or low signal-to-noise ratios, in particular at the resonance frequencies of the source and at the resonance frequencies of the receiver structure.

6.4 Summary

Analytical and numerical models of rods and beams were used to investigate the three methods for the indirect determination of source mobility. The analytical

treatment of rod mobilities verified the applicability of the methods for SDOF systems.

Using numerical solutions for beam mobilities, the validity of the three methods could also be confirmed for a MDOF system. All three methods gave the correct result for a coupled beam system, when all important degrees of freedom were included in the matrix inversion. When important degrees of freedom were neglected, as is often done in practice, all three methods failed. However, additional translational mobilities could compensate for missing rotational mobilities. The rank of the matrix to be inverted had to be at least equal to the number of important degrees of freedom.

The robustness of the three methods was examined next. It was shown that the calculations are highly sensitive to uncertainties often encountered in practical measurement, for example background noise or mismatched phase responses of accelerometers. Positioning uncertainties in particular yielded large errors, due to shifts in the anti-resonances. Method 1 performed best under adverse conditions, while Method 3 showed the highest sensitivity to typical errors.

In Chapter 7, the methods are investigated experimentally.

7 Experimental Validation of Indirect Methods to Obtain Source Mobilities

7.1 Introduction

Three methods were described in Chapter 5 for the indirect determination of source mobilities. Numerical simulations in Chapter 6 confirmed the validity of the three formulations, but also highlighted challenges that may be expected in a practical implementation of these methods.

In this chapter, Methods 1 and 2 were investigated experimentally. Method 3 was not investigated further, since it does not promise any advantage over the other two. Case studies are described, with idealized and representative sources. Both single degree of freedom (SDOF) and multiple degree of freedom (MDOF) cases are considered.

Resiliently supported free plates were used as receiver structures. A variety of sources can be placed on a plate, and mobility measurements are relatively straightforward. A successful implementation of the described methods on a plate receiver would be of significant benefit, especially with respect to building acoustics: most building elements are plate-like.

7.2 Single mass on plate

In the first experimental case study, single lumped masses were considered as sources, and a plate was used as receiver structure. As the connection between source and receiver is only one small contact, this approximates a SDOF system. Only the normal force component was considered, while moments were assumed to be negligible.

7.2.1 Measurement setup

Steel blocks of varying mass were placed on a free aluminium plate of size 2.12 m × 1.50 m × 20 mm, the same plate that was used in Chapter 4. Figure 7.1 shows one of the blocks on the plate. A force transducer (BK 8200) was used as connecting element (shown in Figure 7.1 on the left), though the force was not measured. The insertion of the transducer served two purposes. First, the contact area between transducer and plate was reduced to 16 mm in diameter, approximating a point contact. Secondly, the insertion of the transducer

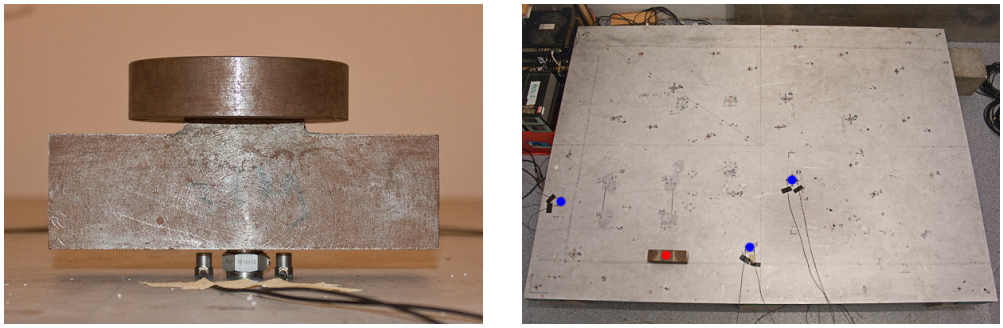

Figure 7.1: Measurement setup for single steel blocks.

allowed the attachment of two small accelerometers (BK 4393V) close to the contact, as shown in Figure 7.1. The force transducer was assumed to behave as mass-like element. It was screwed into the mass, and attached to the plate using beeswax. Four masses were installed, one at a time, to achieve a variety of source-receiver mobility ratios: 1.6 kg, 3.6 kg, 5.2 kg, and 7.5 kg.

Mobilities were measured using an impulse hammer with a plastic tip (BK 8202). The plastic tip ensured a sufficient excitation force on the plate up to 2 kHz. Signals above 2 kHz were not evaluated. For the measurement of point mobilities, two matched accelerometers (BK 4393V) left and right of the point of excitation were used. For the measurement of the coupled transfer mobilities $\mathbf{Y}_{\mathbf{C,ca}}$, the plate was excited at positions a and the response measured at the contact c, using two matched accelerometers, as shown in Figure 7.1. Excitation force and response velocity were recorded as time signals (measurement time T = 1 s, sampling rate f_s = 16384 Hz) and then transformed into the frequency domain. The frequency resolution was 1 Hz. The mobilities were calculated as complex ratios of velocity and force (cf. Section 2.2.2). Each mobility was recorded as the average of three impacts, to limit errors due to misaligned hammer hits or transient background noise.

One contact position and three remote response positions were considered. Therefore, for Methods 1 and 2, the following quantities were recorded:

- $\mathbf{Y}_{\mathbf{R,cc}}$ (1×1), one mobility;
- $\mathbf{Y}_{\mathbf{R,ca}}$ (1×3), three mobilities;
- $\mathbf{Y}_{\mathbf{R,aa}}$ (3×3), nine mobilities;
- $\mathbf{Y}_{\mathbf{C,ca}}$ (1×3), three mobilities for each mass;
- $\mathbf{Y}_{\mathbf{C,aa}}$ (3×3), nine mobilities for each mass.

The three uncoupled plate mobilities were measured once, as they remain constant. The coupled mobilities $\mathbf{Y_{C,ca}}$ and $\mathbf{Y_{C,aa}}$ were measured for each mass.

Figure 7.2 shows the theoretical mass mobilities and the measured receiver mobility at the contact position. The idealized mass mobilities decrease by a factor of ω with increasing frequency. The plate mobility displays strong modal behaviour and fluctuates about the infinite plate mobility. The *infinite plate mobility* is the mobility of a plate with same material properties and thickness, but infinite dimensions [38]:

$$Y_\infty = \frac{1}{8\sqrt{Bm''}} \tag{7.1}$$

Here, m'' is the mass per area, and B is the bending stiffness of the plate:

$$B = \frac{Eh^3}{12(1-\nu^2)} \tag{7.2}$$

E is Young's modulus of elasticity, h is the thickness, and ν is Poisson's ratio. With $\rho = 2700\,\mathrm{kg/m^3}$, E = 70 GPa, h = 0.02 m, and $\nu = 0.33$ (cf. Section 4.3), the value of the infinite plate mobility was calculated as $Y_\infty = 7.4{\cdot}10^{-5}\mathrm{ms^{-1}/N}$.

The modal behaviour of the plate results in variations in the ratio of source and receiver mobilities, with the following trends: The mass mobilities are higher than the plate mobility below 100 Hz, of the same order of magnitude between 100 Hz and 600 Hz, and lower at frequencies above 600 Hz. The exception is the lightest mass (1.6 kg), the mobility of which is higher than the plate mobility up to 300 Hz, and is of the same order of magnitude above 300 Hz.

7.2.2 Effects of over-determination and regularization

In the evaluation, one contact position and up to three response positions were considered. Since only one degree of freedom is involved at the source-receiver interface, one response suffices for the identification of the source mobility. For Method 1, the use of two additional response positions modifies the term $(\mathbf{Y^T_{R,ca}} - \mathbf{Y^T_{C,ca}})$ to become a vector of size 3×1. The two additional signals over-determine the system of linear equations, and the vector can be inverted using a least-square solution. No matrix inversion is required.

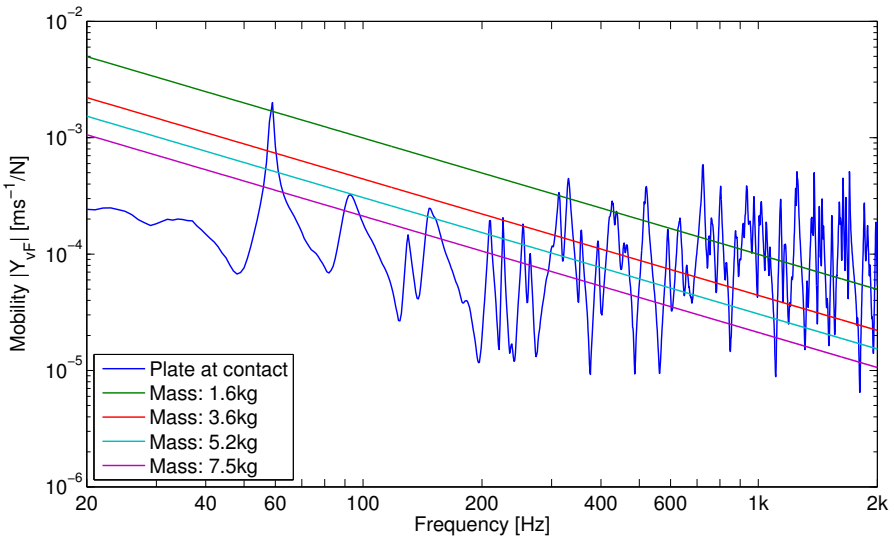

Figure 7.2: Theoretical mass mobilities and measured plate point mobility.

For Method 2, the use of two additional responses alters the inverse term more. The term $(\mathbf{Y_{R,aa}} - \mathbf{Y_{C,aa}})$ becomes a matrix of size 3×3, and therefore a matrix inversion is required. Figures 7.3, 7.4, and 7.5 illustrate the change in the results for both methods, when considering more than the necessary single response position. At this point, only the results for the mass of 5.2 kg are shown. The other results are presented and discussed in Section 7.2.3.

- Figure 7.3 shows the result for one response position: both methods yield similar results, with similar deviations from the theoretical mass mobility. The deviations at high frequencies are clearly indicated in the phase. A detailed discussion of the deviations follows in Section 7.2.3.

- Figure 7.4 shows the result for three response positions and no regularization. For Method 1, the use of three response positions generally improves the agreement with the theoretical mass mobility. For Method 2, two effects can be observed. For low frequencies, the agreement improves, and larger deviations are eliminated. Above 200 Hz, however, results are more variable, both in magnitude and phase. This is due to the matrix inversion, and the resulting amplification of random errors. Figure 7.6 shows the condition number of the 3×3 matrix $(\mathbf{Y_{R,aa}} - \mathbf{Y_{C,aa}})$, with values exceeding 1000, indicating an ill-conditioned matrix.

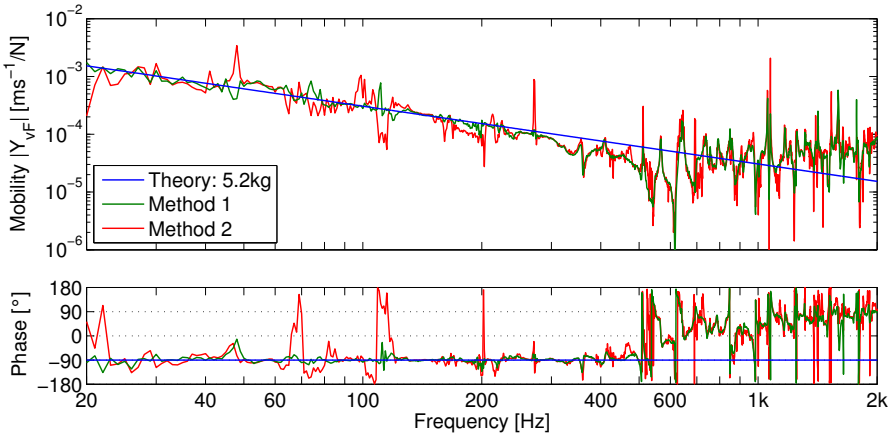

Figure 7.3: Indirectly determined mass mobility using one response position.

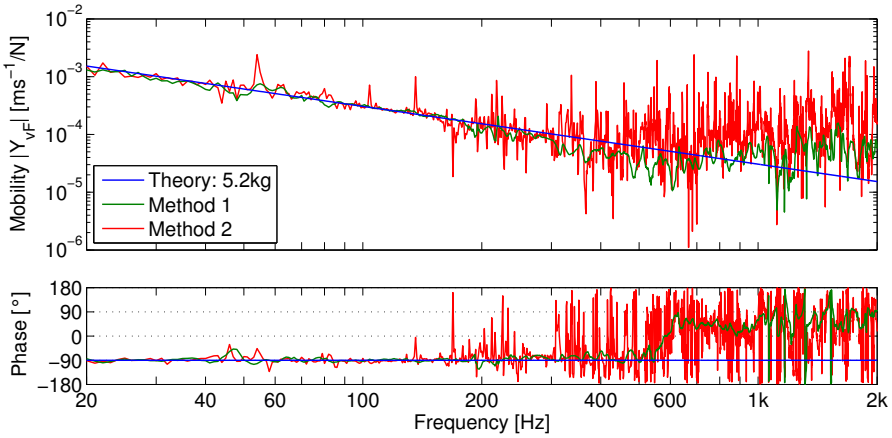

Figure 7.4: Indirectly determined mass mobility using three response positions.

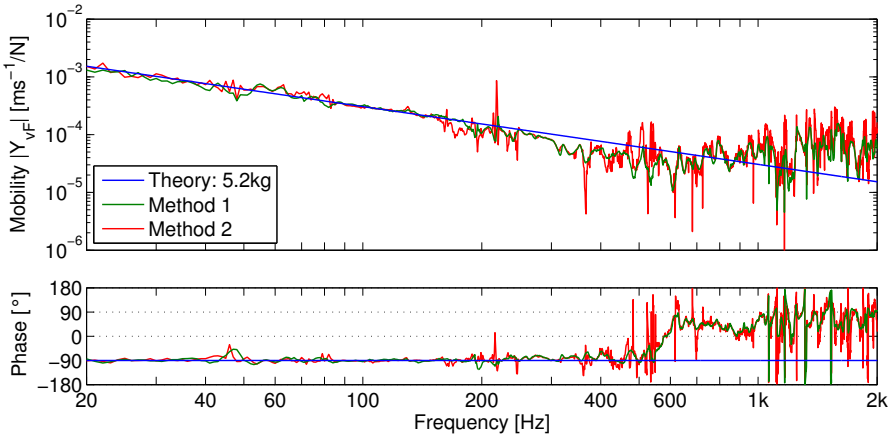

Figure 7.5: Indirectly determined mass mobility using three response positions and SVR (relative threshold of 2% of the largest SV).

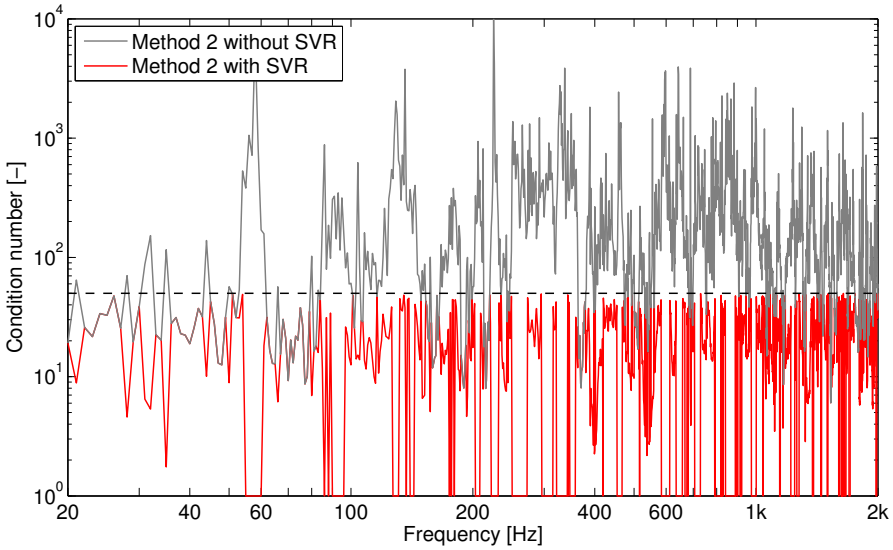

Figure 7.6: Condition number for $(\mathbf{Y}_{\mathbf{R,aa}} - \mathbf{Y}_{\mathbf{C,aa}})$, for three responses.

- Figure 7.5 shows the result when using three response positions and applying SVR with a relative threshold of 2% of the largest singular value. Compared with Figure 7.4, results for Method 1 do not change. This is because a matrix inversion is not involved, and only one singular value exists. Method 2, on the other hand, improves significantly. Since only one degree of freedom is involved at the source-receiver interface, up to two of the three singular values can be rejected. In this case, singular value rejection has only beneficial effects. The determined mobility is now much "cleaner", both in magnitude and phase. Even compared with Figure 7.3, the variability of the result decreases. It can therefore be beneficial to use more than the required single response position, even if this leads to a matrix inversion. Figure 7.6 includes the condition number for the regularized case, with an upper limit of 50 (cf. Section 2.4.2).

7.2.3 Comparison with idealized mass mobilities

In the following comparison and discussion, three response positions were used, and SVR with a relative threshold of 2% was applied. Figure 7.7 shows the theoretical and the indirectly determined mass mobilities for the three other masses, calculated according to Equations (5.53) and (5.54).

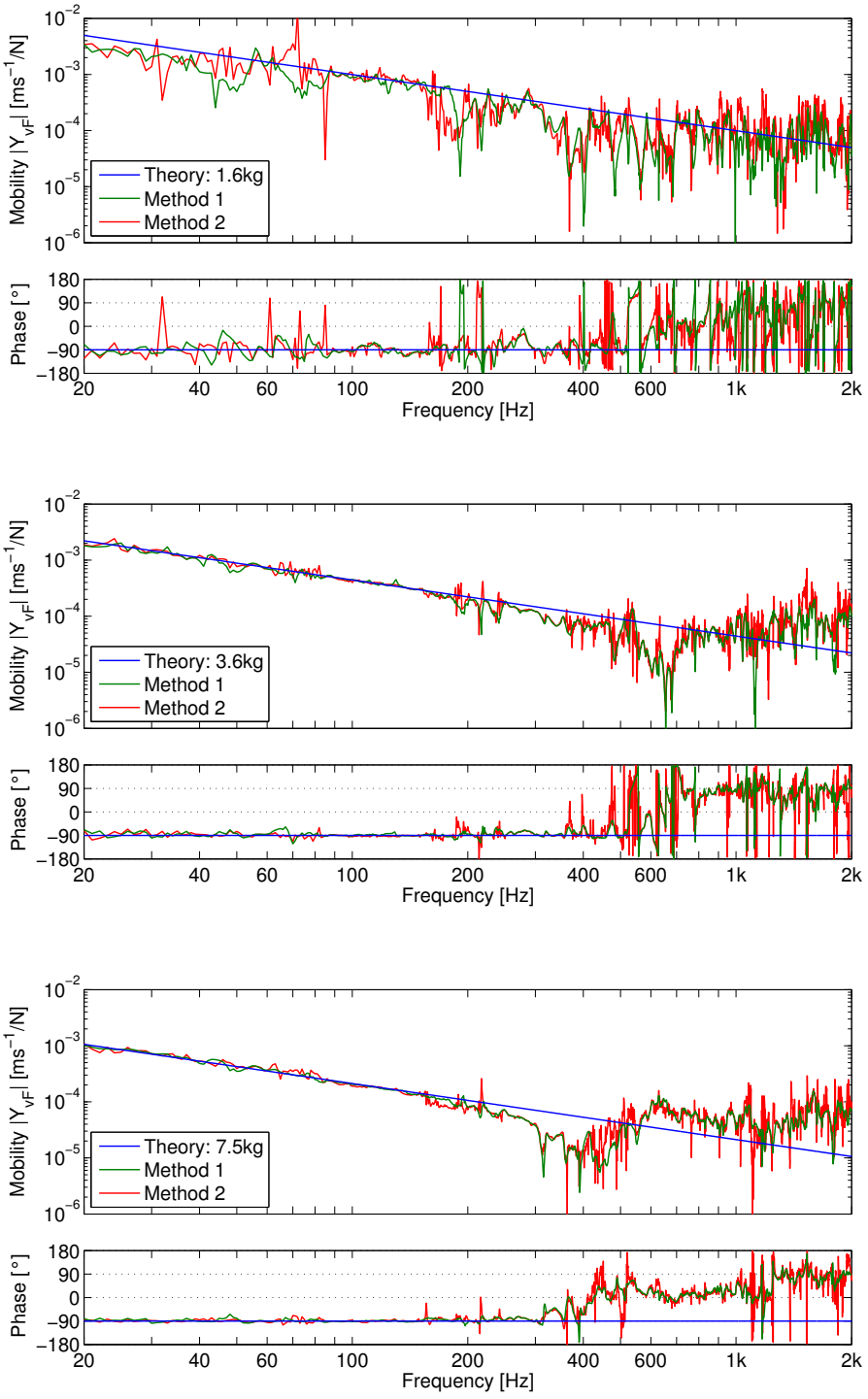

Figure 7.7: Indirectly determined mass mobilities using three response positions and SVR with a relative threshold of 2%.

m	f_0	k
1.6 kg	808 Hz	$4.1 \cdot 10^7$ N/m
3.6 kg	656 Hz	$6.1 \cdot 10^7$ N/m
5.2 kg	585 Hz	$7.0 \cdot 10^7$ N/m
7.5 kg	480 Hz	$6.8 \cdot 10^7$ N/m

Table 7.1: Spring stiffness calculated from mobility data in Figure 7.7.

Method 1 and Method 2 yield similar results. Therefore, in the following discussion they are not discriminated. For all masses, except the lightest (1.6 kg), the trends are the same. At low frequencies, the estimated source mobilities show good agreement with the theoretical values, both in magnitude and phase. The deviations are in the order of ±3 dB[1] up to about 200 Hz. At 200 Hz, a small ripple in the indirect results yields deviations up to ±10 dB. Above 200 Hz, there are systematic deviations. At high frequencies, the estimated curves are dominated by arbitrary, highly variable behaviour, and the source mobilities are over-estimated by up to 20 dB. The transition region, starting at about 250 Hz, shows a prominent dip (except for the 5.2 kg mass), and crosses over into the high frequency region at about 500 Hz for the heaviest mass (7.5 kg), and at about 800 Hz for the two other masses. The deviations in the transition region are up to ±15 dB. The phase in particular shows that there are systematic deviations between the estimates and the ideal mobilities at higher frequencies. It shifts from mass-like behaviour (−90°) to spring-like behaviour (+90°). The approximate spring stiffness was calculated from the measured anti-resonance frequency f_0 and the corresponding mass m: $k = (2\pi f_0)^2 m$. The values for k, obtained for the four cases, are given in Table 7.1. The mobility estimate for the lightest mass (1.6 kg) shows more random behaviour, and larger deviations from the theoretical values (up to ±10 dB below 200 Hz, and up to ±20 dB above 200 Hz).

7.2.4 Discussion of observed deviations

To better understand why the accuracy/reliability of the results varies, a comparison was made between the low frequency region and the high frequency

[1] Mobility error values given in dB in this thesis are calculated as $20 \log |Y_1|/|Y_0|$, where $|Y_1|$ is the magnitude of mobility Y_1, and $|Y_0|$ is the magnitude of the reference mobility Y_0.

region. The underlying question was: What is different between the former, where the agreement is generally good, and the latter, where the results deviate from the theoretical values? Several differences/possible explanations for the deviations were considered:

1. **Mobility of steel blocks.** It was assumed that the steel blocks with attached force transducer behave as lumped masses. This may not be true, in particular at high frequencies. Causes could be longitudinal waves in the material, rocking motion of the blocks due to non-rigid contact conditions, or non-mass-like behaviour of the force transducer. The phase change in the indirectly determined mobilities (Figure 7.7) indicates a mass-spring system. This issue was addressed by directly measuring the mobility of mass with force transducer, see Section 7.3.1. The problem of non-rigid contact conditions between source and receiver was addressed by screwing the force transducer into the plate, see Section 7.3.2.

2. **Source-receiver mobility ratio.** The ratio between source and receiver point mobilities is different between low and high frequencies, see Figure 7.2. Consider the 5.2 kg mass. At low frequencies, the source point mobility is higher than the receiver point mobility. The cross-over region begins at around 100 Hz. Above 600 Hz, the source point mobility is lower than the receiver point mobility. This suggests that indirect mobility determination works best if the source mobility is higher than or equal to the receiver mobility. However, the results for the lightest mass (1.6 kg) only partly support this suggestion. For the lightest mass, the source point mobility is higher than the receiver point mobility up to 600 Hz, but the indirectly determined mass mobility does not agree well with the theoretical values even below this limit.

3. **Data quality.** As shown in Section 6.3.5, background noise can significantly influence results, especially when a matrix inversion is involved. However, it should be more influential at low frequencies, as the background noise level of the velocity signals decreases with increased frequency (by a factor of ω). Since results are good at low frequencies, background noise does not seem to contribute significantly to the errors. Systematic errors in the data, on the other hand, may degrade the results. Systematic errors include misalignment of the impulsive excitation force (both in location and direction), and misalignment of the response

accelerometers, in particular if they are moved around between measurements. This issue was addressed by using a shaker, and by not moving accelerometers between measurements, see Section 7.3.2.

4. **Variable contact conditions.** When applying a load to a structure, the contact area of the load can locally deform the receiver. This is especially the case when the load is a hammer hit, where the pressure at the hammer indenter can become large. In these cases, the surface of the receiver structure may become spring-like at high frequencies. This is known as local stiffness effect [112]. The contact stiffness of the receiver plate can be calculated as [72]

$$k = \frac{2rE}{1-\nu^2}, \tag{7.3}$$

where r is the radius of the circular contact area, E is Young's modulus, and ν is Poisson's ratio. With r $\approx$ 1 mm, E = 70 GPa, and ν = 0.33, the contact stiffness is calculated as $k = 1.6 \cdot 10^8$ N/m. Comparing the mobility of a spring with this stiffness ($Y = j\omega/k$) with the infinite plate mobility of $7.4 \cdot 10^{-5}$ms^{-1}/N reveals that the two mobilities cross at 1900 Hz. Careful examination of point mobility measurement data does not indicate that the local stiffness effect is of importance in this study. The contact conditions may be of importance nevertheless. It was mentioned in Section 7.2.1 that the "source" is in contact with the plate connected with beeswax. This may lead to variable contact conditions. The slightly better agreement for heavier masses may be due to gravity compensating for variable contact conditions. This issue was addressed by screwing the force transducer rigidly into the plate in Section 7.3.

7.3 Single mass on plate - Modified and repeated measurement

In Section 7.2, measurements with steel blocks on force transducers attached to a 20 mm aluminium plate showed promising results at low frequencies, but also raised questions, in particular regarding the performance at high frequencies. Several possible explanations for the observed deviations were identified. In this study, these issues were investigated by modifying the measurement setup and

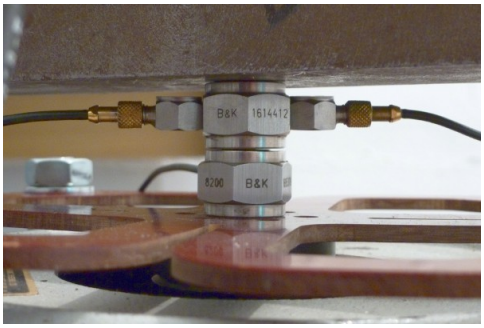

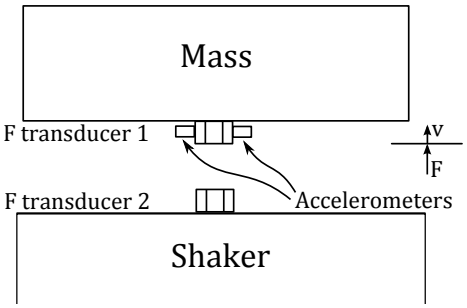

Figure 7.8: Test setup for direct measurement of source mobilities on a shaker.

repeating the measurement series. Several adjustments were made to the setup, explained in Section 7.3.2. The most important were the use of a shaker instead of an impulse hammer to obtain the mobilities, and the change to a more rigid connection between source and receiver. Furthermore, to verify whether the steel blocks on force transducers behave as pure masses, the source mobilities were measured directly.

7.3.1 Direct measurement of source mobilities

The mobilities of the masses with force transducer were measured directly. A large shaker (LDS 400 with support spider) was driven with pink noise (upper limiting frequency of 6.4 kHz), supplied by the BK Pulse analyzer. This allowed the evaluation of a wider frequency range than for the hammer measurements in Section 7.2. The force transducer, which formed part of the source, was rigidly screwed to the mass on one side, and rigidly screwed to a second force transducer on the other side. This second transducer measured the force exerted on the "source" by the shaker. The attachment of accelerometers at a suitable position was difficult, due to limited access. Two accelerometers (Birchall, SN 4305 and SN 4592) were glued to the casing of transducer 1. Figure 7.8 shows the measurement setup, and a schematic of the accelerometer positions. The mobilities were calculated from measured excitation and response signals, using the H_1 estimator. Hanning windows with an overlap of 66% were used, and the estimate was based on $n = 100$ averages. The frequency resolution was 1 Hz, the sampling rate 16384 Hz. These settings resulted in a measurement time of 34 s.

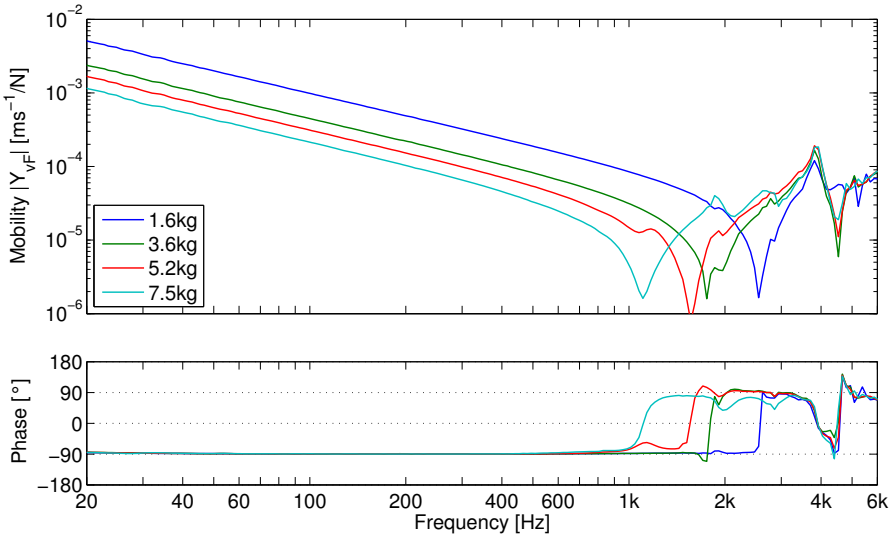

Figure 7.9: Directly measured point mobility of masses with force transducer.

Figure 7.9 shows the directly measured point mobilities of all four masses with attached force transducer. At low frequencies, the mobilities display mass-like behaviour: They are proportional to $1/\omega$, and show a phase of $-90°$. Between 1 kHz and 3 kHz, depending on the mass, the mobilities display a prominent anti-resonance. Above the anti-resonance, the "sources" behave as springs: The mobility magnitudes are proportional to ω, and the phase is $+90°$. Above 3 kHz, the mobilities deviate from pure spring-like behaviour, most likely due to the measurement setup.

Figure 7.9 reveals that the mass and the force transducer act as a mass-spring system. The approximate spring stiffness was calculated from the measured anti-resonance frequency f_0 and the corresponding mass m: $k = (2\pi f_0)^2 m$. The values for k, obtained for the four cases, are given in Table 7.2. They are in the same order of magnitude as, though slightly lower than, the value of $5.0 \cdot 10^8$ N/m quoted in the manual of the force transducer [2].

For the remainder of this section, the directly measured source mobilities displayed in Figure 7.9 are used as reference, for the evaluation and assessment of the indirect methods.

m	f_0	k
1.6 kg	2578 Hz	$4.2 \cdot 10^8$ N/m
3.6 kg	1800 Hz	$4.6 \cdot 10^8$ N/m
5.2 kg	1550 Hz	$4.9 \cdot 10^8$ N/m
7.5 kg	1100 Hz	$3.6 \cdot 10^8$ N/m

Table 7.2: Calculated spring stiffness of force transducer.

7.3.2 Adjusted measurement setup for indirect methods

The adjustments to the measurement setup are explained. First, the impulse hammer was replaced by a shaker. The shaker (Data Physics inertial shaker IV 40) was driven with pink noise (upper limiting frequency of 6.4 kHz), supplied by the BK Pulse analyzer. A force transducer recorded the excitation force. Where possible, the shaker, with force transducer, was screwed to the plate during measurement. In other cases, the shaker was attached to the plate using bees wax, relying on its own weight. To improve data quality and increase SNR, accelerometers with a higher sensitivity than in Section 7.2 were used at remote positions (BK 4371 with 1 pC/ms^{-2}). At the contact between source and receiver, again two small accelerometers were used (BK 4393V with 0.3 pC/ms^{-2}), due to space constraints.

Point and transfer mobilities were calculated from measured excitation and response signals, using the H_1 estimator. Hanning windows with an overlap of 66% were used, and the estimate was based on $n = 100$ averages. The frequency resolution was 1 Hz, the sampling rate 16384 Hz. These settings resulted in a measurement time of 34 s. Typical coherence values for point and transfer mobilities on the plate are displayed in Figure 7.10.

In Section 7.2, the sources were attached to the plate using beeswax. In the repeated measurement, they were rigidly screwed to the plate. This may have made the setup more prone to moment transmission, but ensured a rigid and repeatable contact condition between "source" and receiver. To further reduce the variability of the test setup, the accelerometers were not moved between measurements of $\mathbf{Y}_{\mathbf{R},\mathbf{cc}}$, $\mathbf{Y}_{\mathbf{R},\mathbf{ca}}$ and $\mathbf{Y}_{\mathbf{C},\mathbf{ca}}$. For the measurement of $\mathbf{Y}_{\mathbf{R},\mathbf{aa}}$ and $\mathbf{Y}_{\mathbf{C},\mathbf{aa}}$, accelerometers were moved once.

One contact position and three remote response positions were considered.

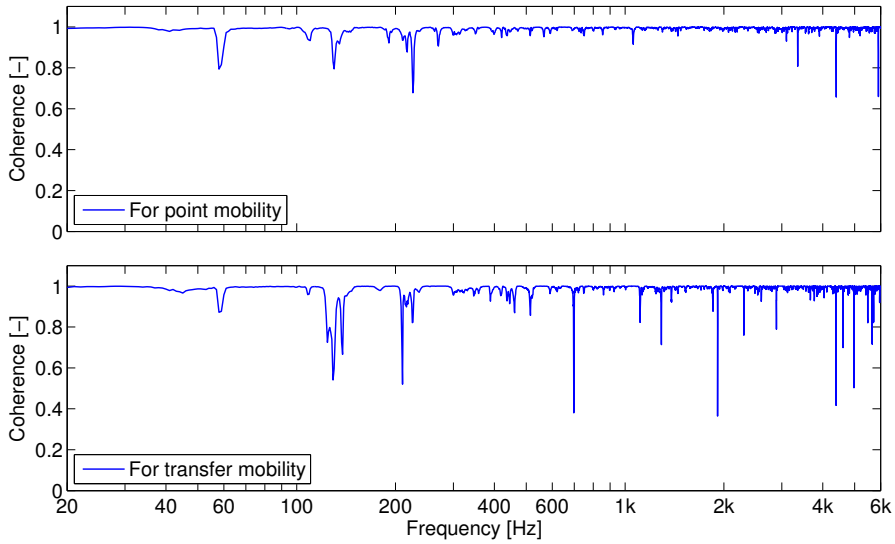

Figure 7.10: Typical coherence for measurement of plate point and transfer mobilities (n = 100, 66% overlap, Hanning window).

Therefore, for Methods 1 and 2, the following quantities were recorded:

- $\mathbf{Y_{R,cc}}$ (1×1), one mobility;
- $\mathbf{Y_{R,ca}}$ (1×3), three mobilities;
- $\mathbf{Y_{R,aa}}$ (3×3), nine mobilities;
- $\mathbf{Y_{C,ca}}$ (1×3), three mobilities for each mass;
- $\mathbf{Y_{C,aa}}$ (3×3), nine mobilities for each mass.

The three uncoupled plate mobilities were measured once, since they were the same for each mass. The two coupled mobilities $\mathbf{Y_{C,ca}}$ and $\mathbf{Y_{C,aa}}$ were measured for each mass.

Figure 7.11 shows the directly measured receiver mobility at the contact position, and the directly measured "source" mobilities, for the four masses considered. The receiver mobility shows characteristic plate-like behaviour, fluctuating about the infinite plate mobility of $7.4 \cdot 10^{-5}$ms^{-1}/N. The source mobilities display mass-spring-like behaviour, with the position of the anti-resonance dependent on the mass. The ratio of source and receiver mobilities can be described with the following trends: The source mobilities are higher than the plate mobility below 100 Hz. They are of the same order of magnitude between 100 Hz and 600 Hz, and are much lower around the anti-resonance frequencies

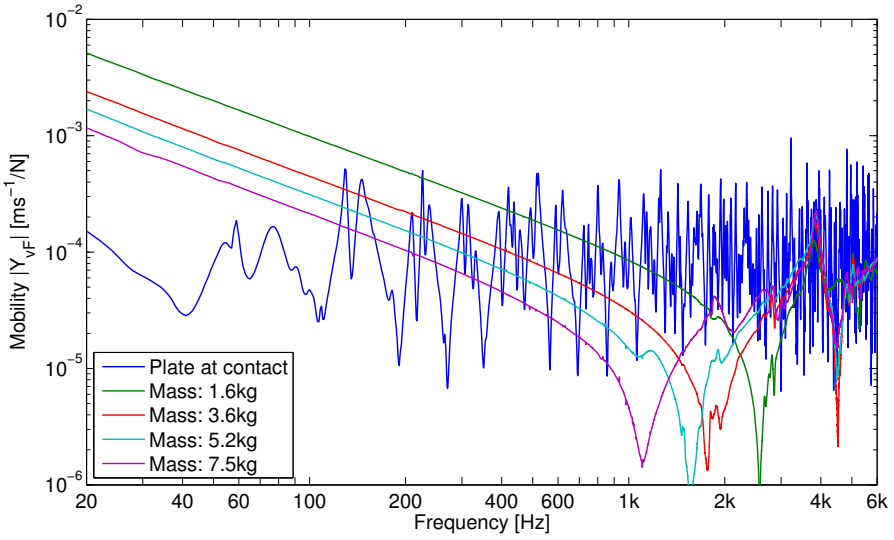

Figure 7.11: Directly measured source mobilities and plate mobility.

(between 800 Hz and 3 kHz). They are again of the same order of magnitude above the anti-resonance frequencies. The mobility of the lightest mass (1.6 kg) is higher than the plate mobility up to 300 Hz, of the same order of magnitude between 300 Hz and 2 kHz, and again above 3 kHz.

7.3.3 Directly and indirectly determined source mobilities

Figure 7.12 shows the mobility of the 5.2 kg mass with force transducer, for three cases: measured directly, and indirectly determined using Method 1 and Method 2. Results are presented as narrowband data. Three responses were used in the calculation, and SVR was applied for Method 2 (rejection of singular values greater than 2% of largest SV).

All three curves exhibit mass-spring-like behaviour. The anti-resonance is clearly identified by direct measurement and Method 1, but less so by Method 2. The anti-resonance frequency of the direct measurement lies at 1550 Hz, while for Method 1, and less clearly for Method 2, it lies at 1275 Hz and 1200 Hz, respectively. This difference is likely the result of different contact conditions, i. e. between force transducer and force transducer for direct measurement, and between force transducer and plate for the two indirect methods. All three

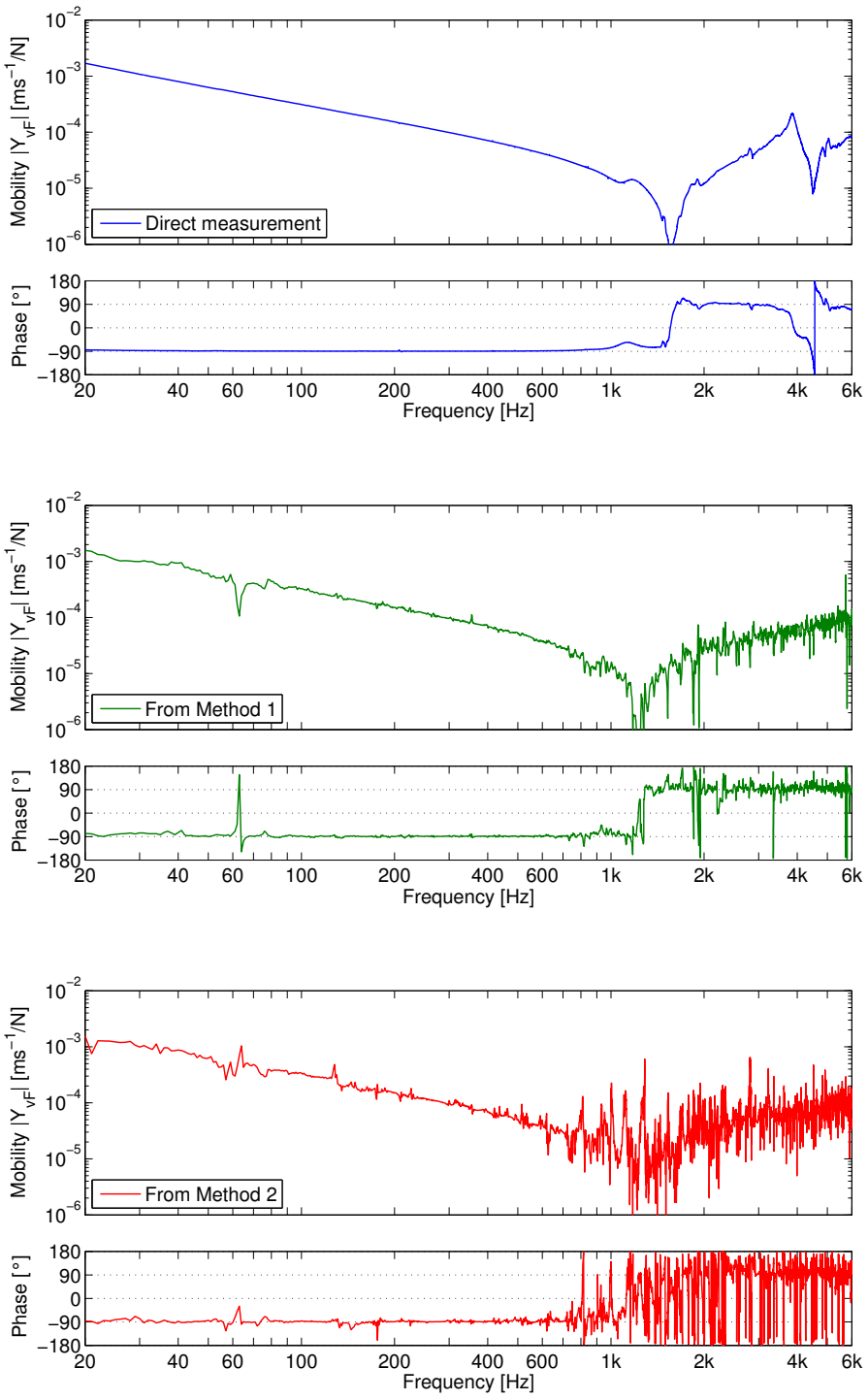

Figure 7.12: Mobility of 5.2 kg mass with force transducer, obtained by different methods: by direct measurement, and indirectly determined using Method 1 and Method 2.

m	f_0 [Hz]			k [N/m]		
	D	**M1**	**M2**	**D**	**M1**	**M2**
1.6 kg	2578	2090	2300	$4.2 \cdot 10^8$	$2.7 \cdot 10^8$	$3.3 \cdot 10^8$
3.6 kg	1800	1535	1700	$4.6 \cdot 10^8$	$3.3 \cdot 10^8$	$4.1 \cdot 10^8$
5.2 kg	1550	1275	1200	$4.9 \cdot 10^8$	$3.3 \cdot 10^8$	$3.0 \cdot 10^8$
7.5 kg	1100	1000	1000	$3.6 \cdot 10^8$	$3.0 \cdot 10^8$	$3.0 \cdot 10^8$

Table 7.3: Calculated spring stiffness of force transducer: **D**: from direct measurement, **M1**: from Method 1, **M2**: from Method 2.

curves show stable results at low frequencies, in the mass-dominated region. Above the anti-resonance frequency, random variations are greater for Method 2 than for Method 1. The deviations between direct and indirect results are within ±2 dB up to 700 Hz for Method 1, and within ±5 dB up to 700 Hz for Method 2. In the region of the anti-resonance frequency, deviations are up to ±30 dB for both methods. Above 2 kHz, deviations are within ±15 dB.

Figures 7.13, 7.14, and 7.15 show the results for the three other masses. The curves are overlayed for comparison. Data is presented in 1/24th-octave bands, for clarity. As for the 5.2 kg mass, the general trend of the mass-spring systems is identified by all three methods, for all three masses. The direct measurement displays the least influence of random errors. Method 1 identifies the anti-resonance frequencies, though the values are generally slightly lower than the values obtained from direct measurements. Table 7.3 shows the anti-resonance frequencies and the calculated spring stiffness. Method 2 is strongly affected by random errors, in particular at high frequencies, and identification of the anti-resonance frequencies is problematical. The deviations between direct and indirect results are generally within ±3 dB in the mass-dominated region for both methods. In the region of the anti-resonance frequency, the deviations reach values up to ±20 dB and ±30 dB for Method 1 and 2, respectively. Above the anti-resonance frequency, the deviations are within ±15 dB, though this high value is likely to be caused by the systematic error in the direct measurement.

In summary, the repeated measurement series with individual steel blocks with force transducer, connected to an aluminium receiver plate, confirms the general applicability of Equations (5.53) and (5.54) for the SDOF case. The influence of measurement inaccuracies is observed, as well as the sensitivity to changes

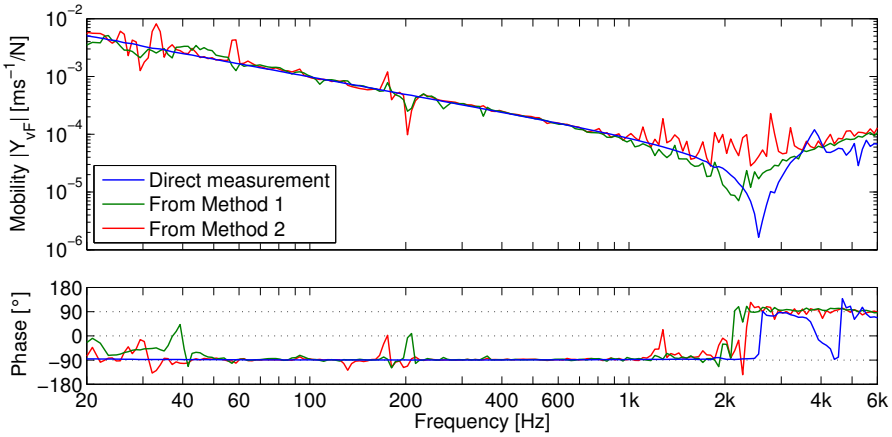

Figure 7.13: Indirectly determined source mobility: 1.6 kg.

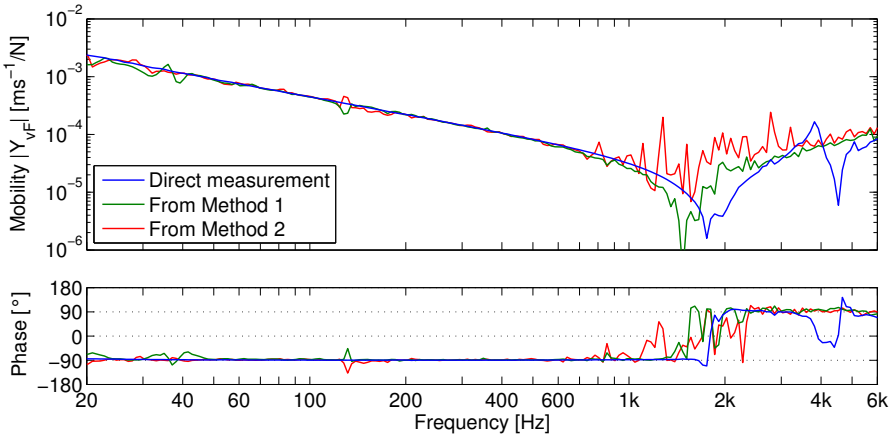

Figure 7.14: Indirectly determined source mobility: 3.6 kg.

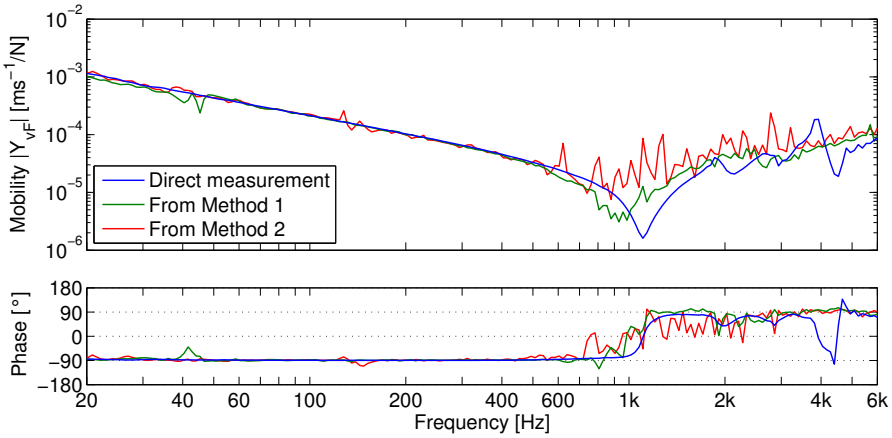

Figure 7.15: Indirectly determined source mobility: 7.5 kg.

in contact conditions. High-quality data therefore is of critical importance for a practical implementation of these methods. The use of a shaker instead of a hammer may improve data quality. Furthermore, relocation of accelerometers between measurements should be avoided. This is considered one reason for the larger errors in the results for Method 2.

7.4 Two masses on plate

In the two previous studies, one contact point and one degree of freedom at the source-receiver interface were considered. In this study, two steel blocks were attached to the aluminium receiver plate at the same time. Together, they formed a MDOF system (one degree of freedom each at the two contacts). The two masses can be thought of as one source, with mass-spring-like point mobilities, and zero transfer mobilities.

7.4.1 Measurement setup

The measurement setup was similar as in Section 7.3. Three combinations of masses were considered, see Table 7.4. The distance between the two mounting points was 0.35 m.

	Mass 1	Mass 2	Difference in mobility
Case A	1.6 kg	3.6 kg	Moderate
Case B	3.9 kg	3.6 kg	Small
Case C	1.6 kg	5.9 kg	Large

Table 7.4: Combinations of masses.

Two contact positions and five response positions were used. Therefore, for Methods 1 and 2, the following quantities were recorded:

- $\mathbf{Y}_{\mathbf{R,cc}}$ (2×2), four mobilities;
- $\mathbf{Y}_{\mathbf{R,ca}}$ (2×5), ten mobilities;
- $\mathbf{Y}_{\mathbf{R,aa}}$ (5×5), 25 mobilities;
- $\mathbf{Y}_{\mathbf{C,ca}}$ (2×5), ten mobilities for each combination;
- $\mathbf{Y}_{\mathbf{C,aa}}$ (5×5), 25 mobilities for each combination.

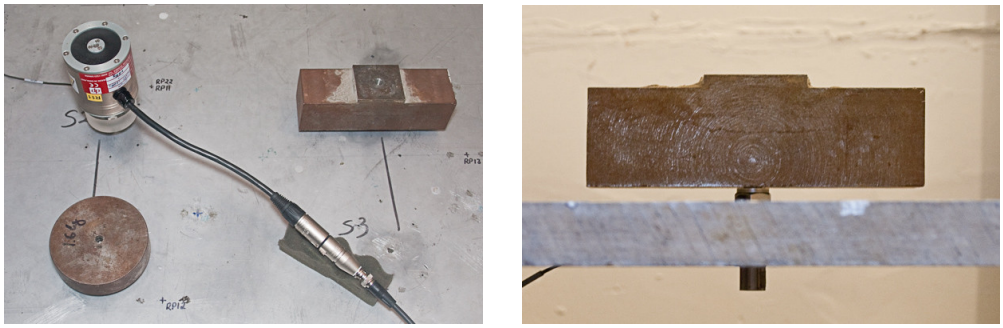

Figure 7.16: Measurement of two steel blocks on 20 mm aluminium plate. Each block is rigidly screwed to the plate, using force transducers as connectors. Accelerometers are attached beneath the plate.

The three uncoupled mobility terms were measured once, as they are the same for each combination of masses. The two coupled mobility terms $\mathbf{Y_{C,ca}}$ and $\mathbf{Y_{C,aa}}$ were measured for each combination.

The response velocities at the contacts were measured by accelerometers, attached beneath the plate. This allowed the use of large accelerometers with higher sensitivity (BK 4371 with 1 pC/ms^{-2}), to improve signal-to-noise ratios. For Method 1, this meant that only two accelerometers and one force transducer were required. For Method 2, two matched accelerometers at each of the response positions were used, to allow for simultaneous excitation and measurement of response velocities. The same shaker as in Section 7.3.2 was used, with the same analyzer settings. Figure 7.16 illustrates the setup.

7.4.2 Directly and indirectly determined source mobilities

Since the two masses are not connected except through the plate, the source mobility matrix consists of two mass-spring-like elements on the diagonal, and zero off-diagonal terms. Figures 7.17, 7.18, and 7.19 show the source mobility matrix for Case A, determined by direct measurement, Method 1, and Method 2, respectively. Again, the narrowband mobilities were converted to 1/24th-octave band data, for clarity of presentation.

The indirectly determined point mobilities in Figures 7.18 and 7.19 show the expected mass-spring-like behaviour. The same observations as in Section 7.3 apply. The anti-resonances are clearly identified by Method 1; less so by Method 2.

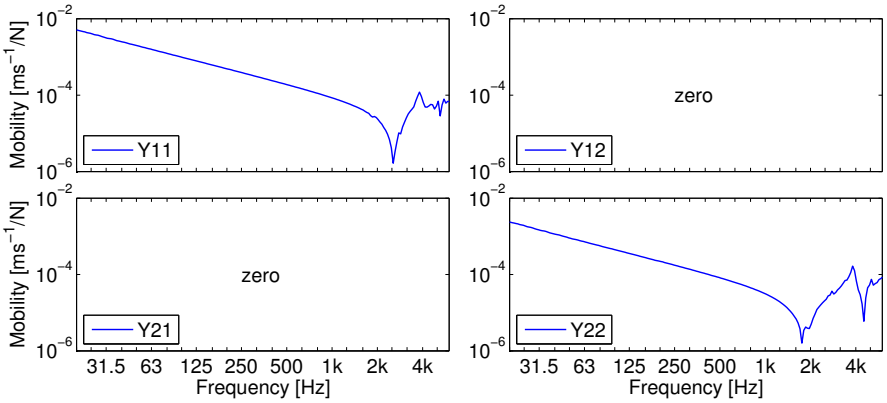

Figure 7.17: Source mobility matrix: Direct measurement.

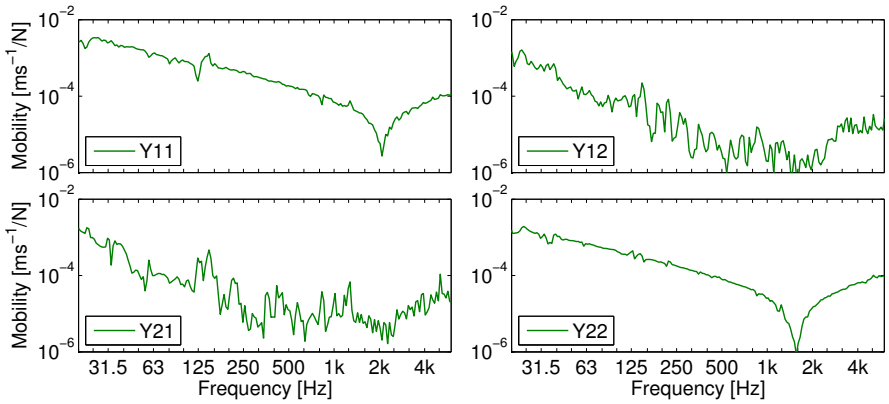

Figure 7.18: Source mobility matrix: From Method 1.

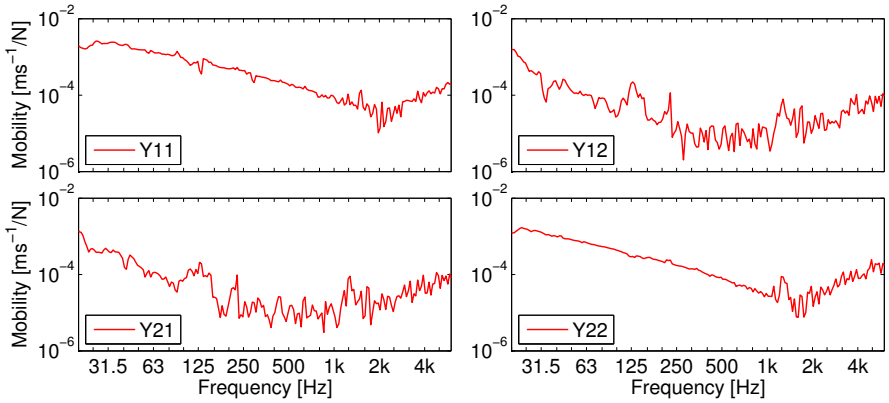

Figure 7.19: Source mobility matrix: From Method 2.

Method 2 is strongly affected by random errors, in particular at high frequencies. The deviations for both methods are within ±3 dB in the mass-dominated region, and up to ±20 dB in the region around the anti-resonance frequency.

While the directly measured transfer mobilities are zero, they are non-zero for the indirect methods. These "phantom" transfer mobility terms result from the matrix inversion. Like low forces in the presence of high forces in Chapter 4, low transfer mobilities in the presence of higher point mobilities are over-estimated. Figures 7.20 and 7.21 show the indirectly determined point and transfer mobilities for Case A, for comparison of the magnitudes.

The trends of the phantom transfer mobilities resemble those of the point mobilities. Compared to the point mobilities, the phantom transfer mobilities for Method 1 are about 20 dB lower in magnitude at most frequencies below the anti-resonance frequencies, and about 10 dB lower above the anti-resonance frequencies. At the resonance frequencies, they are of the same order of magnitude or higher. For Method 2, the phantom transfer mobilities are about 20 dB lower in magnitude at most frequencies below 1 kHz, and of the same order of magnitude above 1 kHz.

Figures 7.22, 7.23, and 7.24 show the point mobilities of both masses for the three cases. In all cases, the mass terms are identified, but the mass estimates tend to be slightly low at low frequencies (about 2 dB for Case A and Case B), in particular for Case C (about 5 dB), where the first mass is much lighter than the second mass. This under-estimate is associated with the phantom transfer mobilities. Instead of identifying the correct point mobilities, the calculation attributes part of the velocity at the contact to the phantom transfer mobility, thus under-estimating the point mobility. Above the anti-resonance frequency, the deviations are up to ±20 dB.

Methods 1 and 2 yield similar results, though once again Method 2 is more sensitive to random errors at high frequencies. Also for Method 2, the anti-resonance is not as clearly visible in the magnitude data. The difference in mobility between the two masses seems to be less important than might have been expected. There is no significant difference between the three figures.

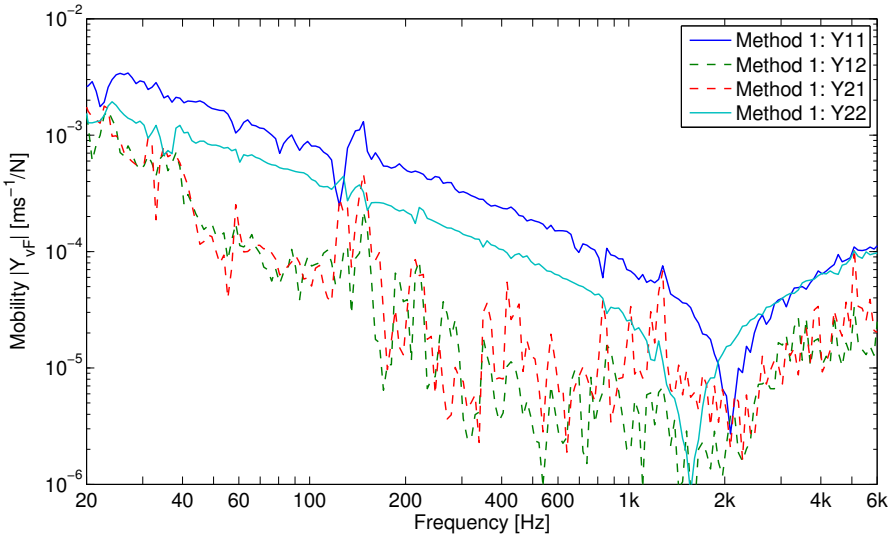

Figure 7.20: Point and transfer mobilities for Case A, indirectly determined using Method 1.

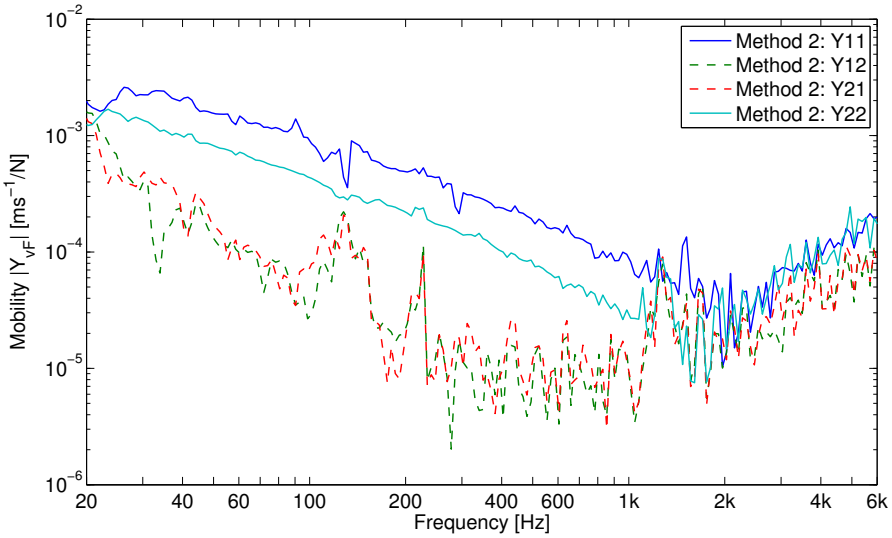

Figure 7.21: Point and transfer mobilities for Case A, indirectly determined using Method 2.

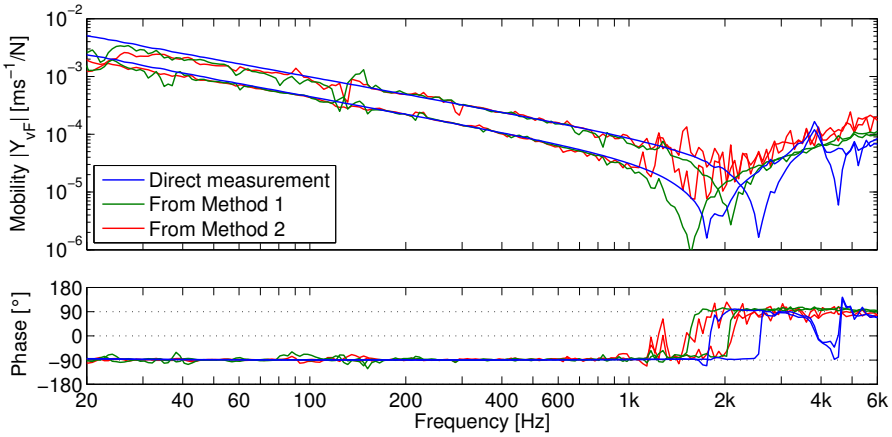

Figure 7.22: Point source mobilities: Case A.

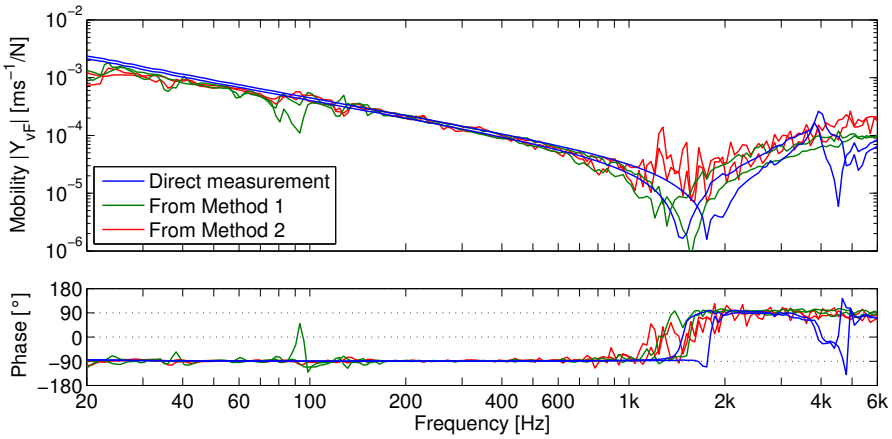

Figure 7.23: Point source mobilities: Case B.

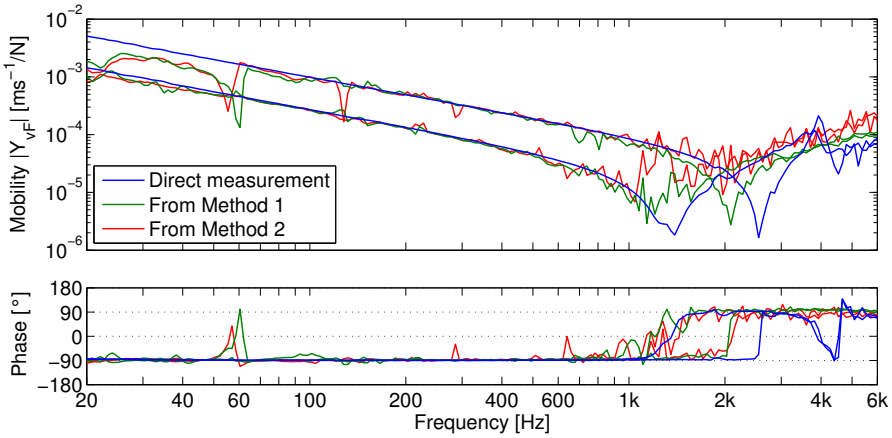

Figure 7.24: Point source mobilities: Case C.

7.5 Free beam on thin plate - One contact

In Sections 7.2, 7.3, and 7.4, simple mass-spring systems were considered. These structures can be described as "well-behaved", meaning that their mobility changes slowly over frequency, except in the region of the anti-resonance frequency. In this study, a more complicated, multi-modal source structure was considered, namely a free Perspex beam. A different plate with smaller thickness was used as receiver, to match the mobility of the Perspex beam. The plate's damping was significantly higher than that of the free aluminium plate considered in Sections 7.2, 7.3, and 7.4. At the same time, the internal loss factor of Perspex is also higher than that of metal. The higher damping of source and receiver was expected to reduce the sensitivity of the methods to experimental errors, as it decreases the rate of change in the mobilities. Sources with lower internal loss factors (e. g. metal structures) are more challenging.

7.5.1 Measurement setup

A free aluminium plate of size 1.95 m $\times$ 1.22 m $\times$ 6 mm was used as receiver. The infinite plate mobility is approximately $8 \cdot 10^{-4}$ $\mathrm{ms}^{-1}/\mathrm{N}$. The plate was placed on open-cell acoustic foam, as used in room acoustics applications. The loss factor was measured using the method described in Appendix D. It is shown in Figure 7.25 on the right, together with the loss factor of the 20 mm free aluminium plate, for comparison. The damping is considerably higher than that of the 20 mm free aluminium plate. Below 60 Hz, the determination of the loss factor was impossible, because the plate bending modes were overshadowed by the rigid mode of the plate and the supporting material. The eigenfrequency of this mass-spring system was at about 80 Hz. On the left of Figure 7.25 is shown the plate with attached beam.

A free Perspex beam of size 1.35 m $\times$ 0.10 m $\times$ 25 mm was used as source structure. The beam was connected to the plate at its centre position (0.675 m), using a cubic Perspex adapter block of approximately 1.5 cm^3. The adapter was rigidly glued to beam and plate, and accelerometers were attached either side of it, to record the contact velocity.

One contact position and four remote response positions were considered. Therefore, for Method 1 and Method 2, the following quantities were recorded:

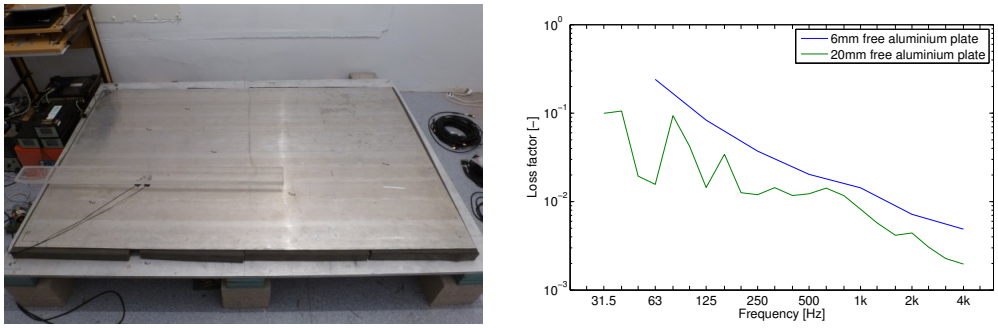

Figure 7.25: Free Perspex beam connected at one contact to 6 mm aluminium plate (left). Loss factor of 6 mm aluminium plate (right).

- $\mathbf{Y_{R,cc}}$ (1×1), one mobility;
- $\mathbf{Y_{R,ca}}$ (1×4), four mobilities;
- $\mathbf{Y_{R,aa}}$ (4×4), 16 mobilities;
- $\mathbf{Y_{C,ca}}$ (1×4), four mobilities;
- $\mathbf{Y_{C,aa}}$ (4×4), 16 mobilities.

A shaker (Data Physics inertial shaker IV 40) was used to excite the plate. Two small accelerometers (BK 4393V with 0.3 pC/ms^{-2}) measured the response velocity at the contact. Two large accelerometers (BK 4371 with 1 pC/ms^{-2}) were used at each of the remote positions, to allow for simultaneous excitation and measurement of responses. Accelerometers were not moved between measurements. Point and transfer mobilities were calculated as described in the previous studies, e. g. in Section 7.3.2. For the direct measurement of the beam mobility, the beam was screwed onto a large shaker, and the force and response velocity measured in a similar way as in Section 7.3.1.

Figure 7.26 shows the directly measured beam and plate point mobilities. The plate mobility fluctuates around the infinite plate mobility of $8 \cdot 10^{-4}$ ms^{-1}/N. The beam mobility shows a characteristic behaviour of well-separated eigenfrequencies in combination with a gradient of $1/\sqrt{\omega}$. Above 3 kHz, other effects come into play, possibly due to the attached adapter. Below 50 Hz, the beam mobility is significantly higher than the plate mobility. Between 1 kHz and 3 kHz, the beam mobility is often significantly lower than the plate mobility. Otherwise, the mobilities of beam and plate are of the same order of magnitude.

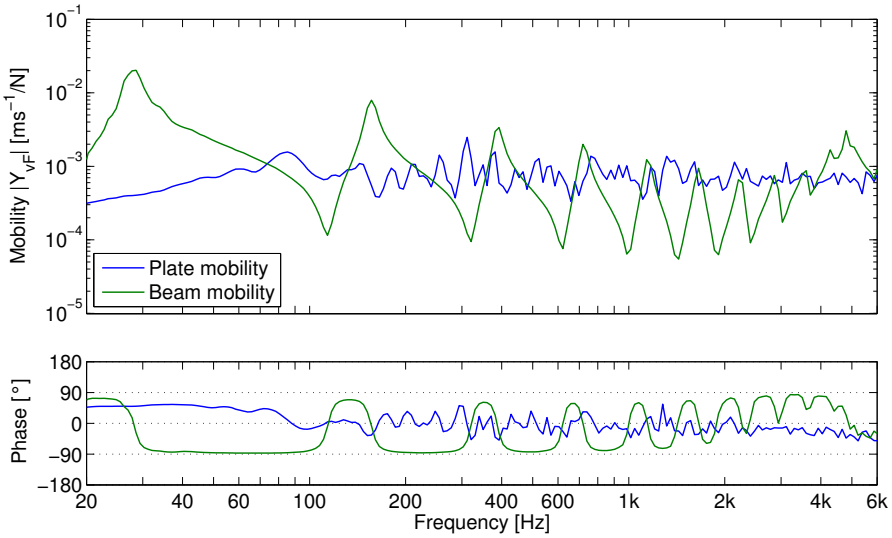

Figure 7.26: Beam and plate point mobilities.

7.5.2 Directly and indirectly determined source mobilities

Figure 7.27 shows the directly measured and indirectly determined beam mobilities. Below 60 Hz, both methods fail to identify the beam mobility. This is because the plate motion in this frequency region is dominated by the whole-body mode. Errors in this frequency region are up to 30 dB. Between 60 Hz and 1 kHz, the agreement between directly measured and indirectly determined mobility is generally within ±5 dB. The resonance frequencies are generally identified correctly by both methods. The indirectly obtained anti-resonances tend to shift down in frequency with respect to the direct values, particularly at higher frequencies. Above 1 kHz, the agreement between direct and indirect results is generally within ±10 dB. The deviations occur mainly at the beam's anti-resonance frequencies. As in the previous studies, the results obtained with Method 1 are more reliable than those obtained with Method 2.

It appears that the source-receiver mobility ratio has a strong influence on the accuracy of the indirect source mobility determination. This is illustrated in Figure 7.28, where the source-receiver mobility ratio is shown together with the directly and indirectly determined source mobility (Method 1 only). Frequency regions where the directly measured beam mobility is significantly higher ($|Y_{S,cc}| \gg |Y_{R,cc}|$) or significantly lower ($|Y_{S,cc}| \ll |Y_{R,cc}|$) than the plate

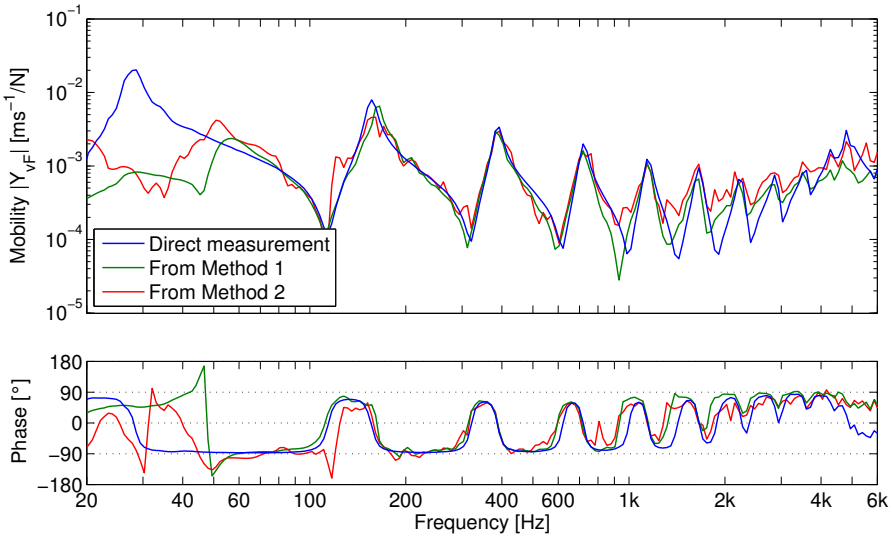

Figure 7.27: Directly and indirectly determined beam mobility.

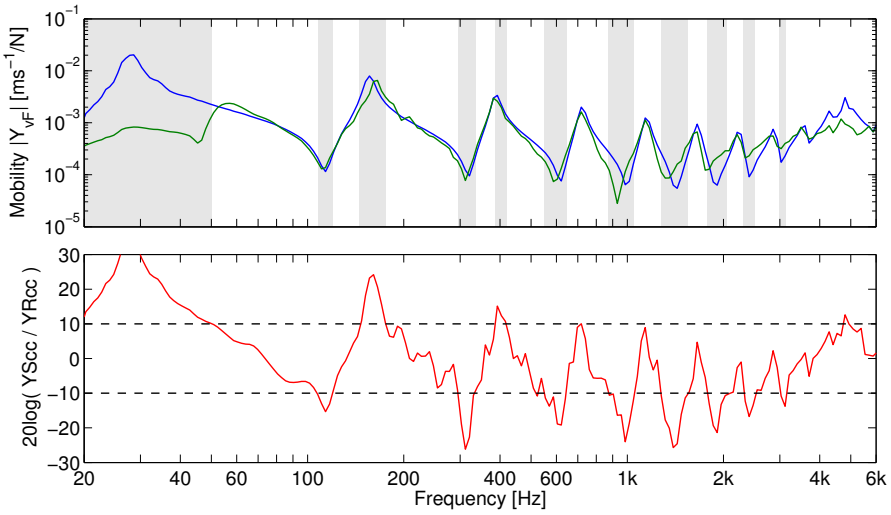

Figure 7.28: Influence of source-receiver mobility ratio.

mobility are indicated as grey areas. An arbitrary limit of ±10 dB is indicated by horizontal lines.

Frequency regions where the beam mobility is much higher or lower than the plate mobility correspond to regions where the agreement between direct and indirect measurement is less. Therefore, the best results are obtained when source and receiver mobility are in the same order of magnitude. This supports the findings of the theoretical considerations in Section 5.4.4. This requirement presents an inherent limitation of the methods. For an unknown source, it is difficult to "engineer" an optimum source-receiver mobility condition.

7.6 Free beam on thin plate - Two contacts

The results described in Section 7.5 provided a basis for an investigation into the importance of transfer mobilities for the described methods. In this study, the free beam was attached to the 6 mm aluminium plate at two positions. This resembles the situation in Section 7.4, where two masses were placed on the receiver plate at the same time. However, while the transfer mobilities were zero for the two unconnected masses, they are non-zero for the beam.

7.6.1 Measurement setup

The free Perspex beam was connected at two positions to the 6 mm aluminium plate. Small Perspex blocks were used as adapters to allow point connections and to allow the attachment of small accelerometers at the contacts. The blocks were glued to the centre of the beam at 0.20 m and at 0.95 m, measured from one end of the beam. The contact locations on the receiver plate were (0.50 m,0.40 m) and (0.90 m,1.035 m), measured from the origin in one of the corners of the plate. Figure 7.29 illustrates the measurement setup.

Two contact positions and four remote response positions were considered. Therefore, for Method 1 and Method 2, the following quantities were recorded:

- $\mathbf{Y_{R,cc}}$ (2×2), four mobilities;
- $\mathbf{Y_{R,ca}}$ (2×4), eight mobilities;
- $\mathbf{Y_{R,aa}}$ (4×4), 16 mobilities;
- $\mathbf{Y_{C,ca}}$ (2×4), eight mobilities;

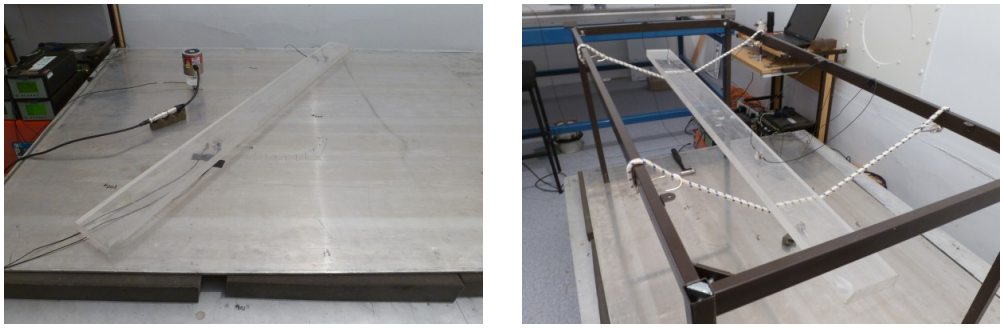

Figure 7.29: Free Perspex beam, attached at two positions to the 6 mm aluminium plate (left), and freely suspended for the direct measurement of point and transfer mobilities (right).

- $\mathbf{Y}_{\mathbf{C,aa}}$ (4×4), 16 mobilities.

The measurement procedure was the same as described in Section 7.5. For the direct measurement of the beam mobilities, the beam was freely suspended using bungees, and excited with a hand-held shaker (see Figure 7.29).

7.6.2 Directly and indirectly determined source mobilities

Figure 7.30 shows the directly measured and indirectly determined beam mobilities. All four elements of the mobility matrix are presented. Three frequency regions are distinguished. Below 100 Hz, the deviations between direct and indirect results are up to ±20 dB. As in Section 7.5, this is likely to be caused by the plate's motion being dominated by the whole-body mode. In point mobility Y_{11}, both Method 1 and 2 fail to fully capture the resonance at 80 Hz. In point mobility Y_{22}, the general mass-like trend below 100 Hz is identified by both methods, though inaccurately. The indirectly determined transfer mobilities below 100 Hz show considerable deviations from the direct value (up to ±20 dB).

The second frequency region ranges from 100 Hz to 700 Hz. Here, the agreement between directly and indirectly determined mobilities is much better than in the low frequency region. For Method 1, the deviations are within ±5 dB, and the average deviation is ±2 dB, for both point and transfer mobilities. For Method 2, the deviations are within ±10 dB, and the average deviation is ±3 dB, for both point and transfer mobilities.

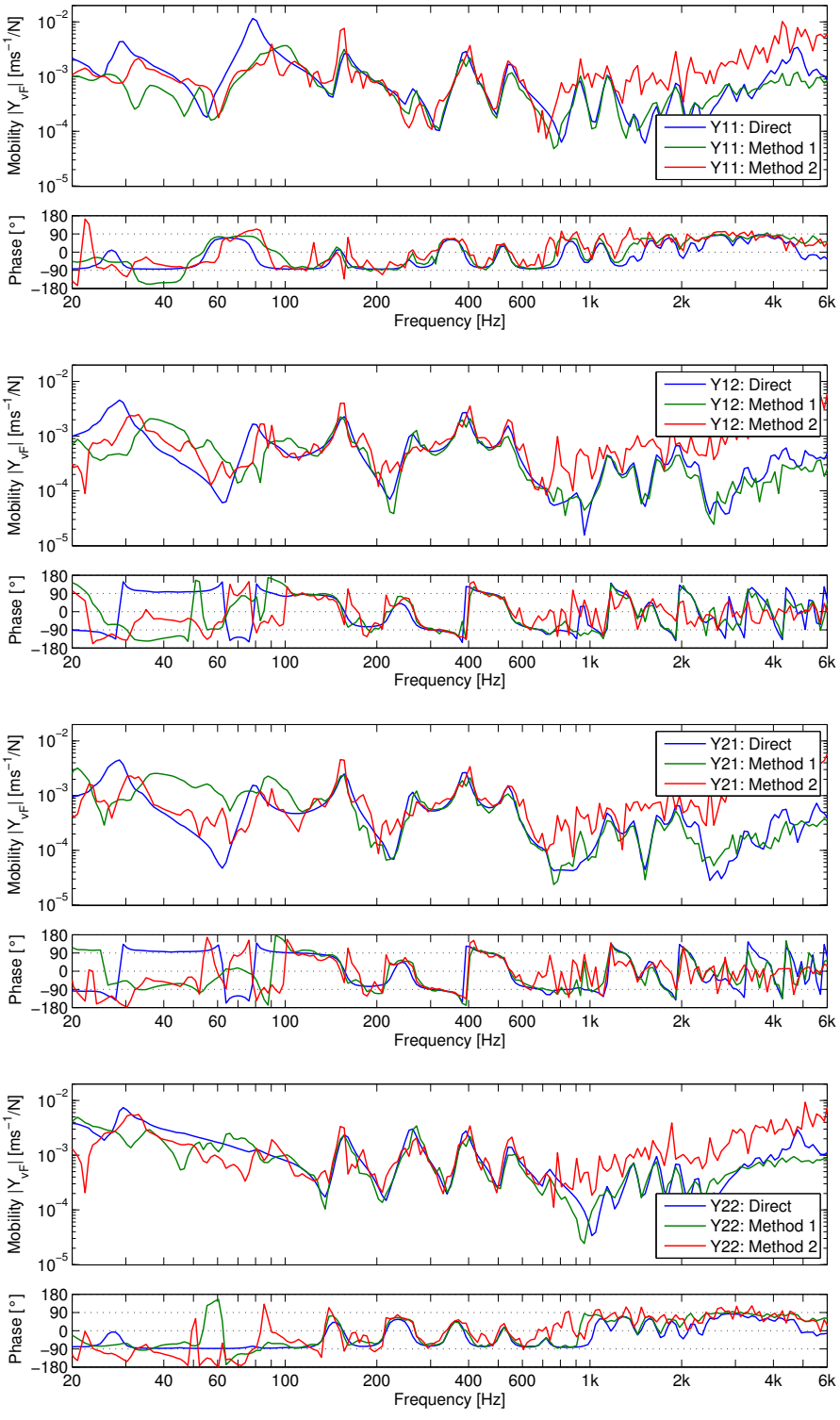

Figure 7.30: Directly and indirectly determined beam mobilities.

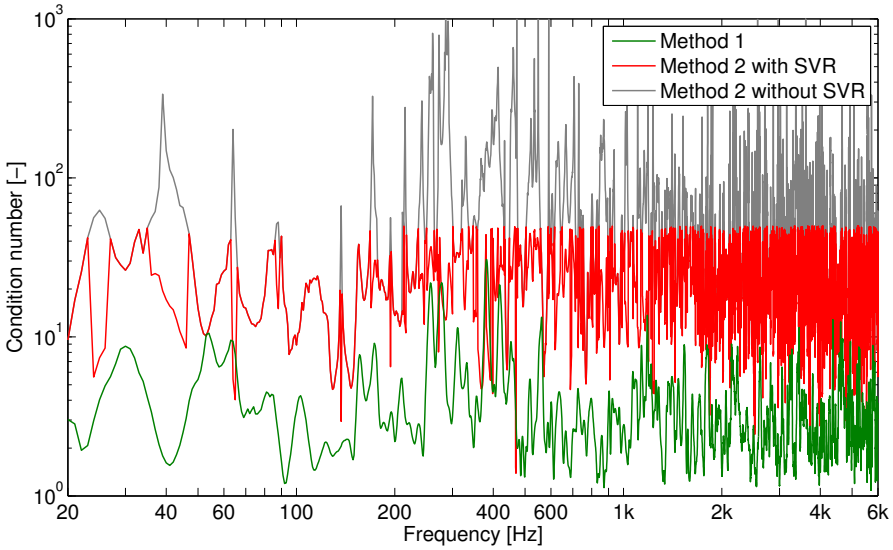

Figure 7.31: Condition number of matrix $\mathbf{Y}^{\mathbf{T}}_{\mathbf{R,ca}} - \mathbf{Y}^{\mathbf{T}}_{\mathbf{C,ca}}$ (Method 1) and matrix $\mathbf{Y}_{\mathbf{R,aa}} - \mathbf{Y}_{\mathbf{C,aa}}$ (Method 2) for indirect determination of mobility of Perspex beam (2 contact positions and 4 remote positions).

Above 700 Hz, Method 1 yields point and transfer mobilities that agree within ±10 dB with the direct measurement. The average deviation between 700 Hz and 6 kHz is ±3 dB. Method 2 results in systematic over-estimates of 11 dB for the two point mobilities, and 14 dB for the two transfer mobilities.

For the results in Figure 7.30, over-determination was employed (four remote positions), and regularization was used for Method 2 (rejection of singular values smaller than 2% of the highest SV). Figure 7.31 shows the condition number for the considered case. For almost the entire frequency region of interest, the condition number for Method 1 is below ten, and never exceeds values of 40. This indicates a well-conditioned FRF matrix. For Method 2, the condition number is often cropped at a value of 50, due to SVR. This indicated that the FRF matrix in this case is not well-conditioned.

The results from this study indicate that it is possible to obtain the complete source mobility matrix using the described methods, including off-diagonal transfer terms. The errors found in point and transfer mobilities ranged from ±5 dB (Method 1 between 100 Hz and 700 Hz) to ±10 dB (Method 2 between 100 Hz and 700 Hz) and up to ±20 dB (Methods 1 and 2 below 100 Hz).

7.7 Multi-contact source on thin plate

In the previous sections (7.2, 7.3, 7.4, 7.5, 7.6), the methods proposed in Chapter 5 have been validated for single contact sources, and for a simple multi-contact structure, namely a free Perspex beam. In this study, a representative multi-contact source was investigated.

7.7.1 Measurement setup

The source under investigation was a centrifugal fan unit, bolted to a framed support structure. Figure 7.32 shows the fan unit, and details of the framed support structure. The combined structure has a mass of 10.9 kg, and the following approximate dimensions: 0.38 m × 0.40 m × 0.42 m. In a typical installation situation, the frame structure is bolted to a receiver at four contacts. In this laboratory study, however, the support frame was glued to the 6 mm aluminium plate at three of the four contacts. This modification ensured stable and repeatable contact conditions. The thin plate was used as receiver, because its mobility is, for much of the frequency range of interest, in the same order of magnitude as the mobility of the centrifugal fan unit, cf. Figure 7.33.

Matched accelerometers (BK 4371 with 1 pC/ms^{-2}) were placed left and right of the contacts. Due to the dimensions of the frame, the distance between accelerometers and the actual contacts was relatively large (30 mm each). This has a detrimental effect on the accuracy of the measured mobilities, but it is representative of the practical situation. Matched accelerometers (BK 4371 with 1 pC/ms^{-2}) were also placed left and right of each remote response position. Accelerometers were moved once, for the measurement of $\mathbf{Y}_{\mathbf{R,aa}}$ and $\mathbf{Y}_{\mathbf{C,aa}}$. The plate was excited with a shaker (Data Physics inertial shaker IV 40), which was driven by pink noise (upper limiting frequency of 6.4 kHz). Point and transfer mobilities were calculated as described in the previous studies, e. g. in Section 7.3.2.

The mobility of the fan unit was measured directly, by resiliently suspending the unit with bungees, and exciting it at the contacts with a hand-held shaker. Due to limited access, two small accelerometers (BK 4393V with 0.3 pC/ms^{-2}) were glued sideways to each source terminal.

Figure 7.32: Fan unit connected at three contacts to 6 mm aluminium plate (left). Detail of framed support structure, glued to receiver (right).

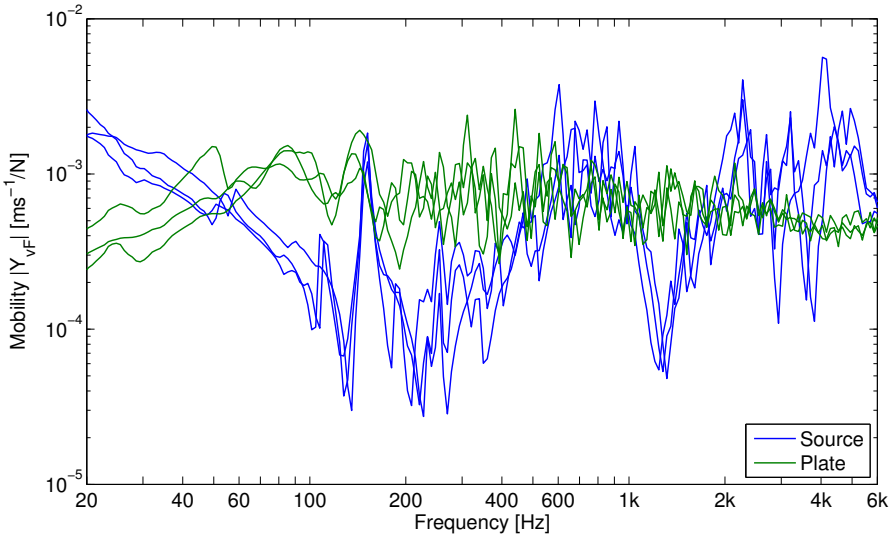

Figure 7.33: Directly measured source and receiver mobilities.

Three contact positions and five remote response positions were considered. Therefore, the following quantities were recorded:

- $\mathbf{Y}_{\mathbf{R,cc}}$ (3×3), nine mobilities;
- $\mathbf{Y}_{\mathbf{R,ca}}$ (3×5), 15 mobilities;
- $\mathbf{Y}_{\mathbf{R,aa}}$ (5×5), 25 mobilities;
- $\mathbf{Y}_{\mathbf{C,ca}}$ (3×5), 15 mobilities.
- $\mathbf{Y}_{\mathbf{C,aa}}$ (5×5), 25 mobilities;

Figure 7.33 shows directly measured source and receiver mobilities. The receiver mobilities display typical plate-like behaviour, fluctuating about the infinite plate mobility of $8 \cdot 10^{-4}$ms^{-1}/N. The source mobilities are more difficult to describe. Below 100 Hz, they are dominated by the mass of the structure. At 150 Hz, a strong resonance is observed. Between 200 Hz and 900 Hz, the mobilities exhibit local resonances in combination with a global stiffness trend, before decreasing sharply to an anti-resonance around 1250 Hz. Above 2 kHz, the source mobilities are in a resonance-controlled region, with a generally constant value. The source and receiver mobilities are approximately of the same order of magnitude, between 20 Hz and 100 Hz, between 400 Hz and 1 kHz, and between 1.5 kHz and 6 kHz. Between 100 Hz and 400 Hz, and between 1 kHz and 1.5 kHz, the source mobilities are significantly lower than the plate mobilities.

7.7.2 Directly and indirectly determined source mobilities

Figures 7.34, 7.35, and 7.36 show the directly and indirectly determined point mobilities of the fan unit. Five response positions were used in the calculation, and SVR was employed for Method 2 (rejection of singular values smaller than 2% of the highest SV). For Method 1, the condition number did not exceed values of 40, as in Section 7.6.

The interpretation of Figures 7.34, 7.35, and 7.36 is not straightforward, as the agreement between directly and indirectly determined mobilities varies strongly. Four frequency regions are distinguished in the following discussion: from 20 Hz to 100 Hz, between 100 Hz and 400 Hz, between 400 Hz and 1 kHz, and from 1 kHz to 6 kHz.

Below 100 Hz, the deviations for Methods 1 and 2 are mostly within ±10 dB, with occasional outliers of up to 20 dB. The average deviation in this fre-

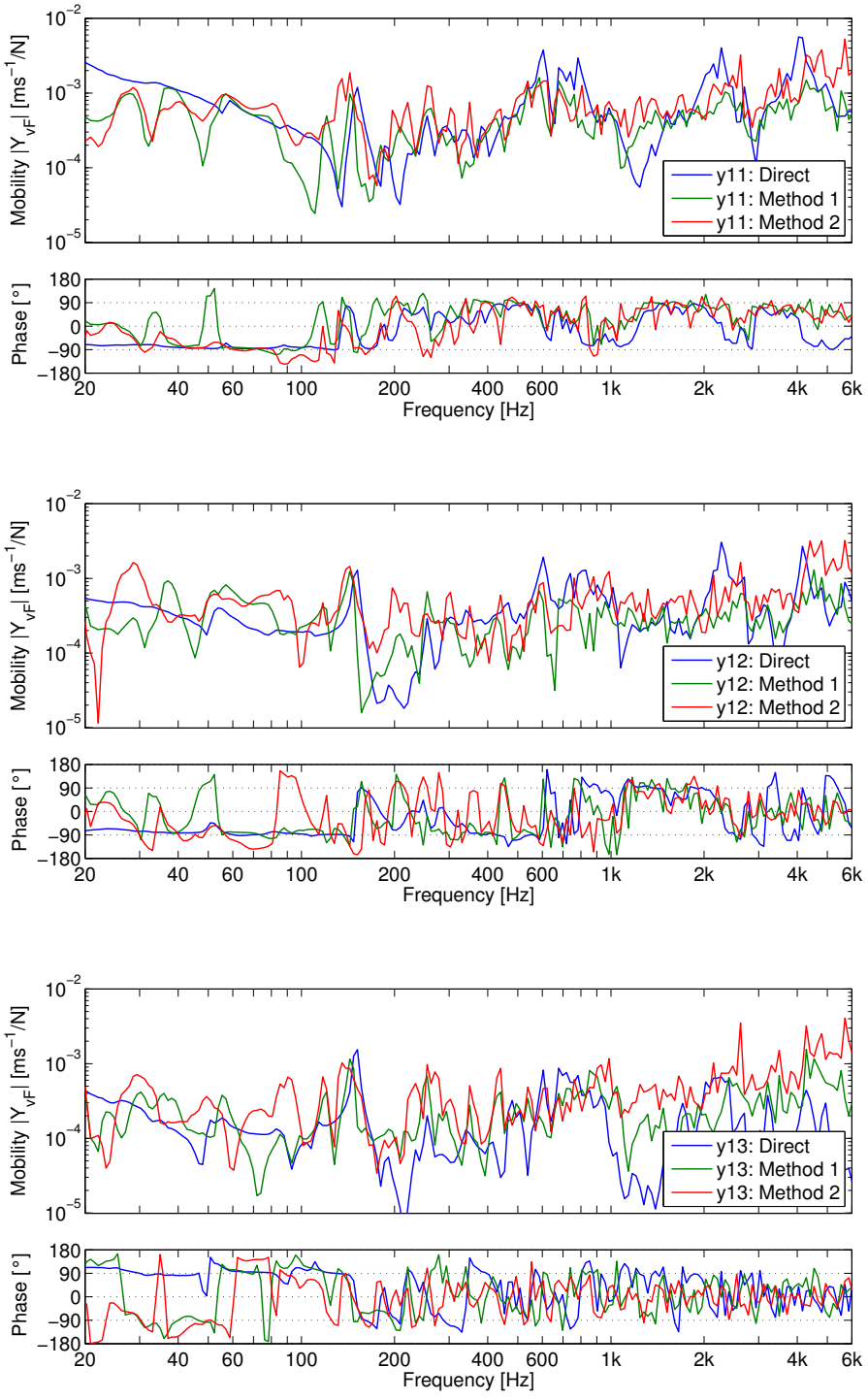

Figure 7.34: Directly and indirectly determined mobilities.

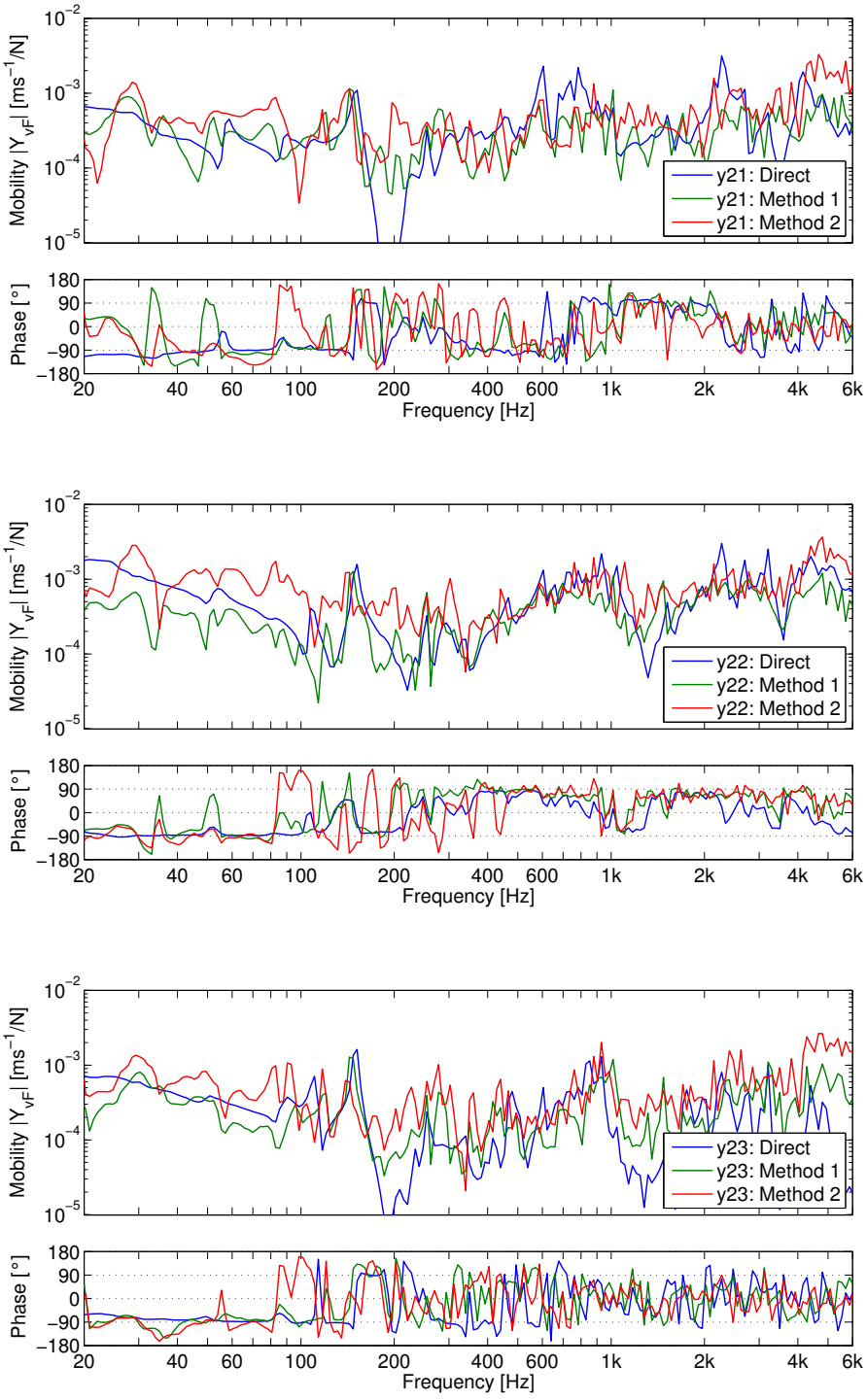

Figure 7.35: Directly and indirectly determined mobilities.

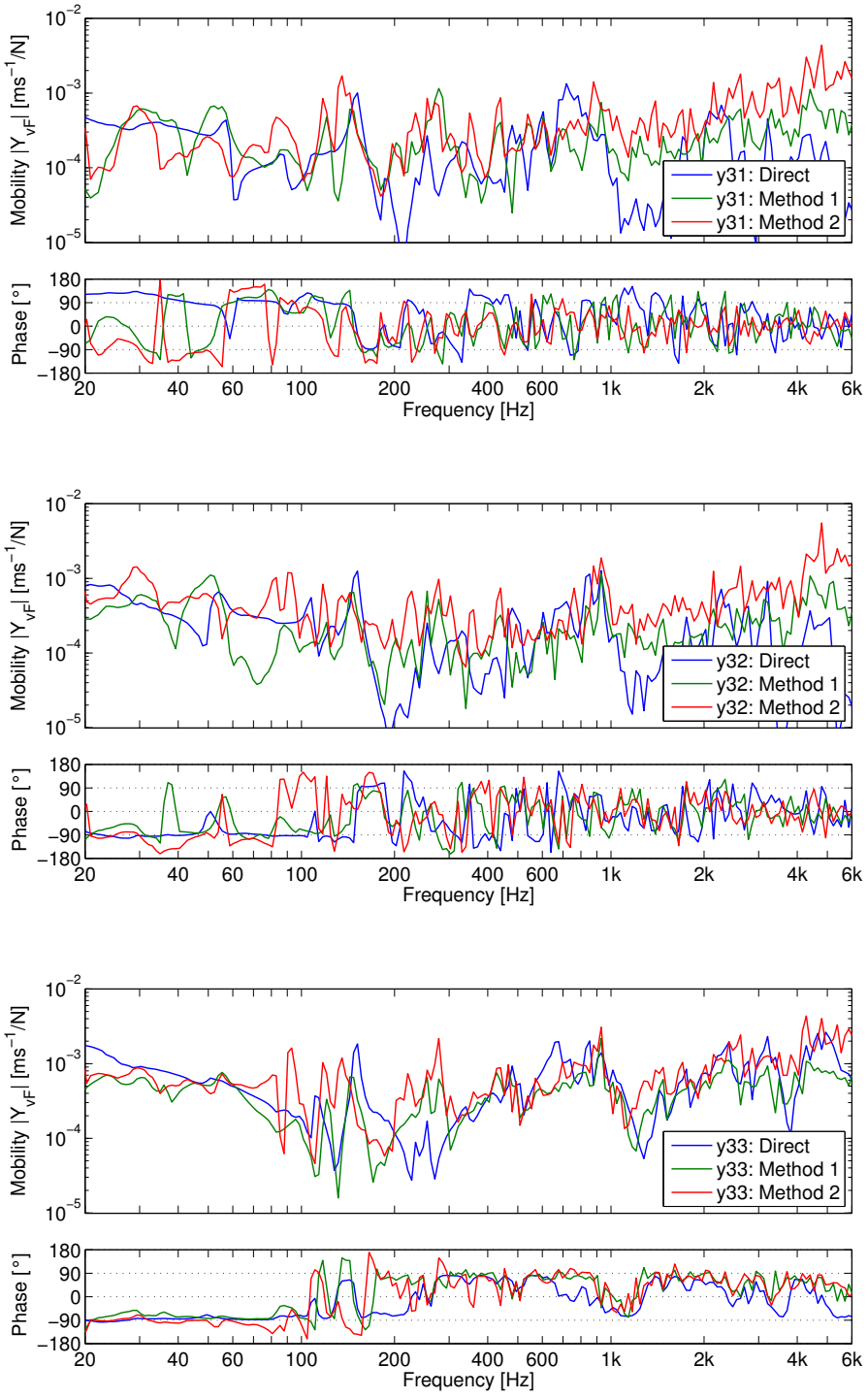

Figure 7.36: Directly and indirectly determined mobilities.

quency region is about ±5 dB for point and transfer mobilities determined with Method 1, and about ±6 dB for point and transfer mobilities determined with Method 2. The directly measured mobilities mainly show mass-like behaviour, while the indirect results display many spurious peaks and troughs.

Between 100 Hz and 400 Hz, the source mobility is significantly lower than the plate mobility, cf. Figure 7.33. The deviations between direct and indirect results range between ±30 dB for both Methods 1 and 2. Most 1/24th-octave bands are within ±20 dB. The average deviation is about ±8 dB for point and transfer mobilities determined with Method 1, and about ±10 dB for point and transfer mobilities determined with Method 2. The resonance at 150 Hz is generally identified by both methods, though with inaccuracies and shifted down in frequency.

Between 400 Hz and 1 kHz, source mobility and receiver mobility are in the same order of magnitude, cf. Figure 7.33. The deviations between direct and indirect results range between ±20 dB for both Methods 1 and 2. Most 1/24th-octave bands are within ±10 dB. The average deviation is about ±5 dB for point mobilities determined with Method 1 or 2, and about ±7 dB for transfer mobilities determined with Method 1 or 2.

Above 1 kHz, the deviations between direct and indirect results range between −15 dB and 30 dB for both Methods 1 and 2. For the point mobilities, most 1/24th-octave bands are within ±10 dB. The average deviation for the point mobilities is ±5 dB for Method 1 and ±7 dB for Method 2. Some of the transfer mobilities, namely Y_{13}, Y_{23}, Y_{31}, and Y_{32}, show systematic over-estimates of 10 dB for Method 1 and 17 dB for Method 2. The anti-resonance at 1250 Hz is not identified by either method.

The results from this study highlight the practical difficulties when implementing the methods proposed in Chapter 5. Care is required in measuring the mobilities involved in the indirect calculation of the source mobility matrix, and in ensuring stable and repeatable contact conditions between source and receiver. The agreement between direct and indirect results can be highly variable. This is because of uncertainties in accelerometer positioning, background noise, secondary transmission paths (e. g. other DOFs), and in the sensitivity of the calculations. The two methods to indirectly determine the source mobilities appear capable of identifying global trends in the mobility data, such

as mass-like or spring-like behaviour. However, this study suggests that the methods are unlikely to be sufficiently accurate to reliably identify details such as individual resonances. In this representative case study, errors of up to 30 dB were found, with average errors ranging between ±5 dB and ±10 dB.

7.8 Summary

Two of the three formulations that were presented in Chapter 5 for the indirect determination of source mobility were investigated experimentally.

In conclusion, the following recommendations are made for a successful implementation of the described methods:

- Method 1 should be preferred over Method 2, as it requires less measurement effort and yields better results. However, if measurement at the contacts is not possible in the coupled state, Method 2 may be used. Both Method 1 and Method 2 should be preferred over Method 3.
- High-quality data is of critical importance. Care should be taken to achieve a good SNR, and to avoid experimental errors of misalignment. Accelerometers should not be moved between measurements, if possible.
- Over-determination should be employed to mitigate problems associated with matrix inversion. SVR further aids in reducing condition numbers.

Initial studies, with single steel blocks on a free 20 mm receiver plate, yielded good agreement in the low-frequency range (deviations within ±3 dB below 200 Hz), and discrepancies in other parts (systematic over-estimates up to 20 dB above 800 Hz). The discrepancies were investigated systematically, and it was found that the assumption of pure mass-like behaviour of the sources was incorrect. Furthermore, the significance of well-defined and repeatable contact conditions was highlighted, as well as the crucial importance of high-quality measurement data.

The measurement setup was modified accordingly (screwed instead of loose connections, shaker instead of hammer excitation, higher-sensitivity accelerometers, no movement of accelerometers between measurements), and the agreement between indirectly and directly determined source mobilities improved significantly. Deviations in the mass-dominated region were within ±3 dB. In the region of the anti-resonance frequency, the deviations reached values up to

±20 dB and ±30 dB for Method 1 and 2, respectively. Above the anti-resonance frequency, the deviations were within ±15 dB, though this high value was likely due to systematic errors in the direct measurement.

The suitability of the two methods (Method 1 and Method 2) for multi-contact sources was tested by placing two masses on the plate at the same time. It was observed that while the point mobilities are quantified with the same accuracy as the single mass-spring systems, phantom transfer mobilities appear which result from the involved matrix inversion.

A free Perspex beam was considered next, representing a highly-damped multi-modal source. A thinner (6 mm) and more damped plate was used as receiver. The agreement between indirectly and directly determined beam mobility was within ±5 dB between 60 Hz and 1 kHz, and within ±10 dB above 1 kHz. The higher damping of the receiver plate reduced the sensitivity of the methods to experimental errors, as it decreased the rate of change in the plate mobilities. Also, the importance of the source-receiver mobility ratio was highlighted. Best results are obtained when source and receiver mobility are in the same order of magnitude.

The free Perspex beam then was connected to the 6 mm plate at two positions, to investigate the ability of the methods to identify source transfer mobilities. It was found that between 100 Hz and 700 Hz, both point and transfer mobilities were quantified within ±5 dB using Method 1, and within ±10 dB using Method 2. While Method 1 showed results within ±10 dB of the direct measurement above 700 Hz, Method 2 yielded systematic over-estimates of about 11 dB in this frequency range.

Finally, a representative source structure was considered, a fan unit on a framed support structure, connected to the plate at three positions. The average deviations between directly and indirectly determined source mobilities ranged between ±5 dB (point mobilities above 400 Hz) and 17 dB (transfer mobilities for Method 2 above 1 kHz), with occasional deviations of up to ±30 dB.

If the power injected by such a source into a receiver structure is calculated from independent source and receiver data (for example according to Equation (2.9) or Equation (2.10)), the uncertainties attached to the source mobilities propagate to the source power data. In addition, the source activity in the form of free velocity or blocked forces is also subject to measurement

uncertainties, cf. Chapters 3 and 4. Considering the errors that are possible in experimentally determined source and receiver mobilities and source activity, the calculated source power can deviate considerably from the actual value. For this reason, more robust methods of obtaining the injected source power are required. One such method is the reception plate method, as described in EN 15657-1:2009 [17]. The reception plate method and a substitution method for the determination of injected source power in heavyweight construction are the topic of Chapters 8 and 9.

8 Indirect Methods to Obtain Source Power

8.1 Introduction

The most important quantity for the transmission of structure-borne noise from vibration sources into building structures is the injected vibrational power. There is a general consensus in the research community that structure-borne sound sources should be characterized in terms of source power [109, 99]. The injected power generally depends on the vibrational activity of the source, and on the dynamic characteristics of both source and receiver, cf. Section 2.3.

This chapter focuses on the case of high-mobility sources on low-mobility receivers, where $|Y_s| \gg |Y_r|$. This is the situation most commonly encountered in heavyweight construction (concrete/masonry buildings). The mobility mismatch between source and receiver allows several important simplifications, as discussed in Section 2.3. For example, it can be assumed that the source of interest behaves similarly on different low-mobility receiver structures. This allows the transformation of measurement data to other, similar receiver structures.

The injected source power usually cannot be measured directly, especially for multi-contact sources with multiple degrees of freedom. Therefore, indirect methods are needed to quantify the injected power. One practical approach, for sources in heavyweight construction, involves a reception plate method.

In Section 8.2, the theory of the isolated reception plate method is reviewed. Section 8.3 considers the application of the reception plate method to coupled plates, for example real walls and floors connected to other building elements. In Section 8.4, a practical implementation of the free reception plate method is discussed, described in EN 15657-1:2009 [17]. Finally, a source substitution method is proposed in Section 8.5, as an extension of the isolated reception plate method, to be used with real walls and floors.

8.2 Theory of isolated reception plates

A structure-borne sound source connected to a free receiver plate injects vibrational power into the plate. The source power level can be obtained by a simple power balance equation: the vibrational power injected from the source into the reception plate is equal to the energy loss of the plate [38].

8.2.1 SEA model of an isolated reception plate

Figure 8.1 illustrates the problem using an energetic approach (Statistical Energy Analysis [89, 36]). Since the reception plate is not connected to any other structure, there is only one subsystem in the model.

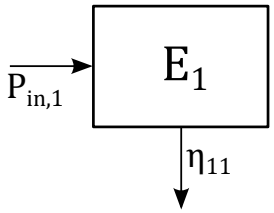

Figure 8.1: SEA model of an isolated plate.

The power balance equation of this system can be written as

$$P_{in,1} = \omega E_1 \eta_{11}, \tag{8.1}$$

where $P_{in,1}$ is the injected source power, η_{11} indicates the internal loss factor of the plate, ω is the radian frequency, and E_1 is the energy of the free plate. The entire injected source power remains in subsystem 1.

From Equation (8.1), it can be observed that in order to obtain the injected source power, two quantities need to be determined: the energy stored on the plate, and the internal loss factor. These quantities are now discussed.

8.2.2 Energy of the isolated reception plate

The bending wave energy conserved in the plate is taken to be twice its kinetic energy [40]. The kinetic energy of the plate is equal to half the product of plate mass m and spatially averaged squared velocity $\langle v^2 \rangle$ in the far field, assuming that most of the kinetic energy is stored in out-of-plane motion:

$$E_{\mathrm{kin}} = \frac{1}{2} m \left\langle v^2 \right\rangle .$$

With $E = 2E_{\mathrm{kin}}$,

$$E = m \left\langle v^2 \right\rangle . \tag{8.2}$$

To determine the energy of the isolated reception plate, it is therefore necessary to measure the plate mass and the velocity field on the plate.

Mass of the isolated reception plate

The plate mass m of the isolated reception plate can be determined either by direct measurement (weighing), or by calculation from the plate dimensions l_x, l_y, l_z and the density ρ:

$$m = V\rho = l_x l_y l_z \rho.$$

Mean square velocity on the isolated reception plate

The mean square velocity $\langle v^2 \rangle$ is obtained by measuring the velocity field on the plate. In practice, only a limited number of measurement positions is considered, and from this statistical sample an estimate of the mean square velocity is obtained. This sampling procedure can result in errors, in particular at low frequencies where the bending wavelength is large. To minimise errors resulting from individual plate eigenmodes dominating entire frequency bands, it is useful to have several eigenmodes in each frequency band of interest (*mode count* N). For a practical implementation of the reception plate method, Späh recommends a minimum number of five eigenmodes per frequency band ($N \geq 5$) [133].

The modal density n is the number of modes per Hertz. For high frequencies, the asymptotic modal density of a plate can be calculated as [72]

$$n_\infty = \frac{\Delta N}{\Delta f} = \frac{A}{2}\sqrt{\frac{m''}{B}}, \tag{8.3}$$

where A is the plate area, m'' is the mass per area, and B is the bending stiffness. At low frequencies, the boundary conditions of the plate assume importance, and a corrected modal density may be used [40]. For free (FFFF) boundaries,

$$n_{\mathrm{FFFF}}(f) = \frac{A}{2}\sqrt{\frac{m''}{B}} + \frac{1}{2}\sqrt{\frac{2\pi}{f}}\left(\frac{l_x + l_y}{\pi}\right)\left(\frac{m''}{B}\right)^{1/4}.$$

The higher the modal density, the more eigenmodes contribute to a given frequency band. However, a high modal density alone does not ensure a high overlap of these eigenmodes. If the total loss factor is low, the individual modes have a high quality and do not overlap sufficiently to limit errors associated with the statistical sampling of the bending velocity field.

A more appropriate measure for the appropriateness of statistical sampling is the *modal overlap factor* M. It is the product of modal density and loss factor, and describes the degree of overlap in the modal response. It is defined as the ratio of the 3 dB modal bandwidth to the average frequency spacing between eigenfrequencies [72]:

$$M = \frac{\Delta f_{3\,\mathrm{dB}}}{\Delta f} = f\eta n. \tag{8.4}$$

In room acoustics, a modal overlap factor of three is often taken as the lower limit of a reverberant field ($M \geq 3$, Schroeder frequency) [72]. For the statistical description of structural coupling of plates in buildings, for example using SEA, a desirable value for the modal overlap factor is unity, with at least five modes in every frequency band ($M \geq 1$, $N \geq 5$) [72]. Davis [40] suggests a modal overlap factor of three, as design target for a reverberant reception plate ($M \geq 3$).

Besides the dominance of individual eigenmodes, a further challenge for the determination of the mean square velocity concerns the distribution of kinetic energy on the plate. A large proportion of the bending wave energy of a free

plate is stored along the edges and in the corners, especially at low frequencies. The increase in kinetic energy density along the plate edges and in the corners is equivalent to the increase in sound pressure level along the walls and in the corners of reverberation chambers. For airborne sound sources, the so-called Waterhouse correction has been introduced to compensate this systematic variation [152]. For reception plates, work is currently being undertaken by Vogel, to investigate this so-called *edge effect*, to quantify the errors and propose an equivalent correction factor [149, 148].

8.2.3 Loss factor of the isolated reception plate

The loss factor η describes the energy loss of a structure when vibrational energy is injected. Energy can be lost by several mechanisms: by internal dissipation, where the vibrational energy is converted into heat; or by radiation, where the vibrational energy is radiated as audible sound; or by structural coupling, where the vibrational energy is lost to connected structures. The total loss factor includes all of these mechanisms [147]:

$$\eta_{total} = \eta_{internal} + \eta_{radiation} + \eta_{coupling}.$$

Experimentally, the total loss factor can be determined from the structural reverberation time T_s [72]:

$$\eta = \frac{6 \ln 10}{2\pi f T_s} \approx \frac{2.2}{f T_s}. \tag{8.5}$$

The measurement and calculation procedure for the structural reverberation time is similar to that for the reverberation time in rooms, as described in ISO 3382-1:2009 [12]. However, the process is more problematic, since the energy decays are shorter. A discussion on the measurement of structural reverberation time and the determination of the total loss factor is provided in Appendix D.

For an isolated plate such as in Figure 8.1, the total loss factor equals the internal loss factor, if the coupling losses and radiation losses can be assumed negligible. The energy decay curve has a single gradient (see Figure 8.5), and estimation of the loss factor is straightforward.

8.3 Theory of connected reception plates

Connected elements significantly change the vibro-acoustic behaviour of the plate system. Whilst all of the injected source power remains on an isolated plate, part of the injected power into real walls or floors is lost to connected elements. In addition, other elements on real walls or floors, such as fittings or pipes, can introduce unwanted transmission paths. This has consequences for the determination of total loss factor and mean square velocity.

8.3.1 SEA model of a connected reception plate

Figure 8.2 illustrates the situation, again using an SEA approach. For reasons of clarity only one connected element is considered.

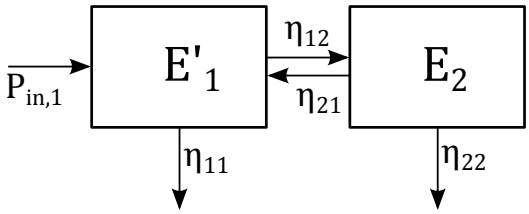

Figure 8.2: SEA model of two connected plates.

The power balance equations of the coupled plate system involve an energy transfer between the two subsystems:

$$P_{in,1} = \omega\eta_{11}E_1' + \omega\eta_{12}E_1' - \omega\eta_{21}E_2 \tag{8.6}$$

$$0 = \omega\eta_{22}E_2 + \omega\eta_{21}E_2 - \omega\eta_{12}E_1' \tag{8.7}$$

Here, the energy stored in subsystem 1 is denoted as E_1', to distinguish it from the isolated reception plate. η_{11} and η_{22} are the internal loss factors of the two plates, and η_{12} and η_{21} are the coupling loss factors between the plates. The first term in Equations (8.6) and (8.7) describes the internal losses. The second term describes the energy lost to the respective other subsystem, while the third term represents the power gain from energy returning from the other subsystem, indicated by the negative sign.

To accurately obtain the injected source power from Equation (8.6), the energy in both subsystems is required (E_1' and E_2), as well as the internal loss factor η_{11} and the coupling loss factors η_{12} and η_{21}. Using only the internal loss factor and energy of subsystem 1 will give a reasonable approximation of the injected source power only if the coupling loss factors to other elements are significantly smaller than the internal loss factor. Otherwise, the determined source power will be erroneous.

The relevant parameters (plate mass, mean square velocity, and loss factor) are now revisited, in the context of coupled plate systems.

8.3.2 Energy of the connected reception plate

The fundamental equation for the kinetic energy of an isolated plate (Equation (8.2)) is also valid for plates coupled to other building elements. The difficulty lies in the determination of mass and mean square velocity.

Mass of the connected reception plate

It can be difficult to estimate the mass of connected plates and real building elements. Direct weighing is impossible in this case. Indirect calculation may also be difficult, because it is not always obvious how much of the support structure should be taken into account. In addition, real building elements may have a composite nature, making it more difficult to estimate the density.

Mean square velocity of the connected reception plate

Hopkins and Robinson [73, 75] investigated the influence of the mean square velocity, when using the reception plate method with connected plates. They found that vibration levels can increase, due to returning energy from connected building elements. If all parameters in Equation (8.6) can be obtained (internal loss factor η_{11}, coupling loss factors η_{12} and η_{21}, and energies E_1' and E_2), then the correct source power is determined. In practice, only the energy of plate 1 is considered. Assuming that the correct loss factors are used, this leads to an over-estimate of the plate energy.

The ratio of the incorrectly determined source power P'_{in} and the actual source power P_{in} is given as

$$\frac{P'_{in}}{P_{in}} = \frac{\omega\eta_1 E'_1}{\omega\eta_{11} E_1}, \tag{8.8}$$

where $\eta_1 = \sum_n \eta_{1n}$ is the total loss factor of subsystem 1, when connected to n other subsystems.

The ratio in Equation (8.8) is now expressed as a function of loss factors only. With

$$\begin{pmatrix} P_{in} \\ 0 \\ \vdots \\ 0 \end{pmatrix} = \omega \begin{pmatrix} \eta_1 & -\eta_{21} & \dots & -\eta_{n1} \\ -\eta_{12} & \eta_2 & \ddots & -\eta_{n2} \\ \vdots & \vdots & \ddots & \vdots \\ -\eta_{1n} & -\eta_{2n} & \dots & \eta_n \end{pmatrix} \begin{pmatrix} E'_1 \\ E_2 \\ \vdots \\ E_n \end{pmatrix}, \tag{8.9}$$

the energy E'_1 is found by inverting the loss factor matrix η:

$$\begin{pmatrix} E'_1 \\ E_2 \\ \vdots \\ E_n \end{pmatrix} = \frac{1}{\omega} \begin{pmatrix} \eta_1 & -\eta_{21} & \dots & -\eta_{n1} \\ -\eta_{12} & \eta_2 & \ddots & -\eta_{n2} \\ \vdots & \vdots & \ddots & \vdots \\ -\eta_{1n} & -\eta_{2n} & \dots & \eta_n \end{pmatrix}^{-1} \begin{pmatrix} P_{in} \\ 0 \\ \vdots \\ 0 \end{pmatrix}. \tag{8.10}$$

Since only the power input into subsystem 1 is non-zero, the solution for E'_1 depends solely on the first matrix element in $\eta^{-\mathbf{1}}$:

$$E'_1 = \frac{1}{\omega}\eta^{-1}(1,1)P_{in} \tag{8.11}$$

With $E_1 = 1/(\omega\eta_{11})P_{in}$, the ratio P'_{in}/P_{in} can now be calculated. For example, for the two-plate system in Figure 8.2,

$$\frac{P'_{in}}{P_{in}} = \frac{\omega(\eta_{11}+\eta_{12})E'_1}{\omega\eta_{11}E_1} = \frac{\eta_{11}+\eta_{12}}{\eta_{11}+\eta_{12}-\left(\dfrac{\eta_{12}\eta_{21}}{\eta_{22}+\eta_{21}}\right)}. \tag{8.12}$$

Figure 8.3 shows three simple coupled plate systems. The source plate is indicated in dark grey. Case A is the two-plate system whose SEA model is shown in Figure 8.2. Case B is a system of three mutually connected plates. Case C consists of a horizontal plate connected to four walls. The walls are mutually connected, except opposite walls. A practical example of such a system is a transmission suite, such as is used as receiver in Section 9.3.

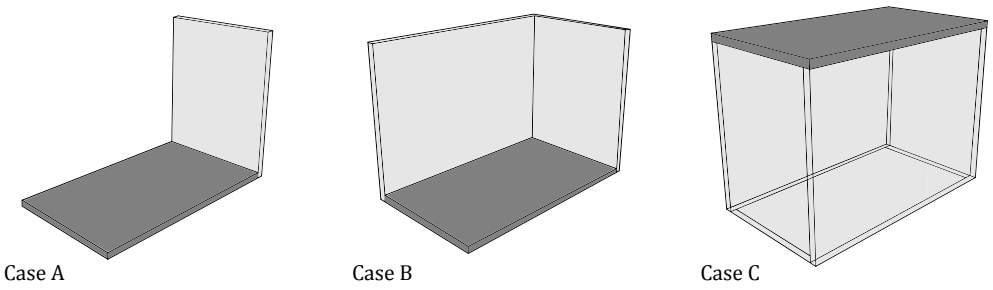

Figure 8.3: Coupled plate systems.

Assuming that all internal loss factors are equal ($\eta_{11} = \eta_{22} = \eta_{ii}$), and all coupling loss factors are equal ($\eta_{12} = \eta_{21} = \eta_{ij}$), the ratio P'_{in}/P_{in} is calculated for varying ratios of η_{ij}/η_{ii} for the three cases depicted in Figure 8.3. Figure 8.4 shows the ratio P'_{in}/P_{in} as a function of the sum of the coupling loss factors divided by the internal loss factor: $\sum_{j,j\neq i} \eta_{ij}/\eta_{ii}$. The higher the coupling losses, the greater the error in the determined source power.

For the practically most relevant situation, Case C, an estimate of the expected error in a real measurement is found using empirical values of loss factors of concrete structures. The total loss factor for bending waves on masonry or concrete plates that are rigidly connected on all sides can be approximated by [35, 72]

$$\eta_i = \eta_{ii} + \frac{X}{\sqrt{f}}. \tag{8.13}$$

The term $X/\sqrt{f}$ denotes the sum of all coupling losses. The value of X depends on the building situation. In the field and laboratory, X has values between 0.3 and 1 [72]. For $X = 0.4$ and at 100 Hz, the sum of the coupling loss factors is 0.04. Assuming an internal loss factor of 0.005 for concrete cast *in-situ* [72], $\sum_{j,j\neq i} \eta_{ij}/\eta_{ii} = 8$. Hence, the expected error in determined source power for Case C is 3.9 dB at 100 Hz. With increase in frequency, the error decreases, as coupling losses get smaller.

The considerations regarding the mean square velocity in this section assume, that the internal and coupling loss factors can be determined accurately. In practice, the determination of loss factors of connected elements is challenging, and the associated errors and uncertainties can significantly reduce the accuracy of the determined source power.

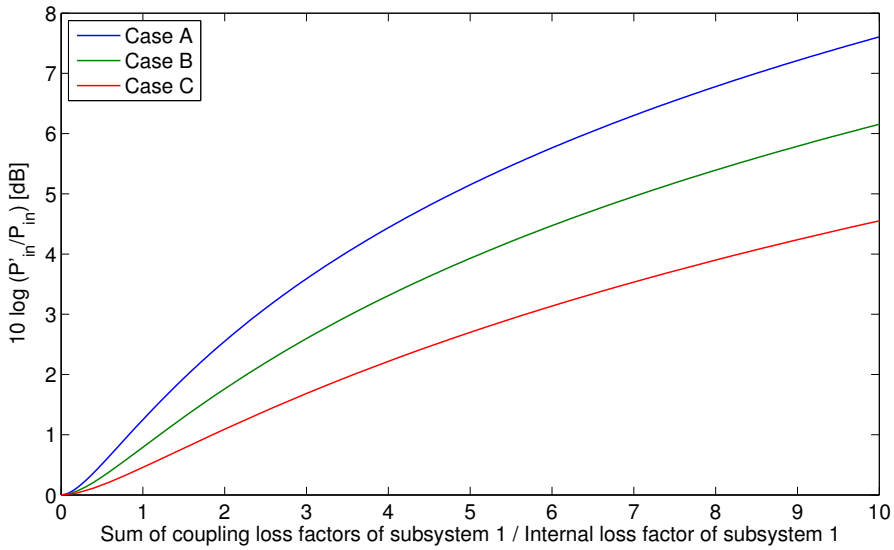

Figure 8.4: Error in source power due to over-estimate of mean square velocity.

8.3.3 Loss factor of the connected reception plate

Measurement of the total loss factor of connected plates is less straightforward than for isolated plates. A typical energy decay curve of a free plate measurement is a straight line (on a logarithmic scale), with a single gradient. For a connected element, the energy decay curve typically shows multiple slopes, due to energy returning from connected elements. Figure 8.5 shows the idealized energy decay curves of a free plate and of the same plate connected to a second plate, calculated using a Transient SEA model according to [117]. The energy decay curve for the connected plate system shows curvature, visible in particular in the early part of the decay.

Evaluation of the structural reverberation time for an energy decay curve with multiple slopes is possible, but requires careful attention to determine the usable range of evaluation [74]. Only the initial decay of the curve should be used, as later parts of the decay include energy returning from other elements. Single gradient fits of such energy decay curves result in an over-estimate of the structural reverberation time, and consequently in an under-estimate of the loss factor and the source power.

A Transient SEA model according to [117] was employed to simulate the energy decay curves for the three cases in Figure 8.3. All internal loss factors were

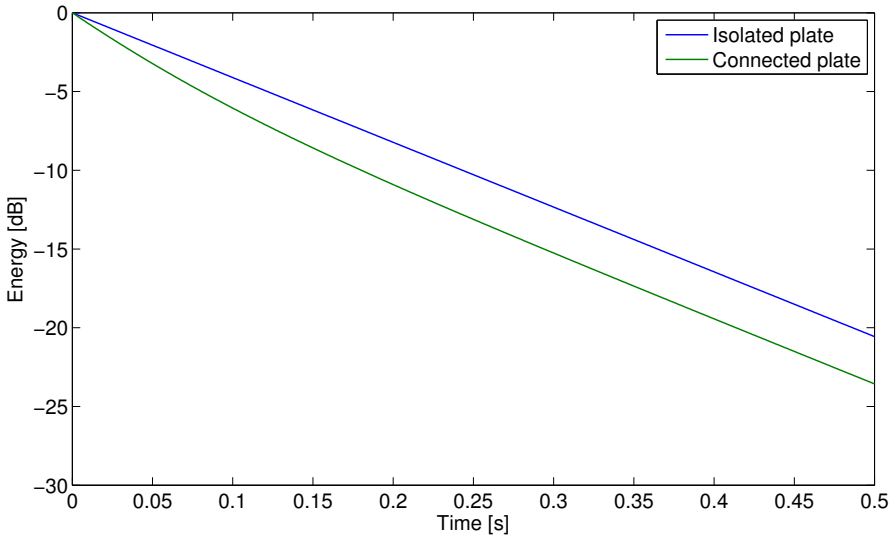

Figure 8.5: Idealized energy decay curves for isolated and connected plate.

assumed equal, and all coupling loss factors were assumed equal. The total loss factor of the source plate was estimated from the energy decay curves, using different evaluation ranges: T5: −5 dB to −10 dB; T10: −5 dB to −15 dB; T20: −5 dB to −25 dB. The determined total loss factor was then compared with the total loss factor that was calculated from internal and coupling loss factors used as input parameters in the TSEA model. Figure 8.6 shows the errors, as a function of the ratio between the sum of the coupling loss factors and the internal loss factor, as in Figure 8.4.

The error in the total loss factor depends on the number of connected elements, the degree of coupling, and the evaluation range used for the estimation of the structural reverberation time. For Case C and a ratio of $\sum_{j,j\neq i} \eta_{ij}/\eta_{ii} = 8$, the under-estimate of the total loss factor is −8.5 dB for T20, and −5.5 dB for T5. At the same time, the mean square velocity is over-estimated by 3.9 dB, as described in Section 8.3.2. The error in the source power therefore lies between −4.6 dB and −1.6 dB, depending on the evaluation range used for the loss factor estimation. The errors in mean square velocity and total loss factor partly compensate each other.

Hopkins and Robinson [73, 75] demonstrated this effect for a range of typical building situations. They conclude that it may be possible to get “the right answer for the wrong reasons.” This depends on the building situation and the

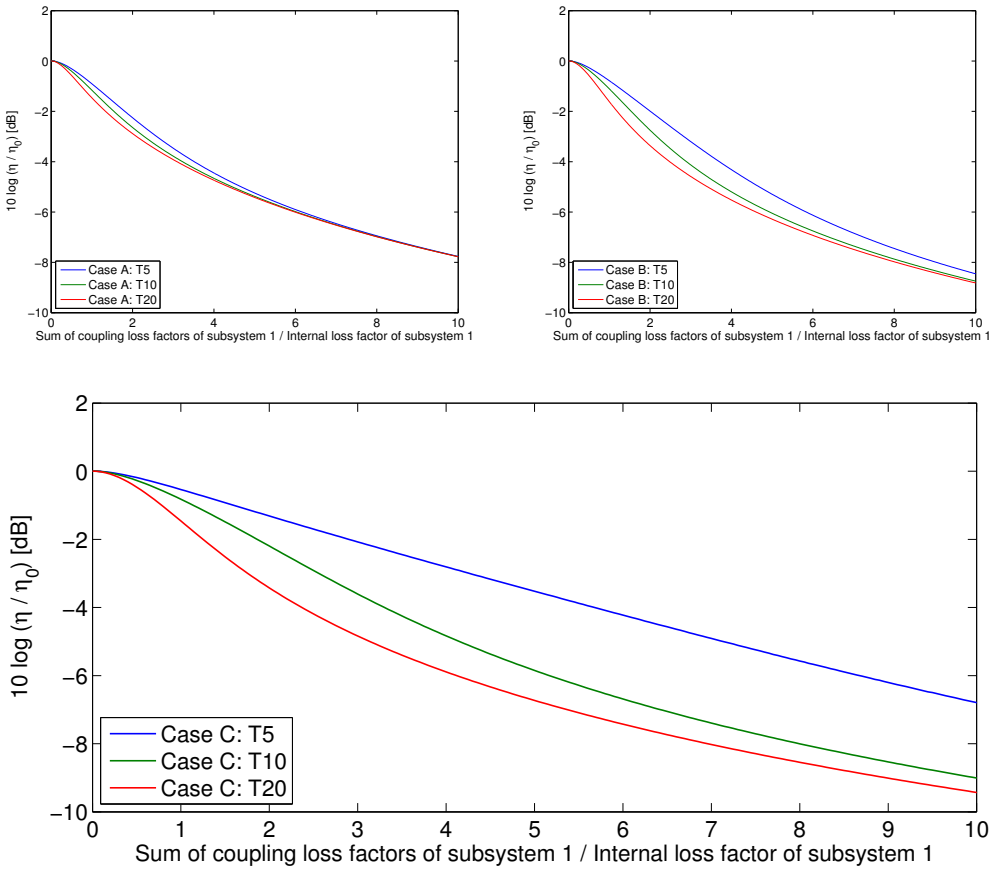

Figure 8.6: Error in source power due to under-estimate of total loss factor.

chosen evaluation parameters. They conclude that in general, using walls and floors in heavyweight buildings as coupled reception plates can incur significant errors, and that alternative approaches should be sought.

8.4 Implementation of the reception plate method

The use of an isolated reception plate for the determination of structure-borne source power has been studied in detail [40, 63, 61, 132, 133, 134]. In this section, the reception plate method for high-mobility sources in heavyweight construction is discussed, as described in EN 15657-1:2009 [17].

8.4.1 EN 15657 Part 1 (2009)

Part 1 of EN 15657 (2009) specifies the source of interest to be operated on a concrete reception plate (density of $2300 \pm 200\,\mathrm{kg/m^3}$) with free boundary conditions. The plate must have a thickness of $10 \pm 1\,\mathrm{cm}$, a minimum surface area of $5\,\mathrm{m}^2$ (preferably more than $7\,\mathrm{m}^2$), and a ratio length/width close to $\sqrt{2}$.

With the source attached and in operation, the average steady-state squared velocity on the plate is recorded. The total power injected by the source into the plate is equal to the bending wave energy loss in the plate. The source power P_{Source} is determined from the power balance (see Section 8.2.1):

$$P_{Source} = P_{Plate} = \omega \eta m \left\langle v^2 \right\rangle . \tag{8.14}$$

The source mobility is assumed to be significantly higher than the receiver mobility ($|Y_s| \gg |Y_r|$). This ensures a similar situation as in the installed condition in heavyweight buildings. P_{Plate} is the source power for this particular source-receiver combination. For the transformation of the source data to other building elements, the average receiver point mobilities of reception plate and building element at the source contacts must be determined. The source power in the installed condition can then be obtained:

$$P_{in-situ} = P_{Plate} \frac{\mathrm{Re}\left\{\langle Y_{in-situ} \rangle\right\}}{\mathrm{Re}\left\{\langle Y_{Plate} \rangle\right\}}. \tag{8.15}$$

For comparison between laboratories, EN 15657-1:2009 also defines a *characteristic reception plate power* P_{char}. To obtain P_{char}, the reception plate power P_{Plate} is normalized with respect to the average real part of the plate point mobilities at the source contacts and an infinite plate mobility Y_∞ of $5 \cdot 10^{-6}$ $\mathrm{ms^{-1}/N}$:

$$P_{char} = P_{Plate} \frac{Y_\infty}{\mathrm{Re}\left\{\langle Y_{Plate} \rangle\right\}}. \tag{8.16}$$

The characteristic reception plate power is considered an independent measure of the source. For the estimation of the source performance in the installed condition, the receiver mobility is required.

8.4.2 Determination of required parameters

Plate mass

The mass of the isolated reception plate can be determined as in Section 8.2.2, either by direct weighing or by calculation from dimensions and density. Typical values for a standardized concrete plate lie between 1000 kg and 1500 kg.

Receiver mobility

The average real part of the reception plate point mobilities at the source contacts is required in third-octave bands. There is currently no standardized method to obtain this data.

For the characteristic power, a representative infinite plate mobility in heavyweight construction is used. The *infinite plate mobility* is the mobility of a plate with same material properties and thickness, but infinite dimensions [38]:

$$Y_\infty = \frac{1}{8\sqrt{Bm''}} \tag{8.17}$$

Here, m'' is the mass per area, and B is the bending stiffness of the plate:

$$B = \frac{Eh^3}{12(1-\nu^2)} \tag{8.18}$$

E is Young's modulus of elasticity, h is the thickness, and ν is Poisson's ratio.

Mean square velocity

It was pointed out in Section 8.2.2 that in order to limit errors associated with the statistical sampling of the bending wave energy on the reception plate, a high modal overlap factor is desirable. For a plate of given material (fixed E, ρ, ν) and with fixed loss factor η, a high modal overlap factor can be achieved by increasing the plate area A, or by reducing the thickness h:

$$M = f\eta n = f\eta \frac{A}{2}\sqrt{\frac{m''}{B}} = f\eta \frac{A}{2h}\sqrt{\frac{12\rho(1-\nu^2)}{E}}. \tag{8.19}$$

While increasing the plate area has practical limitations, due to space in the laboratory, reducing the thickness is in conflict with the requirement for a low receiver mobility – a thicker plate has a lower mobility:

$$Y_\infty = \frac{1}{8\sqrt{Bm''}} = \frac{1}{8h^2}\sqrt{\frac{12(1-\nu^2)}{E\rho}}. \tag{8.20}$$

The modal density of a plate (and with it the modal overlap factor) is directly related to the frequency-averaged driving point mobility of the plate [34, 38]:

$$n = 4m\langle \mathrm{Re}\,\{Y_{Plate}\}\rangle = 4mY_\infty \tag{8.21}$$

Hence, when designing a reception plate for the heavyweight construction sector, a suitable compromise between competing design targets (high modal overlap factor and high modal density on the one hand, and low plate mobility on the other hand) is required. In the design of the standardized reception plate in EN 15657-1:2009, a representative receiver mobility was deemed most important. A target receiver mobility of $5 \cdot 10^{-6}$ $\mathrm{ms}^{-1}/\mathrm{N}$ requires a plate thickness of at least 10 cm for concrete. For a high modal density, the plate area must be chosen as large as possible. However, practical considerations create limitations to this demand. The standard specifies a minimum plate area of $5\,\mathrm{m}^2$.

Figure 8.7 shows the loss factor, mode count, and modal overlap factor of a typical concrete reception plate according to EN 15657-1:2009. Loss factor values were taken from [132]. Only above 600 Hz does the plate have more than five eigenmodes per third-octave frequency band. The modal overlap factor is lower than unity across the frequency range of interest. Especially at low frequencies, random sampling of the bending field can result in errors, due to large variations in the velocity response and few contributing eigenmodes.

Furthermore, the distribution of kinetic energy on a free plate is not homogeneous, as explained in Section 8.2.2. The kinetic energy density increases along the edges and in the corners. Späh suggested an empirical sampling strategy, using at least 12 response positions, including one on a long and one on a short edge, but none at a corner [133]. In his numerical case study with a point source, this sampling strategy resulted in an under-estimate of about 0.5 dB at low frequencies, and an over-estimate of about 0.5 dB at high frequencies.

Frequency [Hz]	Loss factor [-]
50 Hz	0.255
63 Hz	0.237
80 Hz	0.147
100 Hz	0.112
125 Hz	0.054
160 Hz	0.047
200 Hz	0.047
250 Hz	0.036
315 Hz	0.033
400 Hz	0.031
500 Hz	0.028
630 Hz	0.025
800 Hz	0.029
1000 Hz	0.020
1250 Hz	0.018
1600 Hz	0.014
2000 Hz	0.013
2500 Hz	0.012
3150 Hz	0.012
4000 Hz	0.011
5000 Hz	0.009

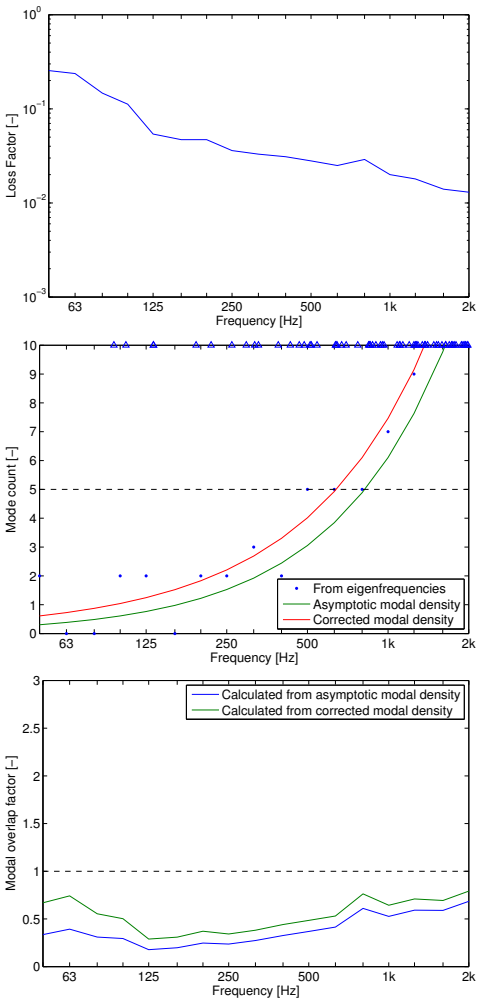

Figure 8.7: Loss factor (after [132]), mode count and modal overlap factor of concrete reception plate according to EN 15657-1:2009.

In his experimental case study with a shaker on a concrete reception plate, the injected power was determined within 1 dB in most frequency bands, with occasional outliers of up to 5 dB. The suggested sampling strategy therefore seems capable of avoiding extreme deviations in the determined source power. However, the standard EN 15657-1:2009 does not define how to sample the velocity field. In fact, due to practical considerations, the standard does not allow the placement of accelerometers in the corners and along the edges. Since the standard addresses sources of different shapes and sizes, a general sampling strategy was not implemented [131]. Since the permitted sampling areas are away from corners and edges, the mean square velocity will generally be under-

estimated, especially at low frequencies. As a consequence, the plate power and the injected source power will generally be under-estimated.

Loss factor

The total loss factor of the isolated reception plate can be determined as described in Section 8.2.3. Typical values for a standardized concrete plate range between 0.01 for high frequencies and 0.25 for low frequencies, see Figure 8.7. The internal loss factor for *in-situ* concrete is 0.005 [72]. The increased total loss factor of the reception plate, especially at lower frequencies, is a consequence of the damping material at the edges. In the design of the standardized reception plate, supports with good isolating properties and high internal damping were selected, in order to isolate the plate while at the same time increasing the total loss factor of the plate system [132]. The supports are made of mixed-cellular polyetherurethane (PUR), with an internal loss factor of 0.6 [4].

8.4.3 Round robin test

The reception plate method for isolated concrete plates, as standardized in EN 15657-1:2009, has recently been tested in a European round robin test, conducted by CEN TC 126 WG 7 [154, 155]. With five participating laboratories using plates according to the standard, a standard deviation of reproducibility of 4 dB in third-octave bands was obtained for the characteristic reception plate power. The standard deviation of repeatability was 3 dB in third-octave bands, for all participating laboratories. These values are larger than values usually encountered in airborne sound power measurements. Given the theoretical inconsistencies described in the previous sections, in particular with regard to the measurement of the mean square velocity, it is almost surprising that the method seems to give reproducible results. In spite of the limitations mentioned earlier, from the author's perspective the reception plate method for free plates as standardized in EN 15657-1:2009 currently appears to be the most practical and most reliable method to determine the structure-borne source power in heavyweight construction.

However, the determination of injected power for sources attached to walls instead of floors is problematical. While there are some laboratories with free

horizontal reception plates, there is (to the author's knowledge) currently only one laboratory in Europe with a free vertical reception plate (HFT Stuttgart).

8.4.4 Real walls and floors as reception plates

For practical and economic reasons, there is interest in using the reception plate method with coupled reception plates, formed by walls or floors that are rigidly connected to other parts of a heavyweight building. Most acoustics laboratories have transmission suites, whose walls or floors could be used as coupled reception plates. In some cases, it may also be difficult to mount the source of interest on a free plate, or even bring it into the laboratory (e. g. lightweight stairs as in [124]). In these cases, the actual installation wall could be used as a reception plate, allowing an *in-situ* measurement. The advantages of using coupled plates/real walls and floors instead of free plates in the laboratory are manifold.

When using real walls and floors as reception plates, the challenges described in Section 8.3 come into play. Loss factor measurements require closer attention, and energy returning from connected elements can increase the measured vibration levels on the receiver plate, leading to over-estimates of the injected source power. As described in Section 8.3.2, the over-estimate due to vibration level measurements may be compensated by the under-estimated loss factors. However, this is difficult to predict reliably.

In the round robin test conducted by CEN TC 126 WG 7 (see Section 8.4.3), three connected concrete plates were investigated in addition to the five free plates [154]. The three connected plates had different dimensions than the free plates, and all were part of transmission suites or laboratory chambers. The results from the non-standardized connected reception plates were found to be "not in contradiction" to results from the standardized plates.

In the following section, the source substitution method is proposed as a possible development of the reception plate method, and as a way of circumventing the problems described.

8.5 Source substitution method

8.5.1 Theoretical background

In seeking an alternative test method to determine structure-borne source power, reference is made to methods for the measurement of airborne source power. The reception plate method is the structure-borne equivalent of the reverberation chamber test method as described in ISO 3743-2:2009 [14]. The source of interest is operated in an environment with no (or very small) losses at the boundaries; a diffuse sound field is assumed, the energy decay curve has a single gradient; the source power can be determined by sampling the energy of the diffuse field.

As an alternative to ISO 3743-2:2009, ISO 3743-1:2010 [13] requires the source to be operated in a hard-walled test room with relatively small losses at the boundaries. The source power is determined by employing a source substitution method. In a first step, a standard source with known power is operated in the room, and the resulting sound pressure level measured at several positions, arbitrarily selected but away from the source and reflecting surfaces. In the second step, the standardized source is replaced by the source of interest, and the sound pressure measured again at the same positions. Assuming that the ratio between source power and sound pressure level does not change, the source power can readily be calculated.

The structure-borne equivalent of a hard-walled test room with relatively small losses at the boundaries is a connected wall or floor with weak coupling to other elements. Unlike for airborne sources, the power of structure-borne sound sources generally depends on both source and receiver properties (see Section 2.3). Therefore, having a standardized source with known power output is not feasible.

Larsson and Simmons [83, 21] employ the standard tapping machine [11] as a substitute reference source. The procedure proposed is as follows: The source of interest is placed on the wall or floor, and the average velocity on the receiver plate measured during operation of the source. Alternatively, the average sound pressure level in a receiver room may be measured. In a second step, the source of interest is replaced by the standard tapping machine. Once again, the average velocity on the receiver plate (or the average sound pressure level) is measured,

at the same positions. The velocity level difference (or sound pressure level difference) can then be used to calculate an "equivalent force" of the source under test:

$$F^2_{\mathrm{Source,eq}} = F^2_{\mathrm{STM}} \, \frac{\langle v^2_{\mathrm{Source}} \rangle}{\langle v^2_{\mathrm{STM}} \rangle}$$

Here, F_{STM} is the force spectrum of the standard tapping machine, which is specified in Annex F of EN 12354-5:2009 [16]. The equivalent force of the source can then be used to estimate a characteristic structure-borne sound power level, which is used in EN 12354-5:2009 for the prediction of sound pressure levels due to service equipment.

The advantage of this substitution method is that it uses the readily available standard tapping machine, and provides data that can immediately be used in prediction models. A disadvantage of this method is that sources attached to walls cannot be measured, as the standard tapping machine cannot be operated in a vertical position. Another disadvantage is that the receiver mobilities still need to be measured, in order to transfer the data to other building elements. Despite these limitations, this substitution method provides a convenient way to determine the source power in heavyweight construction.

The alternative approach, proposed below, makes use of the fact that the emitted power of a reference source can be measured directly by recording force and velocity between source and receiver: $P = \mathrm{Re}\{vF^*\}$. A shaker can be used as calibration source, as it is easily controllable and has a single point connection to the structure. Scheck used this method for a single contact source with pure force excitation, and found good agreement between the method and a reciprocal power measurement [124, 123].

8.5.2 Measurement procedure

The proposed procedure has two stages (see Figure 8.8). In the calibration stage, a known power P_{cal} is injected into the receiver plate (for example by a shaker), and the squared response velocities v^2_{cal} on the plate are recorded. In the second stage, the shaker is replaced by the source of interest, and the squared velocities v^2_{source} on the plate are measured at the same accelerometer positions.

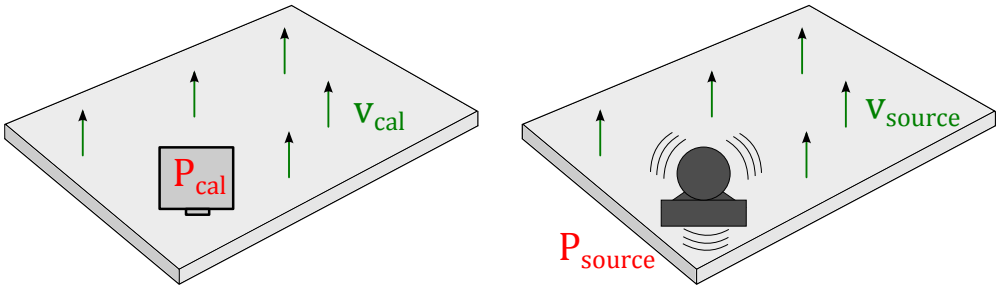

Figure 8.8: Two stages of the source substitution method: calibration with a reference source, and measurement of the source of interest.

Once the input power and the velocity responses have been recorded, there are several ways of evaluating the data. Four procedures are distinguished:

1. $$P_{source} = \langle v^2_{source} \rangle \frac{P_{cal}}{\langle v^2_{cal} \rangle} = \frac{\langle v^2_{source} \rangle}{\langle v^2_{cal} \rangle} P_{cal} \tag{8.22}$$

   Equation (8.22) corresponds to the averaging procedure used in ISO 3743. The mean square velocity on the plate is calculated for calibration and measurement stage. This can be described as an energetical approach, as the mean square velocity is proportional to the energy on the plate. In fact, Equation (8.22) can be derived from the power balance equation that forms the basis of the reception plate method, Equation (8.14). A reasonably reverberant field is required, and response positions close to the source have a larger influence on the result than response positions further away. The ratio $\langle v^2_{cal} \rangle / P_{cal}$ is termed *power calibration factor*.

2. $$P_{source} = \langle v^2_{source} \rangle \langle \frac{P_{cal}}{v^2_{cal}} \rangle \tag{8.23}$$

   Equation (8.23) resembles a transfer function approach, rather than an energetical approach. The individual ratios between input power and velocity response are averaged, and multiplied with the mean square velocity during operation of the source.

3. $$P_{source} = \langle v^2_{source} \rangle \frac{1}{\langle v^2_{cal} / P_{cal} \rangle} \tag{8.24}$$

   Equation (8.24), at first sight, looks very similar to Equation (8.23). It is

also a transfer function approach, but this time uses the ratio v_{cal}^2/P_{cal}. Although the two methods look similar, they can give very different results. On further investigation, it becomes clear that this method is the same as option one. This is confirmed when assuming that P_{cal} is a constant and can therefore be taken out of the averaging brackets. The resulting expression is equal to Equation (8.22).

4.
$$P_{source} = \langle \frac{v_{source}^2}{v_{cal}^2} \rangle P_{cal} \tag{8.25}$$

Equation (8.25) comes closest to the ideal of a substitution method. The differences in velocity between calibration stage and measurement stage are calculated for each individual response position. Then the average velocity difference is calculated. This results in a constant "weighting" of the accelerometer positions, and possibly in a smaller standard deviation. The ratio $\langle v_{source}^2/v_{cal}^2 \rangle$ is referred to as *velocity difference*.

8.5.3 Choice of reference source for calibration

For calibration, force and velocity at the contacts and velocities at remote positions on the receiver are recorded. An electro-dynamic shaker provides control of the excitation spectrum and level (important for a good signal-to-noise ratio), and is a useful tool for many applications in structural acoustics [82]. However, the shaker can pose practical challenges, especially when conducting measurements in the field. For example, suspending a (sometimes relatively heavy) shaker and fixing it to a wall without inducing moments can be problematical. This approach is especially time-consuming for multi-contact sources, when the shaker has to be connected to the wall at various positions.

In this thesis study, an instrumented impulse hammer was considered as a practical alternative. The hammer can easily be moved to different excitation positions. However, it only offers limited control over the excitation level, depending on the operator skill, and very limited control over the excitation spectrum (by use of different hammer tips, i. e. hard or soft indenters).

The use of transient excitation signals (i. e. impulses) instead of steady-state signals (e. g. pink or white noise) increases the involved post-processing effort. This has been the case in the transition from steady-state SEA to Tran-

sient SEA measurements [117]. An important question is whether the ratio of transient velocity response to transient power input is the same as for the steady-state case. If this is not the case, the calibration obtained with a hammer will only be valid for transient sources with similar excitation characteristics. This was investigated in experimental studies in Chapter 9. The advantages in practicability warrant the investigation of a transient calibration source. If the source substitution method is to be used not only in the laboratory but also in the field, then practical implementation assumes great importance.

Also of practical interest would be a single power calibration factor for the entire floor or wall, independent of the source tested in the measurement stage, i. e. independent of number and location of the source contacts. A given wall or floor could then be calibrated once for a fixed set of velocity response positions. After this initial calibration, any source could be tested at any location on the floor, without the need of repeating the calibration procedure. The generation of an average power calibration factor for a given wall or floor would be a useful development, especially if the wall or floor is to be used repeatedly, for example as in a laboratory.

8.5.4 Practical considerations

Multiple contact points

Most structure-borne sound sources have multiple connection points with the receiver structure. The phase relationship between contacts can assume importance at low frequencies. For example, if a source has two feet which move with the same amplitude, but exactly out of phase, then the net power flow into the structure may be zero, depending on the receiver mobilities at the two contacts. As a practical way forward, it is suggested to excite the receiver plate at each of the contact positions, measure input power and response velocities, and then calculate the average. An additional approach could be to place the source at different locations on the receiver plate, or turn it. This will help to limit the influence of source directivity.

Multiple components of excitation

Electro-dynamic shakers and impulse hammers generally only exert a linear force, perpendicular to the receiver structure. Therefore, only one degree of freedom is considered during the calibration stage. A structure-borne sound source, on the other hand, may also induce moment excitation. For the determination of the injected source power, this difference is of no significance. Like the reception plate method in Section 8.4.1, the source substitution method yields a single equivalent value for the source power, which incorporates both force and moment transmission. The component and strength of excitation at the contacts is not obtained.

Number of response positions

Theoretically, the source substitution method requires only one response velocity. However, due to the modal behaviour of the receiver plate, accelerometer positions may be close to nodal lines, and spatial sampling is required. The higher the number of uncorrelated response positions, the better the estimate of source power. The response positions for the calibration stage and the measurement stage should remain the same. Also, the response positions should be chosen far enough from the source, to avoid nearfield effects. The distances from plate boundaries should in principle only have a limited effect, as long as they remain the same. However, response positions at the corners or edges may dominate positions in the centre, depending on the averaging procedure used.

High-mobility source condition

As discussed in Section 2.3, the power injected by a source into a receiver structure depends on the mobilities of both source and receiver. Therefore, the determination of source power with a different receiver structure or mounting situation is only useful if the measurement setup resembles the installed condition. This assumption often applies for high-mobility source situations, where $|Y_s| \gg |Y_r|$. In this case, the acquired source power data is transferable to other, similar installations. However, a mobility correction is usually necessary, as in Equation (8.15). When using the free reception plate method, the

measurement of the average plate mobilities at the source contacts requires an additional measurement step. This is not the case for the source substitution method. Both force and velocity at the source contacts are recorded during the calibration stage, and the average receiver mobility can readily be calculated from the already acquired data.

Matched-mobility source condition

If the source data does not need to be transferable, but is only required for the mounting situation under test, the source substitution method can be useful, if direct power measurement is not possible. Even for matched mobility conditions, the method should yield a good estimate of the source power. However, the method requires a homogeneous receiver structure when using Equation (8.22). When using Equation (8.25), non-homogeneous receiver structures can theoretically be used, too.

Application to large, unmoveable sources

An additional practical advantage is that in certain cases the calibration can be performed with the source already in place. This requires that the source mobility is much higher than the receiver mobility, so as to not dynamically load the receiver plate and influence the vibration field, when excited externally [158]. The second requirement is that the receiver can be excited at the source contacts, or at least near the source contacts. This allows the determination of source power for complicated, distributed sources which cannot easily be brought into the laboratory or disconnected from the receiver structure (for example sanitary installations or heating systems).

8.6 Summary

The theory of isolated and connected reception plates has been discussed, and advantages and challenges were highlighted.

The reception plate method for free concrete plates, as described EN 15657-1:2009, currently appears to be the most practical and reliable method to determine the injected source power into heavyweight building elements. However,

there are potential issues, due to a too low modal overlap factor, and due to neglecting of edge effects.

When using real walls or floors as reception plates, the determination of the total loss factor becomes problematical. This can result in significant errors due to energy returning from connected walls and floors. However, coupled reception plates can sometimes give the right answers for the wrong reasons, because the errors in the loss factor determination are compensated by errors in the mean square velocity measurement.

A source substitution approach was considered as an alternative method to estimate the source power of high-mobility sources in heavyweight construction. The method circumvents the problems described with the reception plate method, namely energy returning from connected walls and floors, and offers a practical extension to the established reception plate method for free plates.

In Chapter 9, the source substitution method is investigated experimentally.

9 Experimental Validation of Indirect Methods to Obtain Source Power

9.1 Introduction

In Chapter 8, the reception plate method for the determination of source power in heavyweight construction was discussed. The challenges for its application to coupled plates were highlighted, and a substitution method was considered as an alternative approach. In this chapter, the substitution method was investigated experimentally. Three experimental studies were conducted.

In the first study, the structure-borne power from a test source into a free aluminium plate was determined, using the reception plate method and the source substitution method. Direct measurements of the injected power, using force transducers and accelerometers at the contacts, were used as benchmark.

The second study considered a coupled receiver structure. The structure-borne power from a test source into the concrete floor of a transmission chamber was determined, using the reception plate method and the substitution method.

In the third study, a combined heating and power unit was operated on a masonry wall of a reverberation chamber. Due to the nature of this source, an *in-situ* measurement method like the substitution method is the only viable option to determine the injected source power.

9.2 Test source on a free aluminium plate

A test source was operated on a free aluminium reception plate. The source was the same that was used in Chapter 4, consisting of a metal base with a top-mounted shaker. It incorporated force transducers at its feet, and was rigidly glued to the plate. Three of the four feet were connected to the plate (foot 2 was not used), to ensure a stable connection at all contacts. The shaker was driven with pink noise, allowing evaluation of the excitation signal across the frequency range of interest.

The same plate that was used in Chapters 3, 4, and 7 was used as receiver structure. It is an aluminium plate of size 2.12 m × 1.50 m × 20 mm, supported at the corners and edges by visco-elastic patches (Getzner SyloDamp HD30). This configuration creates free boundary conditions for the plate, and

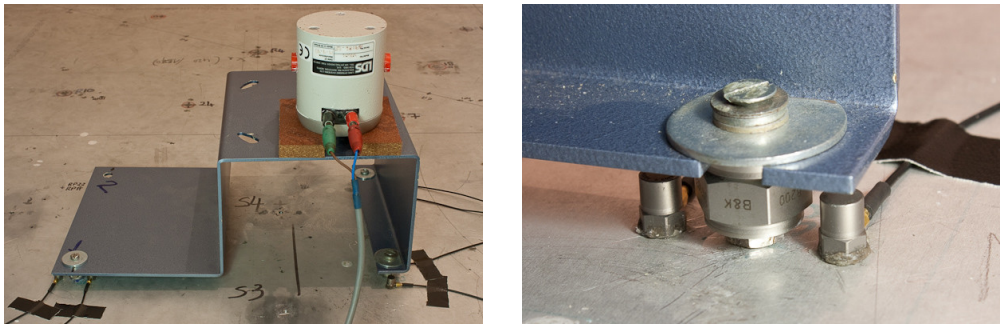

Figure 9.1: Setup for measurement of test source on free aluminium plate.

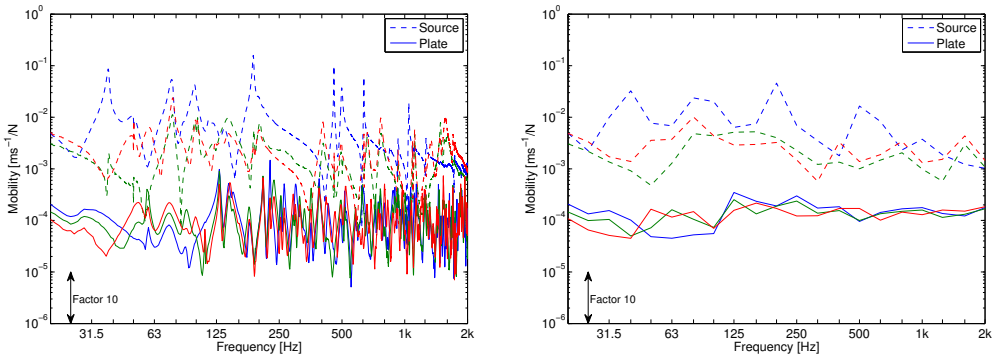

Figure 9.2: Narrowband and third-octave band source and receiver mobilities, for the study with a simple test source on a free aluminium plate.

additionally provides damping, mainly at low frequencies. Figure 9.1 shows details of the measurement setup.

Source and receiver mobilities were measured directly, and are shown in Figure 9.2. In third-octave band values, the source mobilities are significantly higher than the plate mobilities (by a factor of 10 or more), for the entire frequency range of interest. Inspection of the narrowband mobilities reveals that the source mobility is occasionally in the same order of magnitude as the receiver mobility, at its anti-resonances. However, this only assumes importance in the transformation of the measured data to other receiver structures.

Figure 9.3 shows the source positions on the plate (S1, S3, S4), and the response positions used for the reception plate method and the source substitution method. The total loss factor of the plate is shown in Figure 3.3. The internal loss factor of aluminium lies below 0.001 [72], hence the total loss factor is dominated by losses introduced by the support patches.

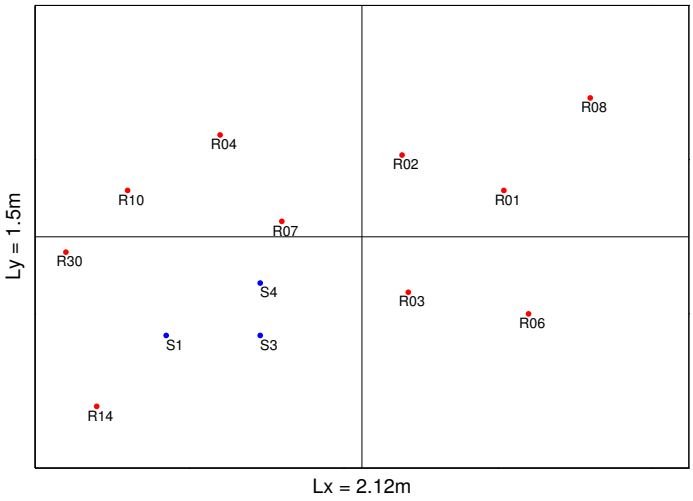

Figure 9.3: Source and response positions on the free plate.

9.2.1 Direct measurement method

The structure-borne power injected by the source into the plate was obtained by recording force and velocity signals at the source contacts. The force transducers, together with accelerometers placed next to the contacts, allowed direct measurement of these quantities. Force and velocity were measured during normal operation of the source (measurement time $T = 10\,\mathrm{s}$), and the source power calculated as

$$P = \mathrm{Re}\{Q\} = \mathrm{Re}\left\{\mathbf{v}^{\mathbf{T}}\mathbf{F}^{*}\right\} = \mathrm{Re}\left\{v_1 F_1^{*} + v_3 F_3^{*} + v_4 F_4^{*}\right\}.$$

The calculation was performed with narrowband data, and then transformed to third-octave band values. The calculated source power is shown in Figure 9.4, together with the results from the reception plate method. A discussion follows in Section 9.2.2. The repeatability and reproducibility of the direct measurement were also obtained. For the former, the direct measurement of forces and velocities at the contacts was repeated, without changing the setup. For the latter, the entire setup was disassembled and reassembled. The same measurement with the same parameters was then performed again. The results are shown in Figure 9.5.

The repeatability of the direct measurement is within $\pm 1.1\,\mathrm{dB}$, above $25\,\mathrm{Hz}$. The reproducibility shows differences of up to $3.5\,\mathrm{dB}$. The average deviation in

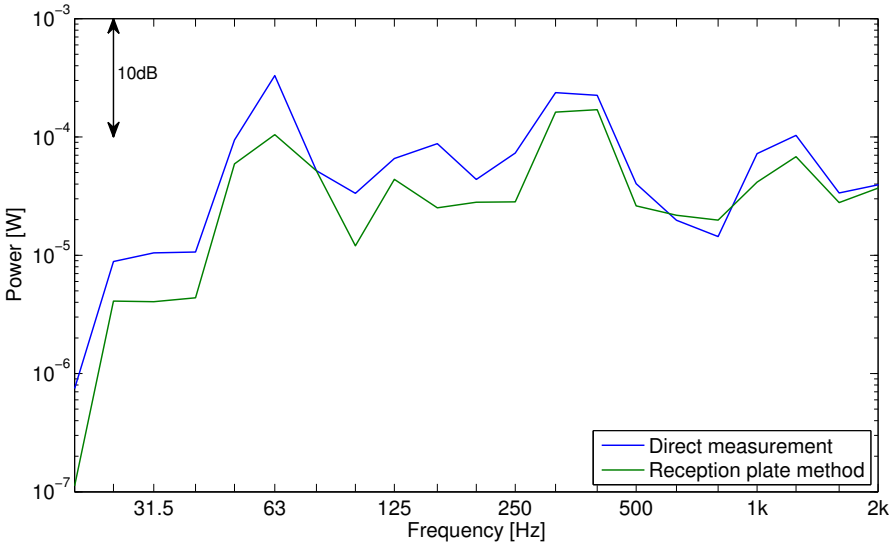

Figure 9.4: Real part of injected power from test source into free plate.

reproducibility in the frequency range between 20 Hz and 2 kHz is −0.3 dB. The reason for this may be found in small changes in the connection of the shaker to the metal base, in slightly different contact conditions between source and plate, in variations in the excitation signal, or in changes to the accelerometer attachment at the contacts.

9.2.2 Reception plate method

The reception plate method was used to determine the injected source power. The mean square velocity on the plate was measured in third-octave bands (averaging time $T = 30$ s), at the ten response positions indicated in Figure 9.3. The source power was then calculated as in Equation (8.14): $P = \omega\eta m\langle v^2\rangle$. Results are presented in Figure 9.4.

The repeatability and reproducibility of the method were tested, by repeating the measurement without changing the setup, and by disassembling and re-assembling the setup once, and performing the measurement again (with the same source and response positions).

Figure 9.4 confirms that the power transmitted to the plate was broadband in character. At low frequencies ($f < 25$ Hz), the shaker was not able to drive the plate sufficiently. The source base and the source-receiver mobility coupling

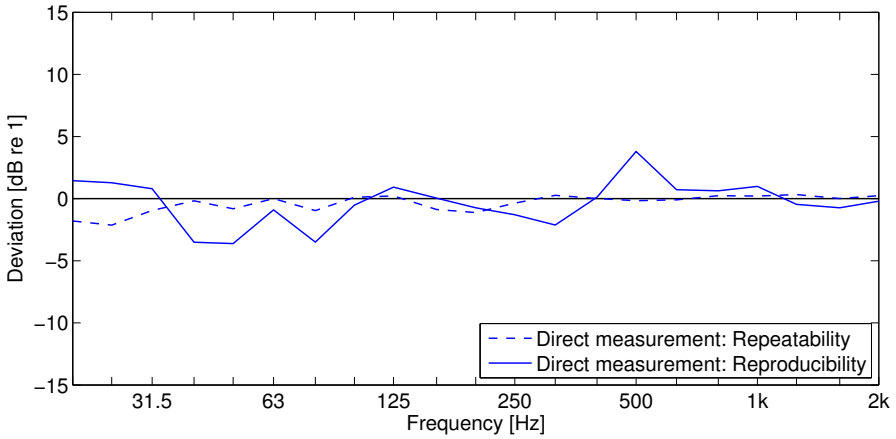

Figure 9.5: Repeatability and reproducibility of direct measurements.

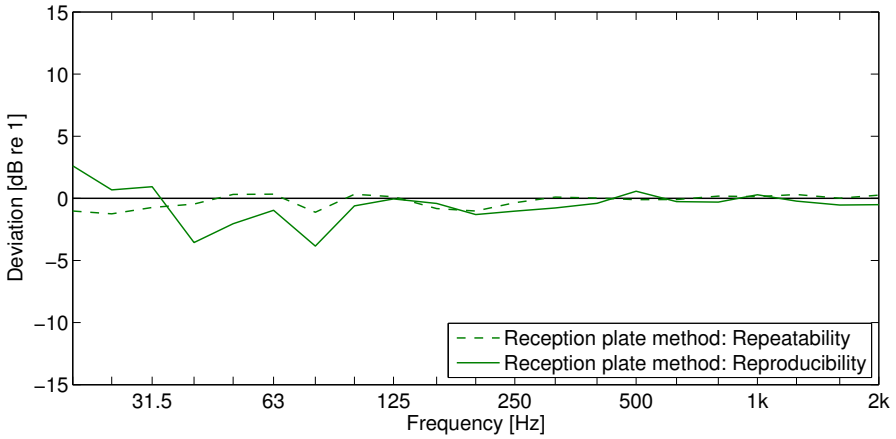

Figure 9.6: Repeatability and reproducibility of reception plate method.

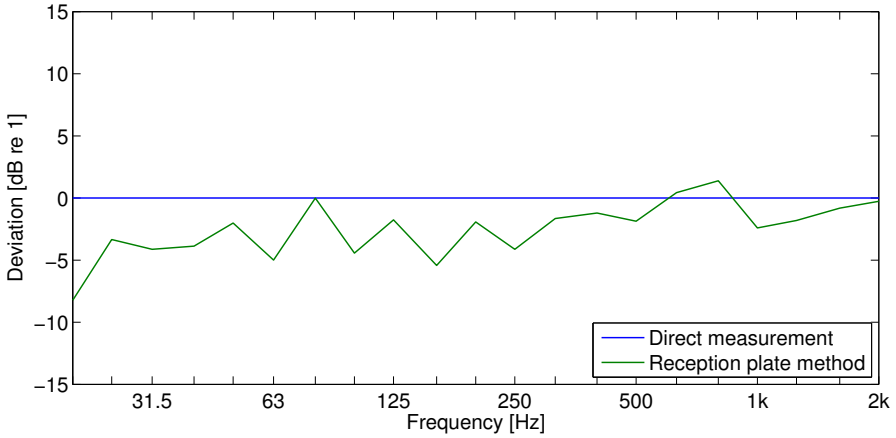

Figure 9.7: Deviation between direct measurement and reception plate method.

filtered the pink noise signal supplied by the shaker. This is indicated for example by peaks at 63 Hz and troughs at 100 Hz in the transmitted power. For the evaluation of the different methods, it is sufficient to note that power is injected in all frequency bands of interest.

Figure 9.6 shows repeatability and reproducibility of the reception plate method. The repeatability is within ±1.1 dB. The reproducibility is within ±1.3 dB in most frequency bands, with larger deviations in the 20 Hz, 40 Hz, 50 Hz, and 80 Hz bands (up to 3.5 dB). For higher frequencies, the reproducibility improves, with an average deviation of −0.4 dB between 100 Hz and 2 kHz.

Figure 9.7 shows the deviation between direct measurement and reception plate method. The reception plate method displays a systematic under-estimate across the entire frequency range of interest. Between 20 Hz and 250 Hz, the reception plate method lies on average 3.7 dB below the direct measurement. Between 315 Hz and 2 kHz, the difference is approximately −1.0 dB on average. This under-estimate is explained by revisiting the fundamentals of the reception plate method, as discussed in Section 8.2. The quantities to be determined are the plate mass, the loss factor, and the mean square velocity. The plate mass can be estimated with very good accuracy, since the plate dimensions and its density are known. Since the plate has free boundary conditions, it can further be assumed that the loss factor is obtained with reasonable accuracy. The mean square velocity depends on careful selection of response positions on the plate, as discussed in Section 8.2. From Figure 9.3, it is observed that most of the response positions lie away from the plate edges and corners, except for position R30. Therefore, the mean square plate velocity is under-estimated. This comes into effect particularly at low frequencies, and gradually loses importance at higher frequencies.

9.2.3 Substitution method: Steady-state calibration

The injected structure-borne power from test source to free aluminium plate was determined using the source substitution method, as described in Section 8.5. First, a shaker was used as calibration source. The source power was calculated according to Equations (8.22) and (8.25). Secondly, the free aluminium plate was calibrated using an impulse hammer (Section 9.2.4). Lastly, an average power calibration factor was determined using the impulse hammer

Figure 9.8: Plate calibration with shaker (left) and hammer (right).

(Section 9.2.5). The three measurement steps are described in the following, and the results compared to each other and to the benchmark results from Sections 9.2.1 and 9.2.2.

The source substitution method was employed with a shaker as calibration source, as shown in Figure 9.8 on the left. The free aluminium plate was excited at the three source contacts with the shaker, and force and velocity at the contact were measured. Pink noise was used as excitation signal. The real part of the input power was taken from the cross-spectrum between contact force and velocity, in third-octave bands (averaging time $T = 10\,\mathrm{s}$). Simultaneously, the autospectra of the velocity responses on the plate v^2 were recorded in third-octave bands. The same ten response positions as for the reception plate method were used, indicated in Figure 9.3.

From input power and mean square velocity, the source power of the simplified source was calculated using Equation (8.22) and Equation (8.25). Figure 9.9 shows the power calibration factor required for Equation (8.22), for excitation at each of the three source contacts. The repeatability at each position is within 0.5 dB (except for the 20 Hz band), and the deviations between the three positions are of the order of 3 dB. The mean value of all measurements, indicated by the black line, was used for the power calculations.

The results of the source power calculation are shown in Figures 9.10 and 9.11, and compared with the results from direct measurement and reception plate

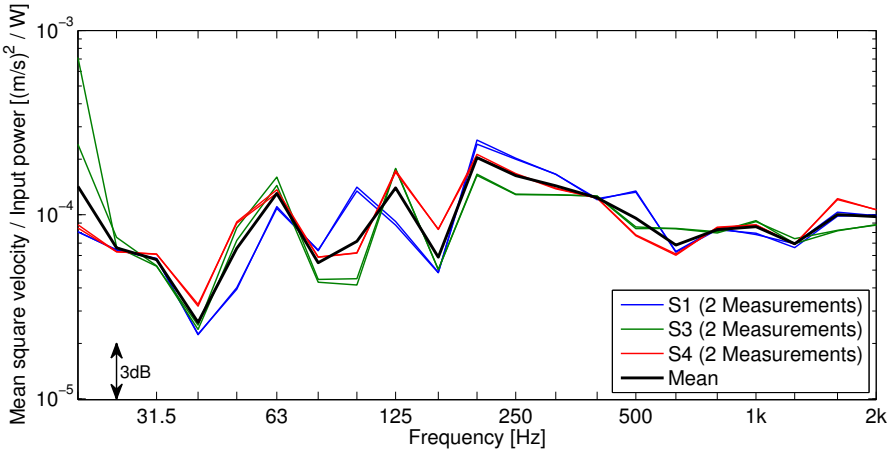

Figure 9.9: Power calibration factor for shaker excitation.

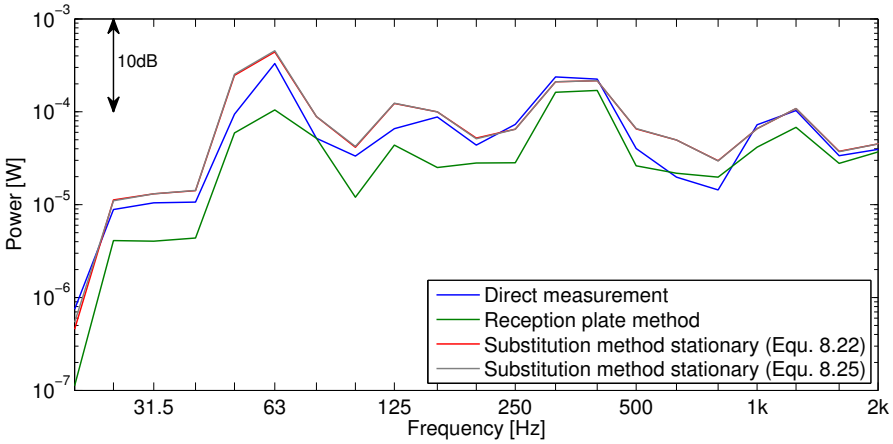

Figure 9.10: Real part of power from test source to free aluminium plate.

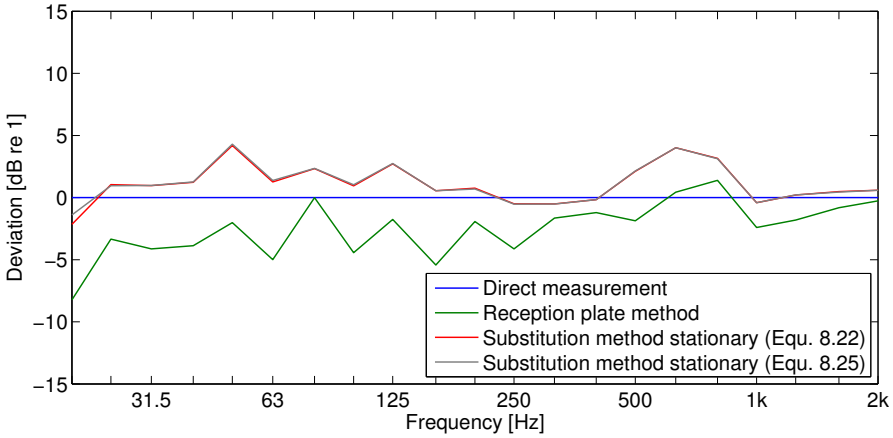

Figure 9.11: Deviations in real part of power.

method. The results obtained with steady-state shaker excitation are virtually indistinguishable from each other, regardless of the averaging procedure used. This is encouraging, since it suggests that Equation (8.22), which uses the power calibration factor, yields the same results as the physically more rigorous approach of using velocity differences. Calculating the power calibration factor is more practicable than storing and matching different velocity responses from different measurements with each other. Compared with the benchmark direct measurement, the source substitution results tend to show an over-estimate of about 1.0 dB on average between 20 Hz and 2 kHz. This deviation is comparable to the deviation found for the reception plate method in Section 9.2.2. For higher frequencies, the agreement tends to get better. These results can be seen to support the source substitution method as an alternative for the reception plate method for a free plate.

9.2.4 Substitution method: Transient calibration

The source substitution method was employed with an instrumented hammer. Using the hammer simplifies the measurement, but increases the amount of signal-processing involved. The plate was excited with the hammer at the three source contact positions (Figure 9.8). Force and velocity at the contacts were recorded as time signals ($T = 1\,\mathrm{s}$, $f_s = 16384\,\mathrm{Hz}$). In post-processing, the signals were time-windowed (uniform window) and transformed to the frequency domain. Since an impulse has a defined signal energy, the Fourier transform was not normalized with respect to the signal length. The narrowband injected power was calculated by taking the real part of the product of velocity and complex conjugate force: $P = \mathrm{Re}\{v_r F_r^*\}$. The narrowband power was then transformed to third-octave band values for further processing. To obtain the average squared velocity response, the same signal processing was applied to the recorded response velocity time signals.

The signal processing chain requires measurement equipment to record time signals, as well as numerical evaluation software for post-processing. However, if only a standard analyzer is available, it is also possible to obtain the power calibration factor by recording auto-spectra and cross-spectra. This is because the power calibration factor is a ratio of two values. Therefore, certain errors in the signal processing (such as incorrect normalization factors) cancel out, as

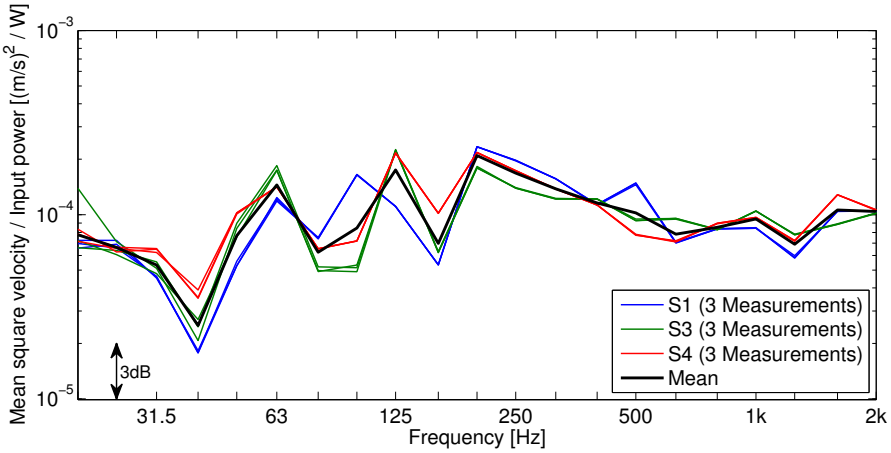

Figure 9.12: Power calibration factor for transient excitation.

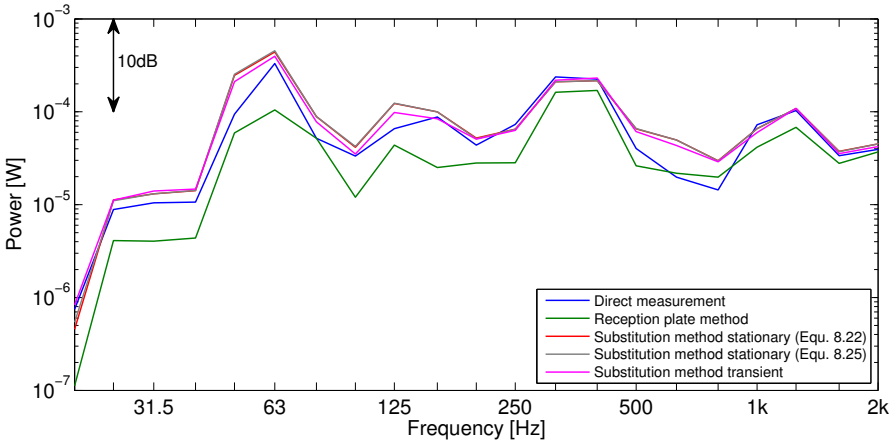

Figure 9.13: Real part of power from test source to free aluminium plate.

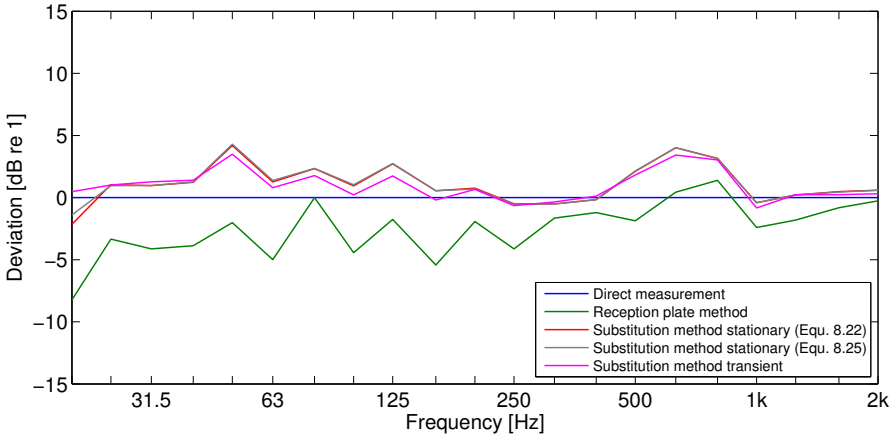

Figure 9.14: Deviations in real part of power.

long as the entire signal is captured and both input power and squared velocity response are calculated in the same way.

From input power and mean square velocity, the power calibration factor was calculated according to Equation (8.22). It is shown in Figure 9.12, for excitation at each of the three source contacts. Once again the repeatability at each position is very good, and the deviations between the three positions of the order of 3 dB. The mean value of all measurements, indicated by the black line, was used for the power calculations.

The results of the source power calculation are shown in Figures 9.13 and 9.14, and compared with the results from direct measurement and reception plate method. The source power determined using transient calibration is within 0.5 dB of the results from stationary calibration, for most of the frequency range of interest. Only in the mid-frequencies, between 50 Hz and 160 Hz, are the results slightly lower than for the stationary calibration. Compared with the benchmark direct measurements, the results are within 3 dB, with an average over-estimate of about 0.9 dB between 20 Hz and 2 kHz. The results from this section indicate that it is possible to use a transient calibration source, such as an impulse hammer, to obtain the power calibration factor of the receiver structure. From the power calibration factor, the source power can readily be calculated. There do not seem to be systematic errors or deviations when using the hammer, provided the signal processing is consistent.

9.2.5 Substitution method: Average calibration factor

The calibrated impulse hammer again was used, but this time the plate was excited at the response positions, remote from the source contacts. The velocity responses were recorded at ten fixed positions. An average calibration factor thus was obtained which is independent of source position. The same procedure and signal processing as in the previous section was employed. Ten excitation positions were used, and the same ten positions were used for the velocity responses. When an excitation position coincided with a response position, the velocity response at that position was not included for the calculation of the mean square velocity. Three hits were performed at each position.

The power calibration factor obtained in this way is shown in Figure 9.15. Once again, the repeatability at each position is within 0.5 dB. The deviations

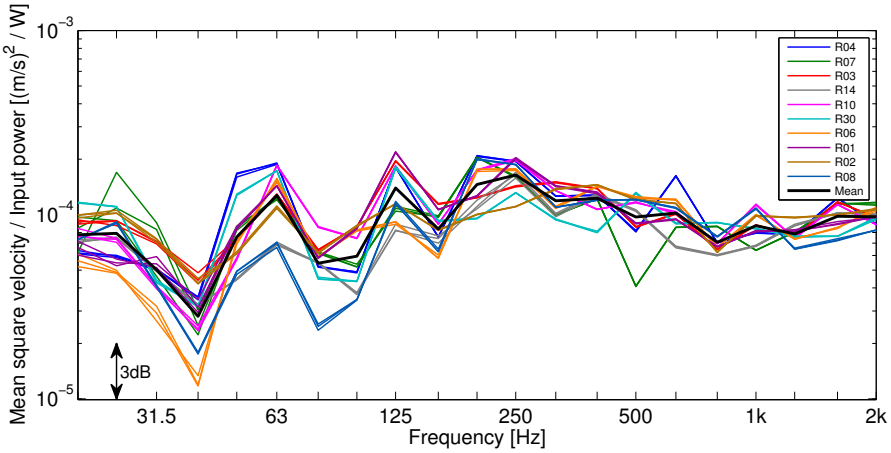

Figure 9.15: Power calibration factor for ten excitation positions.

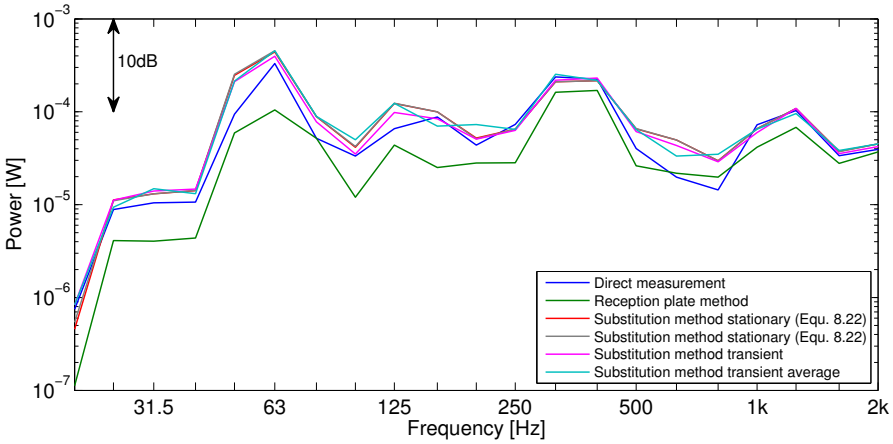

Figure 9.16: Real part of power from test source to free aluminium plate.

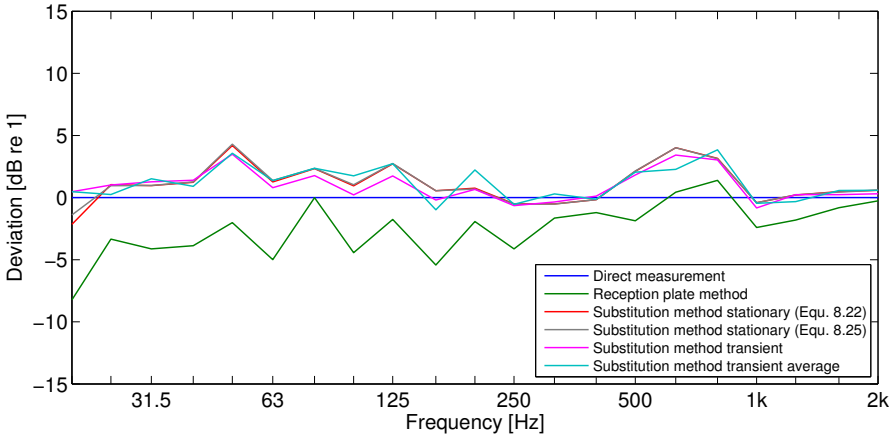

Figure 9.17: Deviations in real part of power.

between individual excitation positions were of the order of 5 dB below 160 Hz, and of the order of 3 dB above 160 Hz. The mean value of all measurements, indicated by the black line, was used for the power calculations.

The resulting source power is shown in Figures 9.16 and 9.17. The four results using the source substitution method are within 1.5 dB of each other. The use of an average power calibration factor instead of an individually measured power calibration factor does not increase the discrepancy. Compared with the benchmark direct measurements, the transient average result is about 1.1 dB too high between 20 Hz and 2 kHz.

The results from this section suggest that obtaining an average calibration factor for a receiver structure yields the same accuracy as individually determined power calibration factors for each source position. This is of practical advantage, as it means that a receiver structure can be calibrated once with a set of fixed response positions, and the calibration factor can then be used for any source position without the need to repeat the calibration procedure.

9.2.6 Summary

The results from the first experimental study confirm the general applicability of the proposed source substitution method for a free receiver plate. The source power could be determined with an accuracy of about 1 dB on average, compared with direct measurements. The use of a transient source for calibration, and the use of an average calibration factor gave the same accuracy, and can therefore be considered valuable alternatives to the existing methods of obtaining the structure-borne source power.

9.3 Test source on a transmission suite floor

In the second experimental study, a test source designed for a round robin test, conducted by CEN TC 126 WG 7 [154, 155], was used. The source consists of an aluminium plate of size 0.5 m × 0.35 m × 10 mm and three feet of length 70 mm. The plate is driven by a shaker, with pink noise as the excitation signal. A detailed description of the source and its design is provided in [121].

Figure 9.18: Floor of transmission suite and WG7 test source.

A concrete floor on a small transmission suite was used as receiver structure. The floor is of size 2.10 m × 3.10 m × 0.13 m and has an 8 mm epoxy mortar layer on top. Figure 9.18 shows details of source and receiver. From measured mobility data, the lowest eigenfrequencies of the floor are at 52 Hz, 69 Hz, 83 Hz and 88 Hz. In the 50 Hz, 63 Hz, and 80 Hz third-octave frequency bands, only one or two modes per band exist. The 100 Hz third-octave frequency band contains no eigenfrequency. The use of statistical methods below the 125 Hz third-octave band is therefore associated with increased uncertainties.

The difficulties of using the standard reception plate method with this configuration are apparent: The boundary conditions of the floor are not well-defined; the mass of the floor is estimated with limited accuracy due to the composite nature and the uncertain dimensions of the floor; the railing presents a potential secondary transmission path; loss factor measurements show that there occurs an energy transfer into the supporting walls. It is for configurations like this that the substitution method is proposed as an alternative to the reception plate method.

Five source positions on the floor were used, to account for modal behaviour: one position near a corner, one near an edge, one in the middle, and two random positions. Source and response positions are shown in Figure 9.19.

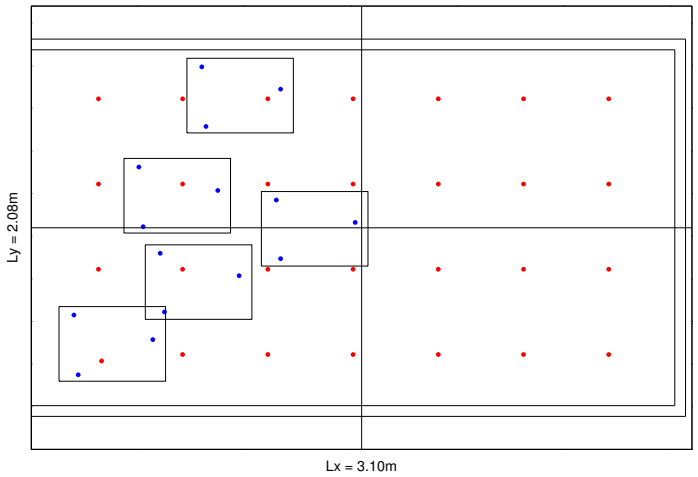

Figure 9.19: The five source positions on the floor, with source contacts (blue) and response positions (red).

9.3.1 Reception plate method

Due to the nature of the test source, the direct measurement of contact forces in the installed situation was not possible. This prevented the direct calculation of the injected source power as in Section 9.2.1. Instead, a reference source power was obtained from the round robin test data [154, 155]. In one of the participating labs, named "Laboratory 2" in [154], the source was operated on a free concrete reception plate, as defined in EN 15657-1:2009, and the injected power calculated by Equation (8.14). It is shown in Figure 9.20.

The injected source power is a function of source and receiver mobility. Since the reception plates in the different laboratories have different thickness and boundary conditions, their mobilities are not the same. The concrete plate from Laboratory 2 has free edges and a thickness of 10 cm, while the concrete plate depicted in Figure 9.18 has a thickness of 13 cm and is connected to other building elements. Figure 9.21 shows the average real part of the plate mobility for the five source positions used in the test, both for the free plate and the connected plate. The lower mobility of the connected plate corresponds to its greater thickness compared with the free plate. In order to compare measurements from the two laboratories, the results must be normalized with respect to the average real part of the floor mobility at the source contacts. This yields the characteristic reception plate power, as defined in Equation (8.16).

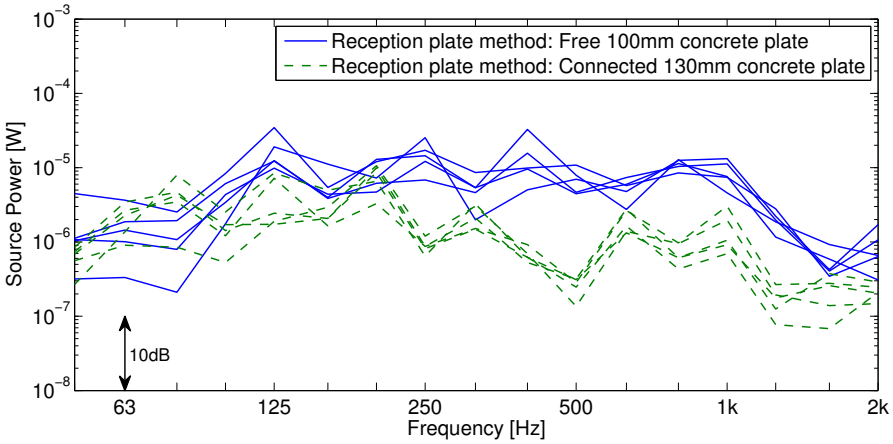

Figure 9.20: Source power from reception plate method.

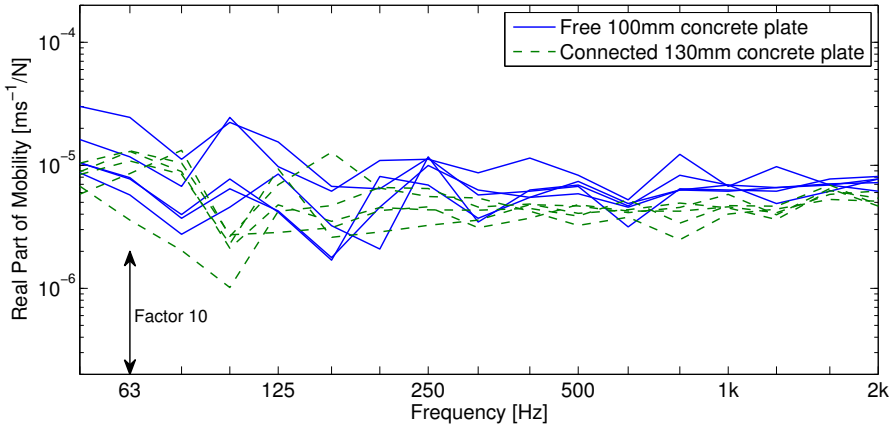

Figure 9.21: Average real part of the receiver mobility at the source contacts.

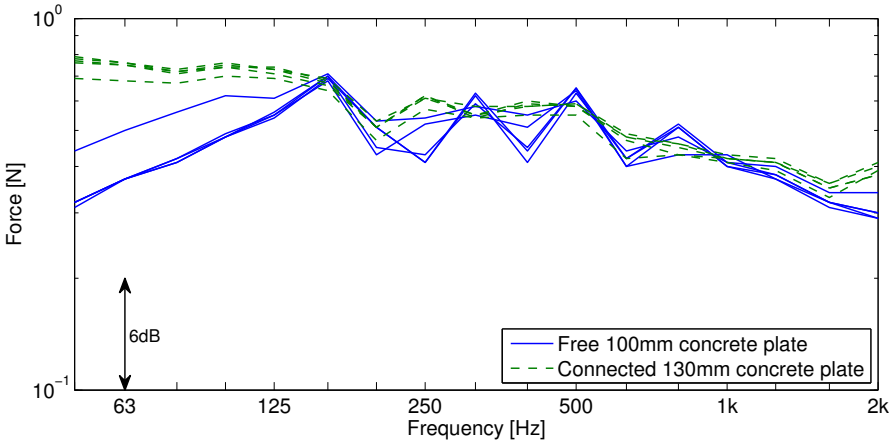

Figure 9.22: Measured force spectrum between shaker and source plate.

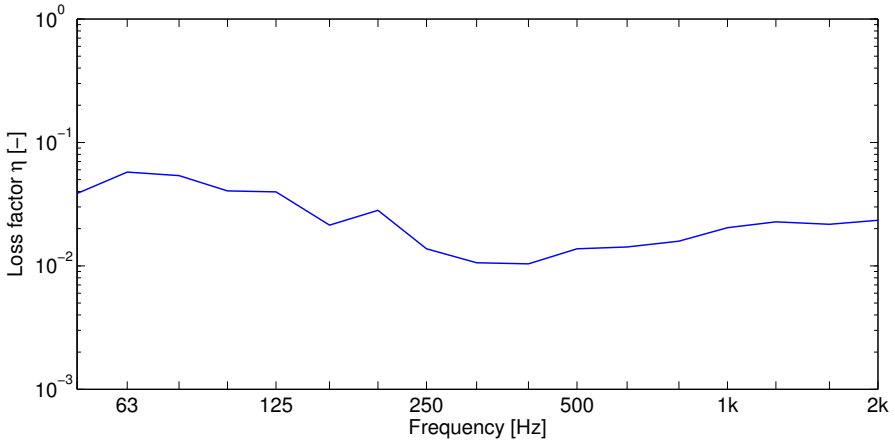

Figure 9.23: Loss factor of 130 mm concrete transmission suite floor.

Furthermore, in the round robin test it was found that even though the source's excitation was meant to be the same in each laboratory, in practice its operation varied between different laboratories, due to different settings of the involved amplifiers/generators. A transducer monitored the force between the shaker and the source plate. The internal forces are shown in Figure 9.22 for operation of the source on the free plate and on the connected plate. In order to compare measurements from different laboratories, the results were normalized with respect to the force excitation spectra. Hence, for inter-laboratory comparisons in the present study, the source power in each frequency band was normalized:

$$P_{norm} = P_{Source} \frac{Y_\infty}{\mathrm{Re}\left\{\langle Y_{Plate} \rangle\right\}} \frac{F_0^2}{F_{op}^2} \tag{9.1}$$

with $Y_\infty = 5 \cdot 10^{-6}$ ms^{-1}/N and $F_0 = 1$ N.

The floor of the transmission suite was used as reception plate, and the source power calculated using Equation (8.14). Figure 9.20 shows the result. The loss factor, measured with the decay method described in Appendix D, is shown in Figure 9.23. The loss factor determination proved difficult, due to a low signal-to-noise ratio and curvature in the energy decay curves. Unlike for the free aluminium plate (cf. Figure 3.3), the loss factor appears relatively constant over frequency, at values between 0.01 and 0.05. This is significantly higher than the internal loss factor of concrete (0.005 [72]). Thus it is assumed that coupling losses contribute significantly to the total loss factor.

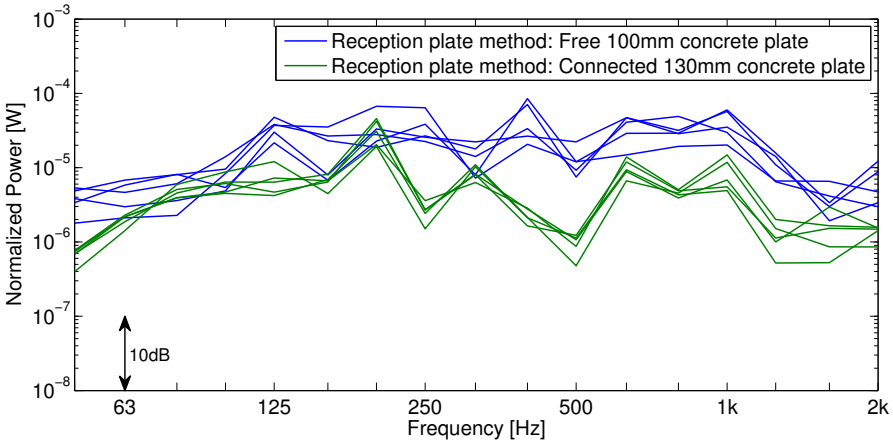

Figure 9.24: Normalized source power from reception plate method.

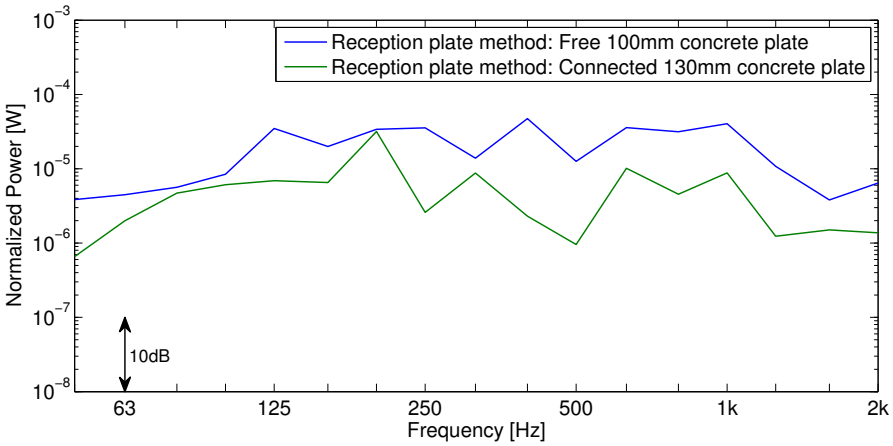

Figure 9.25: Mean values of normalized source power.

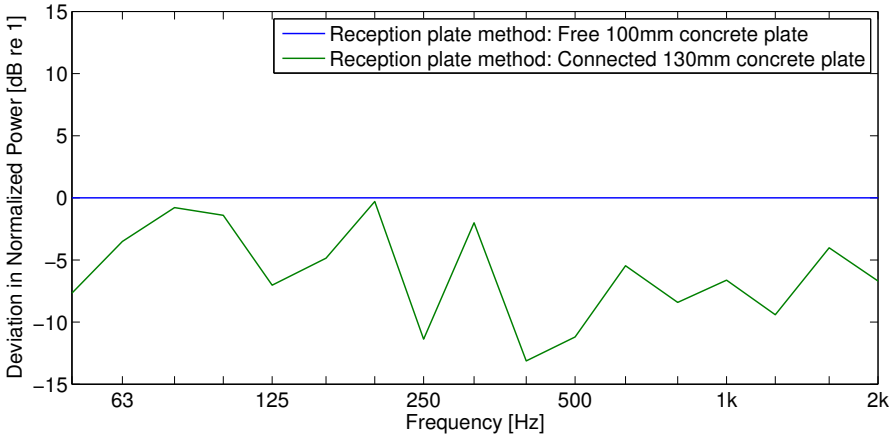

Figure 9.26: Deviations in normalized source power.

The mean square velocity was recorded in third-octave bands (averaging time of $T = 20\,\mathrm{s}$) at the source and response positions indicated in Figure 9.19, and was corrected for background noise. The mass was estimated from the plate dimensions and an estimated density of $2300\,\mathrm{kg/m^3}$.

Figure 9.24 shows the normalized source power injected by the test source into the free concrete reception plate, and into the connected concrete reception plate, at five source positions each. Compared with Figure 9.20, the results give slightly better agreement, in particular at low frequencies. The variability is marginally greater for the free plate results. For clearer comparison, Figure 9.25 shows the mean of the five measurements (linear average). Figure 9.26 displays the deviation in the averaged normalized power, taking the result for the free reception plate as reference. It must be kept in mind that even though the free reception plate method is likely to be the most accurate, its results may still contain errors for the reasons given in Section 8.2.

The entire frequency range of interest (50 Hz to 2 kHz) can be evaluated, as the pink noise excitation signal ensures a sufficient SNR in each frequency band. However, the results using the connected plate show peaks in the 200 Hz, 315 Hz, and 630 Hz frequency bands, and troughs in the 250 Hz and 500 Hz bands. The results using the free plate show a different distribution of peaks and troughs, while generally being more evenly distributed. These differences are attributed to the sampling and averaging operation of the modal vibration field.

Regarding the general shape of the two curves in Figure 9.25, the results from the reception plate method for free and connected plate show strong differences. The latter strongly and systematically under-estimates the reference power, in some bands by more than 10 dB, cf. Figure 9.26. The average under-estimate between 50 Hz and 2 kHz is 6 dB. One reason for this under-estimate may be found in an incorrectly determined total loss factor, see Section 8.3.

9.3.2 Substitution method: Steady-state calibration

The source substitution method was used to estimate the vibrational power injected by the source into the floor. In the first step, the floor was calibrated with a shaker designed to stand on a force transducer (Figure 9.27). Two matched accelerometers on the plate on either side of the force transducer allowed measurement of the input power. The real part of the injected power

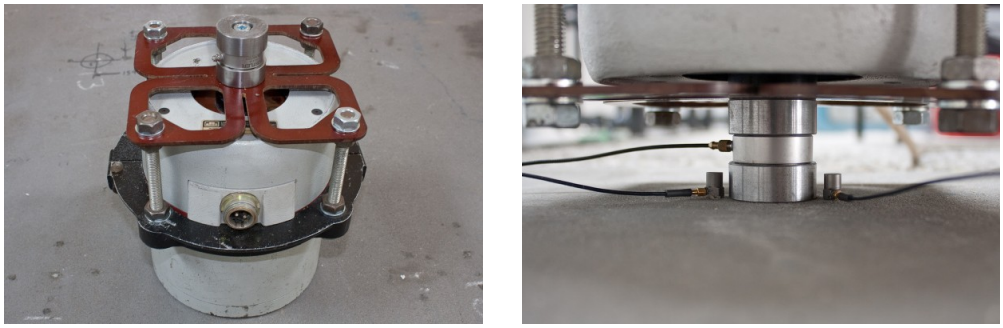

Figure 9.27: Shaker with support spider and force transducer (left), and measurement of power input into the floor (right).

is the real part of the cross-spectrum between contact force and velocity. The velocity responses at nine remote positions on the plate were recorded simultaneously. Results were recorded for five source positions: near the corner, near an edge, in the middle, and at two random positions (see Figure 9.19). For each source position, different combinations of nine response positions were used. The shaker was placed at each of the three source contacts. Data was recorded in third-octave bands (averaging time $T = 20\,\mathrm{s}$).

Figure 9.28 shows the mean values (logarithmic average) of the power calibration factors for the three contacts at the five source positions. The curves show a peak between 80 Hz and 100 Hz, and a steady decrease between 100 Hz and 500 Hz, before assuming a value of approximately 10^{-6} $(\mathrm{m/s})^2/\mathrm{W}$ for frequencies above 500 Hz. The value at the corner position is slightly lower for the mid-frequencies than that at the other positions. These power calibration factors are a property of the floor and the chosen source and response positions.

The normalized source power, presented in Figure 9.29, oscillates around the benchmark result from the free reception plate. The different distribution of peaks and troughs in the normalized power makes the deviations look larger than they actually are. The average deviation across the frequency range of interest is about $-1\,\mathrm{dB}$, and the two curves are within $\pm 6\,\mathrm{dB}$ of each other.

Comparing the result from the reception plate method using a connected plate with the result employing the source substitution method shows that the latter seems to give more accurate results than the former. One reason for this could be that the loss factor determination is circumvented.

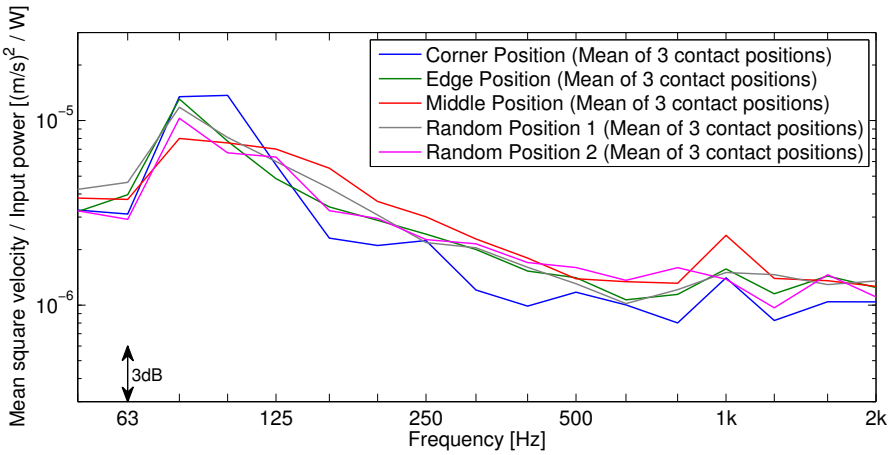

Figure 9.28: Power calibration factor for five source positions.

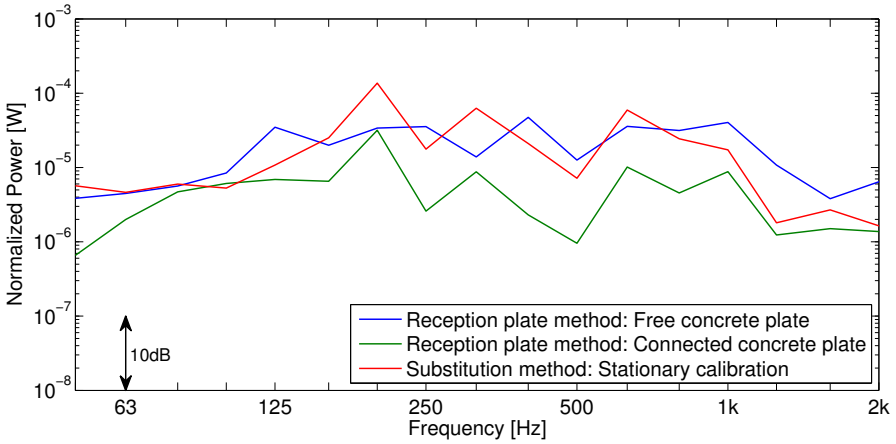

Figure 9.29: Mean values of normalized source power.

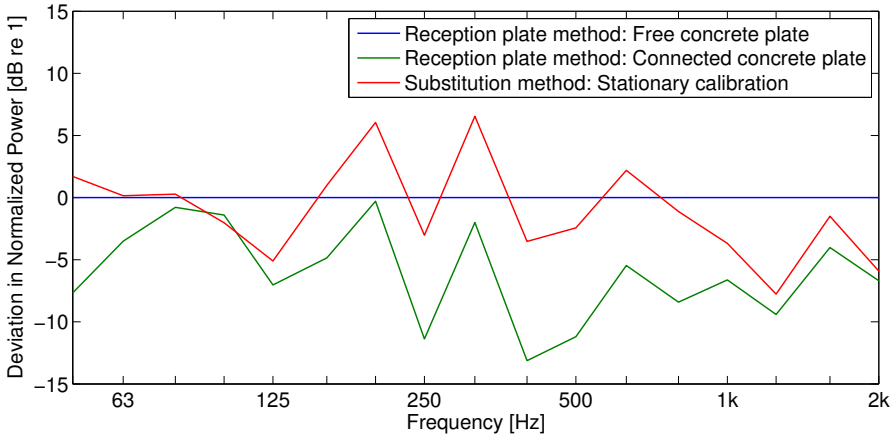

Figure 9.30: Deviations in normalized source power.

9.3.3 Substitution method: Transient calibration

The calibration of the connected concrete floor was performed with a calibrated impulse hammer. Again, the power calibration factors were obtained for all five source positions and all three source contacts. The signal processing applied to the force and velocity time signals was the same as in the first experimental study (Section 9.2.4). Figure 9.31 shows the power calibration factors obtained with the hammer for all five source positions (average of three contact positions). In Figure 9.32, these curves are compared with the results obtained with the shaker for the same positions. The curves are similar in shape, though the transient values are on average about 0.5 dB below the steady-state values.

Since the power calibration factors for stationary and transient calibration agree, so do the determined source powers. Figure 9.33 shows the deviation between the normalized powers. The normalized source power from the transient calibration traces the power from the stationary calibration. It tends to be slightly higher, and the average deviation across the frequency range of interest is about -0.5 dB. As in Section 9.2, the agreement between the two substitution methods suggests that the choice of calibration source does not significantly affect the final result.

9.3.4 Substitution method: Average calibration factor

An average calibration factor was obtained for the floor of the transmission suite and representative velocity response positions. The floor on the transmission suite was excited with the shaker at 28 different positions (indicated by blue dots in Figure 9.34). The response velocities at nine fixed positions (indicated by red squares) were recorded. Figure 9.35 shows the 28 resulting power calibration factors, and the mean value. The 50 Hz band was dominated by mains signal and was excluded from the evaluation. The curves show the same general trend as the individually measured curves in Figure 9.28. Assuming a logarithmic normal distribution, the standard deviation, shown in Figure 9.36, is about 1 dB across the frequency range of interest.

Figure 9.37 shows the deviations in normalized power for all five cases considered: The reception plate method with a free concrete plate, the reception

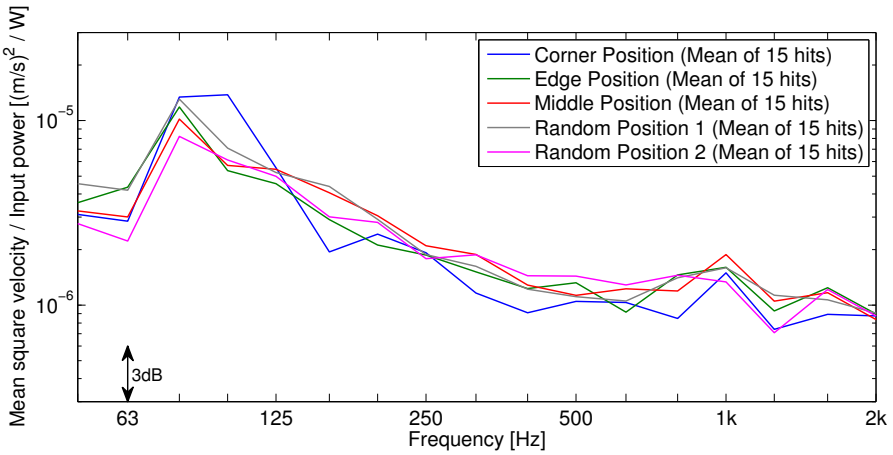

Figure 9.31: Power calibration factor with hammer for five source positions.

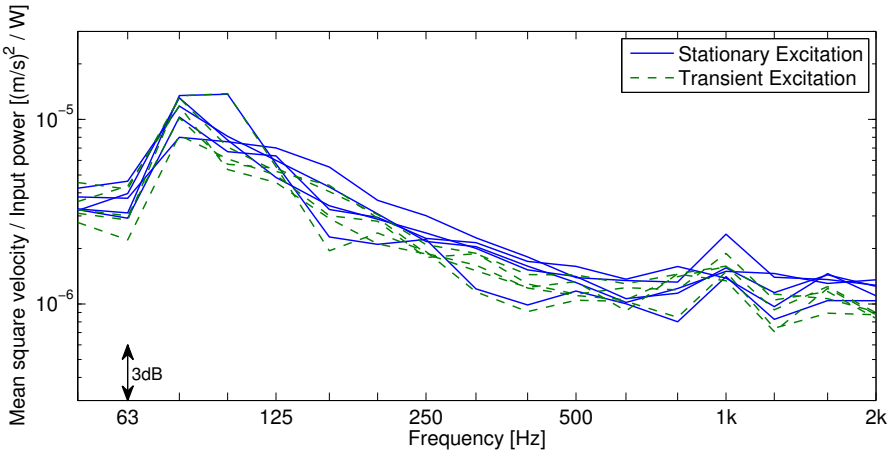

Figure 9.32: Power calibration factors for shaker and hammer measurements.

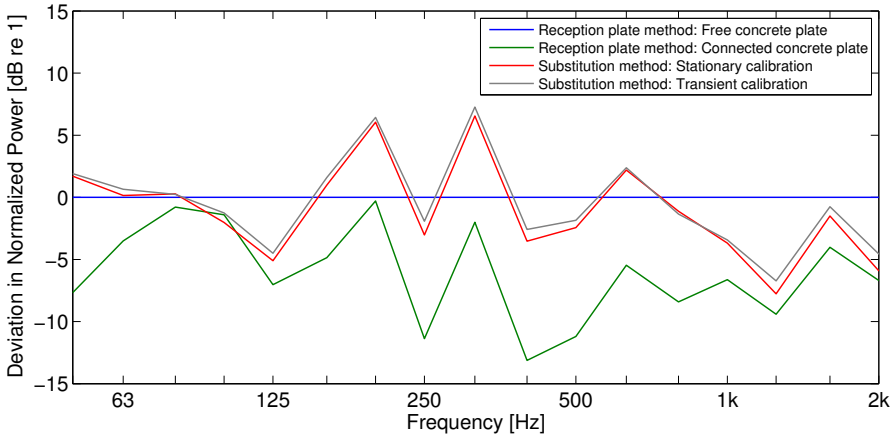

Figure 9.33: Deviations in normalized source power.

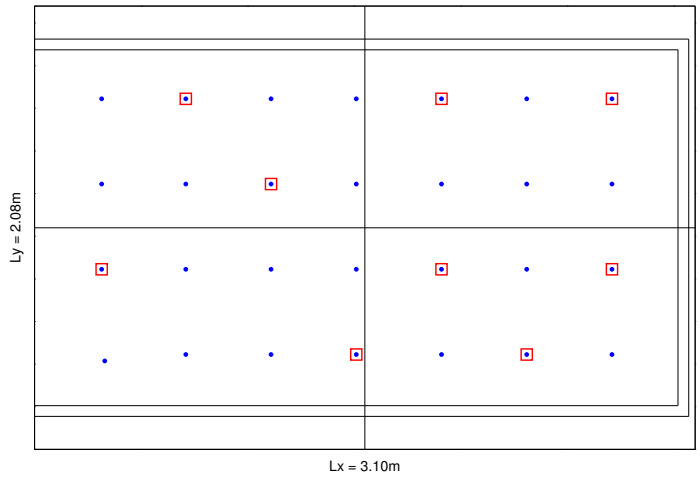

Figure 9.34: Excitation (blue dots) and response (red squares) positions for measurement of average steady-state calibration factor.

plate with a connected concrete plate, the source substitution method with stationary, transient, and average calibration. The results for the three different methods of obtaining the power calibration factor agree very closely with each other. The transient excitation approach gives slightly higher values than the steady-state calibration, about 0.5 dB on average. The average calibration yields very similar results to the steady-state calibration. The difference is less than 0.2 dB on average. Compared with the benchmark free reception plate method, the average deviation is -1.2 dB. Once again, it should be kept in mind that even though the free reception plate method is used as reference here, its results may contain errors for the reasons described in Section 8.2.

9.3.5 Summary

The results from the second experimental study confirm the findings from the first study. The (normalized) source power could be estimated with an accuracy of about ± 6 dB, compared to results obtained with a free reception plate. The choice of calibration source (shaker or hammer) did not significantly affect the results, nor did the use of an average calibration factor. Compared with the results obtained using the reception plate method with coupled plates, the accuracy was improved, by avoiding the total loss factor determination.

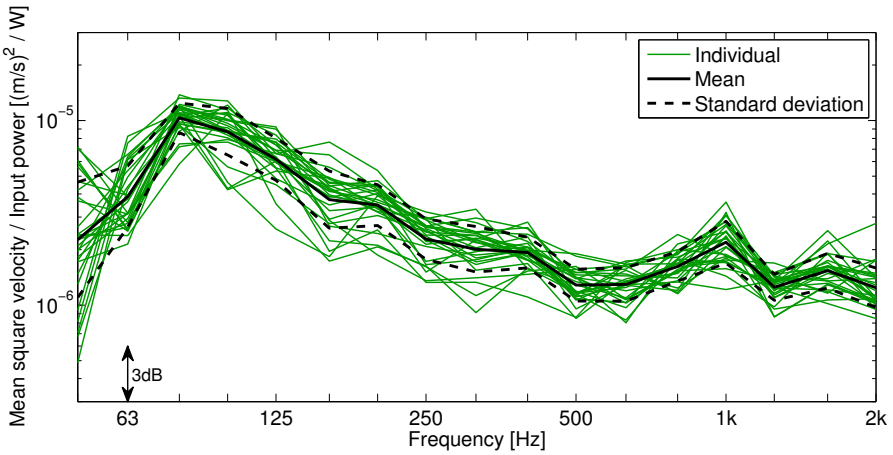

Figure 9.35: Calibration factor (28 excitation positions, 9 fixed responses).

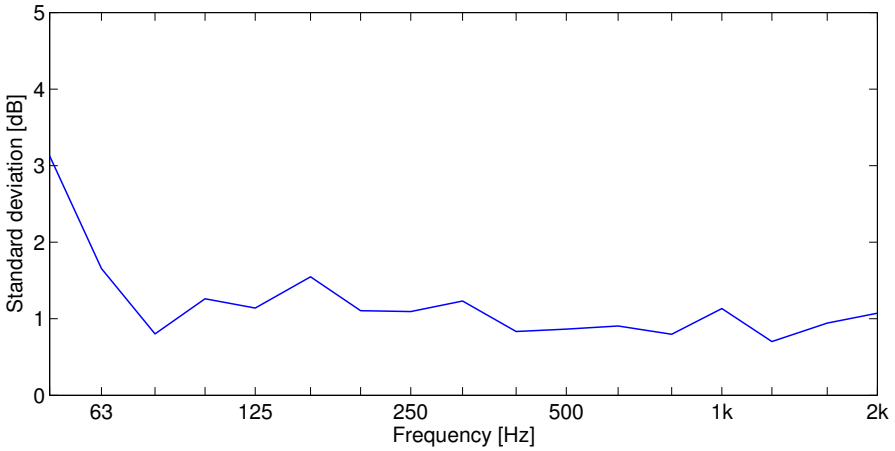

Figure 9.36: Standard deviation of 28 power calibration factors.

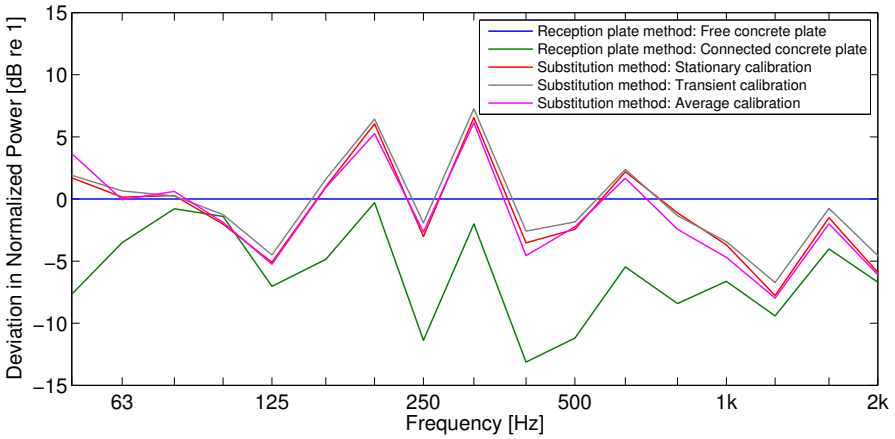

Figure 9.37: Deviations in normalized source power.

Figure 9.38: Details of the combined heating and power unit.

9.4 Micro-CHP unit on masonry wall

In the third experimental study, the source under test was a combined heating and power (micro-CHP) unit (Figure 9.38). Micro-CHP units are usually installed in residential dwellings. In contrast to regular boilers, the excess heat is used to generate electricity, using a Stirling engine.

The unit is of size 0.95 m × 0.45 m × 0.45 m, and has a mass of about 120 kg. To simplify the installation, it is designed to be mounted through a specialized mounting system. A thin back plate is attached to the supporting wall by seven screws, indicated by red circles in Figure 9.38 on the left. The unit is then hooked onto the back plate. It rests on a relatively small lip at the bottom, while six screws at the top secure it from tipping (blue rectangles in Figure 9.38).

The unique mounting procedure has consequences for structural acoustic considerations. While the back plate is rigid when attached to the wall, it is quite flexible on its own. This makes measurement of free velocity and source mobility difficult, and raises questions about the representativeness of the data measured in the free state. Calculation of the injected power from source activity and source and receiver mobilities is therefore prone to errors. Direct power measurement is not possible, due to inaccessible contact points. Therefore, the only way to determine the source power is by *in-situ* methods, such as the reception plate method or the substitution method.

The CHP unit is of particular interest as a structure-borne sound source, for the following reasons:

1. Acoustical treatment of the CHP unit is of great practical relevance, as it is commonly installed in residential dwellings. Low-noise performance can be an important factor in its commercial distribution.
2. The unit's internal excitation mechanisms generate both broadband and tonal components. The gas burner generates a broadband spectrum, mainly affecting mid- and high frequencies. The Stirling engine generates a tonal spectrum, mainly affecting low frequencies. A tonal, low frequency source is among the most challenging for prediction.
3. As already explained, due to the nature of the mounting mechanism, it is difficult if not impossible to determine important source parameters, such as free velocity and source mobility. An *in-situ* measurement is therefore the only way forward.
4. The source is wall-mounted, rather than floor-mounted. This means it cannot be operated on a standard horizontal reception plate as described in EN 15657-1:2009. It may be possible to operate it on a vertical reception plate, however free vertical plates that comply with EN 15657-1:2009 are rare. Using coupled walls as reception plate raises the issues described in Chapter 8.

In this study, the micro-CHP unit was operated on a masonry wall of a reverberation chamber. The wall has a size of 4.30 m × 2.70 m. It consists of a single layer of high-density engineering brick (thickness: 100 mm) and a layer of plaster (thickness: ≈ 20 mm). From measured mobility data, the lowest eigenfrequencies of the wall are at 24 Hz, 40 Hz, 60 Hz, 66 Hz, and 94 Hz. In the 25 Hz, 40 Hz, 63 Hz, and 100 Hz third-octave frequency bands, only one or two modes per band exist. The 20 Hz, 31.5 Hz, 50 Hz, and 80 Hz third-octave frequency bands contain no eigenfrequency. The use of statistical methods below the 125 Hz frequency band is therefore associated with increased uncertainties.

Due to the lack of supply and return pipes, the unit could not be operated under normal operating conditions. Instead, the controller was modified, and the unit was run in reverse. The Stirling engine in this case was supplied with electricity (instead of generating it), and cooled down the gas burner (instead of using the heat supplied by it). The gas burner and other auxiliary devices were not operated in this study.

Figure 9.39: Measurement setup for source substitution method.

The substitution method was employed to determine the injected source power. Due to the problems with the other methods, it was not possible to validate the results of the substitution method. The study described in this section therefore is an example of a practical implementation of the substitution method, rather than a proof of its validity.

9.4.1 Substitution method: Transient calibration

To obtain an estimate of the structure-borne power injected by the micro-CHP unit into a heavyweight receiver wall, the source substitution method was employed. A calibrated impulse hammer with a rubber tip was used for calibration. This allowed evaluation of the data up to about 1 kHz. The receiver wall was excited at the seven contact points, and input power and response velocities at 10 remote response positions were recorded. The measurements were performed at a time when the boiler was temporarily removed from the receiver wall. The mounting holes had already been drilled at this time, and the wall was excited through a screw in the wall, as depicted in Figure 9.39.

Figure 9.40 shows the power calibration factor. It varies little with frequency, though a general decrease from low to high frequencies is observed. In most frequency bands, the values from the seven excitation positions are within 3 dB of each other. For the source power calculation, the mean value was used.

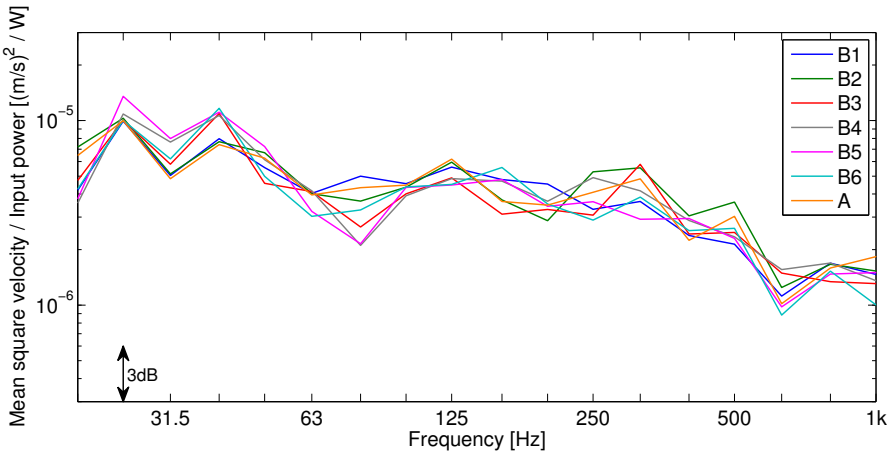

Figure 9.40: Power calibration factor for transient excitation at seven contacts.

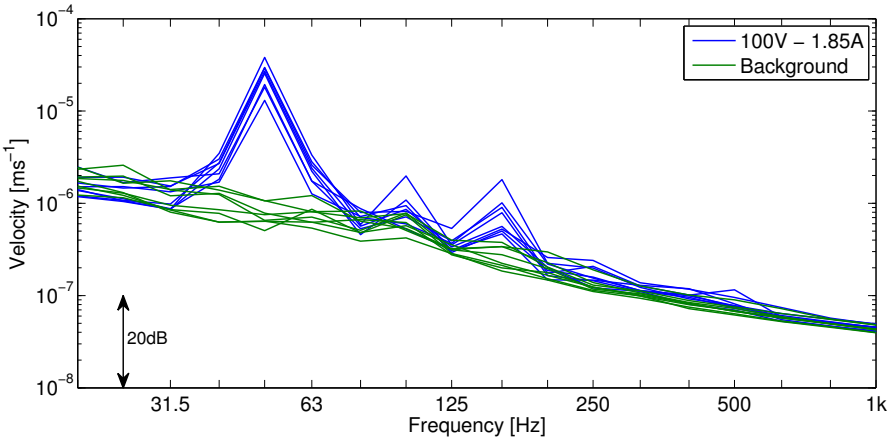

Figure 9.41: Velocities on the receiver wall.

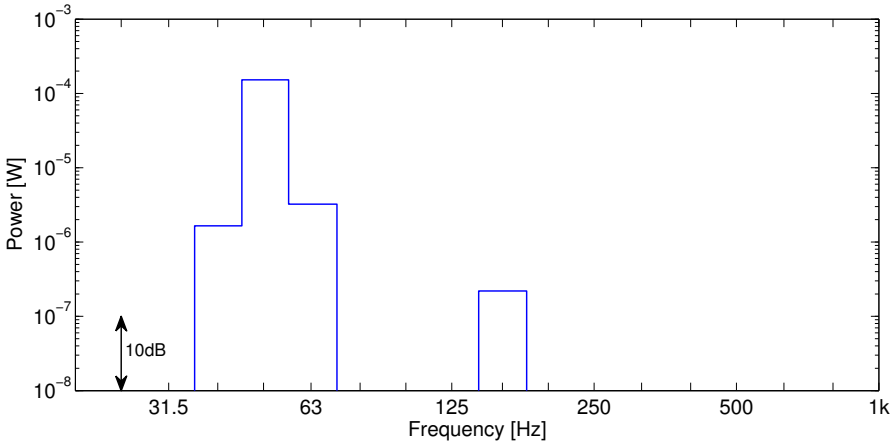

Figure 9.42: Real part of injected source power.

In a second stage, the boiler was operated in reverse, at three operating conditions: 50 V–0.7 A, 80 V–1.3 A, 100 V–1.85 A. Only the last operating condition is presented. The velocity responses were recorded at the same positions as before. Figure 9.41 shows the velocity signals on the wall during operation of the source, and during a background noise measurement. The excitation is dominated by tonal components at 50 Hz, 100 Hz, and 150 Hz. In the other frequency bands, the excitation does not exceed the background noise level.

Figure 9.42 shows the source power, calculated from the mean power calibration factor from Figure 9.40 and the velocity responses from Figure 9.41. Only signals with a SNR of at least 10 dB were considered in the calculation. Valid results were obtained in the frequency bands around 50 Hz and at 160 Hz.

9.4.2 Substitution method: Average calibration factor

In this study, the power calibration factor was determined by exciting the receiver wall at 12 evenly distributed excitation positions, and recording the input power and the squared velocity responses at 10 remote positions. When an excitation position coincided with one of the response positions, that response was not considered in the calculation of the mean square velocity.

Figure 9.43 shows the power calibration factor for 12 excitation positions, and the mean value. Assuming a logarithmic normal distribution, the standard deviation in Figure 9.44 is about 1 dB above 50 Hz, and about 2 dB below 50 Hz.

Figure 9.45 shows the average power calibration factor and the power calibration factors from Section 9.4.1. The agreement is within 2 dB. This suggests that the use of an average power calibration factor yields similar accuracy as a calibration at the source contacts. The determined source powers are shown in Figure 9.49, and discussed in Section 9.4.4.

9.4.3 Substitution method: Average calibration factor with source already in place

The substitution method generally requires the detachment of the source from the receiver, in order to determine the power calibration factor. For compli-

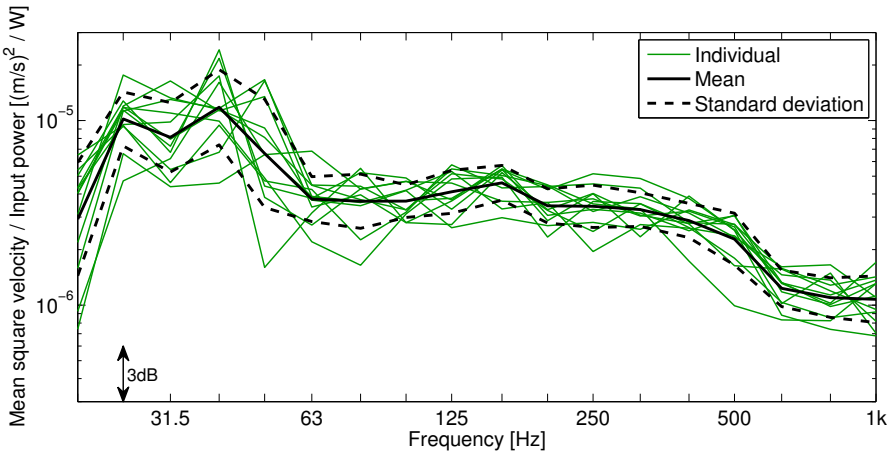

Figure 9.43: Calibration factor (12 excitation positions, 10 fixed responses).

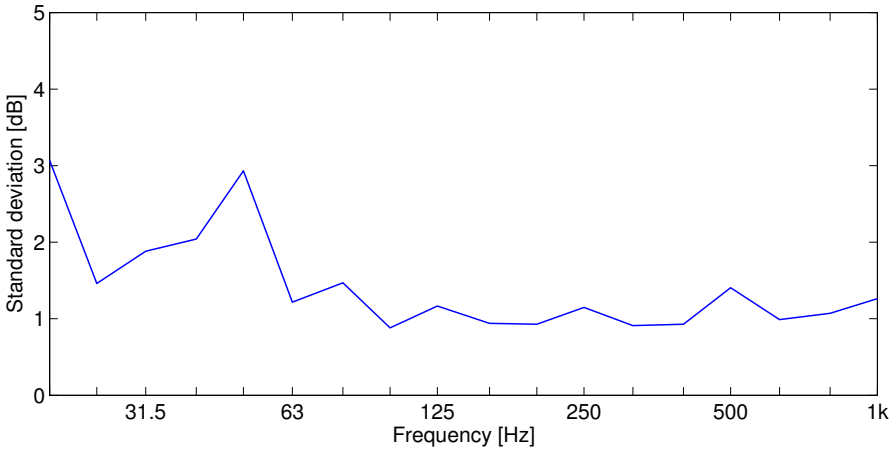

Figure 9.44: Standard deviation of 12 power calibration factors.

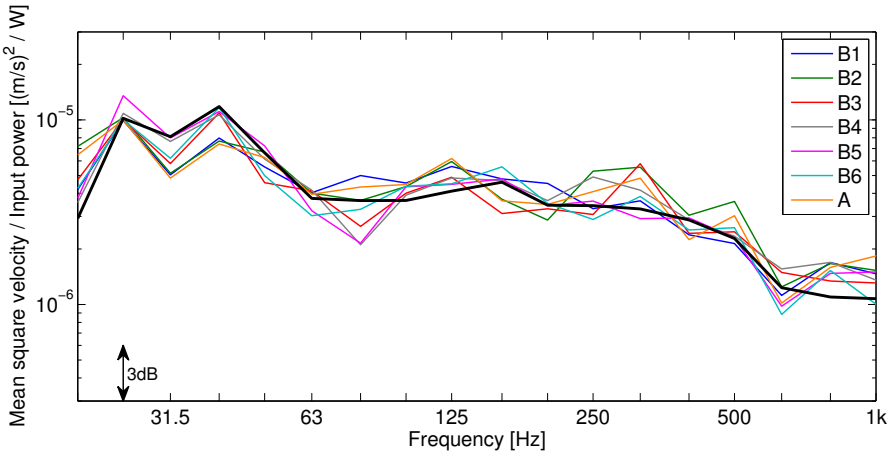

Figure 9.45: Power calibration factor from Section 9.4.1 and Section 9.4.2.

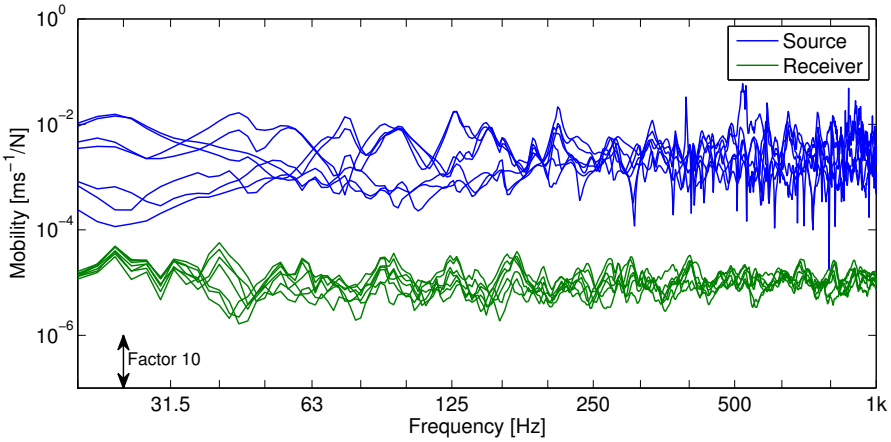

Figure 9.46: Mobility of combined heating and power unit, and of receiver wall.

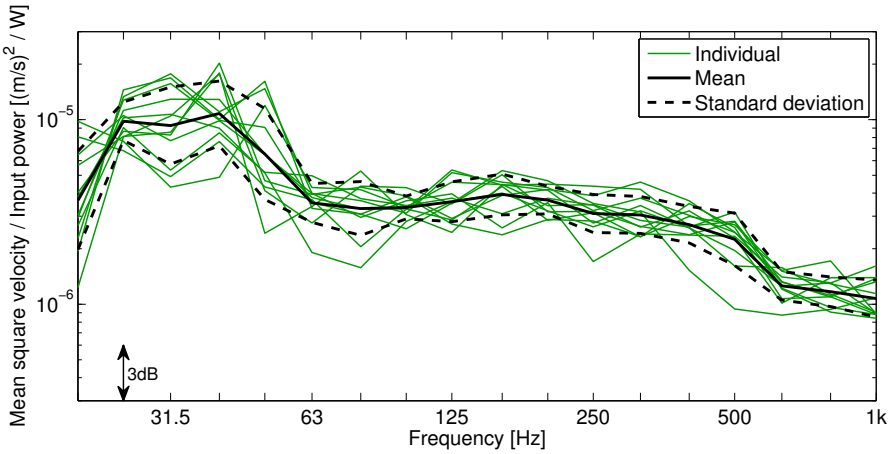

Figure 9.47: Power calibration factor (12 excitation positions and 10 fixed responses), obtained with micro-CHP unit attached to the wall.

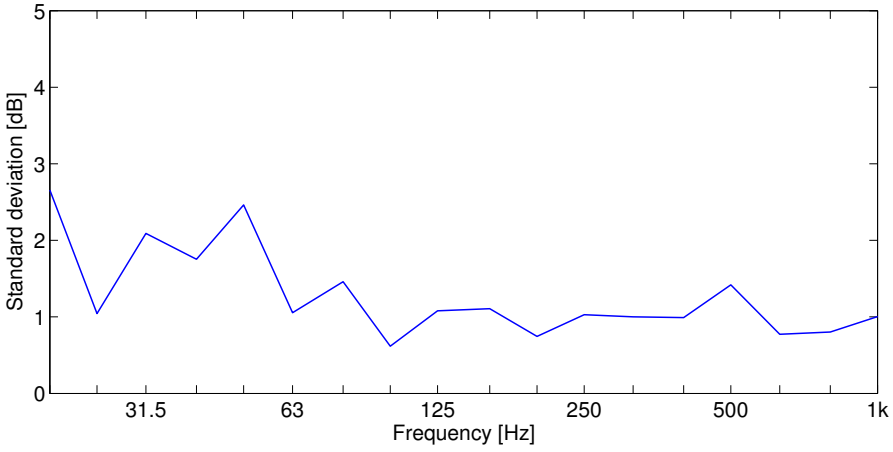

Figure 9.48: Standard deviation of all 12 power calibration factors, obtained with micro-CHP unit attached to the receiver wall.

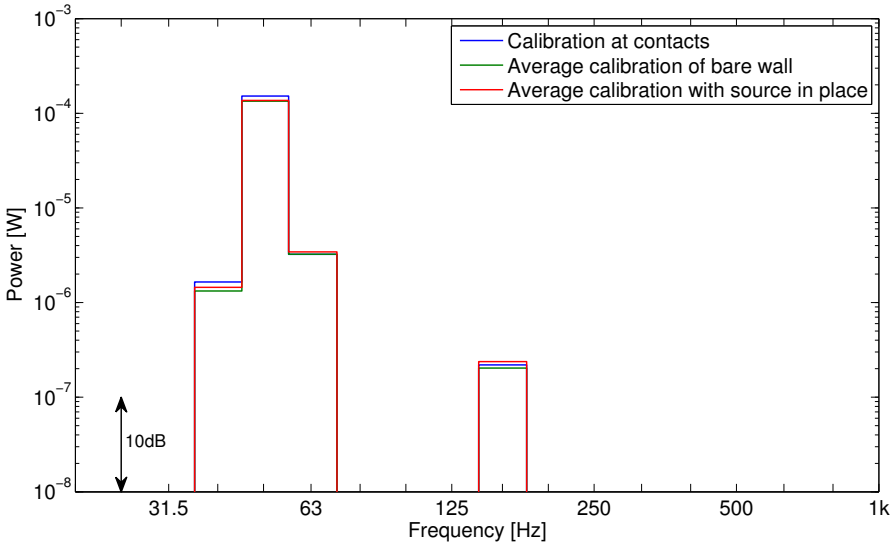

Figure 9.49: Indirectly determined source power of micro-CHP unit.

cated, distributed sources such as sanitary installations or heating systems, this is impractical, if not impossible. The micro-CHP unit is an example of a source that is difficult to remove once installed, especially if the installation includes pipes and pumps. For sources like this, the determination of the calibration factor with the source already in place is of interest. This requires that the source mobility is much higher than the receiver mobility, so as to not dynamically load the receiver plate [158].

The approximate mobility of the combined heating and power unit and of the receiver wall is shown in Figure 9.46. The mobility mismatch is sufficiently large to justify the assumption of a high-mobility source situation. The determination of the power calibration factor with the boiler already in place should therefore yield similar results to the measurements on the bare wall.

Figure 9.47 shows the power calibration factor, obtained using the same 12 excitation positions and the same 10 fixed response positions as in Section 9.4.2. Figure 9.48 shows the standard deviation, assuming a logarithmic normal distribution. Both the mean value and the standard deviation agree closely with the values in Section 9.4.2. It is thus possible to obtain an average power calibration factor with the source already in place, provided the source mobility is much higher than the receiver mobility.

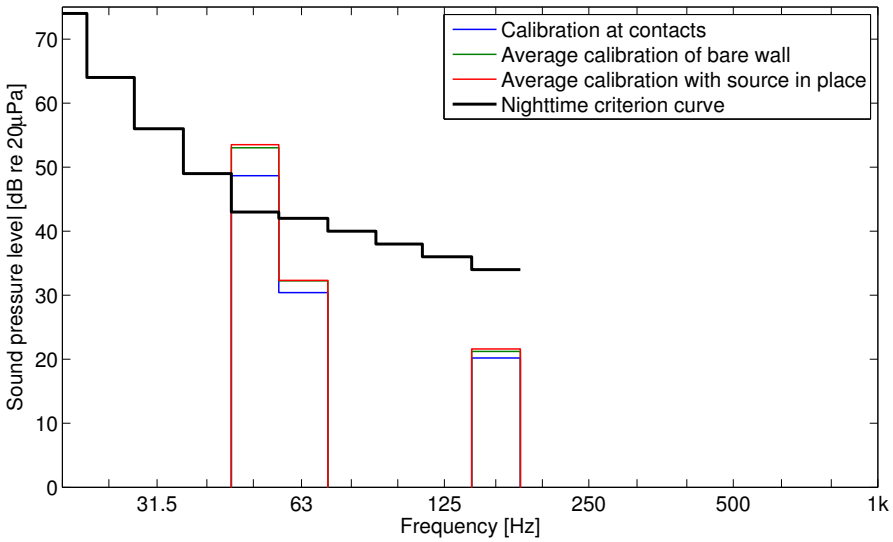

Figure 9.50: Reference sound pressure level in diagonally adjacent receiver room, calculated according to Annex C of EN 15657-1:2009 [17]. The nighttime criterion curve was taken from [102].

9.4.4 Calculation of reference sound pressure level in receiver room

Figure 9.49 shows the determined source power, for the three methods of obtaining the power calibration factor. Due to the low excitation levels, the SNR is sufficient only around the 50 Hz and in the 160 Hz frequency bands. The difference in source power between the three methods is smaller than 1 dB in these bands.

The source power is now used to predict sound pressure levels in a reference building. Annex C of EN 15657-1:2009 gives guidance on the calculation of a reference structure-borne sound pressure level in a receiver room diagonally below the source room. The micro-CHP unit is fictively mounted on a reference wall junction, and only the diagonal transmission is considered. The reference wall is a concrete block wall with a thickness of 10 cm and an infinite plate mobility of $Y_\infty = 5 \cdot 10^{-6}$ ms^{-1}/N. The length of the cross junction between floor and wall is 4 m, and the size of the source and receiver rooms are 3 m × 4 m × 2.5 m and 5 m × 4 m × 2.5 m, respectively [17].

With the transmission function given in Annex C of EN 15657-1:2009, the

reference sound pressure level in a room diagonally below the source room was calculated, using the source power values from Figure 9.49 as input parameters. The results are shown in Figure 9.50. Also shown is a criterion curve for the assessment of low frequency noise complaints during nighttime [102].

Comparison of the predicted sound pressure levels with the criterion curve indicates that complaints are likely for the installation of the micro-CHP unit in a building similar to the reference building, due to the strong 50 Hz component. In the other frequency bands, the predicted sound pressure levels are below the criterion curve. However, it should be noted that the values in Figure 9.50 may not be representative of a real installation, for the following reasons:

- The operating condition during measurement of the wall vibration was not representative. The micro-CHP unit was run in reverse, and no auxiliary devices were in operation.
- In the laboratory installation of the micro-CHP unit, pipes were not present. In a real installation, pipe-borne transmission can significantly affect noise levels in the receiver room.
- The transmission function in Annex C of EN 15657-1:2009 only considers the transmission to a receiver room diagonally below the source room. In a real installation, the unit may be mounted on the ground floor or in the basement, with the receiver room being on the same level or above. The transmission functions for this case can be calculated using EN 12354-5:2009 [16].

Also, since the transmission function in Annex C of EN 15657-1:2009 only gives values from 50 Hz upwards, the reference sound pressure level could not be calculated in the 40 Hz band.

Despite the above cautionary statements, Figure 9.50 demonstrates how source power levels, determined with the reception plate method or the source substitution method, can be used for the prediction of sound pressure levels in receiver rooms. These can then be used for an assessment of noise complaints and compliance with regulations.

9.5 Summary

Three experimental studies were conducted to investigate the source substitution method discussed in Chapter 8.

In the first study, the power injected by a simple test source into a free aluminium plate was determined using direct and indirect methods. The results for the reception plate method proved its usefulness, but also confirmed some of the problems highlighted in Section 8.2. The source substitution method was investigated with different options (steady-state calibration, transient calibration, average calibration). The source power could be determined with an accuracy of about 1 dB on average, compared with direct measurements. The practically most beneficial methods of using transient calibration or using an average calibration factor yielded the same accuracy.

In the second study, the power injected by a test source into a concrete transmission suite floor was determined using the source substitution method with the different calibration methods. The normalized structure-borne power of the test source could be determined within ± 6 dB of the results from the reception plate method for a free plate. The use of an instrumented hammer yielded similar results in this case study, as did the average calibration method. The use of the reception plate method with the connected plate proved difficult, mainly due to the loss factor determination. As a consequence of an under-estimated loss factor, the source power was under-estimated as well.

The third study provided an example of a practical implementation of the substitution method. A micro-CHP unit was operated on a masonry wall. The power calibration factors were obtained with an impulse hammer, on the wall alone and with the source already in place. No significant difference was observed between these measurements, indicating that the receiver can be calibrated with the source already in place, provided the source mobility is significantly higher than the receiver mobility. To demonstrate how the source power can be used, a reference sound pressure level in a receiver room was calculated and compared with a criterion curve for the assessment of low-frequency noise complaints.

In summary, the source substitution method discussed in Section 8.5 is a promising development of the reception plate method. While the latter can

be used if a free concrete reception plate is available, the former circumvents problems of loss factor determination when using coupled plates. The use of the instrumented hammer for the calibration and the use of an average calibration factor significantly increases the usability of the method, and provides a practical alternative for the (engineering-grade) estimation of injected power from a high-mobility source into a low-mobility receiver.

10 Conclusions and Recommendations

10.1 Introduction

In this chapter, the three parts of the thesis are summarized, and the key findings are highlighted. Suggestions are made for further work.

10.2 Conclusions

The objective of this thesis study was to develop and investigate methods for the experimental determination of important parameters for the characterization of structure-borne sound sources. Three source parameters were considered: blocked force, source mobility and source power.

10.2.1 Blocked forces

Matrix inversion methods for the determination of blocked forces were investigated. A method was proposed to circumvent the time-consuming experimental acquisition of FRF matrix elements, and to efficiently deal with the necessary matrix inversion. The proposed method involves a free, low-mobility receiver plate, which is modelled numerically. The use of a fully-defined receiver structure allows the calculation of the FRFs and the determination of favourable response positions, without the need to perform measurements. The numerical model for the calculation of point and transfer mobilities used modal summation, and mode shapes calculated from beam functions or FE simulations.

On comparing calculated and measured mobilities, there was agreement in the trends, but difference in detail, resulting in *large errors at individual frequencies. The beam function model is only approximate for plates with free edges. Better agreement was obtained with FRFs calculated from FE mode shapes.*

The simplified matrix inversion method was investigated experimentally. In the first stage, when using measured FRFs and measured operational velocities to indirectly determine the contact forces between source and plate, it was found that *low forces in the presence of high forces tend to be over-estimated.*

Methods to improve the inverse force determination were examined. *The greatest improvement was obtained when one response position was added to the minimum number.* Over-determination offers a simple strategy of improving force estimates, without significantly increasing the measurement effort or requiring additional calculations. Singular value rejection proved to be useful, too, mainly at low frequencies. However, *the choice of an appropriate threshold is critical*, as too high a value can yield under-estimates.

The choice of response locations was found to be of great importance. Other methods, such as over-determination and singular value rejection, were not capable of compensating for combinations of response positions with a high condition number. Optimizing and selecting favourable response positions should therefore be of primary importance in the pursuit of accurate force estimates.

When using FRFs calculated from beam function mode shapes or FE mode shapes to determine the contact forces, *the accuracy of the force estimates decreased considerably, due to imperfect agreement of measured and calculated FRFs.* FRFs calculated from FE mode shapes yielded better results than FRFs calculated from beam function mode shapes. However, *the errors in both cases were probably too large for the methods to be considered viable alternatives.*

Although errors in the force estimates can be considerable when using calculated instead of measured FRFs, it was found that *the optimization of response positions may nevertheless be performed with calculated FRFs.* Using response positions determined from calculated FRFs, inverse force determination was performed with measured FRFs. The results were within $\pm 1.5\,\mathrm{dB}$ of the directly measured forces, between 50 Hz and 630 Hz. With this approach, *the measurement effort can be reduced, while the accuracy of ordinary inverse force determination can be retained.*

10.2.2 Source mobility

Methods for the indirect determination of source mobility were considered. The source mobility was calculated from the difference between the mobilities of uncoupled and coupled receiver structure. Three methods were examined: The first requires excitation at remote positions and measurement of responses at the contacts; for the second, measurement at the contacts is not necessary in the coupled state; the third method was derived using the concept of reactive forces.

Simulations using analytical and numerical models of rods and beams verified the applicability of the methods for SDOF and MDOF systems. *All three methods yielded the correct result for a coupled beam system, when all important degrees of freedom were included in the matrix inversion.*

When important degrees of freedom were neglected, all three methods failed. However, additional translational mobilities could compensate for missing rotational mobilities. The rank of the matrix to be inverted had to be at least equal to the number of important degrees of freedom.

In further simulations, it was demonstrated that the *calculations are highly sensitive to uncertainties often encountered in practical measurement,* for example due to background noise or positioning uncertainties.

Two of the three formulations for the indirect determination of source mobility were investigated experimentally. The third method was not investigated further, since it does not promise any advantage over the other two. For single mass-spring systems on a plate, both methods yielded source mobility estimates that were within $\pm 3\,\mathrm{dB}$ of the directly measured values, in the mass-dominated frequency range. Around the anti-resonance frequency, deviations up to $\pm 20\,\mathrm{dB}$ and $\pm 30\,\mathrm{dB}$ were found for Method 1 and Method 2, respectively. *An important conclusion from this initial study was, that both methods are prone to experimental errors, and measurements have to be conducted with great care* (rigid connections, shaker excitation, high-sensitivity accelerometers, no movement of accelerometers between measurements).

When two mass-spring systems were placed on the receiver plate at the same time, their *point mobilities were estimated with the same accuracy as the sin-*

gle mass-spring systems, but phantom transfer mobilities appeared due to the involved matrix inversion.

Measurements with a free beam, attached to a receiver plate, confirmed the applicability of the two methods for multi-modal sources, connected at multiple positions. The deviations between direct and indirect point and transfer mobilities were within ±5 dB between 100 Hz and 700 Hz using Method 1, and within ±10 dB using Method 2. While Method 1 showed results within ±10 dB of the direct results above 700 Hz, Method 2 yielded systematic over-estimates of about 11 dB in this frequency range.

The importance of the source-receiver mobility ratio was highlighted. *Best results were obtained when source and receiver mobility were in the same order of magnitude.* This is because the receiver plate is dynamically loaded by the source, and therefore the plate response velocities alter significantly when the source is attached. From a practical perspective, it is difficult to know beforehand which source-receiver mobility ratio occurs at a given frequency. For an operator it is thus impossible to "engineer" a favourable source-receiver mobility ratio, and it is further difficult to know which frequency region is the most accurate once the indirect results have been obtained.

Finally, a fan unit on a framed support structure was considered, connected to the plate at three positions. *The agreement between directly and indirectly determined source mobilities was variable.* The average deviations between directly and indirectly determined source mobilities ranged between ±5 dB (point mobilities above 400 Hz) and 17 dB (transfer mobilities for Method 2 above 1 kHz), with occasional deviations of up to ±30 dB.

10.2.3 Source power

Methods to obtain the power injected by a high-mobility source into a low-mobility receiver were examined. The reception plate method for free concrete plates, as described in EN 15657-1:2009, currently appears to be the most practical and reliable method to determine the power injected into heavyweight building elements. However, there are *potential issues, due to a low modal overlap factor on the reception plate, and due to neglect of edge effects.*

When using real walls or floors as reception plates, the determination of the total loss factor is problematical. This can result in *significant errors due to energy returning from connected walls and floors.* A source substitution approach offers a way to circumvent these problems. Three experimental studies were conducted to investigate the source substitution method.

In the first study, the applicability of the reception plate method and of the source substitution method was confirmed, for application with a free plate. *In third-octave bands, the power injected by a broadband source into a free receiver plate was determined with an accuracy of about 3 dB (reception plate method) and 1 dB (source substitution method) on average, compared with direct measurements.*

In the second study, the use of coupled plates was investigated. The normalized structure-borne power of a test source was determined with an *accuracy of ±6 dB in third-octave bands. The use of an instrumented hammer for the calibration of the receiver and the use of an average calibration factor, independent of source position, yielded the same accuracy as the use of a shaker at the source positions.*

In a third study, an example was provided for a practical implementation of the substitution method, using a micro-CHP unit on a masonry wall. It was shown that *the receiver plate can be calibrated with the source already in place, provided the source mobility is significantly higher than the receiver mobility.*

10.3 Recommendations for further work

10.3.1 Blocked forces

The indirect method to obtain blocked forces should be tested on representative heavyweight wall or floor constructions. Receivers like these ensure a high-mobility source condition for most sources commonly found in residential buildings, which means that the operational forces approximate the blocked forces. The matrix inversion method could be used as an extension of the reception plate method as described in EN 15657-1:2009 [17], which uses a free concrete plate.

It should be investigated whether the use of experimentally determined eigenfrequencies together with calculated mode shapes can improve the accuracy of the calculated FRFs. As explained in Section 3.4.3, the mode shapes from the beam function model are only approximate for the case considered, due to neglected Poisson contraction. Nevertheless, it is expected that using accurate eigenfrequencies will significantly improve the agreement between measured and calculated FRFs.

Following from this, the possibility of (experimental) model updating of an FE model of the receiver structure to correct for material properties could be investigated. This task requires some expertise, but once the FE model has been updated to fit the measured data, the mode shapes can be stored and can be used in a modal summation as described in Section 3.4.1.

Using the matrix inversion method described in Chapter 3, the calculation of blocked moments is possible. This is of particular interest, as there are currently no transducers to measure moments directly. However, there are potential challenges, due to dimensional incompatibilities between forces and moments. Mixing transfer mobilities (v/F) and cross-transfer mobilities (v/M) in the FRF matrix may lead to ill-conditioned matrices, and to significant errors in the force/moment estimates.

10.3.2 Source mobility

To verify the usefulness of the proposed methods, the power injected by a source into a receiver should be calculated from source activity and source and receiver mobilities. The source mobility should be determined indirectly, and a reference source power should be obtained, for example by direct measurement.

The methods proposed for the indirect determination of source mobility require a degree of skill and precision that is probably too high for measurement standards in building acoustics. Therefore, the methods should be tested with sources typical in the automotive and aerospace industries, where such skills may be available.

For applications in building acoustics, simpler methods of obtaining the source mobility should be examined. For example, it should be investigated whether an

effective source mobility in third-octave bands can be obtained from reception plate power and average free velocity.

10.3.3 Source power

More empirical evidence is required for the validity of the source substitution method. The method should be tested with representative sources, connected to real walls and floors in buildings. To verify its validity, accurate reference values for the injected source power are required. Alternatively, the sound pressure in a receiver room could be used as reference.

Of practical relevance would be a method to determine or predict the power injected by a source into typical lightweight receiver structures, such as timber-joist floors or timber-frame cavity walls. The substitution method could provide a way to indirectly determine the injected source power for a given installation, and this could be investigated experimentally. The transferability of source power to other receiver elements, and the propagation of vibrational energy in non-homogeneous receiver structures are topics of future investigation.

Many structure-borne sound sources have a tonal excitation spectrum. For example, the fundamental frequency of most electrical equipment is at 50 Hz or 100 Hz. The application of statistical methods such as the reception plate method to tonal sources needs investigating. What are the penalties for using frequency-band averages instead of narrowband spectra?

Furthermore, while the fundamental frequency of most electrical equipment lies at 50 Hz or 100 Hz, the spinning frequency of washing machines and other rotating machinery is lower (for washing machines typically 12 to 25 Hz). Statistical methods do not apply at low frequencies, because the walls and floors do not support eigenmodes, and the uncertainty in measurement and prediction of transmitted sound is large. Instead of statistical methods, deterministic approaches might be an alternative for noise-control at low frequencies.

References

[1] Brüel & Kjaer: Data sheet for accelerometer type 4393V.

[2] Brüel & Kjaer: Data sheet for force transducer type 8200.

[3] Dassault Systems: ABAQUS.

[4] Getzner: Data sheet for Sylodamp HD 30.

[5] LMS International: Transfer Path Analysis – The qualification and quantification of vibro-acoustic transfer paths.

[6] ISO 5348: Mechanical Vibration and Shock – Mechanical mounting of accelerometers, 1999.

[7] ISO 7626: Vibration and Shock – Experimental determination of mechanical mobility – Part 1: Basic definitions and transducers, 1986.

[8] ISO 7626: Vibration and Shock – Experimental determination of mechanical mobility – Part 2: Measurements using single-point translation excitation with an attached vibration exciter, 1990.

[9] ISO 7626: Vibration and Shock – Experimental determination of mechanical mobility – Part 5: Measurement using impact excitation with an exciter which is not attached to the structure, 1994.

[10] ISO 9611: Acoustics – Characterization of sources of structure-borne sound with respect to sound radiation from connected structures – Measurement of velocity at the contact points of machinery when resiliently mounted, 1996.

[11] BS EN ISO 140: Acoustics – Measurement of sound insulation in buildings and of building elements – Part 7: Field measurements of impact sound insulation of floors, 1998.

[12] BS EN ISO 3382: Acoustics – Measurement of room acoustic parameters – Part 1: Performance spaces, 2009.

[13] BS EN ISO 3743: Acoustics – Determination of sound power levels of noise sources using sound pressure – Engineering methods for small, movable sources in reverberant fields – Part 1: Comparison method for a hard-walled test room, 2010.

[14] BS EN ISO 3743: Acoustics – Determination of sound power levels of noise sources using sound pressure – Engineering methods for small, movable sources in reverberant fields – Part 2: Methods for special reverberation test rooms, 2009.

[15] BS EN ISO 10848: Acoustics – Laboratory measurement of the flanking transmission of airborne and impact sound between adjoining rooms – Part 1: Frame document, 2006.

[16] BS EN 12354: Building acoustics – Estimation of acoustic performance of buildings from the performance of elements – Part 5: Sound levels due to service equipment, 2009.

[17] BS EN 15657: Acoustic properties of building elements and of buildings – Laboratory measurement of airborne and structure-borne sound from building equipment – Part 1: Simplified cases where the equipment mobilities are much higher than the receiver mobilities, taking whirlpool baths as an example, 2009.

[18] BS EN ISO 18233: Acoustics – Application of new measurement methods in building and room acoustics, 2006.

[19] BS ISO 18312: Mechanical vibration and shock – Measurement of vibration power flow from machines into connected support structures – Part 1: Direct method, 2012.

[20] BS EN 61260: Electroacoustics – Octave-band and fractional octave-band filters, 1996.

[21] NT ACOU 117: Acoustics – Determination in the field of structure-borne sound source strength of building service equipment, 2009.

[22] D. M. Allen. The relationship between variable selection and data augmentation and a method for prediction. *Technometrics*, 16(1):125–127, 1974.

[23] S. Bailhache and M. Villot. Comparison of structure-borne sound power injected to heavyweight and lightweight constructions. In *Proceedings of ICSV19, Vilnius*, 2012.

[24] F. D. Bartlett and W. G. Flannelly. Model verification of force determination for measuring vibratory loads. *Journal of the American Helicopter Society*, 24(2):10–18, 1979.

[25] S. F. Bassily and S. M. Dickinson. On the use of beam functions for problems of plates involving free edges. *Journal of Applied Mechanics*, 42(4):858–864, 1975.

[26] J. S. Bendat and A. G. Piersol. *Random Data: Analysis and Measurement Procedures*. John Wiley and Sons, 3rd edition, 2000.

[27] M. Blau. Indirect force spectra identification by FRF matrix inversion: A reliable approach based on quantitative error models. In *Proceedings of INTER-NOISE 1997, Budapest*, 1997.

[28] M. Blau. Error considerations in inverse force synthesis: What is different with respect to sole measurements of FRFs and response spectra. In *Proceedings of EURONOISE 1998, München*, 1998.

[29] M. Blau. Indirect measurement of multiple excitation force spectra by FRF matrix inversion: Influence of errors in statistical estimates of FRFs and response spectra. *Acta Acustica united with Acustica*, 85(16):464–479, July 1999.

[30] M. Blau. Inverse force synthesis: State of the art and future research. In *Proceedings of INTER-NOISE 2000, Nice*, 2000.

[31] H. A. Bonhoff. *The influence and significance of cross-order terms in interface mobilities for structure-borne sound source characterization*. PhD thesis, Technische Universität Berlin, 2009.

[32] H. G. Choi, A. N. Thite, and D. J. Thompson. A threshold for the use of Tikhonov regularization in inverse force determination. *Applied Acoustics*, 67(7):700–719, 2006.

[33] H. G. Choi, A. N. Thite, and D. J. Thompson. Comparison of methods for parameter selection in Tikhonov regularization with application to inverse force determination. *Journal of Sound and Vibration*, 304:894–917, 2007.

[34] B. Clarkson. The derivation of modal densities from point impedances. *Journal of Sound and Vibration*, 77(4):583–584, 1981.

[35] R. J. M. Craik. Damping of building structures. *Applied Acoustics*, 14(5):347–359, 1981.

[36] R. J. M. Craik. *Sound Transmission Through Buildings: Using Statistical Energy Analysis*. Gower Publishing Ltd, 1996.

[37] R. J. M. Craik and P. J. Barry. The internal damping of building materials. *Applied Acoustics*, 35(2):139–148, 1992.

[38] L. Cremer, M. Heckl, and B. A. T. Petersson. *Structure-Borne Sound: Structural Vibrations and Sound Radiation at Audio Frequencies*. Springer, 3rd edition, 2005.

[39] W. Dahmen and A. Reusken. *Numerik für Ingenieure und Naturwissenschaftler*. Springer, 2nd edition, 2008.

[40] E. B. Davis. Characterization of structure-borne noise sources using a reverberant or anechoic plate. In *Proceedings of INTER-NOISE 2006, Honolulu*, 2006.

[41] B. J. Dobson and E. Rider. A review of the indirect calculation of excitation forces from measured structural response data. *Proceedings of the Institution of Mechanical Engineers, Part C: Journal of Mechanical Engineering Science*, 204(2):69–75, 1990.

[42] A. S. Elliott. *Characterisation of structure-borne sound sources in-situ*. PhD thesis, University of Salford, 2009.

[43] A. S. Elliott and A. T. Moorhouse. A quarter vehicle transfer-path analysis by in-situ measurement. In *Proceedings of NOVEM 2012, Sorrento*, 2012.

[44] A. S. Elliott, A. T. Moorhouse, and G. Pavic. Moment excitation and the measurement of moment mobilities. *Journal of Sound and Vibration*, 331(11):2499–2519, 2012.

[45] T. A. Evans. *Estimation of uncertainty in the structure-borne sound power transmission from a source to a receiver*. PhD thesis, University of Salford, 2010.

[46] D. J. Ewins. *Modal Testing: Theory and Practice*. Research Studies Press Ltd., 1986.

[47] D. J. Ewins and J. Griffin. A state-of-the-art assessment of mobility measurement techniques – Results for the mid-range structures (30-3000 Hz). *Journal of Sound and Vibration*, 78(2):197–222, 1981.

[48] J. A. Fabunmi. Effects of structural modes on vibratory force determination by the pseudoinverse technique. *AIAA Journal*, 24(3):504–509, March 1986.

[49] K.-R. Fehse and T. Kohrs. Der Einsatz von (in-)direkten Messverfahren und Berechnungen zur Charakterisierung und Quantifizierung von Körperschallquellen im Design-Prozess von Schienenfahrzeugen. In *Proceedings of DAGA 2005, München*, 2005.

[50] K.-R. Fehse and T. Kohrs. Körperschallquellen-Charakterisierung, Positionierung und Interaktion mit Empfangsstrukturen. In *Proceedings of DAGA 2007, Stuttgart*, 2007.

[51] R. A. Fulford and B. M. Gibbs. Structure-borne sound power and source characterisation in multi-point-connected systems. Part 1: Case studies for assumed force distributions. *Journal of Sound and Vibration*, 204(4):659–677, 1997.

[52] R. A. Fulford and B. M. Gibbs. Structure-borne sound power and source characterisation in multi-point-connected systems. Part 2: About mobility functions and free velocities. *Journal of Sound and Vibration*, 220(2):203–224, 1999.

[53] R. A. Fulford and B. M. Gibbs. Structure-borne sound power and source characterisation in multi-point-connected systems. Part 3: Force ratio estimates. *Journal of Sound and Vibration*, 225(2):239–282, 1999.

[54] P. Gajdatsy. *Advanced Transfer Path Analysis Methods*. PhD thesis, Katholieke Universiteit Leuven, 2011.

[55] P. Gajdatsy, K. Janssens, W. Desmet, and H. V. der Auweraer. Application of the transmissibility concept in transfer path analysis. *Mechanical Systems and Signal Processing*, 24(7):1963–1976, 2010.

[56] P. Gardonio and M. J. Brennan. On the origins and development of mobility and impedance methods in structural dynamics. *Journal of Sound and Vibration*, 249(3):557–573, 2002.

[57] P. Gardonio and M. J. Brennan. *Advanced Applications in Acoustics, Noise and Vibration*, chapter 9: Mobility and impedance methods in structural dynamics, pages 389–447. Taylor & Francis, 2004.

[58] B. M. Gibbs. Granularity in structure-borne sound source characterisation. In *Proceedings of NOVEM 2009, Oxford*, 2009.

[59] B. M. Gibbs. Estimates of mobility for prediction of structure-borne sound transmission in buildings. In *Proceedings of ICSV19, Vilnius*, 2012.

[60] B. M. Gibbs. Uncertainties in predicting structure-borne sound power input into buildings. *The Journal of the Acoustical Society of America*, 133(5):2678–2689, 2013.

[61] B. M. Gibbs, R. Cookson, and N. Qi. Vibration activity and mobility of structure-borne sound sources by a reception plate method. *The Journal of the Acoustical Society of America*, 123(6):4199–4209, 2008.

[62] B. M. Gibbs and A. T. Moorhouse. Case studies of machine bases as structure-borne sound sources in buildings. *International Journal of Acoustics and Vibration*, 4(3):125–133, 1999.

[63] B. M. Gibbs, N. Qi, and A. T. Moorhouse. A practical characterisation for vibro-acoustic sources in buildings. *Acta Acustica united with Acustica*, 93(1):84–93, January/February 2007.

[64] G. H. Golub, M. Heath, and G. Wahba. Generalized cross-validation as a method for choosing a good ridge parameter. *Technometrics*, 21(2):215–223, 1979.

[65] G. H. Golub and C. F. V. Loan. *Matrix Computations*. The John Hopkins University Press, 3rd edition, 1996.

[66] W. G. Halvorsen and D. L. Brown. Impulse technique for structural frequency response testing. *Sound and Vibration*, November:8–21, November 1977.

[67] P. Hansen. Analysis of discrete ill-posed problems by means of the L-curve. *SIAM Review*, 34(4):561–580, 1992.

[68] P. Hansen and D. O'Leary. The use of the L-curve in the regularization of discrete ill-posed problems. *SIAM Journal on Scientific Computing*, 14(6):1487–1503, 1993.

[69] W. Hendricx. Accurate vehicle FRF measurements for indirect force determination based upon matrix inversion. In *Proceedings of 19th International Seminar on Modal Analysis (ISMA), Leuven*, 1994.

[70] B. Hillary. *Indirect measurement of vibration excitation forces*. PhD thesis, Imperial College London, 1983.

[71] C. Höller. Characterization of structure-borne sound sources in buildings. Master's thesis, RWTH Aachen University, 2010.

[72] C. Hopkins. *Sound Insulation*. Elsevier, 1st edition, 2007.

[73] C. Hopkins and M. Robinson. Using transient and steady-state SEA to quantify errors in the measured structure-borne sound power input from machinery with coupled reception plates. In *Proceedings of ICSV19, Vilnius*, 2012.

[74] C. Hopkins and M. Robinson. On the evaluation of decay curves to determine structural reverberation times for building elements. *Acta Acustica united with Acustica*, 99(2):226–244, 2013.

[75] C. Hopkins and M. Robinson. Using transient and steady-state SEA to assess potential errors in the measurement of structure-borne sound power input from machinery on coupled low-mobility reception plates. *Applied Acoustics*, 2013. Submitted for publication.

[76] F. Jacobsen. A note on acoustic decay measurements. *Journal of Sound and Vibration*, 115(1):163–170, 1987.

[77] F. Jacobsen and J. H. Rindel. Time reversed decay measurements. *Journal of Sound and Vibration*, 117(1):187–190, 1987.

[78] M. Kob and M. Vorländer. Band filters and short reverberation times. *Acta Acustica united with Acustica*, 86:350–357(8), March/April 2000.

[79] T. Kohrs and K.-R. Kirchner. Direct vs. in-situ structure-borne sound source characterization – Effect of simplifications on power transmission for a typical railway vehicle source. In *Proceedings of ICSV19, Vilnius*, 2012.

[80] H.-Y. Lai. Alternative test method for measuring structure-borne sound power. In *Proceedings of INTER-NOISE 2006, Honolulu*, 2006.

[81] H.-Y. K. Lai. Integrated reception-plate inverse-force test method for commercial airplane equipment structure-borne noise specification and qualification. In *Proceedings of INTER-NOISE 2012, New York*, 2012.

[82] G. F. Lang. Electrodynamic shaker fundamentals. *Sound and Vibration*, April 1997.

[83] K. Larsson and C. Simmons. Measurements of structure-borne sound from building service equipment by a substitution method – Round robin comparisons. *Noise Control Engineering Journal*, 59(1):75–86, 2011.

[84] A. W. Leissa. Vibration of plates. Technical Report SP-160, NASA, 1969.

[85] A. W. Leissa. The free vibration of rectangular plates. *Journal of Sound and Vibration*, 31(3):257–293, 1973.

[86] M. Lewit. *Inverse Messung von Kräften und Leistungen in gekoppelten, schwingenden Strukturen.* PhD thesis, TU Berlin, 1995.

[87] M. Lievens. Investigation into the importance of the degrees of freedom for the characterisation of structure-borne sound sources. *Acta Acustica united with Acustica*, 96:899–904, September/October 2010.

[88] M. Lievens and M. Vorländer. Investigation into the importance of the degrees of freedom for the characterisation of structure-borne sound sources: Case study of a washing machine on a wooden floor. *Acta Acustica united with Acustica*, 97(6):940–948, 2011.

[89] R. H. Lyon. *Statistical Energy Analysis of Dynamical Systems: Theory and Applications*. MIT Press, 1975.

[90] A. R. Mayr. *Vibro-acoustic sources in lightweight buildings*. PhD thesis, University of Liverpool, June 2009.

[91] A. R. Mayr and B. M. Gibbs. Single equivalent approximation for multiple contact structure-borne sound sources in buildings. *Acta Acustica united with Acustica*, 98(3):402–410, 2012.

[92] K. G. McConnell. *Vibration Testing – Theory and Practice*. John Wiley and Sons, 1995.

[93] S. Mecking, A. R. Mayr, and U. Schanda. Messung von Körperschall-Nachhallzeiten inhomogener Strukturen am Beispiel einer Holzbalkendecke. In *Proceedings of DAGA 2012, Darmstadt*, 2012.

[94] A. Meier. *Die Bedeutung des Verlustfaktors bei der Bestimmung der Schalldämmung im Prüfstand*. PhD thesis, RWTH Aachen University, 2000.

[95] A. Meier and A. Schmitz. Application of total loss factor measurements for the determination of sound insulation. *Building Acoustics*, 6(2):71–84, June 1999.

[96] J. M. Mondot and B. A. T. Petersson. Characterization of structure-borne sound sources: The source descriptor and the coupling function. *Journal of Sound and Vibration*, 114(3):507–518, 1987.

[97] E. H. Moore. On the reciprocal of the general algebraic matrix. *Bulletin of the American Mathematical Society*, 26(9):394–395, 1920.

[98] A. T. Moorhouse. Private Communication. 10 May 2011.

[99] A. T. Moorhouse. On the characteristic power of structure-borne sound sources. *Journal of Sound and Vibration*, 248(3):441–459, 2001.

[100] A. T. Moorhouse, A. S. Elliott, and T. A. Evans. In situ measurement of the blocked force of structure-borne sound sources. *Journal of Sound and Vibration*, 325:679–685, 2009.

[101] A. T. Moorhouse, T. A. Evans, and A. S. Elliott. Some relationships for coupled structures and their application to measurement of structural dynamic properties in situ. *Mechanical Systems and Signal Processing*, 25(5):1574–1584, 2011.

[102] A. T. Moorhouse, D. C. Waddington, and M. D. Adams. A procedure for the assessment of low frequency noise complaints. *The Journal of the Acoustical Society of America*, 126(3):1131–1141, 2009.

[103] A. T. Moorhouse and B. M. Gibbs. Simplified characterisation of multiple point excited structures using mobility matrix eigenvalues and eigenvectors. *Acta Acustica united with Acustica*, 84(5):843–853, September/October 1998.

[104] S. Müller. *Handbook of Signal Processing in Acoustics*, volume 1, chapter 5: Measuring Transfer-Functions and Impulse Responses, pages 65–85. Springer, 2008.

[105] G. J. O'Hara. Mechanical impedance and mobility concepts. *The Journal of the Acoustical Society of America*, 41(5):1180–1184, 1967.

[106] R. Penrose. A generalized inverse for matrices. *Mathematical Proceedings of the Cambridge Philosophical Society*, 51(3):406–413, 1955.

[107] B. A. T. Petersson. Approaches for structure-borne sound source characterisation. In *Proceedings of ICSV16, Krakow*, 2009.

[108] B. A. T. Petersson and B. M. Gibbs. Use of the source descriptor concept in studies of multi-point and multi-directional vibrational sources. *Journal of Sound and Vibration*, 168(1):157–176, 1993.

[109] B. A. T. Petersson and B. M. Gibbs. Towards a structure-borne sound source characterization. *Applied Acoustics*, 61(3):325–343, 2000.

[110] B. A. T. Petersson and J. Plunt. On effective mobilities in the prediction of structure-borne sound transmission between a source structure and a receiving structure. Part 1: Theoretical background and basic experimental studies. *Journal of Sound and Vibration*, 82(4):517–529, 1982.

[111] B. A. T. Petersson and J. Plunt. On effective mobilities in the prediction of structure-borne sound transmission between a source structure and a

receiving structure. Part 2: Procedures for the estimation of mobilities. *Journal of Sound and Vibration*, 82(4):531–540, 1982.

[112] R. J. Pinnington. Approximate mobilities of built-up structures. Technical Report 162, Institute of Sound and Vibration Research, 1988.

[113] J. Plunt. Finding and fixing vehicle NVH problems with transfer path analysis. *Sound and Vibration*, 39(11):12–16, November 2005.

[114] R. E. Powell. *Multichannel inverse filtering of machinery vibration signals*. PhD thesis, Massachusetts Institute of Technology, 1982.

[115] R. B. Randall. *Frequency analysis*. Brüel & Kjaer, 3rd edition, 1987.

[116] A. M. R. Ribeiro, J. M. M. Silva, and N. M. M. Maia. On the generalisation of the transmissibility concept. *Mechanical Systems and Signal Processing*, 14(1):29–35, 2000.

[117] M. Robinson. *Prediction of sound and vibration response using Transient Statistical Energy Analysis*. PhD thesis, University of Liverpool, 2012.

[118] T. J. Roggenkamp. *An investigation of the indirect measurement of broadband force spectra*. PhD thesis, Purdue University, 1992.

[119] S. Rubin. Transmission matrices for vibration and their relation to admittance and impedance. *Journal of Engineering for Industry*, 86:9–21, February 1964.

[120] J. Scheck. *Characterisation of lightweight stairs as structure-borne sound sources*. PhD thesis, University of Liverpool, 2011.

[121] J. Scheck, M. Chamaoun, H.-M. Fischer, and B. M. Gibbs. Preparation of a round robin on the reception plate method to characterise structure-borne sound sources in buildings. In *Proceedings of INTER-NOISE 2010, Lisbon*, 2010.

[122] J. Scheck, H.-M. Fischer, and B. M. Gibbs. Direct and indirect methods to assess the structure-borne power transmission into receiving structures. In *Proceedings of ICA 2007, Madrid*, 2007.

[123] J. Scheck, H.-M. Fischer, and B. M. Gibbs. In-situ measurement of structure-borne sound power of vibrating sources using building elements

as reception plates. In *Proceedings of Forum Acusticum 2011, Aalborg*, 2011.

[124] J. Scheck, F. Mack, H.-M. Fischer, and B. M. Gibbs. Characterisation of structure-borne sound sources using walls and floors as reception plates. In *Proceedings of ICSV16, Krakow*, 2009.

[125] P. Schevenels. *Investigation of the source-structure-sound interaction in the framework of the source characterisation and sound radiation of vibrating sources in buildings*. PhD thesis, Katholieke Universiteit Leuven, 2011.

[126] P. Schevenels, P. J. G. van der Linden, and G. Vermeir. An inverse force measurement method to determine the injected structure-borne sound power from an installation into a building element. *Building Acoustics*, 17(3):199–219, 2010.

[127] M. R. Schroeder. New method of measuring reverberation time. *The Journal of the Acoustical Society of America*, 37(3):409–412, 1965.

[128] S. R. Searle. *Matrix Algebra Useful for Statistics*. John Wiley and Sons, 1982.

[129] W. Soedel. *Vibration of Shells and Plates*. Marcel Dekker Inc., 2nd edition, 1993.

[130] R. Sottek and B. Müller-Held. Binaural transfer path analysis and synthesis (BTPA/BTPS) using sub-structuring techniques based on finite element analysis (FEA) and measurements. In *Proceedings of the SAE Noise & Vibration Conference 2007*, 2007.

[131] M. M. Späh. Private Communication. 24 October 2011.

[132] M. M. Späh. *Characterisation of structure-borne sound sources in buildings*. PhD thesis, University of Liverpool, 2006.

[133] M. M. Späh and B. M. Gibbs. Reception plate method for characterisation of structure-borne sound sources in buildings: Assumptions and application. *Applied Acoustics*, 70(2):361–368, 2009.

[134] M. M. Späh and B. M. Gibbs. Reception plate method for characterisation of structure-borne sound sources in buildings: Installed power and sound

pressure from laboratory data. *Applied Acoustics*, 70(11-12):1431–1439, 2009.

[135] J. W. Strutt (Lord Rayleigh). Some general theorems relating to vibrations. *Proceedings of the London Mathematical Society*, 4:357–368, 1873.

[136] J. Su. *Simplified characterisation of structure-borne sound sources with multi-point connections*. PhD thesis, University of Liverpool, 2003.

[137] T. ten Wolde. Reciprocity measurements in acoustical and mechano-acoustical systems. Review of theory and applications. *Acta Acustica united with Acustica*, 96:1–13, January/February 2010.

[138] T. ten Wolde and G. R. Gadefelt. Development of standard measurement methods for structureborne sound emission. *Noise Control Engineering Journal*, 28(1):5–14, 1987.

[139] A. N. Thite. *Inverse force determination of structure-borne sound sources*. PhD thesis, University of Southampton, 2003.

[140] A. N. Thite and D. J. Thompson. The quantification of structure-borne transmission paths by inverse methods. Part 1: Improved singular value rejection methods. *Journal of Sound and Vibration*, 264:411–431, 2003.

[141] A. N. Thite and D. J. Thompson. The quantification of structure-borne transmission paths by inverse methods. Part 2: Use of regularization techniques. *Journal of Sound and Vibration*, 264:433–451, 2003.

[142] A. N. Thite and D. J. Thompson. A systematic evaluation of different methods to improve inverse force determination. In *Proceedings of EURONOISE 2003, Naples*, 2003.

[143] A. N. Thite and D. J. Thompson. Selection of response measurement locations to improve inverse force determination. *Applied Acoustics*, 67(8):797–818, 2006.

[144] A. N. Tikhonov and Y. Arsenin. *Solution of ill-posed problems*. John Wiley and Sons, 1977.

[145] J. W. Verheij. *Multi-path sound transfer from resiliently mounted shipboard machinery*. PhD thesis, TU Delft, 1986.

[146] J. W. Verheij. Inverse and reciprocity methods for machinery noise source characterization and sound path quantification – Part 1: Sources. *International Journal of Acoustics and Vibration*, 2(1):11–20, 1997.

[147] T. E. Vigran. *Building Acoustics.* Taylor & Francis, 2008.

[148] A. Vogel, O. Kornadt, V. Wittstock, and W. Scholl. Measurement and prediction of structure-borne sound power in plate-shaped building elements. In *Proceedings of INTER-NOISE 2012, New York*, 2012.

[149] A. Vogel, O. Kornadt, V. Wittstock, and W. Scholl. On the measurement of sound power on reception plates. In *Proceedings of ICSV19, Vilnius*, 2012.

[150] H. von Helmholtz. Theorie der Luftschwingungen in Röhren mit offenen Enden. *Journal für die reine und angewandte Mathematik*, 57:1–72, 1860.

[151] G. B. Warburton. Vibration of rectangular plates. In *Proceedings of the Institution of Mechanical Engineers*, volume 168, pages 371–384, 1954.

[152] R. V. Waterhouse. Interference patterns in reverberant sound fields. *The Journal of the Acoustical Society of America*, 27(2):247–258, 1955.

[153] J. H. Wilkinson. *The algebraic eigenvalue problem.* Clarendon Press, Oxford, 1965.

[154] V. Wittstock. Results of a Round Robin on the sound power determination of structure-borne sound sources according to EN 15657-1. Technical report, Physikalisch-Technische Bundesanstalt, 2011.

[155] V. Wittstock, M. Villot, and J. Scheck. Results of a round robin on structure-borne sound power. In *Proceedings of Forum Acusticum 2011, Aalborg*, 2011.

[156] S. H. Yap and B. M. Gibbs. Structure-borne sound transmission from machines in buildings, Part 1: Indirect measurement of force at the machine-receiver interface of a single and multi-point connected system by a reciprocal method. *Journal of Sound and Vibration*, 222(1):85–98, 1999.

[157] S. H. Yap and B. M. Gibbs. Structure-borne sound transmission from machines in buildings, Part 2: Indirect measurement of force and moment

at the machine-receiver interface of a single point connected system by a reciprocal method. *Journal of Sound and Vibration*, 222(1):99–113, 1999.

[158] S. H. Yap, J. X. Su, and B. M. Gibbs. The measurement of the structural dynamic characteristics of floors with installed machines. *Applied Acoustics*, 52(2):105–124, 1997.

[159] S. Zheng, L. Zhou, X. Lian, and K. Li. Technical note: Coherence analysis of the transfer function for dynamic force identification. *Mechanical Systems and Signal Processing*, 25(6):2229–2240, 2011.

A Review of matrix notation and properties

A brief review of matrix notation and properties is provided in this appendix. For a comprehensive treatment, the reader is referred to the literature [65, 153].

A.1 Notation and definitions

An $m \times 1$ column vector $\mathbf{x}$ is defined as:

$$\mathbf{x_{m\times 1}} = \begin{pmatrix} x_1 \\ \vdots \\ x_m \end{pmatrix}$$

An $m \times n$ matrix $\mathbf{A}$ is defined as:

$$\mathbf{A_{m\times n}} = \begin{pmatrix} a_{11} & a_{12} & \dots & a_{1n} \\ a_{21} & a_{22} & \ddots & \vdots \\ \vdots & \vdots & \ddots & \vdots \\ a_{m1} & a_{m2} & \dots & a_{mn} \end{pmatrix}$$

Transposed matrix $\mathbf{A^T}$ and Hermitian transpose $\mathbf{A^H}$:

$$\mathbf{A^T} = \begin{pmatrix} a_{11} & a_{21} & \dots & a_{m1} \\ a_{12} & a_{22} & \ddots & \vdots \\ \vdots & \vdots & \ddots & \vdots \\ a_{1n} & a_{2n} & \dots & a_{mn} \end{pmatrix} \qquad \mathbf{A^H} = (\mathbf{A}^*)^\mathbf{T} = \begin{pmatrix} a_{11}^* & a_{21}^* & \dots & a_{m1}^* \\ a_{12}^* & a_{22}^* & \ddots & \vdots \\ \vdots & \vdots & \ddots & \vdots \\ a_{1n}^* & a_{2n}^* & \dots & a_{mn}^* \end{pmatrix}$$

Identity matrix $\mathbf{I}$ and diagonal matrix $\mathbf{S}$:

$$\mathbf{I_{n\times n}} = \begin{pmatrix} 1 & 0 & \dots & 0 \\ 0 & 1 & \ddots & \vdots \\ \vdots & \vdots & \ddots & \vdots \\ 0 & 0 & \dots & 1 \end{pmatrix} \qquad \mathbf{S_{n\times n}} = \begin{pmatrix} \sigma_{11} & 0 & \dots & 0 \\ 0 & \sigma_{22} & \ddots & \vdots \\ \vdots & \vdots & \ddots & \vdots \\ 0 & 0 & \dots & \sigma_{nn} \end{pmatrix}$$

Symmetric matrix:

$$\mathbf{A} = \mathbf{A^T}$$

Orthogonal matrix:

$$\mathbf{A} = \mathbf{A^{-T}}$$

Unitary matrix:

$$\mathbf{A} = (\mathbf{A}^*)^{\mathbf{-T}}$$

The inverse $\mathbf{A^{-1}}$ of an $n \times n$ matrix $\mathbf{A}$ is defined such that

$$\mathbf{A^{-1}A} = \mathbf{AA^{-1}} = \mathbf{I}.$$

The **norm** of a vector or a matrix is a measure of their length or size. Various definitions exist; one of the most important is the p-norm:

$$\|\mathbf{x}\|_\mathbf{p} = \left(\sum_{i=1}^{n} |x_i|^p \right)^{1/p} \qquad \|\mathbf{A}\|_\mathbf{p} = \max_{\mathbf{x}\neq\mathbf{0}} \frac{\|\mathbf{Ax}\|_\mathbf{p}}{\|\mathbf{x}\|_\mathbf{p}}$$

Setting $p = 2$ gives the Euclidean vector norm and the spectral matrix norm:

$$\|\mathbf{x}\|_\mathbf{2} = \sqrt{\mathbf{x^H x}} = \sqrt{|x_1|^2 + \cdots + |x_n|^2}$$
$$\|\mathbf{A}\|_\mathbf{2} = \sqrt{\lambda_{max}(\mathbf{A^H A})} = \sigma_{max}(\mathbf{A})$$

The **rank** of a matrix indicates the number of linearly independent rows or columns.

A.2 Matrix identities

Matrices must conform for multiplication:

$$\mathbf{A_{m\times n}}\,\mathbf{B_{n\times p}} = \mathbf{C_{m\times p}}$$

Some important relationships regarding inverse and transposed matrices [128]:

$$(\mathbf{AB})^{-\mathbf{1}} = \mathbf{B^{-1}A^{-1}} \tag{A.1}$$

$$(\mathbf{ABC})^{-\mathbf{1}} = \mathbf{C^{-1}B^{-1}A^{-1}} \tag{A.2}$$

$$(\mathbf{A^T})^{-\mathbf{1}} = (\mathbf{A^{-1}})^{\mathbf{T}} \tag{A.3}$$

$$(\mathbf{A+B})^{\mathbf{T}} = \mathbf{A^T + B^T} \tag{A.4}$$

$$(\mathbf{AB})^{\mathbf{T}} = \mathbf{B^T A^T} \tag{A.5}$$

$$(\mathbf{ABC})^{\mathbf{T}} = \mathbf{C^T B^T A^T} \tag{A.6}$$

$$(\mathbf{A^{-1}+B^{-1}})^{-\mathbf{1}} = \mathbf{A(A+B)^{-1}B} \tag{A.7}$$

$$= \mathbf{B(A+B)^{-1}A} \tag{A.8}$$

B Mobilities of Rods, Beams and Plates

In this appendix, analytical and numerical solutions are provided for point and transfer mobilities of free rods, beams, and plates. All of these may be calculated using modal summation. In modal summation, the contributions of each mode shape at excitation and response positions are summed, with regard to the associated eigenfrequency. For accurate results, an infinite number of modes must be considered. In practice, modal summation methods always yield approximate solutions, since only a finite number of modes is considered. For rods and beams, analytical solutions for point and transfer mobilities yield more accurate results, and are also faster to compute.

B.1 Point and transfer mobilities of free rods

The point and transfer mobilities of a free rod excited at an arbitrary internal position are given by the following analytical solution [101]:

$$Y(\omega, x_1, x_2) = \frac{v(\omega, x_2)}{F(\omega, x_1)} = \begin{cases} -\dfrac{j}{\rho A c_L} \dfrac{\cos k_R x_2 \cos k_R (l - x_1)}{\sin k_R l} & x_2 \leq x_1, \\ -\dfrac{j}{\rho A c_L} \dfrac{\cos k_R (l - x_2) \cos k_R x_1}{\sin k_R l} & x_2 \geq x_1. \end{cases}$$

The rod is excited at position x_1 by a force F, which results in a velocity response v at position x_2. ρ is the density, A is the cross-sectional area, c_L is the longitudinal wavespeed, and l is the length of the rod. $j = \sqrt{-1}$ is the imaginary unit and k_R is the rod wavenumber. The longitudinal wavespeed c_L of a rod is given by $c_L = \sqrt{E/\rho}$, where E is Young's modulus. The rod wavenumber is calculated as $k_R = \omega / c_L$.

B.2 Point and transfer mobilities of free beams

The (cross-)point and (cross-)transfer mobilities of a free beam excited by a force or moment at an arbitrary position are given by the following analytical solutions [101, 136]:

$$Y_{vF}(\omega, x_1, x_2) = \frac{v(\omega, x_2)}{F(\omega, x_1)} = \begin{cases} \frac{j\omega}{2Bk_B^3}\left(f_1(x_1)g_1(x_2) + f_2(x_1)g_2(x_2)\right) & x_2 \leq x_1 \\ \frac{j\omega}{2Bk_B^3}\left(f_1(x_2)g_1(x_1) + f_2(x_2)g_2(x_1)\right) & x_2 \geq x_1 \end{cases}$$

$$Y_{vM}(\omega, x_1, x_2) = \frac{v(\omega, x_2)}{M(\omega, x_1)} = \begin{cases} \frac{j\omega}{2Bk_B^3}\left(f_1'(x_1)g_1(x_2) + f_2'(x_1)g_2(x_2)\right) & x_2 \leq x_1 \\ \frac{j\omega}{2Bk_B^3}\left(f_1(x_2)g_1'(x_1) + f_2(x_2)g_2'(x_1)\right) & x_2 \geq x_1 \end{cases}$$

$$Y_{\theta F}(\omega, x_1, x_2) = \frac{\theta(\omega, x_2)}{F(\omega, x_1)} = \begin{cases} \frac{j\omega}{2Bk_B^3}\left(f_1(x_1)g_1'(x_2) + f_2(x_1)g_2'(x_2)\right) & x_2 \leq x_1 \\ \frac{j\omega}{2Bk_B^3}\left(f_1'(x_2)g_1(x_1) + f_2'(x_2)g_2(x_1)\right) & x_2 \geq x_1 \end{cases}$$

$$Y_{\theta M}(\omega, x_1, x_2) = \frac{\theta(\omega, x_2)}{M(\omega, x_1)} = \begin{cases} \frac{j\omega}{2Bk_B^3}\left(f_1'(x_1)g_1'(x_2) + f_2'(x_1)g_2'(x_2)\right) & x_2 \leq x_1 \\ \frac{j\omega}{2Bk_B^3}\left(f_1'(x_2)g_1'(x_1) + f_2'(x_2)g_2'(x_1)\right) & x_2 \geq x_1 \end{cases}$$

The beam of length l is excited at position x_1 by force F or moment M, which results in a linear or angular velocity response v or θ at position x_2. Figure B.1 illustrates the set up. B is the beam bending stiffness, with $B = El_z^3 l_y/12$ for a rectangular cross-section (l_z = height and l_y = width), and $B = Er^4\pi/4$ for a circular cross-section (r = radius). The beam bending wavenumber is $k_B = (\omega^2 m'/B)^{1/4}$, where m' is the mass per unit length.

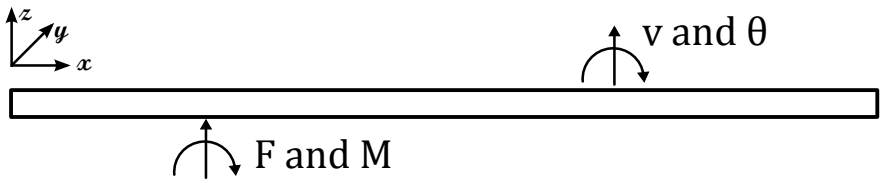

Figure B.1: Schematic of free beam.

The functions f_1, f_2, g_1, g_2, f_1', f_2', g_1', and g_2' are given as:

$$\begin{aligned}
f_1(x) = {} & \cosh k_B x - \cosh k_B(l-x)\cos k_B l - \sinh k_B(l-x)\sin k_B l - \cos k_B x + \\
& \cos k_B(l-x)\cosh k_B l - \sinh k_B l \sin k_B(l-x) \\
f_2(x) = {} & \sinh k_B x + \sinh k_B(l-x)\cos k_B l - \cosh k_B(l-x)\sin k_B l - \sin k_B x + \\
& \cos k_B(l-x)\sinh k_B l - \cosh k_B l \sin k_B(l-x) \\
g_1(x) = {} & -(\sin k_B x + \sinh k_B x)/(2(1-(\cosh k_B l \cos k_B l))) \\
g_2(x) = {} & (\cos k_B x + \cosh k_B x)/(2(1-(\cosh k_B l \cos k_B l))) \\
f_1'(x) = {} & k_B \sinh k_B x + k_B \sinh k_B(l-x)\cos k_B l + k_B \cosh k_B(l-x)\sin k_B l + \\
& k_B \sin k_B x + k_B \sin k_B(l-x)\cosh k_B l + k_B \sinh k_B l \cos k_B(l-x) \\
f_2'(x) = {} & k_B \cosh k_B x - k_B \cosh k_B(l-x)\cos k_B l + k_B \sinh k_B(l-x)\sin k_B l - \\
& k_B \cos k_B x + k_B \sin k_B(l-x)\sinh k_B l + k_B \cosh k_B l \cos k_B(l-x) \\
g_1'(x) = {} & -(k_B \cos k_B x + k_B \cosh k_B x)/(2(1-(\cosh k_B l \cos k_B l))) \\
g_2'(x) = {} & -(k_B \sin k_B x - k_B \sinh k_B x)/(2(1-(\cosh k_B l \cos k_B l)))
\end{aligned}$$

B.3 Point and transfer mobilities of free plates

The point and transfer mobilities of a thin plate with free boundary conditions excited at arbitrary positions are calculated using modal summation:

$$Y_{v_z F_z}(\omega, x_1, y_1, x_2, y_2) = j\omega \sum_{m=1}^{\infty}\sum_{n=1}^{\infty} \frac{\psi_{mn}(x_2, y_2)\psi_{mn}(x_1, y_1)}{\rho h l_x l_y \left[\omega_{mn}^2(1+j\eta) - \omega^2\right]}.$$

The plate is excited at position (x_1, y_1) by a force F_z orthogonal to the plate surface, which results in an out-of-plane velocity response v_z at position (x_2, y_2). Figure B.2 illustrates the set up. ψ_{mn} is the (m,n)th bending mode shape, ω_{mn} is the associated eigenfrequency, h, l_x and l_y are the geometric dimensions of the plate, ρ is the material density, and η is the total loss factor.

The plate mobility is calculated by summing the contributions of every combination of mode shapes. In practice, the upper limit of the sum must be adjusted according to the frequency range of interest. The more mode shapes are included, the better the result will be.

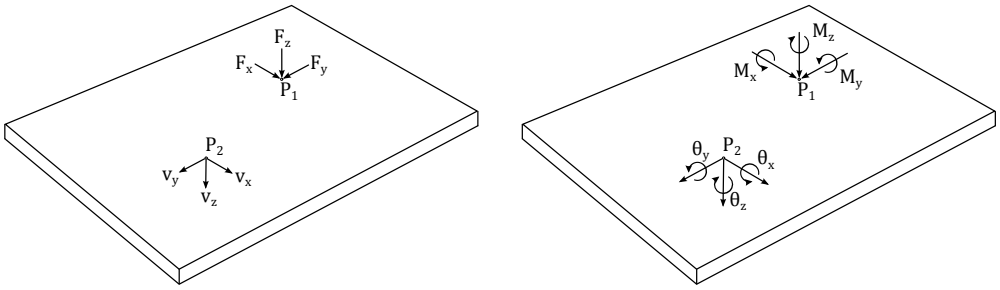

Figure B.2: Notation for linear velocities and forces (left), and for angular velocities and moments (right), acting on a thin plate, after [57].

Cross and cross-transfer mobilities are calculated in a similar fashion:

$$Y_{v_z M_x}(\omega, x_1, y_1, x_2, y_2) = j\omega \sum_{m=1}^{\infty}\sum_{n=1}^{\infty} \frac{\psi_{mn}(x_2, y_2)\psi^x_{mn}(x_1, y_1)}{\rho h l_x l_y \left[\omega^2_{mn}(1 + j\eta) - \omega^2\right]}$$

$$Y_{v_z M_y}(\omega, x_1, y_1, x_2, y_2) = j\omega \sum_{m=1}^{\infty}\sum_{n=1}^{\infty} \frac{\psi_{mn}(x_2, y_2)\psi^y_{mn}(x_1, y_1)}{\rho h l_x l_y \left[\omega^2_{mn}(1 + j\eta) - \omega^2\right]}$$

$$Y_{\theta_x F_z}(\omega, x_1, y_1, x_2, y_2) = j\omega \sum_{m=1}^{\infty}\sum_{n=1}^{\infty} \frac{\psi^x_{mn}(x_2, y_2)\psi_{mn}(x_1, y_1)}{\rho h l_x l_y \left[\omega^2_{mn}(1 + j\eta) - \omega^2\right]}$$

$$Y_{\theta_x M_x}(\omega, x_1, y_1, x_2, y_2) = j\omega \sum_{m=1}^{\infty}\sum_{n=1}^{\infty} \frac{\psi^x_{mn}(x_2, y_2)\psi^x_{mn}(x_1, y_1)}{\rho h l_x l_y \left[\omega^2_{mn}(1 + j\eta) - \omega^2\right]}$$

$$Y_{\theta_x M_y}(\omega, x_1, y_1, x_2, y_2) = j\omega \sum_{m=1}^{\infty}\sum_{n=1}^{\infty} \frac{\psi^x_{mn}(x_2, y_2)\psi^y_{mn}(x_1, y_1)}{\rho h l_x l_y \left[\omega^2_{mn}(1 + j\eta) - \omega^2\right]}$$

$$Y_{\theta_y F_z}(\omega, x_1, y_1, x_2, y_2) = j\omega \sum_{m=1}^{\infty}\sum_{n=1}^{\infty} \frac{\psi^y_{mn}(x_2, y_2)\psi_{mn}(x_1, y_1)}{\rho h l_x l_y \left[\omega^2_{mn}(1 + j\eta) - \omega^2\right]}$$

$$Y_{\theta_y M_x}(\omega, x_1, y_1, x_2, y_2) = j\omega \sum_{m=1}^{\infty}\sum_{n=1}^{\infty} \frac{\psi^y_{mn}(x_2, y_2)\psi^x_{mn}(x_1, y_1)}{\rho h l_x l_y \left[\omega^2_{mn}(1 + j\eta) - \omega^2\right]}$$

$$Y_{\theta_y M_y}(\omega, x_1, y_1, x_2, y_2) = j\omega \sum_{m=1}^{\infty}\sum_{n=1}^{\infty} \frac{\psi^y_{mn}(x_2, y_2)\psi^y_{mn}(x_1, y_1)}{\rho h l_x l_y \left[\omega^2_{mn}(1 + j\eta) - \omega^2\right]}$$

The eigenfrequencies of rectangular plates are given as [151]

$$\omega_{mn} = \sqrt{\frac{Eh^2}{12\rho(1-\nu^2)}} \left(\frac{\pi}{l_x}\right)^2 q_{mn}.$$

E is Young's modulus, and ν is Poisson's ratio. q_{mn} is of the following form:

$$q_{mn} = \sqrt{G^4_x(m) + G^4_y(n)(l_x/l_y)^4 + 2(l_x/l_y)^2\left[\nu H_x(m)H_y(n) + (1-\nu)J_x(m)J_y(n)\right]}$$

The constants G_x, G_y, H_x, H_y, J_x, and J_y are given in Table B.1 for free boundary conditions. The reader is referred to [151] and [57] for a list of the values for other common boundary conditions.

m	G	H	J
Even mode	0	0	0
Rocking mode	0	0	$12/\pi^2$
1	1.506	1.248	5.017
2, 3, ...	$m+\frac{1}{2}$	$\left(m+\frac{1}{2}\right)^2\left[1-\frac{4}{(2m+1)\pi}\right]$	$\left(m+\frac{1}{2}\right)^2\left[1+\frac{12}{(2m+1)\pi}\right]$

Table B.1: Values for the constants G, H, and J, for free plates (after [57]).

Calculation of plate mode shapes from beam functions

The plate mode shapes may be calculated as products of beam functions:

$$\psi_{mn}(x,y) = \phi_m(x)\phi_n(y)$$
$$\psi^x_{mn}(x,y) = \phi_m(x)\frac{\partial\phi_n(y)}{\partial y}$$
$$\psi^y_{mn}(x,y) = -\frac{\partial\phi_m(x)}{\partial x}\phi_n(y)$$

The beam functions for a free beam are given as

$$\phi_n(x) = \begin{cases} 1 & \text{Even mode} \\ \sqrt{3}(1-2x/l) & \text{Rocking mode} \\ \sqrt{2}\left\{\cos\gamma_i\left(\frac{x}{l_x}-\frac{1}{2}\right)+k_n\cosh\gamma_i\left(\frac{x}{l_x}-\frac{1}{2}\right)\right\} & n=1,3,5,\ldots \\ \sqrt{2}\left\{\sin\gamma_j\left(\frac{x}{l_x}-\frac{1}{2}\right)+k_n\sinh\gamma_j\left(\frac{x}{l_x}-\frac{1}{2}\right)\right\} & n=2,4,6,\ldots \end{cases}$$

The argument k_n is of the following form:

$$k_n = \begin{cases} -\dfrac{\sin\frac{1}{2}\gamma_i}{\sinh\frac{1}{2}\gamma_i} & n=1,3,5,\ldots \\ \dfrac{\sin\frac{1}{2}\gamma_j}{\sinh\frac{1}{2}\gamma_j} & n=2,4,6,\ldots \end{cases}$$

The γ-functions γ_i and γ_j obey the following equations:

$$\begin{cases} \tan\frac{1}{2}\gamma_i + \tanh\frac{1}{2}\gamma_i = 0 & n = 1,3,5,\ldots \\ \tan\frac{1}{2}\gamma_j - \tanh\frac{1}{2}\gamma_j = 0 & n = 2,4,6,\ldots \end{cases}$$

The zeros of the γ-functions are tabulated in Table B.2, with $i = (n+1)/2$ for $n = 1,3,5,\ldots$, and $j = n/2$ for $n = 2,4,6,\ldots$. It should be noted that Table 9.10 and Table 9.11 in [57] use slightly confusing indices for the γ-functions: γ_i in Table 9.10 is γ_j in Table 9.11, and vice versa. In Table B.2, indices consistent with the above equations are used.

i, j	$\tan\frac{1}{2}\gamma_i + \tanh\frac{1}{2}\gamma_i = 0$	$\tan\frac{1}{2}\gamma_j - \tanh\frac{1}{2}\gamma_j = 0$
1	4.73004	7.8532
2	10.9956	14.13716
3	17.27876	20.4204
4	23.5620	26.7036
5	29.8452	32.9868
6, 7, 8 ...	$\frac{(4i-1)\pi}{2}$	$\frac{(4j+1)\pi}{2}$

Table B.2: Zeros of the gamma functions γ_i and γ_j.

The first five eigenmode shapes of a free beam are shown in Figure B.3. The first two modes represent whole-body movement (even mode and rocking mode), and from the third mode upwards true modal behaviour is observed.

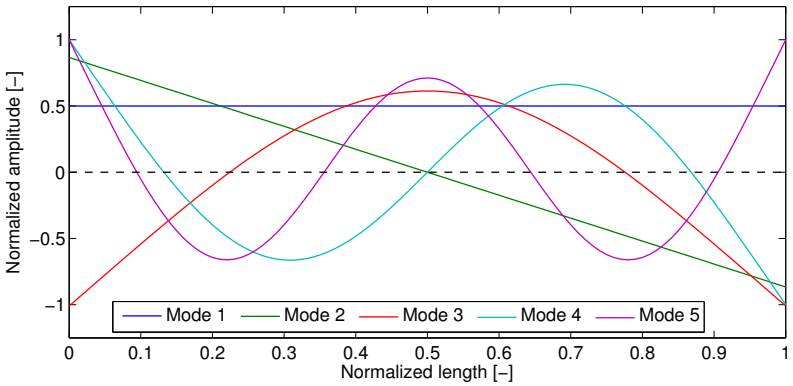

Figure B.3: First five eigenmode shapes of a free beam.

C Proofs from Section 6.2

Proofs are provided for the equivalence of Equations (6.3), (6.4), and (6.5) with Equation (6.2). They involve rearranging the equations to match Equation (6.2), using standard trigonometric properties. The proofs themselves offer no further insights into the methods discussed in Chapter 5, and are provided for completeness only.

C.1 Proof for Method 1

Substituting $Y_{A,cc}$, $Y_{A,ca}$, and $Y_{C,ca}$ into Equation (5.53) yields

$$
\begin{aligned}
Y_{B,cc} &= -\frac{j}{\rho A c_L}\frac{\cos kc}{\sin kc}\left[\frac{\cos ka}{\sin kc} - \frac{\cos k(l-c)\cos ka}{\sin kl}\right]^{-1}\frac{\cos k(l-c)\cos ka}{\sin kl} \\
&= -\frac{j}{\rho A c_L}\frac{\cos kc}{\sin kc}\left[\frac{\cos ka\sin kl - \cos k(l-c)\cos ka\sin kc}{\sin kc\sin kl}\right]^{-1}\frac{\cos k(l-c)\cos ka}{\sin kl} \\
&= -\frac{j}{\rho A c_L}\frac{\cos kc}{\sin kc}\frac{\sin kc\sin kl}{\cos ka\sin kl - \cos k(l-c)\cos ka\sin kc}\frac{\cos k(l-c)\cos ka}{\sin kl} \\
&= -\frac{j}{\rho A c_L}\frac{\cos k(l-c)\cos kc}{\sin kl - \cos k(l-c)\sin kc} \\
&= -\frac{j}{\rho A c_L}\frac{\cos k(l-c)\cos kc}{\sin kl - (\cos kl\cos kc + \sin kl\sin kc)\sin kc} \\
&= -\frac{j}{\rho A c_L}\frac{\cos k(l-c)\cos kc}{\sin kl - \cos kl\cos kc\sin kc - \sin kl\sin^2 kc} \\
&= -\frac{j}{\rho A c_L}\frac{\cos k(l-c)\cos kc}{\sin kl\left[1-\sin^2 kc\right] - \cos kl\cos kc\sin kc} \\
&= -\frac{j}{\rho A c_L}\frac{\cos k(l-c)\cos kc}{\sin kl\cos^2 kc - \cos kl\cos kc\sin kc} \\
&= -\frac{j}{\rho A c_L}\frac{\cos k(l-c)}{\sin kl\cos kc - \cos kl\sin kc} \\
&= -\frac{j}{\rho A c_L}\frac{\cos k(l-c)}{\sin k(l-c)}.
\end{aligned}
$$

C.2 Proof for Method 2

Substituting $Y_{A,cc}$, $Y_{A,ca}$, $Y_{A,aa}$, and $Y_{C,aa}$ into Equation (5.54) yields

$$
\begin{aligned}
Y_{B,cc} &= -\frac{j}{\rho A c_L}\left(\frac{\cos ka}{\sin kc}\left[\frac{\cos ka\cos k(c-a)}{\sin kc}-\frac{\cos k(l-a)\cos ka}{\sin kl}\right]^{-1}\frac{\cos ka}{\sin kc}-\frac{\cos kc}{\sin kc}\right)\\
&= -\frac{j}{\rho A c_L}\left(\frac{\cos^2 ka}{\sin^2 kc}\left[\frac{\cos ka\cos k(c-a)\sin kl-\cos k(l-a)\cos ka\sin kc}{\sin kc\sin kl}\right]^{-1}-\frac{\cos kc}{\sin kc}\right)\\
&= -\frac{j}{\rho A c_L}\left(\frac{\cos^2 ka}{\sin^2 kc}\frac{\sin kc\sin kl}{\cos ka\cos k(c-a)\sin kl-\cos k(l-a)\cos ka\sin kc}-\frac{\cos kc}{\sin kc}\right)\\
&= -\frac{j}{\rho A c_L}\left(\frac{\cos ka}{\sin kc}\frac{\sin kl}{\cos k(c-a)\sin kl-\cos k(l-a)\sin kc}-\frac{\cos kc}{\sin kc}\right)\\
&= -\frac{j}{\rho A c_L}\left(\frac{\cos ka\sin kl}{\cos k(c-a)\sin kl\sin kc-\cos k(l-a)\sin^2 kc}-\frac{\cos kc}{\sin kc}\right)\\
&= -\frac{j}{\rho A c_L}\frac{\cos ka\sin kl\sin kc-\cos k(c-a)\sin kl\sin kc\cos kc+\cos k(l-a)\sin^2 kc\cos kc}{\cos k(c-a)\sin kl\sin^2 kc-\cos k(l-a)\sin^3 kc}\\
&= -\frac{j}{\rho A c_L}\frac{\cos ka\sin kl-\cos k(c-a)\sin kl\cos kc+\cos k(l-a)\sin kc\cos kc}{\cos k(c-a)\sin kl\sin kc-\cos k(l-a)\sin^2 kc}\\
&= -\frac{j}{\rho A c_L}\frac{\cos ka\sin kl-(\cos kc\cos ka+\sin kc\sin ka)\sin kl\cos kc+(\cos kl\cos ka+\sin kl\sin ka)\sin kc\cos kc}{(\cos kc\cos ka+\sin kc\sin ka)\sin kl\sin kc-(\cos kl\cos ka+\sin kl\sin ka)\sin^2 kc}\\
&= -\frac{j}{\rho A c_L}\frac{\cos ka\sin kl-\cos^2 kc\cos ka\sin kl-\sin kc\sin ka\sin kl\cos kc+\cos kl\cos ka\sin kc\cos kc+\sin kl\sin ka\sin kc\cos kc}{\cos kc\cos ka\sin kl\sin kc+\sin^2 kc\sin ka\sin kl-\sin^2 kc\cos kl\cos ka-\sin^2 kc\sin ka\sin kl}\\
&= -\frac{j}{\rho A c_L}\frac{\cos ka\sin kl-\cos^2 kc\cos ka\sin kl+\cos kl\cos ka\sin kc\cos kc}{\cos kc\cos ka\sin kl\sin kc-\sin^2 kc\cos kl\cos ka}
\end{aligned}
$$

$$
\begin{aligned}
&= -\frac{j}{\rho A c_L} \frac{\sin kl - \cos^2 kc \sin kl + \cos kl \sin kc \cos kc}{\cos kc \sin kl \sin kc - \sin^2 kc \cos kl} \\
&= -\frac{j}{\rho A c_L} \frac{\sin kl(1 - \cos^2 kc) + \cos kl \sin kc \cos kc}{\sin kc(\cos kc \sin kl - \sin kc \cos kl)} \\
&= -\frac{j}{\rho A c_L} \frac{\sin kl \sin^2 kc + \cos kl \sin kc \cos kc}{\sin kc \sin k(l-c)} \\
&= -\frac{j}{\rho A c_L} \frac{\sin kl \sin kc + \cos kl \cos kc}{\sin k(l-c)} \\
&= -\frac{j}{\rho A c_L} \frac{\cos k(l-c)}{\sin k(l-c)}.
\end{aligned}
$$

C.3 Proof for Method 3

Substituting $Y_{A,ca}$, $Y_{A,da}$, $Y_{C,da}$, and $Y_{C,dc}$ into Equation (5.55) yields

$$
\begin{aligned}
Y_{B,cc} &= -\frac{j}{\rho A c_L}\left(\frac{\cos ka}{\sin kc}\left[\frac{\cos kd\cos k(c-a)}{\sin kc}-\frac{\cos kd\cos k(l-a)}{\sin kl}\right]^{-1}\frac{\cos kd\cos k(l-c)}{\sin kl}\right)\\
&= -\frac{j}{\rho A c_L}\left(\frac{\cos ka}{\sin kc}\left[\frac{\cos kd\cos k(c-a)\sin kl-\cos kd\cos k(l-a)\sin kc}{\sin kc\sin kl}\right]^{-1}\frac{\cos kd\cos k(l-c)}{\sin kl}\right)\\
&= -\frac{j}{\rho A c_L}\left(\frac{\cos ka}{\sin kc}\frac{\sin kc\sin kl}{\cos kd\cos k(c-a)\sin kl-\cos kd\cos k(l-a)\sin kc}\frac{\cos kd\cos k(l-c)}{\sin kl}\right)\\
&= -\frac{j}{\rho A c_L}\frac{\cos ka\cos k(l-c)}{\cos k(c-a)\sin kl-\cos k(l-a)\sin kc}\\
&= -\frac{j}{\rho A c_L}\frac{\cos ka\cos k(l-c)}{(\cos kc\cos ka+\sin kc\sin ka)\sin kl-(\cos kl\cos ka+\sin kl\sin ka)\sin kc}\\
&= -\frac{j}{\rho A c_L}\frac{\cos ka\cos k(l-c)}{\cos kc\cos ka\sin kl+\sin kc\sin ka\sin kl-\cos kl\cos ka\sin kc-\sin kl\sin ka\sin kc}\\
&= -\frac{j}{\rho A c_L}\frac{\cos k(l-c)}{\cos kc\sin kl-\cos kl\sin kc}\\
&= -\frac{j}{\rho A c_L}\frac{\cos k(l-c)}{\sin k(l-c)}.
\end{aligned}
$$

D Determination of total loss factor

The determination of the total loss factor of a structure is a vital component of many engineering methods, including the reception plate method (Section 8.2). There are various methods to determine the total loss factor, for example:

1. Determination of loss factor by modal parameters;
2. Determination of loss factor by power/energy balance methods;
3. Determination of loss factor by decay methods.

An overview and comparison of available methods is provided by Meier [94]. In this thesis, only decay methods were used. A thorough discussion of this approach is given by Hopkins [72]. Using decay methods, the total loss factor is estimated from the structural reverberation time T_s:

$$\eta = \frac{6 \ln 10}{2\pi f T_s} \approx \frac{2.2}{f T_s} \tag{D.1}$$

The measurement and calculation procedure for the structural reverberation time is explained in ISO 10848-1:2006 [15]. It is similar to the procedure for the reverberation time in rooms, as described in ISO 3382-1:2009 [12]. The method, sometimes called "Schroeder method" after the original publication by M. R. Schroeder [127], uses a backward-integrated squared impulse response to calculate the energy decay in the system of interest:

$$E(t) = \int_t^\infty h^2(\tau)\,\mathrm{d}\tau = \int_\infty^t h^2(\tau)\,\mathrm{d}(-\tau) \tag{D.2}$$

In the following paragraphs, a brief overview is provided of the involved steps. To obtain the impulse response $h(t)$, the structure of interest is excited with an impulse hammer, and the response (initial pulse and decay) measured with an accelerometer in the far field. Alternatively, the impulse response can be obtained from shaker measurements and subsequent signal processing [18, 95].

The broadband impulse response is band-filtered, using octave band or third-octave band filters as specified in [20]. An inherent limit of this operation is the length of the band filter impulse response. If the decay of the structure in a frequency band is shorter than the decay of the respective filter, the reverberation time estimate will reflect the filter decay time, and not the structural decay time. The length of the filter impulse response therefore constitutes a lower limit of the measurable decay time. This is an issue especially at low frequencies, where the filter responses are longer than at high frequencies.

To evaluate short decays, advantage can be taken of the fact that filter rise times are shorter than their decay times. If the convolution of signal and filter in the time domain is performed time-reversed, the influence of the filter response can be limited. Jacobsen [76, 77] and Kob [78] showed that time-reversed filtering allows evaluation of decay curves with $BT > 4$, where BT is the product of filter bandwidth and reverberation time. For forward-filtering, reverberation time estimates are only valid if $BT > 8$. Using $B \approx 0.232 f_c$ for third-octave bands and $B \approx 0.707 f_c$ for octave bands, an upper limit for the measurable loss factor is calculated from Equation (D.1), see Table D.1.

	Octave bands	Third-octave bands
Forward filtering	$\eta < 0.1944$	$\eta < 0.0638$
Reversed filtering	$\eta < 0.3889$	$\eta < 0.1276$

Table D.1: Upper limit of measurable total loss factor.

In the next step, the band-filtered time signals are averaged linearly or exponentially. In this thesis, only exponential averaging was used. For room reverberation times, ISO 3382-1:2009 requires the time constant of an exponential time window to be less than, but as close as possible to, $T/30$. Using smaller time constants is possible, but offers little advantage. In the loss factor calculations in this thesis, a time constant of $\tau = 0.5\,\mathrm{ms}$ was used throughout. A discussion on errors in loss factor calculation due to the averaging procedure can be found in [74].

In Equation (D.2), the integration of the squared impulse response is performed between t and ∞. In practice, background noise will at some point interfere

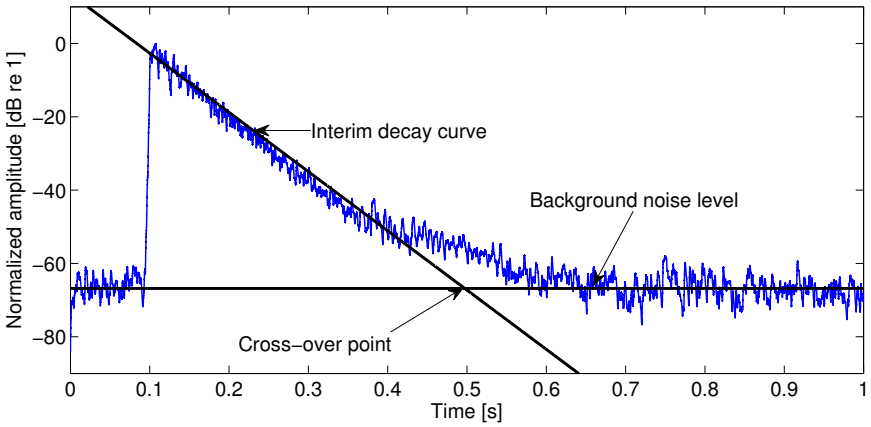

Figure D.1: Determination of cross-over point t_x between background noise level and interim decay curve.

with the impulse response. To minimise the influence of background noise, the integration should only be performed between t and the point where the impulse response crosses the background noise level. To determine the cross-over point t_x, it is necessary to estimate the background noise level. This can be done, for example, by calculating the root-mean-square value of a late part of the signal, when the impulse response has been allowed to decay below the background noise level. Once the background noise level has been estimated, an approximate interim decay curve is used to estimate the cross-over point. The interim decay curve may be obtained by calculating a sloped line through a representative part of the squared impulse response. Figure D.1 shows an example. The interim decay curve must not be confused with the energy decay curve used to evaluate the reverberation time.

When the cross-over point t_x between the squared impulse response and the background noise level has been determined, the backward-integration of the squared impulse response is performed:

$$E(t) = \int_t^{t_x} h^2(\tau)\,\mathrm{d}\tau + C = \int_{t_x}^{t} h^2(\tau)\,\mathrm{d}(-\tau) + C, \tag{D.3}$$

where C is an optional correction term for the energy between t_x and ∞. The result is an energy decay curve (EDC), such as in Figure D.2. The slope of the EDC indicates the damping of the structure. In highly-damped structures, the energy dissipates quickly. In lightly-damped structures, the energy decay

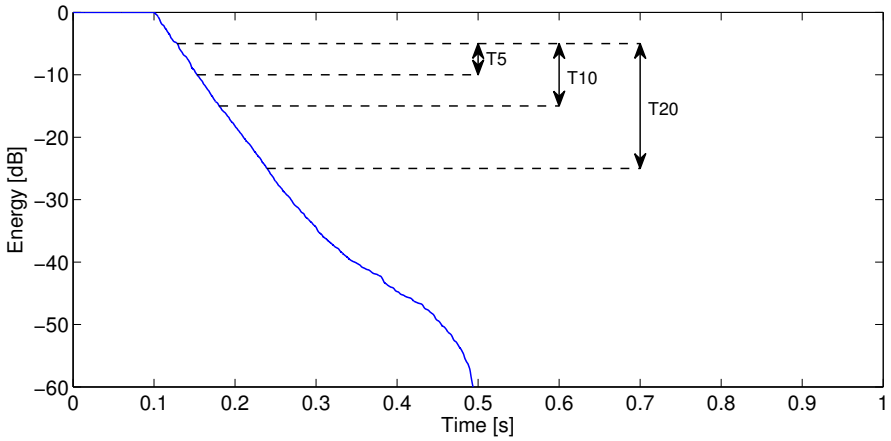

Figure D.2: Energy decay curve, calculated by backward-integration.

takes longer. The EDC also indicates whether the structure is coupled to other structures. Isolated structures typically have an EDC with a single gradient, while EDCs for coupled systems show multiple slopes. Figure 8.5 in Chapter 8 shows a simulated example. The initial decay indicates the total loss factor, while later slopes also contain energy returning from connected elements.

The final step in the calculation of the structural reverberation time is the evaluation of the EDC. A linear regression line is fitted to the EDC, using a least-squares procedure, and the reverberation time calculated from its slope. The reverberation time is defined as the time in which the energy in the system decreases by 60 dB from an initial value. Since it is often not possible to achieve a dynamic range of 60 dB, the regression line is usually fitted to a shorter decay. For example, the regression line obtained from an evaluation range of 10 dB yields a reverberation time estimate called T_{10}, to distinguish it from estimates using different evaluation ranges. The first 5 dB of a decay are generally discarded, to avoid the influence of the filters. T_{10} thus uses the decay between -5 dB and -15 dB for the calculation of the regression line.

For EDCs with a single gradient, estimates using different evaluation ranges give similar results. Figure D.3 shows an example: T_5, T_{10}, and T_{20} are within 0.03 s of each other. For EDCs with multiple gradients, however, the choice of evaluation range can significantly affect the reverberation time estimate. To estimate the total loss factor, only the initial slope should be used, excluding the part that is affected by the filters. While usually the first 5 dB are discarded

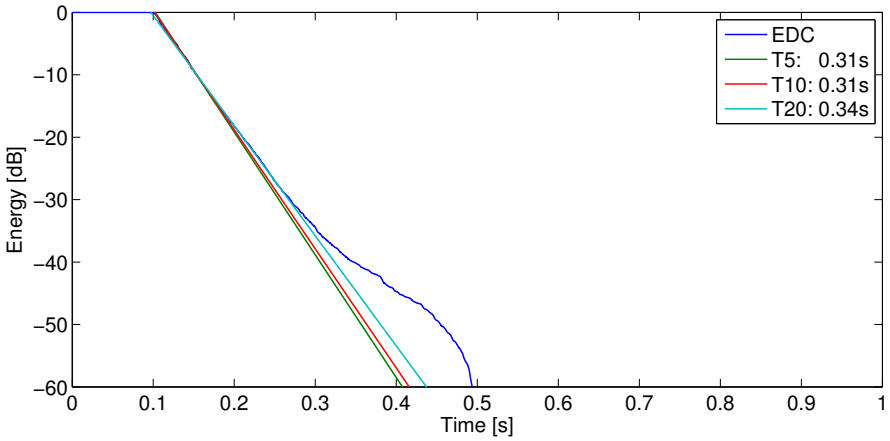

Figure D.3: Energy decay curve and estimated reverberation times.

to exclude filter effects, Hopkins and Robinson [74] suggest that the evaluation start point may lie at $-2\,\mathrm{dB}$, to ensure errors in the total loss factor are less then $0.5\,\mathrm{dB}$ between $50\,\mathrm{Hz}$ and $500\,\mathrm{Hz}$. They also propose a procedure for an automated optimization of the evaluation range. An indicator of the agreement between EDC and regression line is the correlation coefficient. For EDCs with multiple slopes, the correlation decreases. Curves with low correlation (for example $R_x < 0.95$) should not be considered in the reverberation time estimation.

To obtain a representative loss factor estimate, a sufficient number of excitation positions and response positions must be used. ISO 10848-1:2006 requires at least three excitation points and at least three response positions. The results of individual measurements vary, due to modal behaviour of the structure. ISO 10848-1:2006 suggests taking the arithmetic average (mean value) of the individual structural reverberation times. However, it has been suggested [93] that the median value is a better representation, as it attaches less importance to outliers than the mean value. The author's experience supports this statement.

Finally, from the obtained structural reverberation time, the total loss factor is calculated according to Equation (D.1).